LAWRENCE
LIVERMORE
NATIONAL
LABORATORY

LLNL-JRNL-765064

Turbulent Mixing and Transition Criteria of Flows Induced by Hydrodynamic Instabilities

Y. Zhou, T. Clark, D. Clark, S. Glendinning, M. A. Skinner, C. Huntington, O. Hurricane, A. Dimits, B. Remington

January 7, 2019

Physics Plasma

Disclaimer

Turbulent Mixing and Transition Criteria of Flows Induced by Hydrodynamic Instabilities*

Ye Zhou[1a)], Timothy T. Clark[2], Daniel S. Clark[1], S. Gail Glendinning[1], M.Aaron Skinner[1], Channing M. Huntington[1], Omar A. Hurricane[1], Andris M. Dimits[1], Bruce A. Remington[1]
[1] *Lawrence Livermore National Laboratory*
Livermore, California, 94550
[2] *University of New Mexico*
Albuquerque, New Mexico, 87131
(Dated: June 14, 2019)

In diverse areas of science and technology, including inertial confinement fusion (ICF), astrophysics, geophysics, and engineering processes, turbulent mixing induced by hydrodynamic instabilities is of scientific interest as well as practical significance. Because of the fundamental roles they often play in ICF and other applications, three classes of hydrodynamic instability-induced turbulent flows– those arising from the Rayleigh-Taylor (RT), Richtmyer-Meshkov (RM), and Kelvin-Helmholtz (KH) instabilities– have attracted much attention. The ICF implosion, supernova explosion, and other applications illustrate that these phases of instability growth do not occur in isolation, but instead are connected so that growth in one phase feeds through to initiate growth in a later phase. Essentially, a description of these flows must encompass both the temporal and spatial evolution of the flows from their inception. Hydrodynamic instability will usually start from potentially infinitesimal spatial perturbations, will eventually transition to a turbulent flow, and then will reach a final state of a true multiscale problem. Indeed, this change in the spatial scales can be vast, with hydrodynamic instability evolving from a just few microns to thousands of kilometers in geophysical or astrophysical problems. These instabilities will evolve through different stages before transitioning to turbulence, experiencing linear, weakly, and highly nonlinear states. The challenges confronted by researchers are enormous. The inherent difficulties include characterizing the initial conditions of such flows and accurately predicting the transitional flows. Of course, fully developed turbulence, a focus of many studies because of its major impact on the mixing process, is a notoriously difficult problem in its own right. In this pedagogical review, we will survey challenges and progress, as well discuss outstanding issues and future directions.

CONTENTS

* CT3, Bulletin of the American Physical Society (2018)
a) Invited review speaker.
Electronic address: yezhou@llnl.gov

I. INTRODUCTION

The related topics of fluid dynamical instabilities, the transition of laminar flow fields to turbulence, and the evolution of fully turbulent flow, as well as the effects these flows have on mixing rates, have presented significant challenges to researchers for over 100 years. Although substantial progress has been made in these fields, each topic remains an active topic of research.

In this paper we will limit our discussion to turbulence (Figure 1) and mixing of fluids or collision-dominated (dense) plasmas induced by three classes of instabilities–the Rayleigh-Taylor Instability (RTI) [1, 2], the Richtmyer-Meshkov Instability (RMI) [3, 4] and the Kelvin-Helmholtz Instability (KHI) [5, 6].

This work complements and further elaborates the recent comprehensive reviews on hydrodynamic instability induced flows [7, 8]. In these flow scenarios, an initially perhaps infinitesimal perturbation at an interface induces an instability. For the cases of RTI and RMI, the fluid may be initially quiescent, whereas the initial state of the KHI is a laminar flow. The instability may lead to a transitionally chaotic state exhibiting the emergence of both small-scale and increasingly larger scales of fluid motions. These instabilities are present in a wide variety of important circumstances involving engineering processes, geophysical and astrophysical flows, as well as in inertial confinement fusion (ICF).

Motivated by the need to better understand the instability processes that occur in astrophysical contexts [10–14] and in ICF [15–19], as well the behavior in materials with strength subjected to rapid and large compressions [20, 21], and coupled to the need to test the veracity of the computer simulations that are commonly used to model these processes, the field of high energy density physics (HEDP) has developed. HEDP experiments, used to test and validate theoretical models as well as simulation predictions, characteristically deposit tens of kilo-Joules to mega-Joules of energy in millimeter-scale targets on timescales of nanoseconds, thus directly generating plasmas of $\sim 1-100$ megabar pressures. With the additional use of an implosion, pressures of ~ 100's of gigabars can be achieved [22]. The resulting flows emulate, by design, important processes at the plasma conditions of interest. In some cases, HEDP experiments are designed to have a certain aesthetic as well as scientific value [23], and result in stunning data images [24], that may lead to a new areas of study that are productive for students and researchers in HEDP [25–36]. Beyond studying instability, applied physics problems sometimes require that instabilities be mitigated in order to achieve a practical goal.

To study the problems of interest in this paper, it is generally desirable to allow the instability to evolve to a fully-developed turbulent state. This poses stringent requirements for numerical simulations, laboratory experiments, and HEDP platforms. A key objective of this paper is to highlight the necessary and sufficient conditions for the transition process that marks the onset of a fully turbulent state to occur. To make it self-contained, this manuscript is structured as follows: in Section II, we first characterize "fully developed turbulence" from the perspective of Kolmogorov's theory [37–41]. In Section III, we turn our attention on the initiation of turbulence. In particular, we restrict ourselves to hydrodynamic instability-induced flows, as we are focused in the applications to ICF implosions (Section IV) and supernova explosions (Section V). In Section VI, we detail the criteria for these instability-induced flow to transition to fully-developed turbulence. This is followed by discussion of two important issues, the importance of the initial conditions (Section VII) and the need for enhanced diagnostic measurements (Section VIII) in high energy density platforms. Next, we address the question whether two-dimensional (2D) turbulence resemble three-dimensional (3D) turbulence (Section IX). Before we conclude, some especially interesting issues and outstanding problems will be discussed.

II. THE TURBULENT STATE

A. Governing equations and Reynolds number

Generally, researchers assume that fluid motions from the instabilities to turbulent flows are described by the Navier-Stokes equations [42, 43];

$$\frac{\partial \rho u_i}{\partial t} + \frac{\partial \rho u_i u_n}{\partial x_n} = \frac{\partial \sigma_{in}}{\partial x_n} + f_i(t) \tag{1}$$

where σ_{ij} is the stress tensor,

$$\sigma_{ij} = \mu \left[\frac{\partial u_i}{\partial x_j} + \frac{\partial u_j}{\partial x_i} - \frac{2}{3}\delta_{ij}\frac{\partial u_n}{\partial x_n} \right] - \delta_{ij} p \tag{2}$$

where ρ is the fluid density, p is the pressure, μ is the dynamic viscosity, and $f_i(t)$ is the forcing term, which

FIG. 1: Illustration of turbulent flows by Leonardo da Vinci.

equal to zero in a decaying flow [44, 45]. The equation governing the transport of the density, ρ is

$$\frac{\partial \rho}{\partial t} + \frac{\partial \rho u_n}{\partial x_n} = 0. \tag{3}$$

The Reynolds number (Re) characterizes the state of the flow field and is defined as

$$Re = Lu/\nu. \tag{4}$$

Here, L and u are the characteristic length scale and velocity field, respectively, and ν is the kinematic viscosity given by $\nu = \mu/\rho$ [46]. This dimensionless parameter is obtained by comparing the nonlinear and viscous terms of the Navier-Stokes equations [47, 48] and represents the ratio of inertial forces to viscous forces. Depending on the values of Reynolds number, the flow field is either laminar or else evolving toward a turbulent flow or already turbulent. In fact, the onset of turbulence occurs when the Reynolds number is larger than a threshold value. When the viscous action is strong, the flow is laminar and any perturbations from smooth motion are damped away. When the flow is fully turbulent, however, it contains eddy motions of all sizes admissible within the flow geometry. A large part of the mechanical energy in a turbulent flow goes into the formation of these eddies, and the effects of viscosity eventually dissipates their energy as heat [49].

In Van Dykes book, *An Album of Fluid Motion*, photographs showing flow passing through spheres demonstrate how dependent these flows can be on the Reynolds number. At $Re = 100$, the flow separates and a recirculating region forms. As Re increases to $Re = 15000$ and $Re > 200000$, the flow develops both the large-scales structures and small-scale motions [50]. The same is true for the jet flows shown in Figure 2. When Re is not extremely high, there are many organized large-scale features. However, when Re is increased significantly, the flows exhibit an extremely wide range of scale of motions [51].

B. Cascade

The well known poem by Richardson [52] vividly illustrates some key features of the evolution of turbulent flows:

Big whirls have little whirls
Which feed on their velocity,
And little whirls have lesser whirls
And so on to viscosity.

The sketch in Figure 3 is a good starting point for study of high Re 3D flows. Here, the large-eddies reflect the inhomogeneities characteristic of the forces and boundary conditions which produce them. Nevertheless, since the characteristic time-scales associated with the eddies decreases geometrically with eddy size, a large number of generations is produced during the lifetime of the large anisotropic eddies. The flow will evolve into a quasi-stationary self-similar hierarchy of eddies, frequently termed a cascade process, whose wavenumbers form a geometric progression [40, 53, 54]. The smallest eddies will be limited by the viscous action at the smallest length scales, the Kolmogorov dissipation scales, η, a

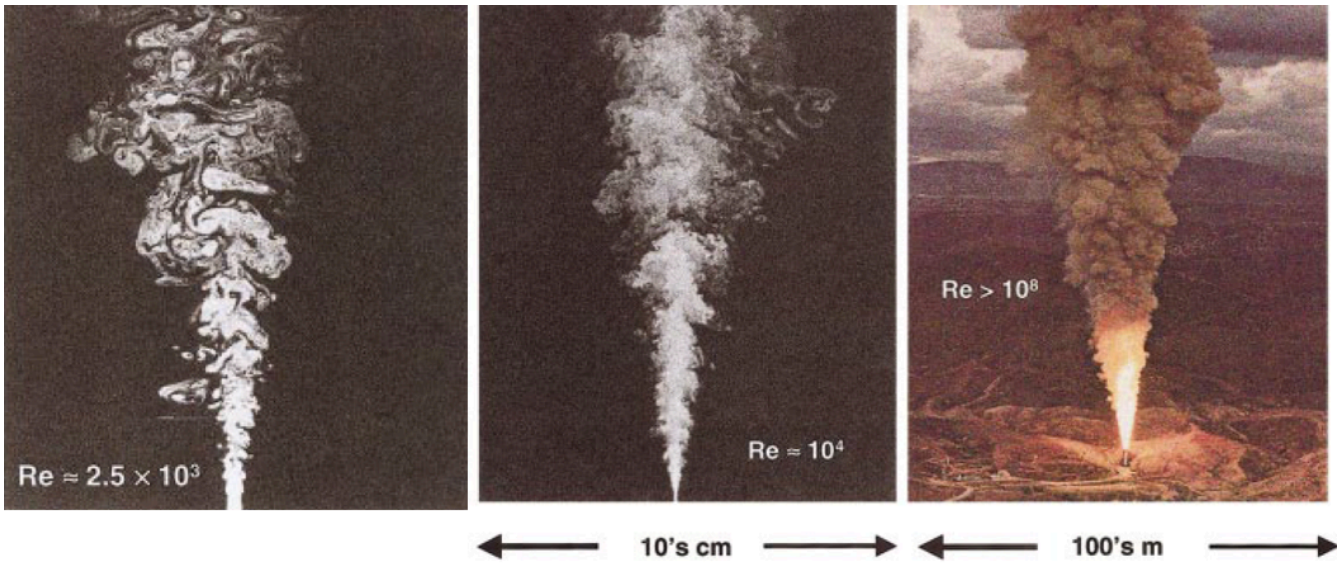

FIG. 2: Jet-fluid concentration in the plane of symmetry of round turbulent jets for $Re \approx 2.5 \times 10^3$ (left frame) and $Re \approx 10^4$ (center frame). Rocket testing in the Los Angles hills, $Re > 10^8$ (right frame). See Ref. [51]. Reproduced from *Phys. Fluids*, **26**, 3185 (1983), with the permission of AIP Publishing.

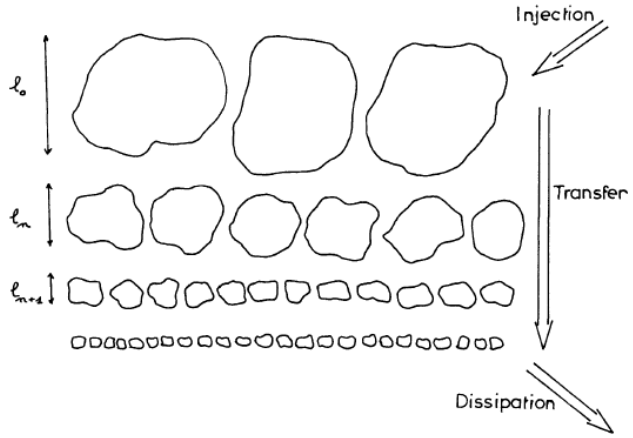

FIG. 3: The energy cascade according to the 1941 Kolmogorov theory. Notice that at each step the eddies are space filling [54]. Reproduced with permission from *J. Fluid Mech.*, **87**, 719 (1978). Copyright 1978, Cambridge University Press.

precise definition of which will be given in Eq. 20.

The energy injection takes place at the largest eddy length-scales. The energy transfer process in the cascade process in 3D turbulence proceeds from large to small scales. The time required for an eddy to be distorted and, in this distortion process, generate smaller eddies is called an eddy-turnover-time. Finally, the energy is dissipated from the smallest eddies due to viscous effects.

Figure 4 provides a sense of the various length scales from a flow visualization obtained from direct numerical simulation (DNS) of homogeneous isotropic turbulence [55, 56]. The Reynolds number is very high, at Re=216,000. [Note that the Reynolds number based on the Taylor microscale (λ), $Re_\lambda = 1131$, is given in the original article. However, $Re_\lambda = (20/3)^{1/2} Re^{1/2}$ for homogeneous and isotropic flow, see Tennekes and Lumley [57]. The important length scales, including the Taylor microscale, will be defined more precisely later in subsection II C].

Some fiducial markers are included in the image as a point of reference. The first is the length scale of the large-eddies and a precise definition, termed the integral length scale, will be provided later. Also shown is 100 times the Kolmogorov dissipation scale, η. This figure demonstrates that turbulence is a true multi-scale problem and extremely difficult to describe numerically and analytically due to the wide range of length scales in the underlying physical problems.

C. Statistics and length scales

Beginning with the pioneering work of Osborne Reynolds [58], mathematical descriptions of turbulent flows have been essentially statistical, representing, for example, the velocity, u_i as the sum of an averaged value, $\langle u_i \rangle$ and a fluctuating value. In many published papers, the definition of the average is left readers imagination. For our case, where we are concerned with the temporal evolution of a strongly inhomogeneous field, neither temporal nor spatial averages seem appropriate, so we assume an ensemble average over a number of realizations wherein the supposedly larger-scale details of the field such as the geometry, may be identical across each realization, but the finer-scale details, for example, the

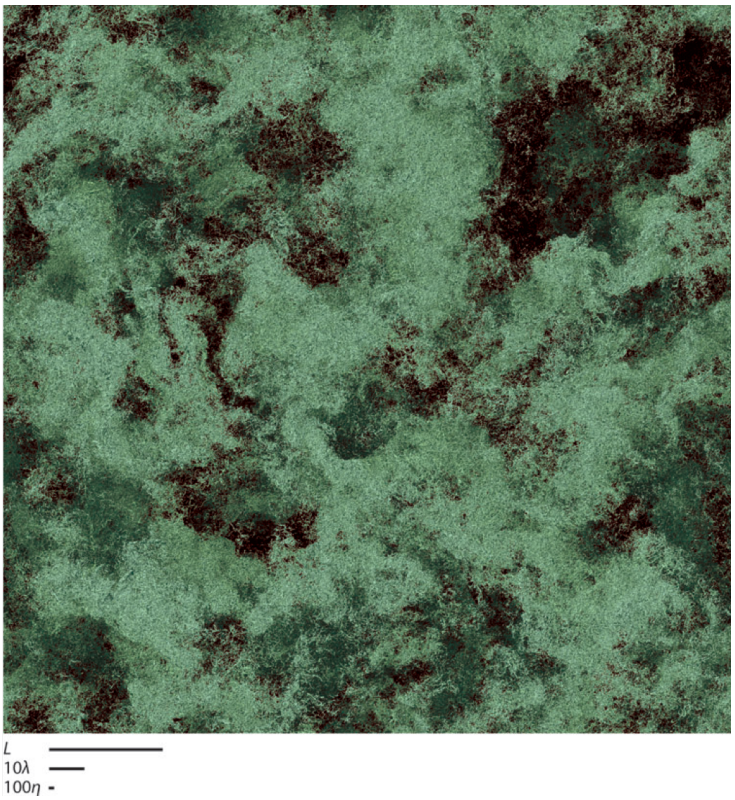

FIG. 4: Regions of intense vorticity in DNS at the Taylor-microscale Reynolds number $R_\lambda = 1131$ [55]. Reproduced with permission from Ishihara *et al.*, *Flow, Turbulence and Combustion*, **91**, 895 (2013). Copyright 2013, Springer

perturbations at an interface may vary across the individual realizations.

It worth noting that time-averaging is inappropriate in that these flows are rapidly evolving in time. Spatial averaging may be appropriate in circumstances wherein (a) the scale of fluctuations is much smaller than the bulk motions of the fluid, or (b) when there is a homogeneous direction(s) over which to average. It must be noted that the assumption of homogeneity is not equivalent to an assumption of periodicity, and that assuming homogeneity may mask effects of large scale flow features in the presumed homogeneous directions. The ensemble average provides the most generally applicable approach, but is difficult to realize both experimentally and via direct numerical simulations. However, for the task of deriving fundamental evolution equations, and for theoretical study, the ensemble average provides the most succinct description. Hence, from a fundamental point of view, the ensemble average is the appropriate definition of the averaging process. However, for most time evolving applications the ensemble average is approximated by averaging over any available statistically homogeneous directions e.g. planar averaging.

We therefore let the angle brackets represent an ensemble average. Then the average of a variable, say the velocity, is

$$\langle u_i(\mathbf{x})\rangle = \frac{1}{N_e}\sum_{n=1}^{N_e} u_i^{(n)}(\mathbf{x}), \tag{5}$$

where N_e is the number of elements in the ensemble and the superscript (n) represents the n^{th} realization in the ensemble. The fluctuational part, denoted with a prime, is then simply

$$u_i'(\mathbf{x}) = u_i(\mathbf{x}) - \langle u_i(\mathbf{x})\rangle, \tag{6}$$

and obviously, $\langle u_i'(\mathbf{x})\rangle = 0$ by construction. Many of the so-called Reynolds Averaged Navier-Stokes (RANS) turbulence models [59–61] are constructed by applying this decomposition (or the related mass-averaged statistical decomposition) to the Navier-Stokes equations and deriving an exact equation for the mean. Unfortunately, the mean flow equation will have second-order moments which must either be modeled or for which an additional evolution equation must be derived. For our current purpose - describing the Kolmogorov cascade process - we will assume an incompressible, constant density flow. Under these restrictions, the evolution equation will have a quadratic nonlinearity in the fluctuating velocity;

$$R_{ij}(\mathbf{x}) = \left\langle u_i'(\mathbf{x})\, u_j'(\mathbf{x})\right\rangle, \tag{7}$$

where $R_{ij}(\mathbf{x})$ is the so-called Reynolds stress, which is related to the turbulent kinetic energy, K by

$$K(\mathbf{x}) = \frac{1}{2} R_{nn}(\mathbf{x}), \tag{8}$$

where the repeated index implies a summation. The notion of the Reynolds stress can be generalized by considering the correlation of velocities at two different points in space,

$$R_{ij}(\mathbf{x_1}, \mathbf{x_2}) = \left\langle u_i'(\mathbf{x_1})\, u_j'(\mathbf{x_2}) \right\rangle. \tag{9}$$

Letting

$$\begin{aligned} \mathbf{x_c} &= \frac{1}{2}\left[\mathbf{x_1} + \mathbf{x_2}\right], \\ \mathbf{r} &= \left[\mathbf{x_1} - \mathbf{x_2}\right], \end{aligned} \tag{10}$$

allows the equation 9 to be rewritten as

$$R_{ij}(\mathbf{x_c}, \mathbf{r}) = \left\langle u_i'\left(\mathbf{x_c} + \frac{1}{2}\mathbf{r}\right) u_j'\left(\mathbf{x_c} - \frac{1}{2}\mathbf{r}\right) \right\rangle. \tag{11}$$

If we assume that the field is homogeneous [37], then the two-point Reynolds stress tensor is independent of $\mathbf{x_c}$ and can be written as;

$$R_{ij}(\mathbf{x_c}, \mathbf{r}) \rightarrow R_{ij}(\mathbf{r}). \tag{12}$$

Applying a Fourier transform yields the three-dimensional spectrum

$$R_{ij}(\mathbf{k}) = \iiint_{-\infty}^{+\infty} R_{ij}(\mathbf{r})\, e^{i\mathbf{k}\cdot\mathbf{r}} \mathrm{d}\mathbf{r}, \tag{13}$$

Finally we can "average" over all angles in Fourier space to arrive at

$$E_{ij}(k) = \frac{1}{2} \int R_{ij}(\mathbf{k}) \frac{\mathrm{d}\Omega_k}{(2\pi)^3}, \tag{14}$$

where $k = |\mathbf{k}|$. The turbulent kinetic energy spectrum is thus $E(k) = E_{nn}(k)$ and the turbulence kinetic energy density (that is, the energy per unit of mass) is thus

$$K = \langle u_n' u_n' \rangle = \int_0^\infty E(k)\, \mathrm{d}k, \tag{15}$$

and

$$K_\alpha = \langle u_\alpha' u_\alpha' \rangle = \int_0^\infty E_\alpha(k)\, \mathrm{d}k, \tag{16}$$

where $E_i(k)$ is the component energy spectrum.

The velocity autocorrelation [47, 62], $\mathcal{R}_{ii}(r)$ is defined as

$$\mathcal{R}_{ii}(r) = \frac{R_{ii}(r)}{R_{ii}(0)}. \tag{17}$$

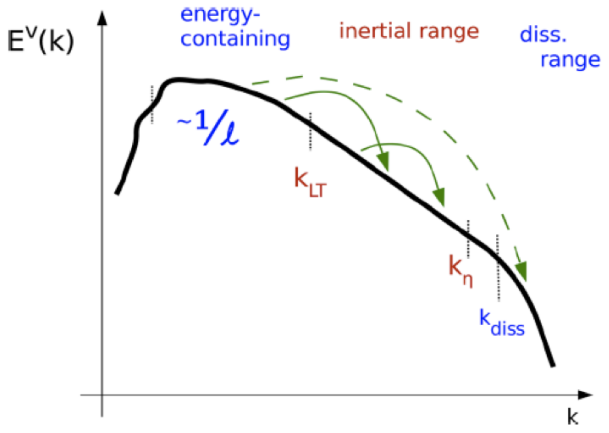

FIG. 5: Sketch of a kinetic energy spectrum indicating the energy-containing, inertial, and dissipation ranges and their wavenumber boundaries. The idea behind the minimum state is that the inertial range should be long enough so that direct interactions between modes in the energy-containing and dissipation ranges are energetically weak, indicated by the dashed (green) arrow. Some "strong" interactions are indicated via the solid (green) arrows [63]. Reproduced from *Phys. Plasmas,* **18**, 072304 (2011), with the permission of AIP Publishing.

D. Kolmogorov Phenomenology

Kolmogorov's 1941 "Phenomenology", which is basically a dimensional argument, is of particular significance owing to limitations of computational resources in the foreseeable future. Figure 5 [63] shows the relevant features of the Kolmogorov 1941 theory. Essentially, a flow field always has an energy-containing scale, which corresponds to the large-eddies discussed in the previous subsection. The "energy spectrum", $E(k)$, defined above, provides a useful mathematical object for understanding Kolmogorov's theory. The contributions to the energy spectrum, $E(k)$, from the energy-containing scale, are located in the vicinity of the low wavenumbers. At the other end of the energy spectrum is the so-called dissipative scale, where $E(k)$ decreases exponentially as a result of the viscous action. Moreover, Kolmogorov predicted that if the Reynolds number is sufficiently large, the energy-containing scale will be separated from the dissipation scale by an inertial range in which $E(k)$ scales as $k^{-5/3}$. The larger the Reynolds number, the wider the inertial range will be.

The Phenomenology makes the following assumptions:

- The turbulence is locally isotropic, i.e., at small scales the turbulence statistics are invariant under translation and rotation.
- The turbulence is near "equilibrium," i.e., the energy injection (the forcing on the turbulence),

$\mathcal{F}$ that drives the turbulence is approximately matched by the rate, $\mathcal{E}$ at which the viscous effects dissipate the energy, i.e., $\mathcal{F} \approx \mathcal{E}$.

- The wave number characterizing the energy injection, k_F is much smaller than the wave number k_d characterizing where the energy is dissipated, $k_F \ll k_d$
- The cascade process through k-space is "local", i.e., that the transfer through wavenumber k depends on the dynamics in the neighborhood near k [64–66].

It is also essential to the analysis that the energy transfer in Fourier space is conservative due to the nature of the nonlinearities of the Navier-Stokes equations.

Under these sets of assumptions, the energy in the cascade is assumed to be independent of the details of the forcing as well as the details of the dissipation process, and is simply a function of the energy traversing from the small wavenumbers to the large wave numbers. However, since the transfer is conservative, this energy transfer rate is equal to the injection rate $\mathcal{F}$, which is equal to the dissipation rate $\mathcal{E}$. Under these conditions, one can choose to express $E(k)$ either in terms of the injection rate or in terms of the dissipation rate. In terms of the dissipation rate, the generic form is thus

$$E(k) = C_K \mathcal{E}^p k^q, \tag{18}$$

where C_K is the so-called Kolmogorov Constant, and the exponents p and q are determined by dimensional arguments. Since $E(k)$ has units of $[Length^3/Time^2]$, $\mathcal{E}$ has units of $[Length^2/Time^3]$ and k has units of $[1/Length]$, the time scaling of E can only be reconciled if the exponent of $\mathcal{E}$ is $p = 2/3$, where now $\mathcal{E}^{2/3}$ has units of $[Length^{4/3}/Time^2]$. Thus the exponent of k must be $q = -5/3$ to produce the correct length scaling for E. The result is the Kolmogorov scaling law

$$E(k) = C_K \mathcal{E}^{2/3} k^{-5/3}. \tag{19}$$

There is no consensus regarding whether C_K is a universal constant, but it appears to be approximately $C_K \approx 1.5$ [67–70]. In addition, Kolmogorov deduced that the length scale, $\eta \sim 1/k_d$ (the "Kolmogorov microscale") which characterizes the range of scales where energy is dissipated by viscous processes should be independent of the large-scales, and a function only of the active variables at fine scales, e.g. viscosity, ν and the dissipation rate itself, $\mathcal{E}$. Dimensional analysis then gives the result that

$$\eta = \left(\frac{\nu^3}{\mathcal{E}}\right)^{1/4}. \tag{20}$$

Figure 6 is a compilation of experimental measurements of the energy spectrum [71]. The longest inertial ranges are especially noteworthy: Grant *et al.* collected their data from the Discovery Passage, a tidal channel of the west coast of Canada [72]. Praskovsky *et al.* obtained their results from a return channel in the large wind tunnel of the Central Aerohydrodynamic Institute [73]. Saddoughi and Veeravalli carried out their experiments with the 80 x 120-foot Full-Scale Aerodynamics Facility at NASA Ames Research Center [71]. Clearly, the energy-containing and dissipation scales in these and other high Re flows are very well separated by an extended inertial range. Moreover, the measured energy spectrum confirms the $k^{-5/3}$ scaling predicted by Kolmogorov. For contrast, a number of low Re flows energy spectra are also included in Figure 6. For these experiments, the energy-containing scales are closely linked to the dissipation scales. As a result, no inertial range can be discerned.

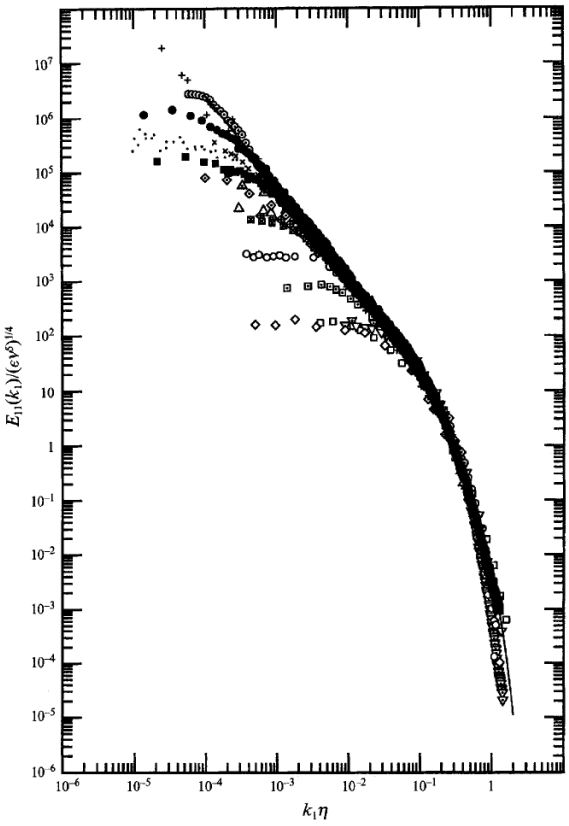

FIG. 6: Kolmogorov's universal scaling for one-dimensional longitudinal power spectra [71]. Reproduced with permission from Saddoughi & Veeravalli, *J. Fluid Mech.*, **268**, 333 (1994). Copyright 1994, Cambridge University Press.

The Kolmogorov theory addresses the behavior of the statistics of the covariance of the velocity field but says nothing about the density statistics. For those flows where density variations are intrinsic to the behavior (RTI, RMI and KHI with buoyancy), the density behaves as an active scalar. Obukhov [74] and Corrsin [75] applied/extended the Kolmogorov 1941 theory to the case

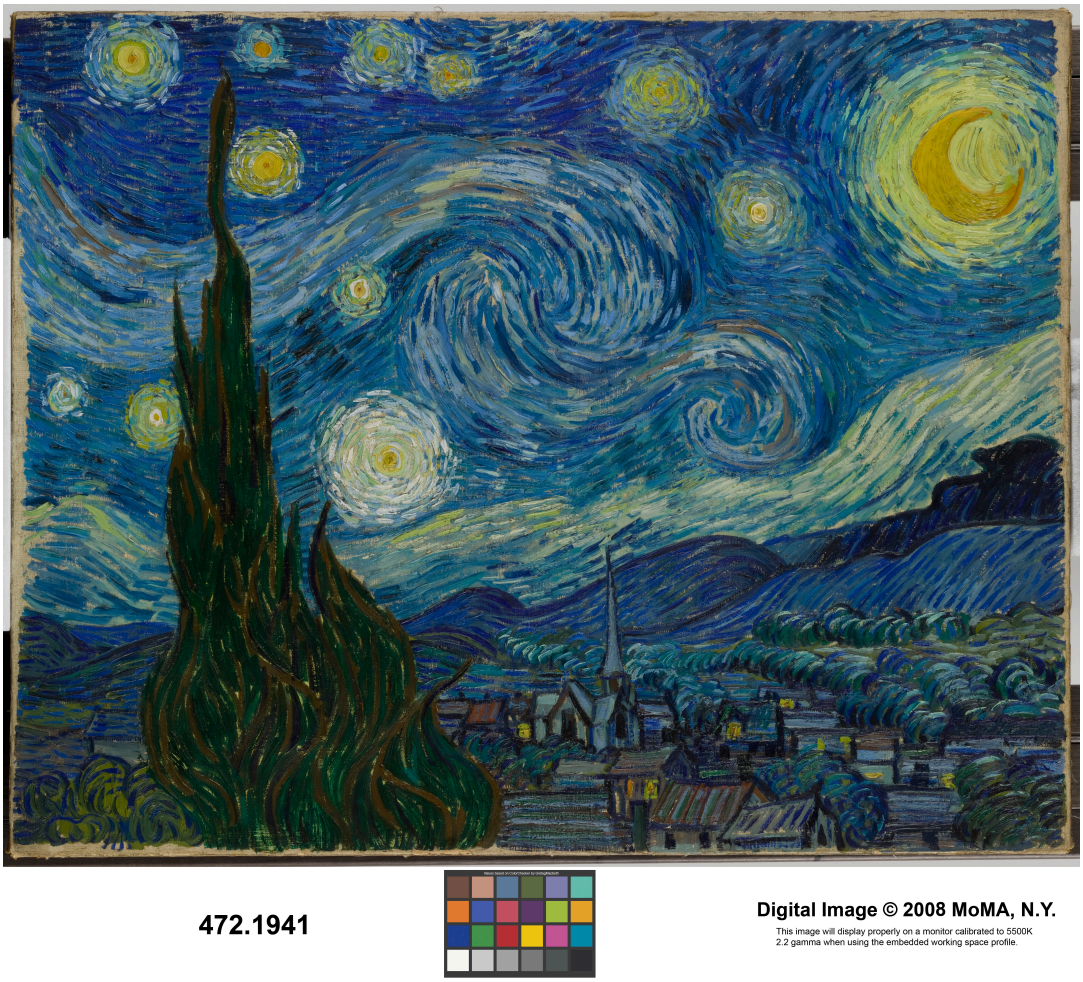

FIG. 7: Vincent van Gogh, The Starry Night, Saint Rémy, June 1889. ©The Museum of Modern Art, New York. https://www.moma.org/collection/works/79802

of a passive scalar, e.g. weak temperature fluctuations, and deduced that the scalar spectrum, $T(k)$ behaves as

$$E_T(k) = C_T \mathcal{E}_T \mathcal{E}^{-1/3} k^{-5/3}, \tag{21}$$

where $\mathcal{E}_T$ is the dissipation rate of the scalar due to diffusion, and is assumed to be equal to the injection rate to the scalar spectrum, and C_T is a constant. The scalar microscale, η_T is then equal to

$$\eta_T = \left(\frac{\mathcal{D}^3}{\mathcal{E}} \right)^{1/4}. \tag{22}$$

where $\mathcal{D}$ is the diffusivity of the scalar. There are also potentially different "subranges" in the scalar spectrum depending on the Schmidt number, $Sc = \frac{\mathcal{D}}{\nu}$. This topic is beyond our current scope and the reader is referred to [57] for further details. For RTI flows, $Sc \sim 600$ for the brine/water experiments of Dalziel *et al.* [76] and the follow-up experimental work by Banerjee and Mutnuri [77] has $Sc \sim 10^3$. Molecular mixing measurements were reported [78] for a high-Schmidt-number ($Sc \sim 10^3$) buoyancy-driven turbulent RT mixing layer in a water channel facility with a weakly buoyant flow.

The dominant, most energetic scales, L of the turbulence are typically independent of viscous effects, and are a function of the large-scale variables, i.e.,the energy injection rate, F which, in turn, is usually related to the overall geometry of the flow domain). Again dimensional analysis produces

$$L = \frac{K^{3/2}}{F}, \tag{23}$$

but because $F = \mathcal{E}$ for our near-equilibrium case, we more commonly see this as

$$L = \frac{K^{3/2}}{\mathcal{E}}, \tag{24}$$

which is generally preferred since it does not depend on a variable that is extrinsic to the description of the turbulent field itself.

In cases where the largest scale is not obvious from the

FIG. 8: A multi-wavelength image of the Crab Nebula with data from radio waves to X-rays. This image contains data from Chandra X-Ray Observatory (purple), VLA (red), Spitzer (yellow), Hubble (green), and XMM-Newton (blue). Image Credit: NASA. http://chandra.harvard.edu/photo/2017/crab/

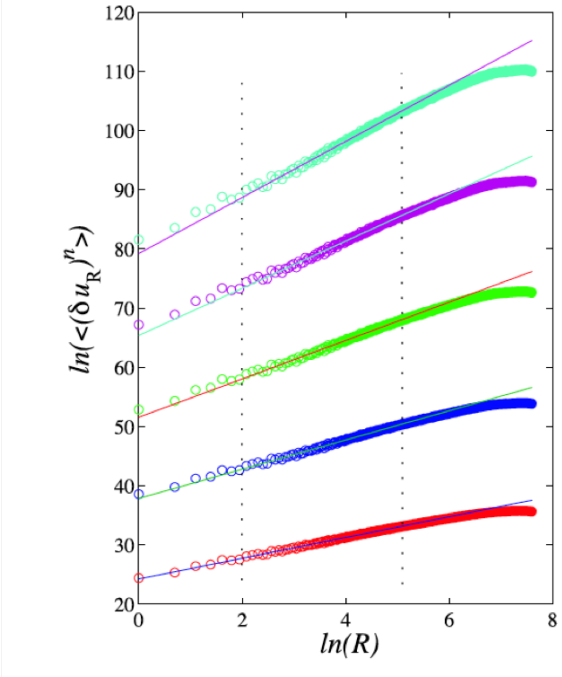

FIG. 9: Log-log plot of the statistical moments, with n = 1, 2, 3, 4, 5 (from bottom to top). In each case the straight line indicates the least-squares fit to the range of scales limited by the two dashed lines in the plot [82]. Reproduced with permission from *J. of Mathematical Imaging and Vision*, **30**, 275 (2008). Copyright 2008, Springer.

flow geometry, an integral scale can be obtained as

$$L = \int_0^\infty \mathcal{R}_{ii}(r,t)dr \tag{25}$$

which is a measure of the longest connection or correlation distance between two points in the flow that are separated either by distance or time [47].

When the total or component energy spectrum is available, the energetic scales defined above, are also known as the integral length scales and take the form

$$L = \frac{\int_0^\infty k^{-1}E(k)dk}{\int_0^\infty E(k)dk}, \tag{26}$$

or

$$L_i = \frac{\int_0^\infty k^{-1}E_i(k)dk}{\int_0^\infty E_i(k)dk}. \tag{27}$$

Another key turbulent scale is the Taylor microscale, λ, where

$$\lambda = \sqrt{10\nu\frac{K}{\mathcal{E}}}, \tag{28}$$

(See pages 66–68 of Tennekes and Lumley [57] for more details.) This definition is particularly convenient for application to simulation data.

A standard way to compute the Taylor microscale is from the curvature of the velocity autocorrelation [62], $\mathcal{R}(r)$. Note that $\mathcal{R}(r)$ is an even function, so that it is symmetric $\mathcal{R}(r) = \mathcal{R}(-r)$. Performing the Taylor expansion, the leading terms are

$$\mathcal{R}(r) = 1 - \frac{r^2}{\lambda^2}, \tag{29}$$

where the Taylor microscale is defined as

$$\lambda = \left[-\frac{1}{2}\frac{d^2\mathcal{R}(0)}{dr^2}\right]^{-1/2}. \tag{30}$$

Another way of estimating the Taylor microscale from experimental data has been utilized with the variance of the velocity and the variance of the first derivative of velocity, is [79, 80]

$$\lambda = \left[\frac{2 < u^2 >}{(< \frac{\partial u}{\partial x})^2 >}\right]^{1/2}. \tag{31}$$

E. Astrophysical flows, turbulence, and the masterpiece

"The Starry Night" (Figure 7) was painted by van Gogh in 1889 during his periods of prolonged psychotic agitation [81]. The tie between the distant star observed by Hubble (Figure 8) and this famous artwork was noted

by NASA. The Museum of Modern Art (MoMA), New York City also noted that "the whirling forms in the sky match published astronomical observations of clouds of dust and gas known as nebulae." While highly suggestive, can the masterpiece be linked to the fluid flows of turbulence?

Aragón *et al.* used digital images of these paintings of van Gogh to show that the statistics of luminance contains the characteristic fingerprint of turbulent flow [82]. Indeed, these authors showed that Starry Night, and other impassioned van Gogh paintings, transmitted the essence of turbulence with high realism. This was shown by comparing the "structure functions" deduced from the paintings (analogous to those for computed for turbulence [83]), shown in Figure 9 to actual measurements of structure functions from a wind tunnel [84].

The Reynolds number for the astrophysical flows are very high. For the degenerate carbon-oxygen white dwarf explosion (Type Ia), Kuhlen *et al.* [85] and Woosley *et al.* [86] found

$$Re \sim 10^{14}, \tag{32}$$

and for the core-collapse of a massive star (Type II), Abdikamalov *et al.* [87] determined that

$$Re \sim 10^{17}. \tag{33}$$

A more detailed classification of supernovae will be offered in subsection V A. For Supernova remnants (SNR), it is estimated that

$$Re \sim 6 \times 10^{8}. \tag{34}$$

[88, 89]. Hence, an extended inertial range is expected for these flows.

F. Turbulence and mixing

Why do we care about turbulence? Usually due to its effect on mixing. In turbulent flows, the mixing of the mass, momentum, and energy occurs at a significantly more rapid rate than for laminar flows.

Turbulent mixing can be grouped into three categories [90], based on increased role of mixing. The first category is composed of those cases where turbulent flow drives mixing, but the mixing itself plays essentially no role in the dynamics of the turbulent velocity field. A good example is mixing of dye in a liquid, where the scalar is the dye concentration [91], which does not influence flow dynamics for this type of mixing.

The second category is characterized by the situation where the scalar being mixed plays an intrinsic role in driving the dynamics of the velocity field. Flows induced by the RTI, wherein the scalar is the density field and the forcing on the momentum field is due to the coupling of the scalar to the acceleration vector are an example of this category of mixing. For the third and last category, the scalar being mixed has the dominant active role in the behavior of the overall flow field. Examples for this category include flows driven by combustion [92, 93] and/or by detonation and deflagration phenomena [94–96].

III. TIME-DEPENDENT FLOWS INDUCED BY HYDRODYNAMIC INSTABILITIES

Because of our interest in supernova explosions and in ICF, we will restrict our attention to turbulent flows induced by hydrodynamic instabilities with perturbed interfaces. The three "classical" instabilities that play a significant role in these applications are the RTI, RMI, and the KHI. Each of these instabilities involves a perturbed interface between two fluid regions. For the case of the RTI, the density varies across the interface whereas for the RMI, the acoustic speed varies across the interface, though this variation in acoustic speed is typically associated with a density difference as well. The KHI typically involves an interface across which the fluid velocity varies–in the classical case, the variation in velocity is discontinuous. The KHI interface may also be associated with a density difference across the interface. The nature of the interface varies with the circumstances of the problem. The interface maybe discontinuous in the fluid properties, or it may be diffuse. Molecular interactions such as surface tension, diffusion-induced fluid stresses, or reactions may be involved. These complications may play a substantial role in the evolution of the layer. Also, in most practical situations, an accurate and precise description of the interface maybe difficult to obtain. Additionally, these instabilities can appear in a number of circumstances, and can occur in convergent, or divergent geometries in addition to the usual planar cases. Finally, it is typical in many astrophysics and HEDP circumstances to have all three instabilities concurrently.

Again, the fluid motions of the instabilities are governed by the Navier-Stokes equations (Equations 1-3). For the case of a compressible flow, an equation for the energy must also be included

$$\frac{\partial \rho e}{\partial t} + \frac{\partial \rho u_n e}{\partial x_n} = -\frac{\partial \left(q_j - u_i \sigma_{ij}\right)}{\partial x_j}, \tag{35}$$

where q_i represents a heat flux. It should be noted that q consists of a conduction flux $\sim -\nabla T$ and an enthalpy flux (this has not always been correctly treated, see Cook [97] for example).

In some cases, it is convenient to include an equation for fluid species mass-fractions (this may typically replace the density equation);

$$\frac{\partial \rho Y_i}{\partial t} + \nabla \cdot (\rho Y_i \mathbf{u}) = \nabla \cdot (-\mathbf{J}_i), \tag{36}$$

where Y_i is the mass-fraction of the i^{th}-species and we have assumed a Fickian diffusion model wherein $\mathcal{D}_i$ is an effective binary species diffusion coefficient [98]. The

diffusional fluxes are given by [97, 99]

$$\mathbf{J}_i \approx -\rho\Big(\mathcal{D}_i\nabla Y_i - Y_i\sum_{j=1}^{N}\mathcal{D}_j\nabla Y_j\Big). \tag{37}$$

For simplicity, we will assume that the $\mathcal{D}$s are the same. If the fluids are mutually diffusive, and the Mach Number, Ma is small ($Ma \to 0$) the divergence of the velocity field becomes [100–102]

$$\frac{\partial u_n}{\partial x_n} = \frac{\partial}{\partial x_n}\left\{\rho\mathcal{D}\frac{\partial}{\partial x_n}\left(\frac{1}{\rho}\right)\right\}, \tag{38}$$

and the velocity field is thus solenoidal in the incompressible, immiscible limit. In addition, these equations may also be augmented with an equation governing the surface tension between immiscible fields. These are the equations that serve as the basis for the various stability analyses, theories, models and computations. Instability theory deals with the initial growth of the perturbed interface in these flows, and the classical solutions for the RTI and KHI are discussed in detail by Chandrasekhar [103]. The typical approach is a perturbative expansion. However, if the perturbations of the interface between the two fluids continue to grow, they quickly move beyond the regime in which instability theory is applicable. Numerous theories have been proposed to describe the nonlinear regime, with varying degrees of success. However, in finite time, these instabilities typically end up as an inhomogeneous turbulent mixing layer where in the core of the mixing layer is in a "fully turbulent" state.

A. The Rayleigh-Taylor Instability

The RTI occurs at a perturbed interface between two fluids with different densities. If the fluids experience an acceleration in the direction from the lighter fluid toward the heavier fluid, the interface becomes unstable, and the perturbations will grow. This corresponds to the configuration of an heavier fluid over a lighter fluid in a gravitational field [104]. This instability was first studied in detail by Lord Rayleigh (J.W. Strutt) [1], and later by G.I. Taylor [2], and continues to be subject to much theoretical, experimental and computational scrutiny (for an example of a rigorous mathematical treatment, see References [105–107]). The "classical" case concerns an incompressible fluid, and an interface between the heavier and lighter fluids is represented by a two-dimensional surface described by a single two-dimensional Fourier mode, i.e.,

$$S\left(x,y\right) = a_0\Re\left[e^{i(k_x x + k_y y)}\right], \tag{39}$$

where the acceleration is assumed to be applied parallel to the z-axis, k_x and k_y are the Fourier wave numbers in the x and y directions, respectively and $\Re$ denotes the real part of its argument. The perturbed interface represented by equation (39) can be viewed as a simple one-dimensional single-mode perturbation with a wavenumber of $k = \sqrt{k_x^2 + k_y^2}$. In general, the RTI occurs whenever

$$\nabla p \cdot \nabla\rho < 0. \tag{40}$$

However, if $\nabla p \cdot \nabla\rho > 0$, the flow is stable, and the perturbation will typically oscillate and eventually vanish under viscous damping. The two-dimensional case clearly shows that the misalignment of the pressure gradients with the density interface leads to the production of vorticity via

$$\frac{D\omega}{Dt} = \frac{1}{\rho^2}\nabla\rho\times\nabla p, \tag{41}$$

as illustrated in Figure 10 [108].

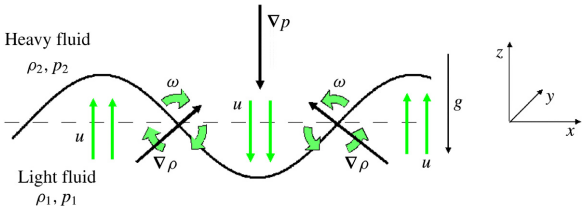

FIG. 10: Illustration of the generation of baroclinic torque at an unstable RT configuration. The interface creates vorticity and induces a velocity field that increases the baroclinic torque [108]. Reproduced with permission from *J. Fluid Mech.,* **787**, 50 (2016). Copyright 2016, Cambridge University Press.

Chandrasekhar [103] and Drazin & Reid [109] present detailed derivations of the RTI linear stability analyses for the case of a sinusoidal perturbation at the interface, assuming no diffusion. Chandrasekhar includes analyses for the cases with and without surface tension, and for inviscid fluids as well as viscous fluids and fluids with differing viscosities. However, he only presents results for inviscid fluids and fluids with identical kinematic viscosities. In addition, he extends the analysis to include hydromagnetic effects.

For the case of inviscid fluids without surface tension in an infinite domain, the results is that the amplitude, $a(t)$ of the Fourier mode describing the interface initially grows as

$$a\left(t\right) = a_0 e^{t\sqrt{\mathcal{A}gk}}, \tag{42}$$

where a_0 is the initial Fourier amplitude, and is equivalent to half the width, $h(t)$ of the interface (peak-to-valley), g is the acceleration applied to the interface, k is the wavenumber of the sinusoidal perturbation and $\mathcal{A}$ is the Atwood number;

$$\mathcal{A} = \frac{\rho_2 - \rho_1}{\rho_2 + \rho_1}, \tag{43}$$

where $\rho_2 > \rho_1$, ρ_2 and ρ_1 are the densities of the two fluids. The linear stability analyses are limited to very small times. However, numerous attempts have been made

to extend perturbative-type models to higher order in the perturbative expansions, and to include nonlinear effects, as well as account for a greater variety of initial perturbations–examples include (but are by no means limited to) Refs.[110–122]. These models have been extended in various ways, including to non-planar geometries, and non-constant accelerations. In addition they show reasonable congruence to experiments up to some point in time (a more extensive discussion can be found in [7]). It is also interesting to note that Zhang and coworkers [123, 124] have advanced quantitative theories for RTI and RMI for all density ratios, using the methods of asymptotic matching [125] and two-point Padé approximations [126–128].

David Alfaro Siqueiros, a well known Mexican muralist (Figure 11), used this method of absorption of two or more superimposed colors which infiltrate one into another (Figures 12-13). The technique is referred to as "accidental painting" [129, 130].

An obvious difficulty in applying some of these models to practical circumstances is in characterizing the initial interface perturbation with sufficient accuracy to reliably apply these analyses. Also, these analyses are typically limited to the evolution of a small number of modes. This is problematic if the mixing layer transitions to a fully developed turbulent state. In a circumstance with a multi-modal initial condition, the RTI quickly tends toward an apparently chaotic turbulent behavior. At late times (beyond the linear stability theory regime) the lighter fluid "rises" up through the heavier fluid, which in turn "drops" through the lighter fluid. The characteristic structures of the lighter fluid penetrating the heavier fluid are usually referred to as "bubbles" and the heavier fluid forms "spikes" as it penetrates the lighter fluid (Figure 14). The evolution of the mixing layer width can be obtained from both numerical simulations or experimental measurements.

To clarify further why the term "spikes" is used, we recall that at very high density ratios e.g. water/air, as used in the early RT experiments, the dense fluid forms spikes as it penetrates the lighter fluid. Most notably, "mushroom" shapes form on the spike tips at lower density ratios and for small density differences there is little asymmetry. However, use the terms "bubble" and "spike" at all density ratios has persisted in the RT/RM literature.

Figure 15 presents images from an experiment [131] demonstrating the emergence of the spikes and bubbles from an initial perturbation, and an apparent transition toward a turbulent state. One feature of RTI seen in this figure is the emergence of the "mushroom" shape at the tips of the bubbles and spikes [132]. This feature is also observed in many RMI simulations and experiments, as well as in some instances of the KHI. For the case of the RTI and RMI, these mushroom features are due to the shears induced at the tips of the bubbles and spikes as the fluid being penetrated must move laterally as well as in the direction of the penetrating fluid to accommodate the penetrating fluid.

The Rayleigh-Taylor instability and the subsequent transition to a turbulent Rayleigh-Taylor mixing layer (RTML) have been the subject of intense experimental scrutiny. A typical laboratory RTI experiment consists of a test chamber (or "ampoule") with two liquids of differing densities in a stably stratified configuration. This ampoule is then driven toward the floor of the test facility with an acceleration of greater than $1g$, thus rendering the fluid configuration unstable. The first notable RTI experiment was due to Lewis [133] and used compressed air to drive the test ampoule. Various mechanisms have been used to drive the ampoule, including rocket motors [134], linear electric motors [135, 136], gas guns [137] and weights and pulleys [131].

Experiments have also been conducted to examine the behavior if the acceleration is not strictly normal to the fluid interface (e.g., [134]), and the behavior under variable acceleration histories, e.g., [136]. In this context, the RMI is frequently treated as an impulsively-driven RTI. Note that many of the experiments do not attempt to "characterize" the initial perturbative state of the interface, but instead initialize the RTI with mutually immiscible fluids, or with weakly diffusive fluids that are essentially quiescent at the moment the acceleration is applied. However, experiments to investigate the behavior of single mode perturbations have also been conducted, e.g, [131, 138].

An alternate approach to generating the RTI and RTML is to use co-flowing streams of two fluids with different densities that pass a "splitter" plate [139–143],. This approach permits the combining of the RTI with the KHI and also allows the formation of long-time averages of the mixing layer statistics. The disadvantage is that the applied acceleration is limited to $1g$ and mixing layers are spatially evolving, rather than temporally evolving, and thus the statistics only roughly approximate the axisymmetry present in the accelerated ampoules.

Another method of experimentally producing RTI was described by Dalziel et al. [76] and Banerjee & Mutnuri [77], in which the heavy and light fluids are kept apart by a slider-plate, with the heavy fluid above the plate and the light fluid below. When the plate is removed, the RTI is initiated. Dalziel *et al.* [76] discuss and use numerical simulations to assess the effects of the vorticity layer deposited by the plate as it is removed. Again, as with the approach with the co-flowing streams, the splitter plate approach is limited to accelerations of $1g$.

Other novel experiments of RTI and RTML have been conducted in cylindrical geometries using pressurized gas-driven gelatin layers [144, 145]. The use of laser driven fusion facilities has allowed the design and execution of three-dimensional spherical and cylindrical and spherical RTI and RTML experiments as well albeit introducing complexities in terms of the physical models required to describe the events.

The RTI has also been the subject of investigation via numerical simulation. The RTI problem presents signif-

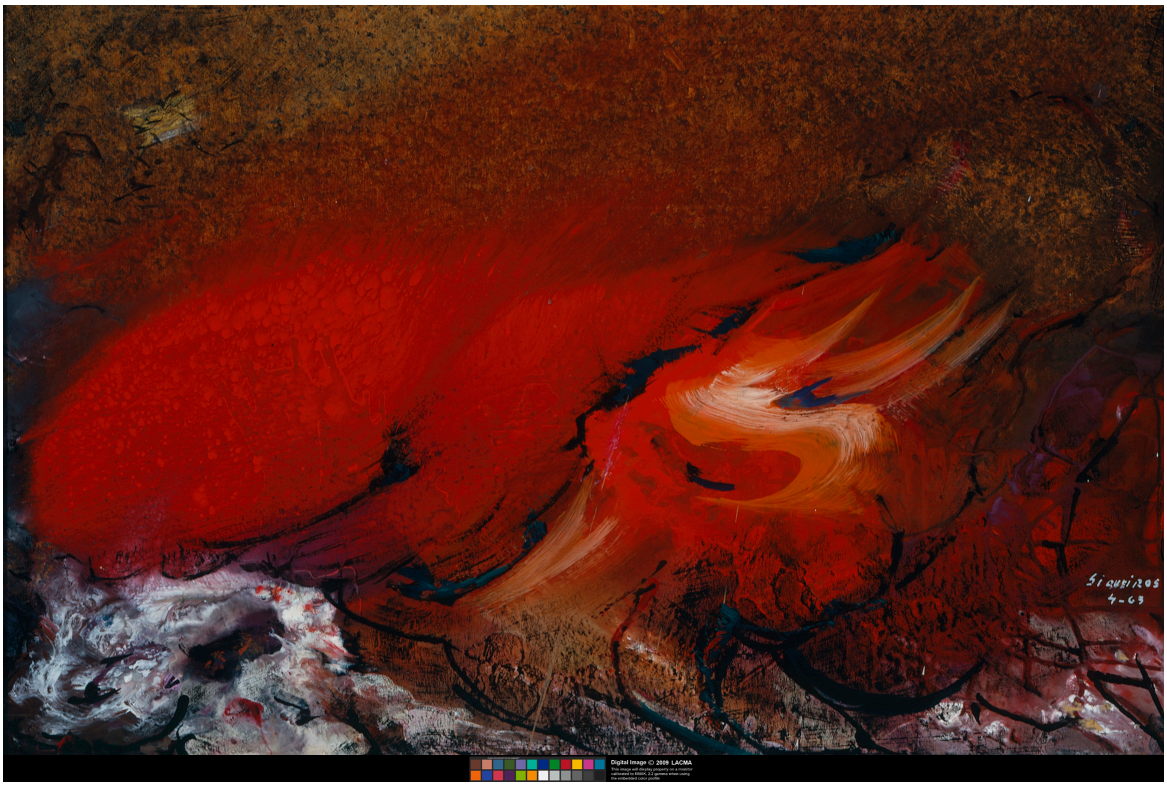

FIG. 11: Landscape in Red (Paisaje en rojo), David Alfaro Siqueiros (Mexico, Santa Rosalía de Camargo, active Mexico City and Cuernavaca, 1896-1974). Los Angeles County Museum of Art. https://collections.lacma.org/node/193844. ©LACMA ©2019 Artists Rights Society (ARS), New York / SOMAAP, Mexico City

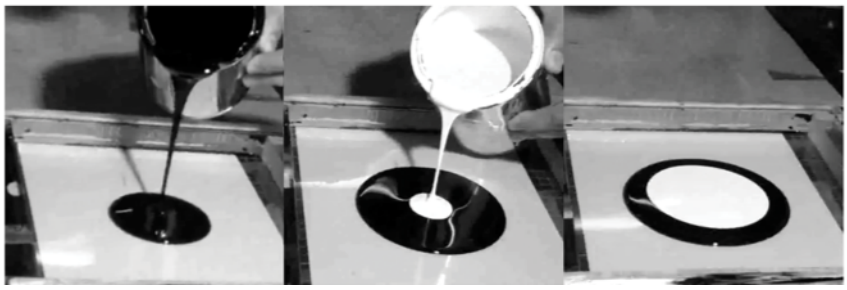

FIG. 12: Image sequence of the preparation of the experiment. Black paint over white paint. Atwood number $\mathcal{A} = 0.05$. Zetina *et al.* [129], PLoS ONE 10: e0126135; licensed under a Creative Commons Attribution (CC BY) license.

icant numerical challenges beyond those seen in simulations of single-fluid incompressible fluids. Unless the Boussinesq limit of small density fluctuations is enforced, or the fluids are deemed immisicible, the velocity field is no longer solenoidal (see equation 38). In addition, as the fluids interpenetrate each other and the edges of the mixing layer begin to accelerate, the density gradients at the tips of the spikes and bubbles increase, in spite of the effects of diffusion, placing enormous demands on the ability of the numerical algorithms to resolve the gradients. A pioneering effort to simulate the RTI and subsequent RTML was presented by Youngs [146, 147]. Examples include those of large-eddy simulations (LES) of [148], and the direct numerical simulations (DNS) of [101, 149–151]. The DNS studies require the inclusion of molecular viscosity and molecular diffusion to regularize the field and permit resolution of the boundaries between the fluids. Simulations of these flows with immiscibile fluids have been presented by, for example by [152] and [153]. The immiscible case generally involves a "front-tracking" method [153] or a "volume-of-fluid" method [146]. Another approach to simulating these flows is the so-called implicit large eddy simulation (ILES) methodology [154–156], which relies on the implicit damping in certain classes of finite difference methods to treat the sharp gradients and discontinuities present in the under-

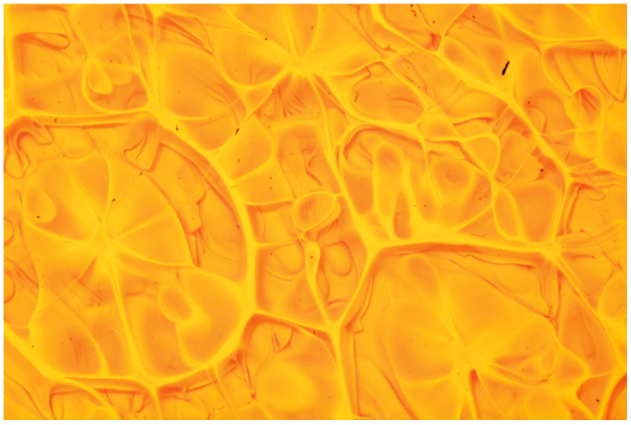

FIG. 13: Final pattern, yellow paint over transparent lacquer. Atwood number $\mathcal{A} = 0.02$. Zetina *et al.* [129], PLoS ONE 10: e0126135; licensed under a Creative Commons Attribution (CC BY) license.

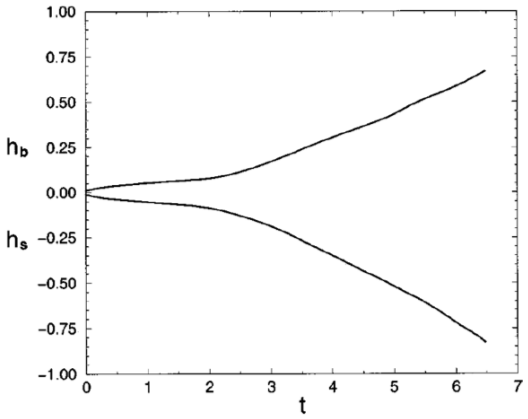

FIG. 14: Amplitude of bubbles (h_b) and spikes (h_s) in the mixing region [101]. The total width of the layer is $h = h_b - h_s$. Reproduced with permission from Cook & Zhou *Phys. Rev. E,* **66** 026312 (2002). Copyright 2002, American Physical Society.

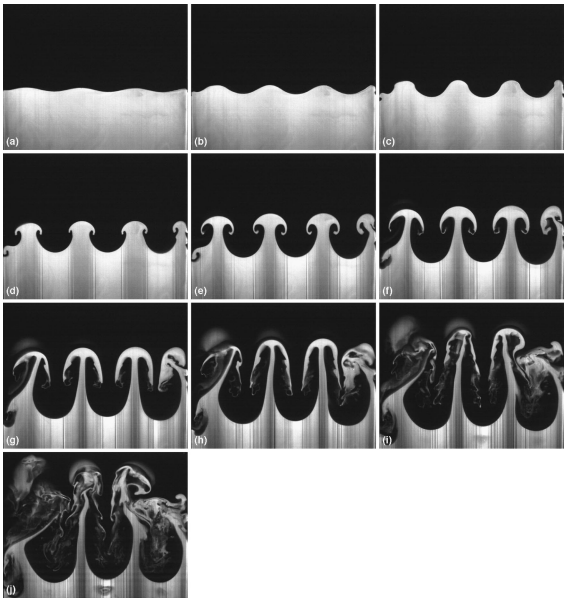

FIG. 15: A sequence of planar laser-induced fluorescence (PLIF) images showing the development of an immiscible system with Atwood = 0.336 accelerated at 1.34 g with an initial perturbation wavelength of 35 mm. The first frame was taken immediately after the test sled was released and there is a 0.033 s increment between each subsequent image [131]. Reproduced from Waddell *et al.*, *Phys. Fluids*, **13**, 1263 (2001), with the permission of AIP Publishing.

lying flow field [157]. The interesting reader is referred to Youngs [158] for a comparison between ILES and DNS for four test cases.

B. The Richtmyer-Meshkov Instability

The RMI shares a great many features with the RTI. The RMI occurs at a perturbed interface between two fluids with different densities. The instability is then initiated by the abrupt and temporary application of a pressure gradient, typically a shock-wave traversing the interface in a direction normal to the interface, or in some cases, an impulsive application of an acceleration - in essence, and impulsively-driven RTI. Note that if the incident shock-wave is weak, i.e., low Mach Number, and the perturbations are small, than the compressible case is well-matched by the impulsive RTI case. However, unlike the RTI, the RMI perturbations will grow for both the case of $\nabla p \cdot \nabla \rho > 0$ as well as for $\nabla p \cdot \nabla \rho < 0$. For the case where $\nabla p \cdot \nabla \rho > 0$ the interface will undergo a phase inversion prior to the growth of the amplitude of the perturbation. Unlike the RTI, since the pressure gradient in the RMI is not sustained, and therefore the RMI-induced mixing layer is not a driven turbulent field. Consequently, if the initial shock-wave, or impulsive acceleration is not sufficiently large, the RMI may not develop into a "fully developed" turbulent state.

The RMI was first described by Richtmyer in 1960 [3], and the first successful experimental reproduction of the instability was due to Meshkov in 1969 [4]. Richtmyer's analysis of the RMI used Taylor's linear theory [2], and assumed an interface perturbation like that given by equation (39). His analysis treated only the case of the shock-wave moving from the lighter to the heavier fluid, and also treated the shock as an impulsive acceleration. It is important to note that, for the RMI, the linear theory only applies to the case where $ka_0 \ll 0$ where k is again the wavenumber of the perturbation and a_0 is the initial amplitude. Richtmyer modeled the impulse as $g = \Delta V \delta(t)$ where ΔV is the change in velocity of the interface as the shock passes through, and $\delta(t)$ is the Dirac delta function. The equation governing the growth of the

amplitude is then

$$\frac{d^2a}{dt^2} = k\mathcal{A}\Delta V\delta(t)a_0. \tag{44}$$

A complication that arises from the compressibility of the fluids in the RMI case is that the compression due to the passing of the shock changes both the Atwood number, $\mathcal{A}$ and the initial amplitude of the perturbation. Richtmyer choose to use the post-shock values, (denoted by a superscript $+$) to arrive at

$$\frac{da}{dt} = k\mathcal{A}^+\Delta V a_0^+. \tag{45}$$

Various modifications to this formulation have been proposed, and the interested reader is referred to the reviews [7, 159]. Richtmyer only considered the instance of the shock moving from lighter to the heavier fluid, which turns out to be the case most relevant to ICF. The case of the shock moving from the lighter to the heavier fluid produces a reflected shock-wave in addition to the forward propagating wave. For the case of the shock moving from the heavier to the lighter fluid, the reflected wave is a rarefaction wave. Also, these two cases (lighter/heavier versus heavier/lighter) result in deposition of vorticity of opposite signs. This is illustrated in Figure (16), showing the lighter/heavier on the left and the heavier/lighter case on the right. The case wherein the shock moves from the heavier gas to the lighter gas causes a phase-reversal of the interface to occur before the interface begins to grow, whereas the lighter-heavier case causes a direct growth of the interface [160].

Other RMI analyses have been based on an initial velocity or vorticity distribution at the interface – for examples, see references [161–163]. Indeed, the linear theory gives modes $\exp(\pm nt)$. So there is a choice of an $a = a_0\cosh(nt)$ (initial amplitude) mode or an $a = a_0\sinh(nt)$ mode (which assumes an initial velocity distribution, see for example, Eq. (11) of Mikaelian [161]). Historically, before RM was considered, most researchers took $\dot{a}(0) = 0$, a natural choice. For example, Taylor explicitly said that if the initial amplitude is finite and if "the initial velocity is zero" then the solution is $\cosh(nt)$. Indeed, one had no incentive to consider a finite initial $\dot{a}(0)$ when RTI is the only consideration [163]. It should be noted that when both an initial vorticity and an initial velocity (in the sense of $\dot{a}$) are given, the two can be related as was done by Jacobs and Sheeley [162] [see their Eq. (17)]. If initially both the amplitude (a) and velocity ($\dot{a}$) are provided, however, then the two may be degenerate and cancel each other out at late times as Mikaelian [163] discussed recently.

The most obvious way to experimentally generate the RMI and RMML (Richtmyer-Meshkov mixing layer) is to use a shock tube. The first experiments to demonstrate the RMI where due to Meshkov [4]. Meshkov used an extremely thin nitrocellulose membrane with a an imposed sinusoidal perturbation to separate the light and heavy fluids in a shock tube prior to initiating the shock-wave. When the shock-wave encounters the membrane, the membrane is destroyed, and the RMI behavior is observed. Meshkov examined both the light/heavy configurations as well as the heavy/light configurations. Although the membranes are reduced to small fragments, these fragments have some effect on the flows. Prasad *et al.* [164] used a polymeric membrane supported by a wire mesh to separate the gases and studied (among other things) the effect of the membrane and mesh on the evolution of the mixing layer (see also, Erez *et al.* [165]).

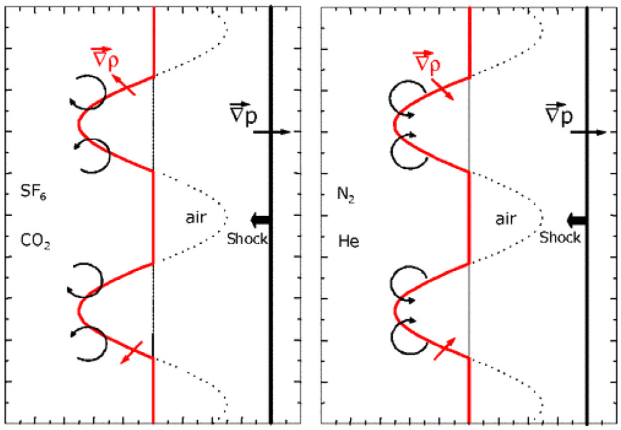

FIG. 16: An illustration from Jourdan & Houas [160], showing the differences in vorticity deposition for the cases of the shock traveling from lighter to heavier fluids (left side) and vice-versa (right side). Reproduced with permission from *Phys. Rev. Lett.*, **95**, 204502 (2005). Copyright 2005, American Physical Soc.

Jones & Jacobs [166] generated a perturbed interface in a vertical shock tube without a membrane by flowing the heavy gas in through the bottom of the vertical shock tube, and the light gas through the top, and removing them through slots in the test section, thus maintaining a smooth flat interface. A sinusoidal perturbation is then induced in this flat interface by oscillating the shock tube. However, molecular diffusion tends to "smear" the interface between the two-fluids. For multi-mode interfaces RMI, Figure 17 shows a sequence of PLIF images for a He/Ar interface [167, 168].

Another approach to avoid the use of membranes in shock-tubes is to use a "slider plate" to separate the two

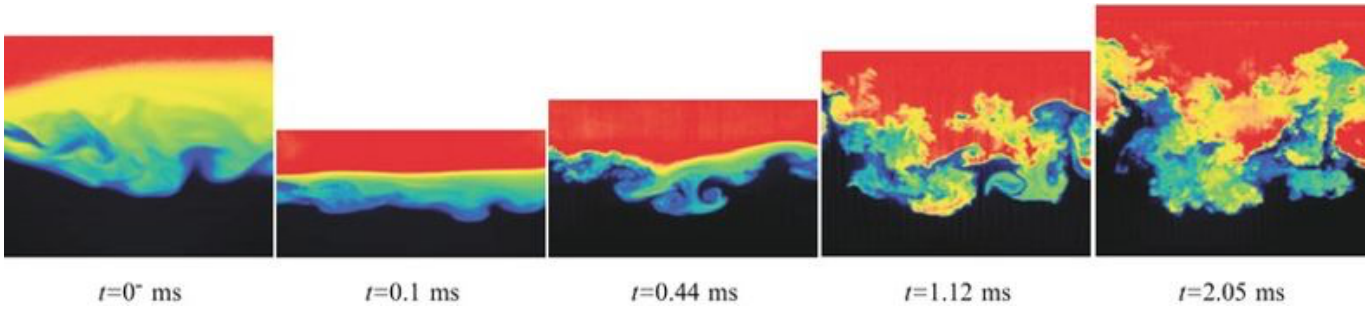

FIG. 17: Sequence of PLIF images for a He/Ar interface, $Ma = 2.2$. Times are from initial shock interaction [167]. Reproduced with permission from Weber *et al.*, *J. Fluid Mech.*, **748**, 457 (2014). Copyright 2014, Cambridge University Press.

fluids, and then remove the slider plate immediately before initiating the shock-wave, see for example Brouillette & Sturtevant [169] and Puranik *et al.* [170].

The third approach to generating the RMI is to explicitly generate an impulsive RTI. This approach allows certain types of RTI experimental facilities to be repurposed for RMI experiments. For example, Ref. [162] vertically accelerated an ampoule containing the test fluids by "bouncing" it off a fixed coil spring. Prior to dropping it on the spring, a sinusoidal standing wave was induced at the interface between the heavy and light fluids by oscillating the ampoule. Likewise Dimonte & Schneider [136] used their linear electric motor to impulsively drive the ampoule. The reader is referred to Ref. [175] for recent discussions of experimental measurements of RMI and RMML.

Explosively driven experiments of RMI and RMML in metals have been studied by Buttler *et al.* [171], Prime *et al.* [172], among others [173]. As in the case of the RTI and RTML, laser-driven experiments provide the ability to conduct experiments of the RMI and the RMML [174], but additional physical processes, such as equations of state, are introduced.

Numerical methods have proven to be a useful tool for studying the RMI and RMML. However, in addition to all the numerical challenges presented by the RT problem, the RM cases now compound these issues with the necessity of treating compressibility and the presence of shock waves and rarefaction waves. Recently, Wong *et al.* carried out high-resolution 2D and 3D shock-capturing adaptive mesh refinement simulations of multi-species mixing driven by RMI [176]. Direct resolution of the shock wave is generally extremely computationally costly in three dimensions. As a result, front-tracking methods or ILES approaches are frequently used in two-dimensional simulations, e.g., [177], whereas in three-dimensions the useful tools appear to be LES [99, 178, 179] and ILES, e.g., Refs. [157, 180–183]. It should be noted that the ability to track shock waves and fronts can be highly useful for studying internal shock wave interactions in the mixing layers at high Mach number [177]. Yet, for highly turbulent scenarios, the dynamics of the turbulence are intrinsically three-dimensional [the two-dimensional case is, in some sense pathological (see Subsection IX)], and thus three-dimensional simulations are required to capture the phenomena with physical fidelity. The ILES approach has also been applied to the shock/reshock problem, and to similar problems regarding the effects of compressibility on the development of RMI in the case where ka is not much smaller than unity [183]. Note that again, numerical simulations afford the ability to easily simulate arbitrary, e.g. convergent geometries, and provide access to all the field variables [184–188].

One additional phenomenon frequently encountered in experiments [189–191], modeling [192], as well as simulations [193–196] of RMI and ICF, is the so-called "reshock" event. A reshock event occurs when a shock wave traverses a RM-induced mixing layer. This can occur, e.g., when a shock-wave reflects off the end of the shock-tube and strikes the mixing layer again. Reshock events typically result in a rapid growth of the turbulence within the mixing layer - much more than produced during the initial RTI initiation. Taylor's linear theory, (as applied by Richtmyer and others) generally does not apply to a reshock event since, at the time of reshock, the requirement that $ka_1 \ll 0$ (where a_1 is the amplitude of the perturbation when the reshock event occurs) is usually not true. The production mechanism is due in part to Kelvin-Helmholtz-induced shear layers induced by the shock crossing the mixing layer. Figure 18 shows the development of the RMI and RMML, with a subsequent reshock event from a shock tube experiment by Tomkins *et al.* [197]. The initial incident shock had a Mach number of $Ma = 1.2$. After the first shock crosses the interface, the emergence of the characteristic mushroom shapes are observed. The reshock event occurs in the figure, and the mixing layer subsequently evolves rapidly toward a chaotic, turbulent state.

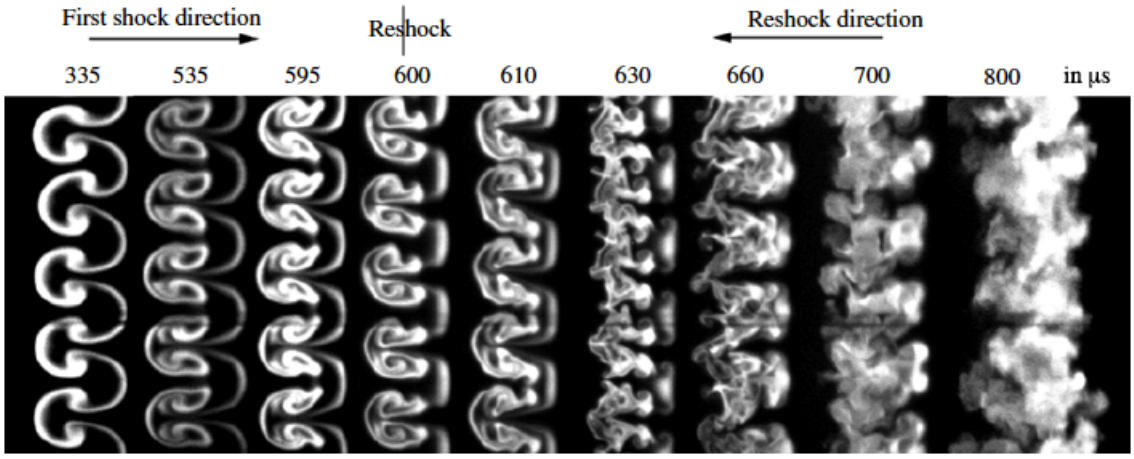

FIG. 18: Rapid transition of the varicose RM fluid layer into a well-mixed state after reshock [197]. Reproduced with permission from Tomkins *et al.*, *J. Fluid Mech.*, **735**, 288 (2013). Copyright 2013, Cambridge University Press.

C. The Kelvin-Helmholtz Instability

The Kelvin-Helmholtz Instability occurs at the interface between two counter-flowing streams of fluids. If the interface between the two fluids is absolutely smooth, the fluids will, in principle (at least mathematically!) maintain laminar flow. If the interface is perturbed, the perturbation may grow. The growth of such a perturbation gives rise to the KHI. The KHI was first studied by Helmholtz [6] and subsequently by Lord Kelvin [5]. As in the case of the RTI and RMI, the classical instability analysis assume a sinusoidal perturbation and an initially exponential growth rate for the unstable mode(s). The analyses presented by Chandrasekhar [103] and by Drazin & Reid [109] include the effects of buoyancy, surface tension, rotation and a diffuse, rather than discontinuous interface. For the case of buoyancy, and with a discontinuous interface, the growth rate of the interface is given by

$$\gamma_K = \pm \left\{ gk\mathcal{A} + \rho_1\rho_2 k^2 \left[\frac{V_1 - V_2}{\rho_1 + \rho_2}\right]\right\}^{1/2} - ik\left\{\frac{\rho_1 V_1 + \rho_2 V_2}{\rho_1 + \rho_2}\right\}, \tag{46}$$

where g is the acceleration normal to the interface, V_1 and V_2 are the fluid velocities across the interface (parallel to the interface), $\mathcal{A}$ is the Atwood number, k is the wavenumber of the disturbance, and ρ_1 and ρ_2 are the fluid densities on each side of the interface.

It is generally assumed that the KHI will evolve toward an approximately self-similar turbulent state [198]. The mechanisms of the transition process have been studied using both DNS, for example by Metcalfe *et al.* [199] and experimentally, for example by Winant and Browand [200]. When the KHI achieves a chaotic state it is typically referred to as a *temporally* evolving shear layer. This is terminology distinguishes it from the closely related *spatially* evolving shear layer. A temporally evolving shear layer is difficult to realize in experiments, but easier to simulate than the spatially-evolving case. The spatially evolving shear layer is usually experimentally generated by conjoining two fluids with different speeds downstream from a splitter plate, as shown in Figure 19 [201].

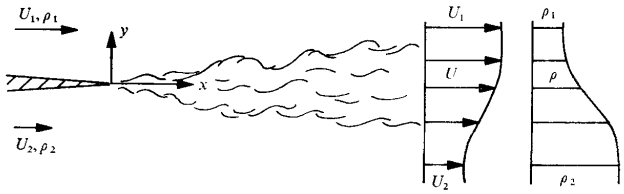

FIG. 19: Schematic diagram from Brown & Roshko [201] showing splitter plate between to fluid streams, and the downstream mixing layer profile. Reproduced with permission from *J. Fluid Mech.*, **64**, 775 (1974). Copyright 1974, Cambridge Univ. Press.

It should also be noted that the KHI and KH mixing layer (KHML) can be initiated by a shock wave passing through a density interface at an angle that is oblique to the interface [202]. In this case, the difference in acoustic velocities between the two fluids gives rise to different rates at which the shock travels through the fluids, resulting in a velocity difference across the interface, thus inducing a shear instability. As mentioned in the Introduction, many authors have performed experiments in which shock-induced shear layers have been generated on laser-driven ICF platform.

An early and pioneering experimental study of the turbulent shear layer was due to Liepmann & Laufer [203]. More recent significant experiments have been published in Refs. [204], [205], and [206], amongst others. Sev-

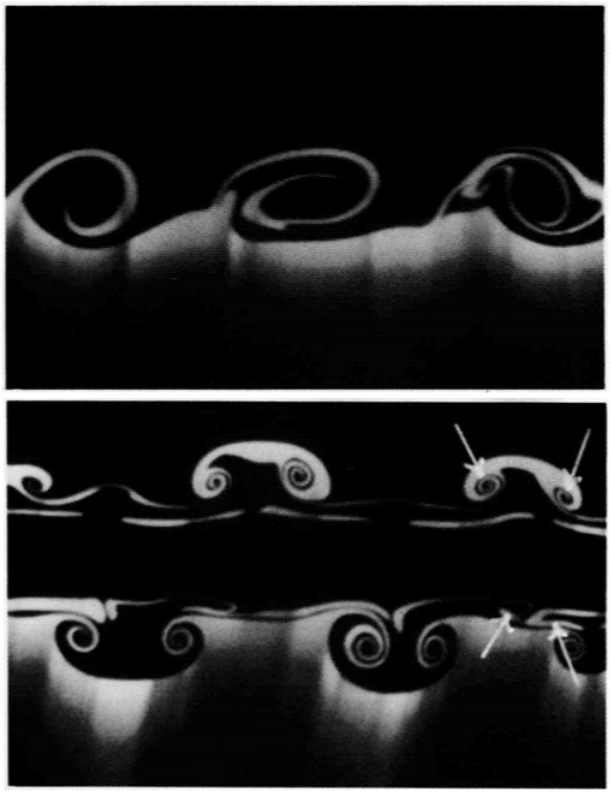

FIG. 20: Images from the experiments of Schowalter *et al.* [208] showing a side view (top) and end view (bottom) of a KH shear layer. The end view is from an experiment without buoyancy effects, yet it exhibits the mushroom shaped structures. Reproduced with permission from *J. Fluid Mech.*, **281**, 247 (1994). Copyright 1994, Cambridge Univ. Press.

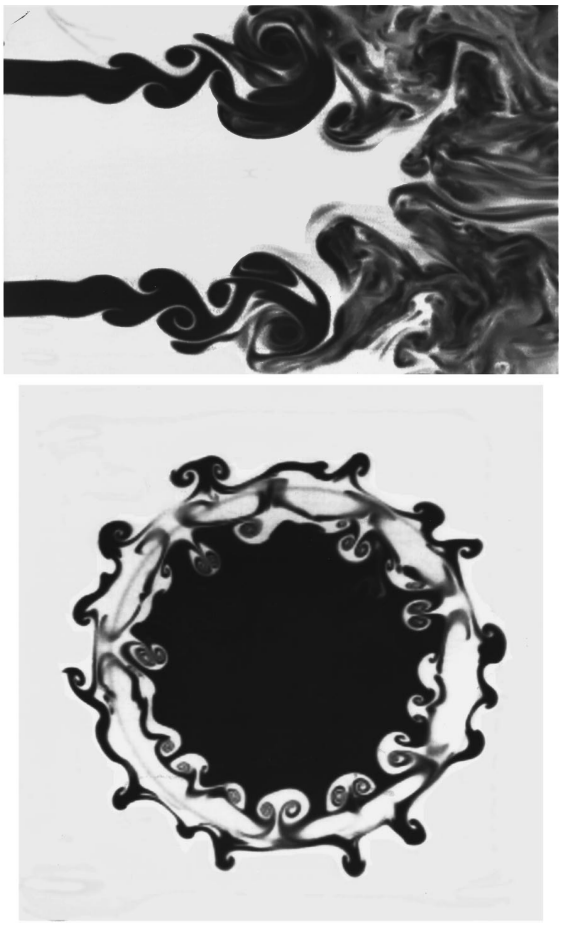

FIG. 21: Images from the experiments of Villermaux *et al.* [232] showing a side view (top) and the an end view (bottom) of circular jet. Both the inner shear layer and the outer shear layer exhibit the mushroom shapes in the end view. Reproduced from *Phys. Fluids*, **10**, S2 (1998), with the permission of AIP Publishing.

eral experiments on spatially evolving shear layers have been designed to be able to study the coupled effects of buoyancy and shear, for example [207, 208] as well as the effects of compressibility on the evolution of the free shear layers [201, 209]. Recently, San & Maulik [210] and Rahman & San [605] studied the stratified KH turbulence of compressible shear flows, while Gan *et al.* [212] and Lin *et al.* [213] carried out simulations of nonequilibrium KHI.

Explosively driven shock-induced shears have been examined by Silver *et al.* [214], which represented a mix of RT and KH instabilities and mixing. The experiment was conducted by using explosively-lined cylinders and employed radiography for diagnostics.

Computations of shear layers have been conducted using a variety of algorithms. In fact shear layers have been an important topic of turbulence research and CFD (computational fluid dynamics) studies for decades (The series of biennial Turbulence and Shear Flow Phenomena Symposia is the main venue for disseminating recent and ongoing research. http://www.tsfp-conference.org/index.html).

D. Nonlinear behavior and transition to self-similarity

Historically, the initial growth of these instabilities has been treated as a linear (or weakly nonlinear) process. However, as the velocities grow, and the mixing widths increase, the nonlinearities inherent in the the Navier-Stokes equations begin to grow and eventually play a dominant role in the mixing process. When the flow fields achieve a state of "fully developed turbulence" (the precise meaning of which will be discussed later), the flows tend to exhibit approximately self-similar behaviors. These self-similar behaviors can generally be deduced from fairly simple dimensional arguments - much like those employed by Kolmogorov. However, the transition mechanisms that lead to the approximately self-similar behavior are subtle. We will now discuss the characteristics of the self-similar states, and describe some metrics that indicate when the transition to self-

similarity will occur.

Self-similar scalings of RTI, RMI and of KHI are directly related to the assumption of time-translation-invariance [217, 218]. The appropriate scaling groups are [198, 224]

$$\tau' = \tau(t + t_0) - t_0, \tag{47}$$

and

$$L' = \xi L \tag{48}$$

Self-similarity requires

$$\xi h(t) = h(\tau(t + t_0) - t_0). \tag{49}$$

where h is a characteristic length-scale of the mixing layer, e.g., the bubble or spike size, or the mixing layer width. The two parameter group (τ and ξ) is assumed to be restricted to a simple power-law subgroup, $\xi = \tau^\zeta$ thus yielding

$$h(t) = h_0 \left[\frac{(t + t_0)}{t_0}\right]^\zeta. \tag{50}$$

For the KH mixing layer at late times $\zeta = 1$. For the RTI mixing layer at late times, $\zeta = 2$, but the growth will look almost linear when $0 < t \approx t_0$, and only when $t \gg t_0$ will the growth be obviously quadratic. This alone might account for some variations in reported measurements. The same is true for the late-time, RMI induced mixing layer, where $\zeta = \theta$. The t^θ scaling is only valid when $t \gg t_0$. The time required for the late-time similarity scaling laws to be observed can be easily met if the temporal transition criteria are satisfied (see subsection VI C).

When the mixing layer becomes "fully turbulent", the consensus of experiments and models of the RT mixing layer (RTML) suggest an asymptotic approximately self-similar state wherein the width of the mixing layer grows as ($t \gg t_{b/s,0}$)

$$h_{b/s}(t) = \alpha_{b/s} \mathcal{A} g t^2, \tag{51}$$

where $\alpha_{b/s}$ is a constant and the subscript b refers to the bubble-side and the subscript s refers to the spike side [104, 146, 148, 152, 219–223]. This is precisely the form suggested by the equation 50 when $\zeta = 2$ and $\alpha_{b,s}\mathcal{A}g = h_{b/s,0}/t^2_{b/s,0}$. Under this limit, one obtains,

$$h_s(t)/h_b(t) \to \alpha_s/\alpha_b. \tag{52}$$

At late times, the RM-induced mixing layer exhibits traits of an approximately self-similar decaying anisotropic, inhomogeneous turbulent field wherein the width of the mixing layer grows as a power-law in time

$$h_{b/s}(t) \approx \tilde{h}_{b/s,0} \tau^{\theta_{b/s}}. \tag{53}$$

where $\tilde{h}_{b/s}$ has a dimension of a length scale. We must emphasize that τ must be nondimensional for the values of $\tilde{h}_{b,0}$, $\tilde{h}_{s,0}$, θ_b and θ_s to be physically meaningful. Clark and Zhou [198] represent the dimensionless time scale shown in equation 50, i.e., as $\tau = (t + t_{b/s,0})/t_{b/s,0}$. Note that if $\theta_b = \theta_s = \theta$, then we can identify $\zeta = \theta$ in equation 50, and the layer is self-similar. The values of the exponents range from 0.17 to 0.667. Table 6.4 of Zhou [7] provides a rather complete picture of the variation in the estimates of the coefficients.

The perspective [136] that $\theta_s > \theta_b$ implies that the ratio of the spike and bubble widths grows without bound in time implying non-self-similar internal structure. On the other hand, the viewpoint of References [181, 224, 225], where a single value of θ for the layer as a whole is assumed, indicates ($t \gg t_{b/s,0}$)

$$h_s/h_b \to [\tilde{h}_{s,0}/\tilde{h}_{b,0}][t_{b,0}/t_{s,0}]^\theta, \ (\theta = \theta_s = \theta_b). \tag{54}$$

Note that the values of virtual time origin could be "folded" into the definitions of $\tilde{h}_{s,0}$ and $\tilde{h}_{b,0}$, but doing so would change their dimensionality.

It is worth mentioning three recent publications relevant to this issue. Thornber *et al.* [225] compared and contrasted the RMI scaling exponent from the numerical simulation databases from several independently developed codes. Elbaz & Shvarts [226] evaluated a new formulation based on the well known mode-coupling models of Haan [110, 111], Shvarts *et al.* [114], and Ofer *et al.* [115]. In addition to providing a self-consistent extension of previous RTI theoretical studies, Elbaz & Shvarts found that the results of RMI scaling exponent, θ (2/5 in 2D and 1/3 in 3D). Using the Eddy Damped Quasi-Normal Markovian theory (EDQNM) [227–230] of turbulence, Soulard *et al.* found that $\theta = 1/4$ at low Atwood number, $\mathcal{A} \to 0$ [231]. It would be interesting to further confirm that the values of θ from these publications will be valid at late-time.

It has been observed experimentally and in simulations that both the temporal and spatial KHI mixing cases, the turbulent shear layers transition toward an approximately self-similar state. If compressibility and buoyancy effects are negligible, the temporally-evolving shear layer width grows linearly in time [198], i.e. $\zeta = 1$ in equation 50, and the spatially-evolving shear layer width grows linearly with position downstream from the splitter plate [201]. The turbulent kinetic energy (defined in II) on the centerline of the layer becomes constant with respect to time for the temporally evolving layer, and constant with respect to downstream position for the spatially evolving case. Like the RMML, the KH shear layer represents an anisotropic inhomogeneous driven turbulent field, where the driver is the differential velocity across the layer.

The Kelvin-Helmholtz shear layer plays a significant role in the RTML and RMML cases as well, where the characteristic mushroom-shapes of the tips of the spikes and bubbles are induced by a shear instability between the penetrating and penetrated fluids. As the bubbles and spikes continue to grow, the shear between the light fluid and the heavy fluids within the mixing layer will give rise to secondary KHI growth and mixing. The mushroom shape is, in fact, physically associated with the shear process itself, rather than the RTI or RMI pro-

cesses - see Figure 20 [208]. The mushroom features appear also in other sheared flows, e.g., around jet, shown in Figure 21, where the fluids are the same in both the inflowing jet, and the fluid into which the jet flows [232]. The fluids are distinguished in the experiment via a dye.

In particular, if viscous effects are small, short wavelength perturbations grow quickly then saturate. Long wavelength perturbations grow at a slower rate and saturate at a larger amplitude. This implies that the dominant length scale should increase for the RT,RM and KH cases. If the dominant length scale increased in proportion to the width of the mixing zone the process tends to become self-similar. A number of empirical models have been proposed and the interested reader is referred to Ref. [7, 215, 216] for details.

A criterion for transition to self-similarity (which is related to the transition to turbulence) should also be mentioned. A factor ∼10 increase in dominant length scale is often given for this transition. Upon the transition toward self-similarity, the RTML mixing layer grows as

$$h_{b/s}(t) = \alpha_{b/s}\mathcal{A}g\left(t + t_{b/s,0}\right)^2. \tag{55}$$

The parameter $t_{b/s,0}$ is a virtual time origin, consistent with the notion of time-translation invariance (Eqs. 47 - 50). Alternatively, Equation 55 can be rewritten as

$$h_{b/s}(t) = \alpha_{b/s}\mathcal{A}gt^2 + \left(4\alpha_{b/s}\mathcal{A}gh_{b/s,0}\right)^{1/2}t + h_{b/s,0}, \tag{56}$$

where $h_{b/s,0} = \alpha_{b/s}\mathcal{A}gt_{b/s,0}^2$ is a virtual starting thickness [149].

The corresponding behavior of the RMML observed in experiments and simulations is generally represented by form given in equation 53, where $\theta_b < 1$, and $\theta_s < 1$, and generally $\theta_s \neq \theta_b$. Typically, the experimentalist or simulationist will assign different power-law exponents and prefactors to the bubble-side and spike-side of the RMML, but the reader should be warned this matter has some subtlety - if $\theta_b \neq \theta_s$, the behavior is not truly self-similar, as noted above.

Summarizing for RTI and RMI at onset of self-similarity, it is reasonable to expect the following:

- For RTI, the virtual starting thickness, $h_{b/s,0}$, depends on how long it takes for the flow to become self-similar, which in turn depends on the spectrum of initial perturbations [149].
- For RMI, it is difficult to run simulations or experiments far enough to achieve self-similarity (Youngs, see pages 38-39 of Ref. [8]) and in many cases, the time origin, $t_{b/s,0}$, must be incorporated for the influence of initial conditions [198].

The value of θ is sensitive to the choice of the point where self-similarity is assumed to be established, as illustrated by Thornber [233]. The value of α obtained in Eq. 55 for a turbulent mixing layer is dependent to some degree on the definition of the edge of the mixing layer, so caution should be exercised when comparing various estimates of the mixing layer growth rate [234]. Indeed, it is important to note that there is no universally accepted definition of the "edge" of as turbulent mixing layer – different authors may use different metrics to define the edge of a mixing layer. For example, the edge might be defined as that position (in a planar layer) where the penetrating liquid occupies some small specified volume-fraction, or perhaps mass-fraction of the overall fluid.

A more robust metric is the actual amount of mixed mass [235]

$$\mathcal{M} = \int 2\rho Y_1 Y_2 dV, \tag{57}$$

where Y_1 and Y_2 are the volume fractions of the two fluids, could be viewed as a more direct marker of the evolution of the mixing layers due to hydrodynamic instabilities than the mixing layer width. An especially attractive feature of the mixed mass $\mathcal{M}$ is that it is a conserved quantity.

The importance of the mixed mass is evident from recent measurements using the high-energy-density-physics platform [18, 236–238]. Figure 22 shows the measured total neutron yield across the ensemble of cryogenic low-foot DT experiments against their inferred CH(Si) mix mass. While there is large variability in the amount of measured mix, there is clearly a trend of neutron yield dropping with increasing mix [18].

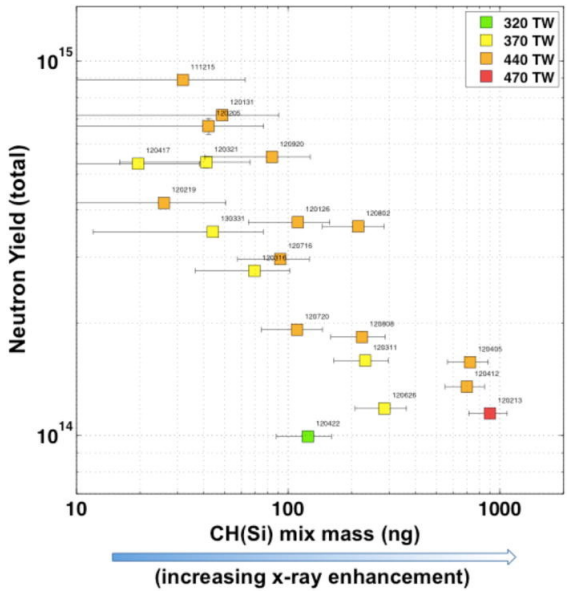

FIG. 22: DT neutron yield versus inferred mix mass (which scales with the x-ray enhancement factor) for the layered low-foot implosions. Points are color coded by peak laser power. Reproduced from Ma *et al.* [18], *Phys. Plasmas*, **24**, 056311 (2017), with the permission of AIP Publishing.

E. Other Interesting Plasma Instabilities

The RTI, RMI and KHI are hydrodynamic instabilities in that they arise in purely hydrodynamic descriptions and do not fundamentally depend on additional plasma properties (e.g., electric or magnetic fields) nor on kinetic effects. While this article focuses on situations in ICF/HEDP and astrophysics where these instabilities play a key role, there are also many cases where instabilities and turbulence that are not purely hydrodynamic occur in plasmas. For example, kinetic instabilities also arise in the above mentioned settings, and there is a whole "ecosystem" of instabilities that arises in magnetized plasmas, in which the "background" magnetic field plays a key role. A detailed discussion of these topics is beyond the scope of current article and we will only provide a very concise sketch here for completeness.

Kinetic streaming instabilities can arise in ICF and HEDP experiments and can result in rapid (much faster than collisional) transfer of flow energy into heat [239]. The Weibel instability is an electromagnetic streaming instability that has been postulated as a dissipation mechanism important in collisionless astrophysical shocks [240], and has been produced and observed in specially designed HEDP experiments [241]. A variety of plasma instabilities can cause unwanted scattering of laser energy [242, 243] or (sometimes desireable) conversion into different waves [244].

In the case of tokamaks, as an important example of laboratory magnetized plasmas, various categorizations of the instabilities and turbulence are of value. Denoting n, m as the toroidal and poloidal mode numbers there are "macro" or global instabilities for which the modes are large scale and have low n and m, and small-scale "micron"-instabilities, for which the modes have the high n and m. The simplest extension of hydrodynamics that allows for significant electromagnetic effects is the "magnetohydrodynamic" (MHD) description [245–248], which allows for self-consistent evolution of the magnetic field along with the usual fluid fields (e.g., velocity, pressure, mass density). A relevant and useful (if singular) limit of MHD is "ideal" MHD, in which dissipative effects such as resistivity and viscosity are neglected. Large-scale ideal MHD instabilities can be particularly virulent and can result in large rapid losses of tokamak energy or plasma up to the complete loss of the plasma. When the plasma is ideal-MHD stable, it may still be unstable to "non-ideal" modes, i.e., those fundamentally dependent on resistivity or other dissipation mechanisms. These act on slower time scales but can nevertheless also lead to loss of plasma or significant degradation in plasma confinement.

Plasma instabilities can also be classified according to the driving source of free energy. Current-driven instabilities, i.e., those driven by equilibrium electrical plasma currents include ideal and resistive "kink" modes. The latter are also known as "tearing" modes [249] as they involve a tearing of magnetic flux surfaces, resulting in a rearrangement of their topology. There is a variant known as "neoclassical" tearing modes, in which the "bootstrap" current associated with magnetically trapped particle orbits and collisions plays a significant role. Finer scale current driven modes in the edge pressure "pedestal" region are known as "peeling" modes. Pressure driven modes, include RT-like interchange modes. Here, if the pressure gradient is in the same direction as the mean curvature or magnetic-field gradient then an "internal" RT-like instability can result in which whole magnetic "flux tubes" of plasma will interchange. If this "bad" magnetic field gradient and curvature are localized poloidally, i.e., in the outside region of the toroidal tokamak plasma, then "ballooning" modes result, in which the flux-tube interchange is also poloidally localized. An additional potentially important source of free energy that can cause instabilities is energetic ions, which may result (via resonant charge exchange) from neutral beams used for plasma heating or arise as fusion products.

The MHD modes are "electromagnetic" in that they involve coupled evolution of the flows and the (solenoidal) magnetic field, and the (irrotational) electric field is unimportant. There are also electrostatic modes in which the electric field evolution is dominant over that of the magnetic field. These tend to arise at fine to very fine spatial scales, but can degrade the plasma (particle and energy) confinement in plasmas that are stable to large scale modes. The toroidal ion [250] and electron temperature gradient modes [251] are electrostatic internal RT-like instabilities driven by the combination of temperature gradients and the magnetic field gradient and curvature. In the absence of magnetic field gradients and curvature, temperature gradients can still drive an instability by creating an effective negative compressibility [252, 253]. Pressure, temperature and density gradients can drive various (diamagnetic) drift instabilities through a variety of effective dissipation mechanisms such as collisional resistivity [254] and Landau damping [255]. Trapped-particle instabilities are typically drift modes in which collisional or collisionless responses of trapped particles provide effective dissipation [256]. Radial shear in the parallel velocity gradient, due to toroidal rotation shear driven typically by the momentum imparted by neutral beams can also be an important source of instability drive.

Good pedagogical references on ideal MHD instabilities include Bateman [245] and Freidberg [246], and and a more general treatment of instabilities (especially global/macro instabilities) can be found in Wesson [247].

Some of the instabilities discussed above have been shown to have major consequences. "Disruption" events, [257, 258], which can result in complete rapid loss of plasma and current, large populations of highly energetic "runaway" electrons, large inductive forces and material damage, are due to various causes including phase locking of multiple large-scale MHD modes. "Mirnov oscillations" [259] seen in magnetic signals result from tearing modes and reconnection near the outer surface with n=1, m=q_a, the number of toroidal circuits a field line makes

for each poloidal circuit near the edge of the plasma. Large "sawtooth" oscillations in the central temperature and density [260] can result from internal m=n=1 reconnection. Magnetically trapped energetic ions can drive "fishbone" oscillations [261] via resonance between their precession and m=n=1 MHD perturbation. Fine scale ballooning modes act in combination with the peeling modes at the pressure pedestals that arise in high-confinement ("H-") mode plasmas and result in a phenomenon known as "edge-localized modes" [262] in which the pedestal confinement cyclically collapses or degrades. A key way to limit power flow to material surfaces in a tokamak is to create a "detached" plasma region near material plates in which a layer of cold plasma radiates away the much energy before it can reach the plates. The creation of this detached layer is tricky because a "MARFE" instability [263] can arise in which the cold plasma expands into the core region. Finally, even in the absence of such large-scale events, the finer scale turbulence results in transport of heat and particles that sets the limits on fusion plasma performance.

Nowadays, there is a vast body of work using kinetic and fluid simulations of both large-scale instabilities and "events" and small-scale instabilities and the associated turbulence. In addition to quantitative calculation and parameterization of transport and comparison of predicted turbulence signatures with experiment [264], interesting fundamental phenomena have been discovered and characterized. For example, there is a nonlinear upshift in the gradients needed to drive significant turbulence relative to the thresholds for the underlying linear modes [265–268] and the saturation by stable modes at wavenumbers similar to those of unstable modes [269, 270] as opposed to the wavenumber "cascades" familiar in hydrodynamic turbulence.

Before closing this section, it is worth mentioning some other instabilities and turbulence found in space plasma and geophysics (see for example, Seropian et al. [271]). The magneto-rotational instability is an instability that arises in accretion disks due to the decrease in angular velocity as a function of distance, and which results in a turbulent viscosity (transport of angular momentum) in the disk. The reader is referred to classical references by Velikhov [272] and Chandrasekhar [273]. In the magnetospheres of the Earth, planets and stars, reconnection, shocks, plasma jets are important issues (see for example, Collinson et al. [274]). The link between shocks, turbulence, and magnetic reconnection in collisionless plasmas has been addressed, for instance, by Karimabadi et al. [275]. Finally, the Sun and stars exhibit a variety of observable phenomena, including flares, eruptions, prominences, sunspots, turbulent dynamo (Mackay et al. [276]).

IV. INERTIAL CONFINEMENT FUSION IMPLOSION

A. Spherically converging implosion

ICF aims to achieve thermonuclear fusion by compression of deuterium-tritium (DT) fuel to extreme densities and temperatures [277]. ICF requires both the heating the fuel to sufficiently high temperatures to initiate fusion burn (i.e., reach a sufficiently large DT fusion reaction cross section) and also to compress the fuel to high densities so that the inertia of the fuel itself can confine the burning plasma long enough to achieve significant fuel burn up. Experiments are currently under way to demonstrate the first steps of ICF ignition at the National Ignition Facility (NIF) at Lawrence Livermore National Laboratory (LLNL) [278]. In these experiments, the indirect drive approach to ICF is being pursued where NIF's 1.8 MJ of laser energy are first converted to soft x-rays inside of a high-Z enclosure or hohlraum [16]. These soft x-rays then ablate the outer surface of a spherical low-Z capsule suspended in the middle of the hohlraum, driving strong shocks into the capsule to implode and heat the fuel. Experiments where the capsule is driven directly by laser beams (direct drive) are also being studied, principally at the University of Rochester's Laboratory for Laser Energetics (LLE) [279].

In the typical ignition scheme, a spherically converging implosion is arranged to heat a low-density but high temperature central hot spot, while a surrounding colder fuel layer is compressed to high density but at much lower temperatures to achieve the necessary confinement [280]. This separation into a high-temperature hot spot ($\sim$10 keV) and a cold but dense main fuel ($> 500\mathrm{g/cm}^3$) minimizes the overall energy investment necessary to reach ignition conditions. Ideally, if the central hot spot is large enough that the fusion product α-particles slow down within and self-heat the hot spot, run away fusion ignition can occur, propagating a detonation wave into the surrounding dense fuel. At a hot spot density of $\sim$100 $\mathrm{g/cm}^3$, this requires a hot spot radius of $\sim$30 μm and an energy investment of $\sim$ 40 kJ. With $\sim$ 100 mg of surrounding DT fuel compressed to $> 500\mathrm{g/cm}^3$, a burn duration of $\sim$ 50 ps is possible resulting in a burn-up fraction of $\sim$ 1/3 and a yield of $\sim$ 10 MJ. Assuming a total coupling efficiency of $\sim$10%, this idealized scaling suggests that substantial energy gain is possible with only $\sim$ 400 kJ of absorbed energy. Decades of experimental and theoretical ICF research have shown this scaling to be highly optimistic, however, in large part due to the impact of hydrodynamic instabilities during the implosion.

B. Various phases of hydrodynamic instabilities

The high compression necessary to achieve the relevant densities for ICF inevitably implies a high convergence

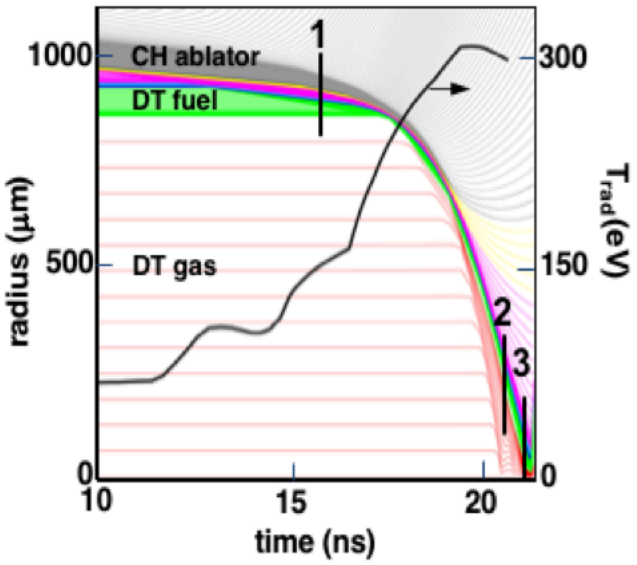

FIG. 23: Typical ICF implosion.

and high velocity implosion. In turn, this high convergence and acceleration to high velocity provide ample opportunity for hydrodynamic instabilities to develop, dominantly the well-known RT and RM instabilities.

Details of a typical ICF implosion are shown in Figure 23. The figure shows radius vs. time of an imploding ICF capsule from a 1-D Lagrangian simulation. The different colored traces show the different materials making up the shell: the interior volume is filled with low-density DT gas, the main fuel is a thin layer of DT ice shown in green, and the outer shell is composed of various layers of doped plastic (CH) that are ablated by the incident x-ray flux. The time dependence of the hohlraum radiation temperature (or x-ray flux) that drives the implosion is shown by the thick black curve with the scale on the right. Each step in the radiation temperature launches a shock into the capsule and ultimately accelerates the shell to a velocity of more than 350 km/s by the peak of the x-ray drive. Stagnation, and hopefully fusion ignition, occurs in the last few hundred picoseconds of the implosion.

Line-outs of the shell density from the three representative times marked in Figure 23 are shown in Figure 24. During the first time shown in Figure 24, several strong shocks can be seen propagating through the DT fuel and plastic ablator shell. As the shocks cross the various interfaces in the capsule, including the ablation front (or outer surface of the imploding capsule), RM instabilities can develop. While the RM modulation amplitudes are generally quite small due to the very smooth surfaces of the initial capsule and grow only slowly with time, RM growth is important in setting the initial amplitudes (and phases) for subsequent RT growth [281]. After the shocks break out from the inside of the shell, the shell begins to accelerate, and a subsequent RT unstable phase of the implosion begins, as represented by the second time in the figure. This phase again involves instability growth at both the ablation front and at any interior interfaces with an unstable density gradient.

At the ablation front, the ablation of the outer capsule surface exerts a strong stabilizing effect on RT growth [282–284]. This stabilization is essentially due to the "polishing away" of the perturbations that occurs under ablation: the steepened temperature gradients in the neighborhood of a perturbation maximum causes enhanced heat flux and enhanced drive pressure near that maximum, both of which tend toward the suppression of the perturbation maximum and an effective reduction in its growth. Sufficiently short wavelengths are in fact completely stabilized and only a finite spectrum of modes can grow in the presence of ablation, unlike in the classical case (see also, subsection IV C).

At the interior interfaces, however, particularly the interface between the DT fuel and plastic ablator, there is no ablative stabilization and classical RT instability growth can occur [285, 286]. The only means of controlling this instability growth is by managing the amplitude of the unstable Atwood number at this interface throughout the implosion. It is precisely for this reason that the dopant layers shown in Figure23 are added to the plastic ablator. By doping the plastic and increasing its opacity, the interior layers of the ablator are subject to less x-ray heating from the driving x-ray radiation. This causes the interior ablator layers to remain relatively cool and hence dense if they are compressed to the same pressure. In turn, this reduces the unstable Atwood number and subsequent instability growth between the DT fuel and ablator. This interior stabilization comes at a cost, however, in that adding dopant to the ablator also steepens the outside ablation front during the implosion causing that surface to become more RT unstable. ICF implosion design, and indeed the success of ICF, depend on properly managing these competing instability demands.

Finally, in the last few hundred picoseconds of the implosion, the shell stagnates to form a low density but high temperature and high pressure hot spot. In this phase, labeled as three in Figures. 23 and 24, the low density hot spot now decelerates the denser shell, and again RM and RT instabilities can develop at the interface between them. If the perturbation seeds are large enough or the instability growth fast enough during this phase, perturbations of the hot spot-main fuel boundary can grow to amplitudes large enough to quench the desired hot spot ignition.

Note that none of the various phases of instability growth shown in Figures. 23 and 24 occurs in isolation. Indeed, a principle complicating factor of ICF is that instabilities that develop at the ablation front during the acceleration phase of the implosion can feed through the finite thickness shell and act as seeds for instability growth during deceleration around the edge of the hot spot. Moreover, there are multiple initial imperfections in real ICF targets that can act as initial seeds for RM and RT growth. These include the roughnesses inherent

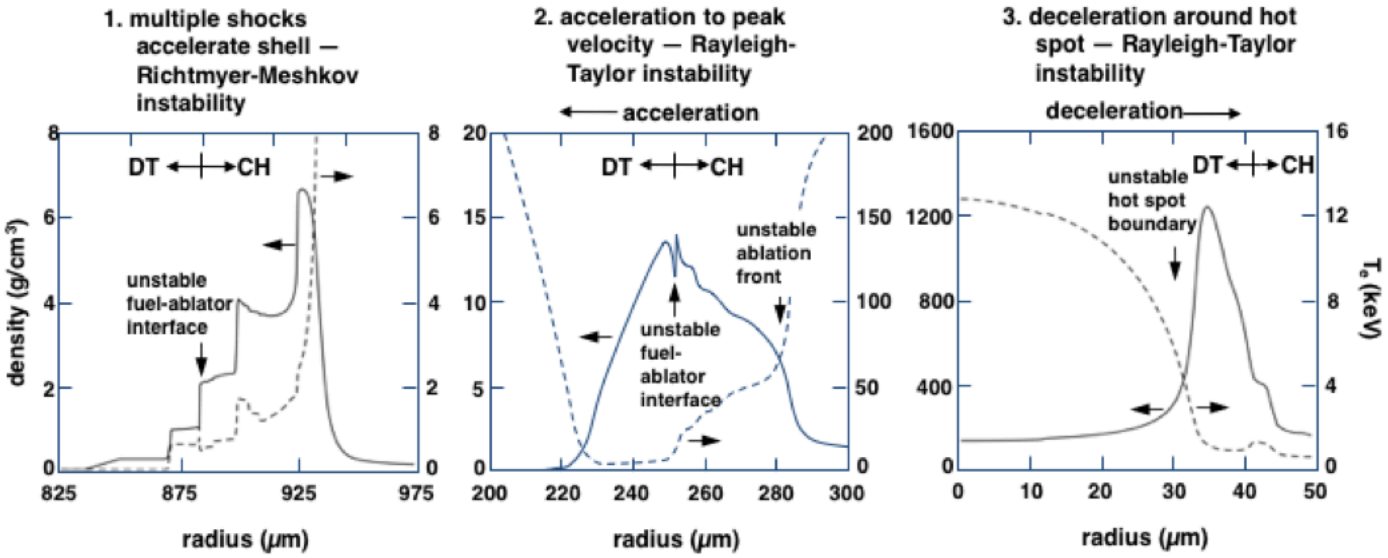

FIG. 24: Distinctive hydrodynamic instabilities during the ICF implosion process

to each surface in the capsule at the start of the implosion, both the external ablator surface and all of the internal surfaces between the ablator layers, ablator and DT fuel, and finally the inner surface of the DT ice layer. Bulk inhomogeneities, either in density or opacity, can also seed instabilities, as can asymmetries in how the implosion is driven, either by x-rays or directly by lasers. Finally, all of the discrete features inherent in any practical target are also very important seeds to instabilities, the 45 nm thick plastic membrane or "tent" used to support the capsule at shot time and the micron-scale fill tube used to fuel the capsule with DT prior to the shot are the leading examples of these.

The interactions of all of these multiple effects and the reality that instabilities in ICF implosions typically evolve into a weakly nonlinear phase, make a detailed understanding of hydrodynamic instability evolution in ICF extremely complicated. Naturally, heavy reliance must then be made on numerical simulation for a quantitative understanding. Over the previous decades, instability modeling in the ICF context has become quite sophisticated relying on highly developed multi-physics codes that couple radiation transport, hydrodynamics, thermonuclear burn, and detailed material properties (equations of state and opacities) in realistic 3D geometry [287–289]. Indeed, quantitative comparisons between simulation and experimental data from high-convergence NIF implosions have only proven feasible with these fully 3D, multi-effect simulations [290–293].

C. Ablative Rayleigh-Taylor Instability

Here, a slightly enhanced discussion will be provided on the ablation-front Rayleigh-Taylor instability (ARTI) [282, 284, 294–302]. ARTI was responsible for a significant fraction of the degraded implosion performance observed during the National Ignition Campaign (NIC) on the National Ignition Facility (NIF) [303–306]. The subsequent high-foot implosion [307–313], which was designed to mitigate ARTI performed much better. The essential stability benefits of the high-foot scheme can be understood from examining an expression for the linear growth-rate of ablation driven RTI [314]

$$\gamma_{A-RTI} = \alpha_2(Fr,\nu)\sqrt{\frac{kg}{1+kL_\rho}} - \beta_2(Fr,\nu)kv_a \qquad (58)$$

where k is the perturbation wavenumber, g is the ablator acceleration, L_ρ is the density gradient scale-length of the ablation front, and α_2 and β_2 are parameters of order unity whose exact values depend upon a heat conduction scale-length parameter, ν, and the Froude number, $Fr = v_a^2/(gL_\rho)$. The classical RT growth-rate, $\gamma_{RT} = \sqrt{kg}$ is easily recognizable in Eq. 58.

The key stabilizing effects of the high-foot drive enter through the higher ablation velocity increasing the $\beta_2 kv_a$ ablative stabilization term of Eq. (58) and through an increase in L_ρ which reduces the $\sqrt{kg}$ unstable RT drive term. The increase in L_ρ is primarily due to a stronger 1^{st} shock designed into the high-foot implosion which increases the adiabat of the implosion and prevents the ablator from becoming so highly compressed (risking break-up) during the implosion. It is also worth noting that the $1+kL_\rho$ factor comes from a paper by LeLevier *et al.* [315] on density gradient stabilization. Recent indirect drive, planar experiments have been carried out at NIF to study the ARTI in transition from a weakly nonlinear to highly nonlinear regime [316]. In these experiments, a planar package is accelerated by a 175 eV radiative temperature drive used to accelerate this planar sample over millimeter distances and tens of nanoseconds intervals. This ex-

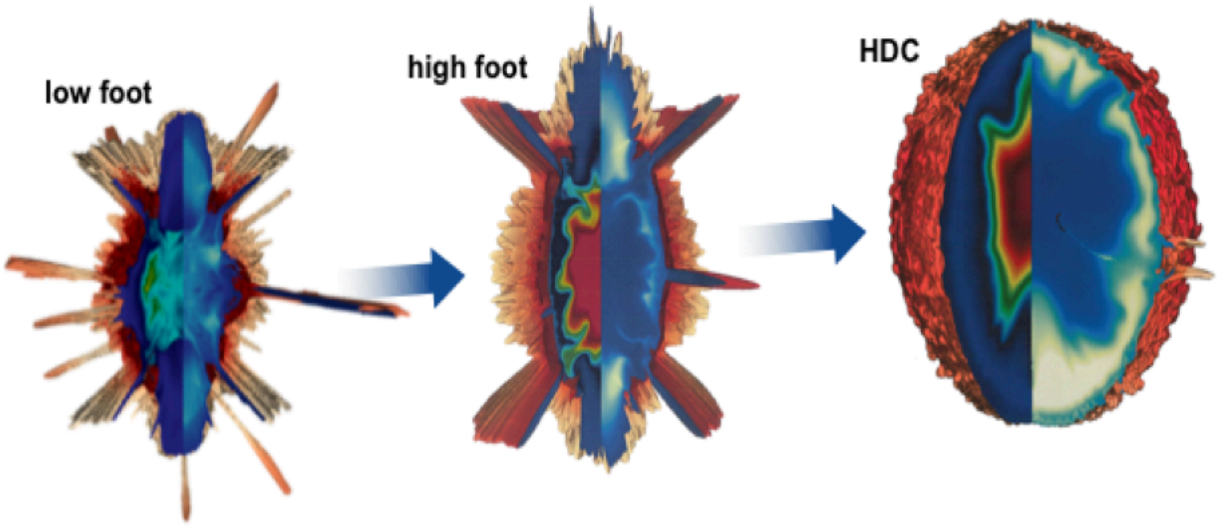

FIG. 25: 3D simulations of NIF implosion.

tended acceleration allows experiments on NIF to enter a turbulent-like regime where simultaneous measurements of the foil trajectory and the subsequent RTI growth were performed and compared with radiative hydrodynamics simulations. This work demonstrated in indirect-drive a bubble- competition, bubble-merger regime for the RTI at ablation front in planar geometry [317].

A planar direct-drive platform has been developed on the NIF, which allows the acceleration of targets over an interval of 30 ns. Planar plastic samples were directly irradiated by 300 450 kJ of UV laser light (351 nm) and very good planarity of the laser drive was demonstrated. No detrimental effect of imprint was observed in the case of these thick plastic targets (300 μm). The long-duration direct-drive platform is utilized to study the ARTI in direct drive in planar geometry, where the growth of two dimensional pre-imposed perturbations is measured through time-resolved face-on x-ray radiography and used to test models and radiative hydrocode simulations. The ARTI is then measured in its highly nonlinear stage starting from intentionally large 3D imprinted broadband modulations. Two generations of bubble mergers were observed in direct drive, planar experiments [318, 319].

While much progress in ICF has been made with high-foot and derivative designs [320], now bringing the field to the threshold of a burning plasma [321–323], hints of yet another form of RTI – now at the deuterium-tritium fuel-ablator interface [324] on the inside of the ablator – may be limiting further progress until further mitigation actions are taken.

Controlling hydrodynamic instabilities is essential to the success of ICF implosions. This is evident in the experimental data from NIF where neutron yields have increased two orders of magnitude in progressing from highly unstable low foot implosions to much more stable HDC ablator implosions and is visually apparent in the simulation results in Figure 25. Further mitigating the growth of these instabilities or reducing the perturbation sources that seed them will be key to further progress.

V. SUPERNOVAE

There are many phenomena in astrophysics that lead to hydrodynamic instabilities in the deep nonlinear to a turbulent state, one example being a core-collapse supernova, as depicted in the simulation results shown in Figure 26, [9, 325], and in the Cas-A supernova remnant (SNR) and the Crab Nebula SNR [326, 327].

A. Supernova Classification

Supernovae (SNe) are the energetic explosions that mark the end stage of certain types of stars. They come with a variety of observational signatures depending on the structure of pre-collapse progenitor star, typically in the form of spectra—typically in the visible frequencies—and light curves, i.e., the spectral intensity as a function of time. For historic reasons, SNe are broadly categorized into two groups: Type II SNe, which indicate the presence of hydrogen in their spectra, and Type I SNe, which do not. From there, supernovae are further classified based on additional spectral features. Notably, the Type I class of SNe are subdivided into Type Ia SNe, which indicate the presence of Si II absorption lines, and Types Ib and Ic, which do not. Similarly, the class of Type II SNe is further subdivided based on various spectral features as well as the broad shapes of their light curves. Each of these observational signatures says something fundamental about the physical circumstances of the pre-explosion progenitor star and the mechanism of the explosion itself.

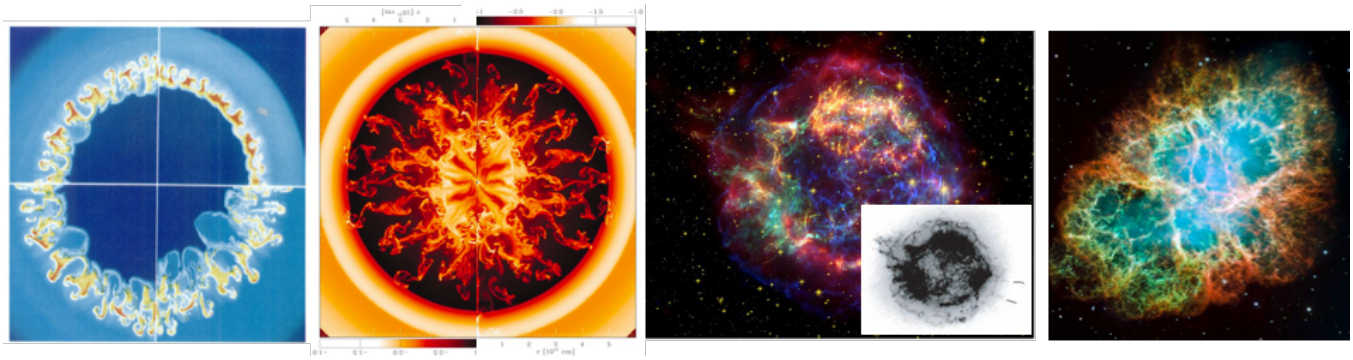

FIG. 26: Results from two core-collapse supernova simulations and two supernova remnant astronomical observations. (a) Supernova simulation of Müller *et al.* [9], shown at 3039, 5534, 7126, and 12557 sec after core collapse. Reproduced with permission from *Astronomy and Astrophysics,* **251**, 505 (1991). (b) Kifonidis *et al.* shown at t = 100, 300, and 1500 sec after core-collapse [325]. Reproduced with permission from *Astronomy and Astrophysics*, **408**, 621 (2003). (c) Cassiopeia A supernova remnant (SNR) astronomical observation, and lower right corner inset is greatly over-exposed to show what looks like RT bubbles and spikes [326]. Reproduced with permission from Hwang *et al.*, *Astrophys. J.*, **615**, L117 (2004). Copyright 2004, Institute of Physics. (d) The Crab Nebula SNR (https://www.spacetelescope.org/images/heic0515a/) showing significant nonuniformities and filamentary structures, which have been interpreted to be, in part, due to magnetized RT [327]. Image Credit: NASA.

Before these things were fully understood, the classifications could only be based on the only things that were known for certain, namely, observational features of SN spectra and light curves. It is now widely believed that Type Ia SNe are the thermonuclear explosions of lower-mass white dwarf (WD) stars and that the remainder, including Types Ibc and II, are primarily caused by the gravitational collapse of the progenitor star's core.

B. Stellar Evolution

Most stars, including our own Sun, fall onto an evolutionary track called the main sequence. Figure 27 shows a Hertzsprung-Russell diagram (HRD) of absolute magnitude versus color for a large sample of stars (over 4 million, selected for low extinction) from the Gaia mission's second data release catalogue [328]. A star's location on the HRD is almost entirely a function of the star's mass, though it changes as the star evolves. This mass largely affects the method of energy production and energy transfer within the star, hence it primarily determines a star's internal hydrodynamic structure. Stars with masses below about 1.5 $M_\odot$ primarily fuse hydrogen into helium via proton-proton chain reactions, while for more massive stars, the core temperature is high enough to allow fusion via the carbon-nitrogen-oxygen (CNO) cycle. Since the energy production rate for proton-proton chains is not so sensitive to temperature, the cores of lower-mass stars are typically stable to convective overturn. In this case, energy is instead transported in the core via radiation. If the outer shells of lower-mass stars are cool enough that hydrogen remains neutral, then the opacity to absorption of ionizing ultraviolet (UV) radiation will be very high, hence this outer layer will be unstable to convective overturn. In contrast, the energy production rate in the CNO cycle depends very sensitively on the star's temperature, thus in higher-mass stars the temperature gradient is steep enough to drive core convection. The outer layers of these stars tend to remain hot enough that hydrogen is kept fully ionized, hence these layers are transparent to UV photons and are not usually convective. These various details combine to determine the equilibrium structure that supports the star against its own self gravity during its main-sequence lifetime.

As stars burn through their fuel, first fusing hydrogen into helium and then potentially on to successively heavier elements, they release energy in the form of radiation and heat. At a given point in time, a star's internal structure is arranged such that the inward self-gravitational force is balanced by the outward pressure gradient [329]. As the initial hydrogen fuel runs out, the star begins to move off the main sequence, and its subsequent evolution depends on the star's mass [330]. If there isn't enough fuel to maintain a sufficient pressure gradient to support itself against gravitational collapse, the star must contract. This contraction both heats the helium core and brings hydrogen from the cooler outer layers into a region that is hot enough to continue fusion within a shell surrounding the core.

As hydrogen continues to burn, the helium core grows in mass and eventually either loses the ability to oppose gravitational contraction via thermal pressure and becomes degenerate [331] or else the core becomes hot enough ($\sim 10^8$ K) to ignite helium burning via the triple-alpha process. For stars in the mass range $\sim 0.8 - 2\,M_\odot$, the core reaches degeneracy first, but since degenerate

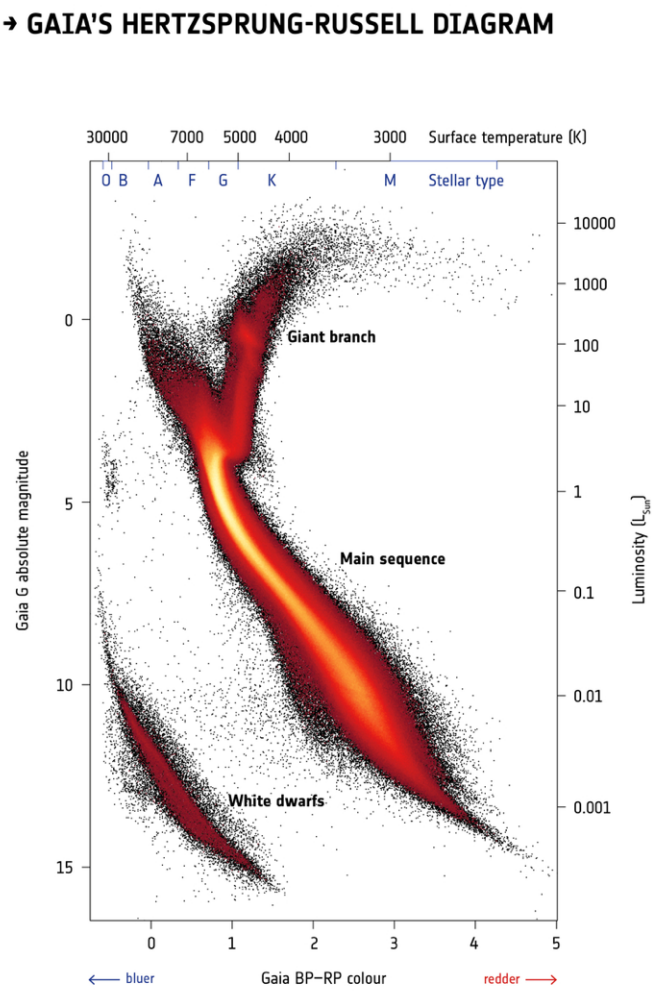

FIG. 27: Hertzsprung-Russell diagram based on a sample of more than 4 million stars from Gaia's second data release catalogue. The color of the points indicates the probability density of stars plotted at a given absolute magnitude (a proxy for brightness) and color (a proxy for surface temperature). The prominent band of stars running diagonally from the upper left to the lower right is known as the main sequence. Also visible is the red giant branch and the white dwarfs.
Gaia Collaboration *et al.* [328]. *Astronomy & Astrophysics*, **616**, A10 (2018); licensed under a Creative Commons Attribution (CC BY) license.

matter does not expand to cool in response to an increasing central temperature, the core is no longer in thermal equilibrium with the surrounding shells. Once the core temperature reaches $\sim 10^8$ K and helium burning is ignited, the temperature increases, which in turn makes helium burning more efficient, thus nearly the entire helium core is burned into carbon and oxygen in a runaway flash within a matter of hours. For more massive stars, the central temperature reaches $\sim 10^8$ K before the onset of degeneracy, igniting helium burning more slowly. In either case, the shell hydrogen burning via the CNO cycle becomes much more efficient as the shell contracts and heats up along with the core, causing the outer hydrogen envelope to expand and cool and giving the star a reddish appearance; the star is now said to have entered the red-giant branch (RGB) phase of its evolution.

Once the core helium is exhausted, the star then enters the asymptotic giant branch phase in which a core of carbon and oxygen builds up. Eventually, the core contracts once more, becoming degenerate, then heats up and ignites helium fusion in a shell surrounding the core, with a shell of burning hydrogen surrounding that. After the helium-burning shell eventually runs out of fuel, the hydrogen shell continues burning. The star then undergoes a series of thermal pulses in which a layer of helium periodically builds up below the hydrogen-burning shell, contracting and heating up enough to reignite helium burning in a runaway flash that puffs up the star and may eject the outer shell of material. Meanwhile, mass is also continuously lost through strong stellar winds such that most of the star's mass is lost as a planetary nebula [332] during this phase of its evolution. For stars with mass below $\sim 8\ M_\odot$, the carbon-oxygen core will never reach sufficient temperatures to ignite the next stage of fusion, thus the hot remnant core of degenerate matter will eventually cool to a white dwarf. In more massive stars, fusion continues to produce successively heavier elements at an increasingly rapid pace but releasing less and less binding energy. Eventually, fusion can no longer produce sufficient energy to prevent the imminent gravitational collapse of the core.

C. Type Ia Supernovae

Most stars end their evolutionary lifetimes as white dwarfs, although the time to arrive at this state varies as a function of stellar mass. White dwarfs are the very dense carbon-oxygen cores of stars that have exhausted their supply of fuel to sustain further nuclear burning. As a result, they can no longer produce sufficient thermal pressure to support themselves against gravity, although electron degeneracy pressure is sufficient to prevent further gravitational collapse. As the mass of a white dwarf increases, degeneracy forces the average electron energy to higher and higher levels in order to resist gravity. Eventually, the energies of these electrons must approach their rest-mass energies, at which point they become relativistic particles. At a mass of approximately 1.4 $M_\odot$, a white dwarf reaches the Chandrasekhar limit [333], a fundamental stability threshold beyond which electron degeneracy can no longer prevent imminent collapse.

If a white dwarf can somehow continue to gain mass and approach this limit, collapse will become inevitable. The star will explode as a Type Ia supernova with a canonical explosion energy of a few 10^{51} erg, which is

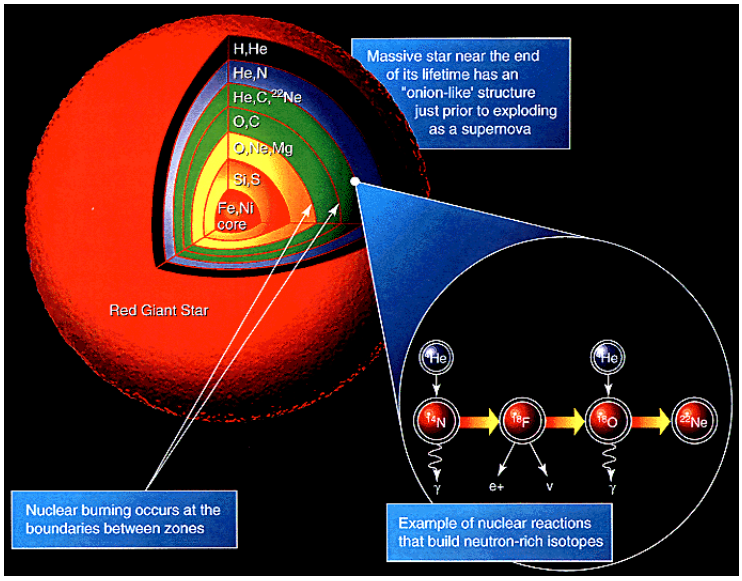

FIG. 28: Just before its end of life, supernova resembled a many-layer, enormous onion as successively heavier layer of fuel ignited and burned. Image Credit: NASA. https://helios.gsfc.nasa.gov/onion.html

sufficient to unbind and destroy such a star completely. Unlike Type II SNe, these events are observed in all kinds of galaxies and are believed to be the end of long-lived stellar systems. The peak luminosity of Type Ia SNe exhibits a strong correlation with its subsequent rate of decline in luminosity known as the Phillips relation [334], which has been used to correct for variations in the peak luminosity to high accuracy. This allows Type Ia SNe to be used as a standard candle to measure the distances to their host galaxies, and since they can be observed much further away than other types of distance measurements would allow, they therefore play an important role in cosmology. However, the identification of the progenitors of Type Ia SNe remains an unsolved problem.

There are two main proposed routes to Type Ia SNe: the single- and double-degenerate models. In the single degenerate scenario, a binary system containing a white dwarf and a red giant orbit each other close enough that as the outer layers of the giant expand, they begin to spill over into the gravitational potential well of the white dwarf. In this process, known as Roche lobe overflow, a steady amount of mass is accreted onto the surface of the white dwarf, pushing it closer to the Chandrasekhar limit. As this limit is neared, the white dwarf becomes unstable and contracts enough to ignite carbon fusion. This dramatically increases the temperature of the white dwarf, but since degeneracy is a quantum-mechanical phenomenon not a thermal process, the star cannot respond to or regulate this process, leading to a rapid, runaway thermonuclear explosion. Because the evolutionary paths of white dwarfs lead their progenitors to be so similar in mass and composition, this may explain the uniformity of their peak luminosities. However, the accretion of material onto a white dwarf should cause significant X-ray emission, which seems to missing in X-rays observations of nearby galaxies [335].

In the double-degenerate scenario, a binary system consisting of two white dwarfs emits gravitational waves and spirals in on itself, eventually merging into a single super-Chandrasekhar-mass object that must eventually explode. However, no such gravitational wave signatures have yet been detected. Furthermore, the inspiral model implies a much longer evolution with a distribution of delay times between the formation of these systems and their explosion as supernovae that should be observable. So far the data are still inconclusive, but there are clearly different observed Type Ia SN rates in active star-forming galaxies versus passive galaxies [336] and recent observations of Type Ia SNe within a few days of their explosions show differences in spectral features between two distinct populations [337]. Yet another mechanism has been proposed wherein a triple system becomes dynamically unstable, leading to the head-on collision of two white dwarfs [338].

Although the specific progenitor details are still uncertain, a Type Ia SN explosion originates with the onset of carbon burning at one or more sites deep within the star. The increased heat provided by nuclear burning is not lost to the expansion of the star, but instead, increases the efficiency of local fusion reactions and leads to thermal runaway. Due to the high sound speed in the interior of the star, this leads to a subsonic deflagration front that expands outward via the RTI. The interaction of the burning front with the turbulent outer layers

of the star leads to a complicated explosion morphology that is not yet well understood. Furthermore, the explosion itself will interact with the companion star and with circumstellar material, possibly fueled by the radioactive decay of 56-Ni created from material dredged up from the deep interior of the star by convective overturn prior to explosion.

The details of these various interactions play a key role in determining the variability of peak luminosity among Type Ia SNe. Accurate numerical modeling of the RTI within the star is needed to understand the dynamics of the deflagration front, which is complicated by the very high Reynolds numbers ($\mathcal{R}e \approx 10^{14}$) of the flow [86][339] and the scale limitations of direct numerical simulations. In particular, numerical models must be able to produce sufficient energy to unbind the star, explain the production of intermediate-mass elements at observed abundances, and their ejection at very high velocities. Simulations with Reynolds number in range $10^4 - 10^5$ have demonstrated a weak Reynolds number dependence of the explosion kinetic energy to the released gravitational potential, which underscores the need for accurate numerical modeling in the high-Reynolds-number regime [149].

D. Core-collapse Supernovae

Core-collapse supernovae (CCSNe) are the end-stage events of the stellar evolution of massive ($\gtrsim 8\ M_\odot$) stars. They are extremely energetic events with a canonical diagnostic explosion energy of 10^{51} erg, a unit often referred to as 1 Bethe [340], distributed in a range of about 0.1-10 Bethe. They often leave behind a neutron star core, although sometimes the core can collapse directly into a black hole, and due to explosion asymmetries, they are often "kicked" at velocities of $\sim 50 - 200$ km s^{-1}. A major unsolved problem in CCSNe is an explanation of the mechanism that leads to explosion.

Electron degeneracy does not play a significant role in halting the nuclear evolution of CCSNe progenitors. Instead, they continue contracting, heating up, and igniting fusion of successively heavier elements. The density, temperature, and chemical profiles of the pre-collapse progenitors play an enormous role in the outcome of the explosion. The least massive progenitors ($8 - 9\ M_\odot$) are believed to possess cores of oxygen, neon, and magnesium [341]. These "O-Ne-Mg" cores lose support through a process whereby electrons are "captured" onto proton-rich nuclei, producing a neutron and an electron neutrino that radiates energy out of the core. The sudden drop in pressure collapses the core, leads to runaway oxygen burning all the way to iron, and subsequent explosion of the core into a rather tenuous outer envelope with a very steep density drop-off. This results in a prompt yet under-energetic ($\sim$0.1 Bethe) neutrino-wind-driven explosion [342, 343].

In more massive stars ($\gtrsim 9\ M_\odot$), fusion proceeds until a degenerate iron core is formed, surrounded by "onion"-like layers of silicon-, oxygen-, neon-, carbon-, helium-, and hydrogen-burning layers, respectively (Figure 28). Each new stage of burning provides successively higher temperatures and correspondingly faster nuclear burning rates accompanied by significant neutrino losses that dramatically speed up the evolution of the star, with the silicon-burning phase lasting just a few days. Approaching the "iron peak," the nuclear binding energy per nucleon released by fusion decreases until it reaches a point beyond which fusion becomes an endothermic process. Thus, iron represents the final stage of nuclear burning, and when degeneracy pressure can no longer support the core against gravity, it collapses (Figure 29) [344].

The collapse of the inner core ($\lesssim 5,000 - 10,000$ km) proceeds within less than a second. Upon infall, the central density and temperature continue to rise. Because the increase in temperature is, in part, directed into excited nuclear states instead of kinetic energy, the temperature increase is moderated, allowing the nuclei to survive until the core reaches nuclear densities ($\sim 2.6 \times 10^{14}$ g cm^{-3}) [345]. The core separates into a subsonic inner core that collapses homologously (i.e., with $v_r \propto r$) as a unit and a supersonic outer core. Once nuclear densities are reached, the strong nuclear force dramatically stiffens the equation of state, and the subsonic inner core "bounces" off of itself, halting collapse and shooting like a piston outward from the sonic Mach point into the supersonically collapsing outer core. This generates a shock wave that must travel through the outer-core material with sufficient energy not only to overpower the ram pressure of the infalling material but eventually to unbind the entire outer envelope; otherwise, the supernova "fails" and instead collapses directly to a black hole, an event that is very difficult to detect observationally. Unfortunately, neutrino losses almost always sap a huge amount of energy from the bounce shock, causing it to stall out into a standing accretion shock.

The primary reason the bounce shock stalls is due to neutrino trapping. As the central density and temperature increase in the collapsing core, the rate of electron capture onto nuclei shoots up rapidly, producing neutrinos with increasingly higher energies. So, too, do the cross sections for coherent scattering off the infalling nuclei, rapidly decreasing the scattering mean-free-paths such that the neutrinos begin to diffuse outward. At the point where the diffusion speed becomes comparable to the infall rate, the neutrinos become "trapped" and subsequently compressed into excited degenerate states with typical Fermi energies of $\sim 100 - 300$ MeV. As the bounce shock propagates into the outer core, it dissociates nuclei and lowers the optical depth to coherent neutrino scattering. These nucleons are then free to capture electrons via the charged-current reaction, producing an enormous fluence of neutrinos that lasts $\sim$10 ms. This "breakout burst" is extremely luminous ($\sim 3 - 4 \times 10^{53}$ erg s^{-1}) and robustly drains the bounce shock of energy to the point that it stalls [345]. If the CCSN explosion is to

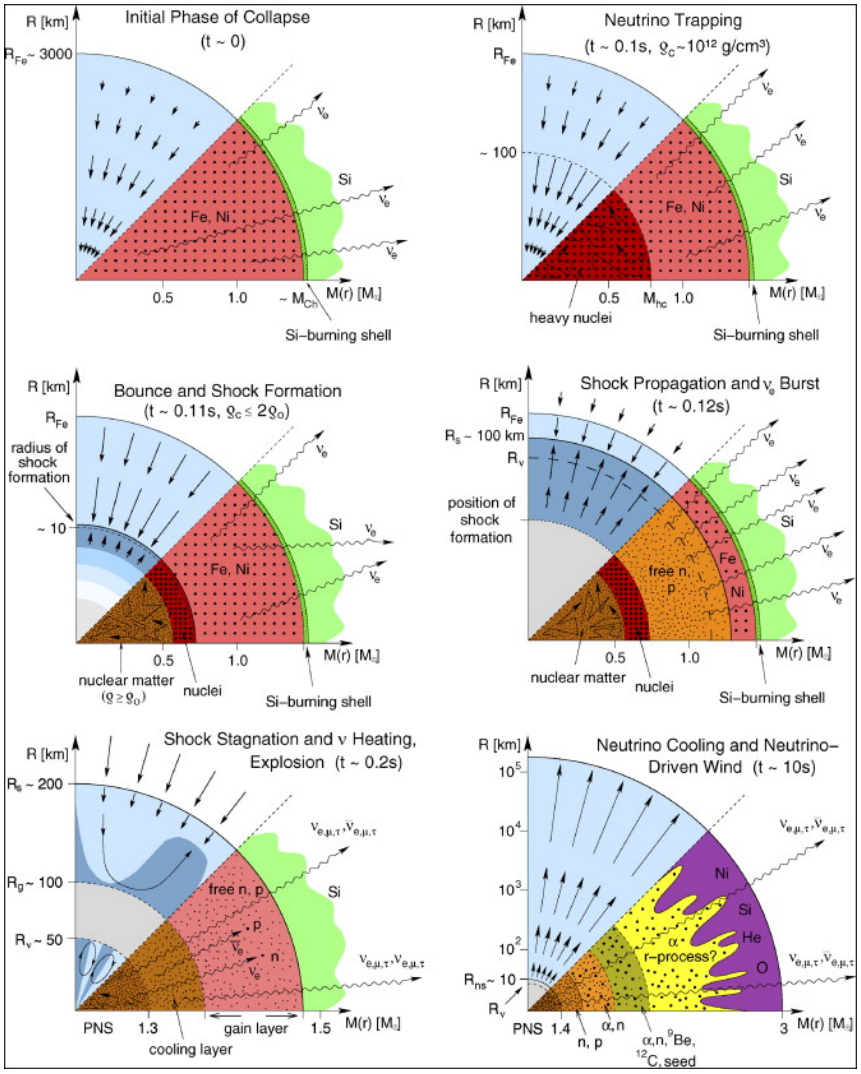

FIG. 29: Schematic representation of the evolutionary stages from stellar core collapse through the onset of the supernova explosion to the neutrino-driven wind during the neutrino-cooling phase of the proto-neutron star (PNS) [344]. The panels display the dynamical conditions in their upper half, with arrows representing velocity vectors. The nuclear composition as well as the nuclear and weak processes are indicated in the lower half of each panel. The horizontal axis gives mass information. M_{Ch} means the Chandrasekhar mass and M_{hc} the mass of the subsonically collapsing, homologous inner core. The vertical axis shows corresponding radii, with R_{Fe}, R_s, R_g, R_{ns}, and R_ν being the iron core radius, shock radius, gain radius, neutron star radius, and neutrinosphere, respectively. The PNS has maximum densities ρ above the saturation density of nuclear matter ρ_0. Reproduced with permission from Janka *et al.*, *Physics Reports*, **442**, 38 (2007). Copyright 2007, Elsevier.

be successful—they occur quite regularly at a volume-averaged rate of roughly 1 yr^{-1} Mpc^{-3} [346]—the shock must be revived somehow.

The current leading theory for the revival of the stalled bounce shock is the delayed neutrino-heating mechanism, whereby neutrinos produced near the core are captured in a region behind the shock, heating it and pushing the shock further out. This also leads to a negative entropy gradient in the "gain region," i.e., the region behind the shock where neutrino heating outpaces neutrino cooling, which is unstable to convective overturn. Such turbulent, convective motions may allow infalling material to dwell in the gain region for longer periods. In order for the supernova to explode, the characteristic heating time for material in the gain region must be comparable to the time scale for advection of material through the gain region; otherwise, the heated material will simply accrete onto the core [347]. Therefore, turbulence plays a critical role in the understanding of the explosion mechanism of CCSNe. For CCSNe, the physical Reynolds number for the turbulent flow in the gain layer can be estimated using a characteristic length scale of ∼100 km, a charac-

teristic flow velocity of $\sim$10,000 km s^{-1}, and a characteristic kinematic viscosity of $\sim$0.2 cm^2 s^{-1} for neutrons at a density of $\sim 10^{10}$ g cm^{-3} and temperature of $\sim$10 MeV to be $\mathcal{R}e \approx 10^{17}$ [87]. Although recent 3D simulations of CCSNe exhibit numerical Reynolds numbers less than a few hundred [see, e.g., 87, 347], there are other factors to consider in assessing the physical fidelity of numerically-modeled turbulence, including the role of buoyancy in converting gravitational potential into kinetic energy and subsequently into thermal energy via turbulent dissipation [348].

E. Instabilities, turbulence, mixing, and astrophysical flows

In this subsection, we take a closer look at the instability, mixing, and turbulence in a few selected astrophysical flows. What makes SN explosions so complex is that each of these phases of instability growth do not occur in isolation, but growth in one phase feeds through to initiate growth in a later phase.

As illustrated by Wongwathanarat *et al.* [349], the evolution of the SN shock and the neutrino-heated ejecta within the stellar envelope involve several types of hydrodynamic instabilities. During the shock transit phase of the core-collapse, the RM instability is triggered at each discontinuity in the density profile of the star. As the explosion ensues, conditions arise where dense material is accelerated by lighter material, the classic environment for the RTI. This is prominently the case at the boundary between the denser helium core ([C+O]/He, He/H) that is decelerated by the lower-density hydrogen envelope. Similar effects can occur with smaller amplitude at inner-core composition boundaries (Si/O, for instance). Shear associated with RT fingers or other effects triggers KHI, and shocks propagating across steep density gradients near composition discontinuities induce RMI [350].

The outward mixing of the higher-density, radioactive core material (e.g., ^{56}Ni, ^{56}Co, ^{44}Ti) brings the radioactive heat source toward the surface of the star. These explosion products decay by the emission of γ-rays, which Compton scatter off electrons in their vicinity. This reheats the photosphere and causes the secondary maximum in the light curve at 40–120 days. The RT mixing induces this reinvigoration of the light curve to start earlier, broadening the secondary maximum. Observations of the light curve of SN1987A unambiguously showed this broadening of the secondary peak, suggesting enhanced transport from the core out to the photosphere [351–353].

Müller *et al.* [354] note the role of RTI for the evolutionary pathways of core-collapse supernova progenitors at the low-mass end of the spectrum. In recent years, a variety of evolutionary channels has been discovered in addition to the classical electron-capture supernova channel of super-AGB stars. The key to these differences lies in the development of overturning driven by the RTI in the wake of the rapidly expanding shock between deeper layers of high-entropy, neutrino-driven ejecta and colder ejecta shocked at early times. Also, the discoveries of many double neutron star systems and their detection as LIGO-Virgo merger events call for a detailed understanding of their origin [355]. Explosions of ultrastripped stars in binary systems are a potential explanation for rapidly evolving hydrogen-free transients and requires an understanding of the mixing by RTI during the propagation of the shock through the envelope. Müller *et al.* stressed that the question of mixing in Type Ib/c SNe is, in fact, relevant not only for ultrastripped progenitors, but for the entire class of hydrogen-free progenitors.

In another interesting case, Duffell and Kasen [356] noted that the interaction of the ejecta from a SN explosion with a surrounding circumstellar medium (CSM) can give rise to synchrotron radiation at radio wavelengths. To infer how strong magnetic fields can become when amplified by this turbulence, the authors computed the growth of turbulence due to RTI. Assuming rough equipartition between kinetic and magnetic energy in the turbulence [357], the RT instability may produce turbulent fluctuations strong enough to amplify magnetic fields to a few percent of equipartition with the thermal energy. Inoue *et al.* [358] studied the influence of the magnetic field amplified by the RMI on the polarization of synchrotron emission. For Tycho's SNR, in which the synchrotron emission region is known to be a spherical shell, Shimoda *et al.* [359] find that for the magnetic field distribution of turbulent SNRs driven by the RMI—in other words, the effect of a rippled shock—the magnetic energy spectrum shows a Kolmogorov-like scaling.

A memory of the initially unstable and structured explosion of the core-collapse supernova may be responsible for an amazing array of knots, filaments, and flocculi in the relatively young ($\sim$300-year old) Cassiopeia A supernova remnant (Cas A SNR). [360–363]. There are "bubbles" and "spikes" at various places around the outer boundary that appear RT-like [10]. The Crab Nebula filaments (Figure 26) may be generated by the expanding bubbles of a shocked pulsar wind that sweeps up thin shells of ejecta accelerating approximately in accordance with the observed acceleration of the filaments [364]. The shell is subject to the RTI, which provides an explanation for the filamentary structure observed in the Crab Nebula. The RTI gives rise to inner filaments that effectively broaden the swept-up shell [365].

In another matter that has a strong parallel to the ICF implosion, Branch & Wheeler pointed out that initial conditions might be an issue of significant concern for SN explosion studies [350]. Indeed, the RTI, RMI, and KHI in the early SNe explosion stage tend to lead to small-scale mixing of composition in the ejecta. The strong turbulence beneath the shock can impose rather large-scale initial asymmetries. These asymmetries can also trigger RTI that may produce large-scale plumes in the nonlinear limit. Wongwathanarat *et al.* also noted that the metal-rich ejecta in homologous expansion still carries fingerprints of asymmetries at the be-

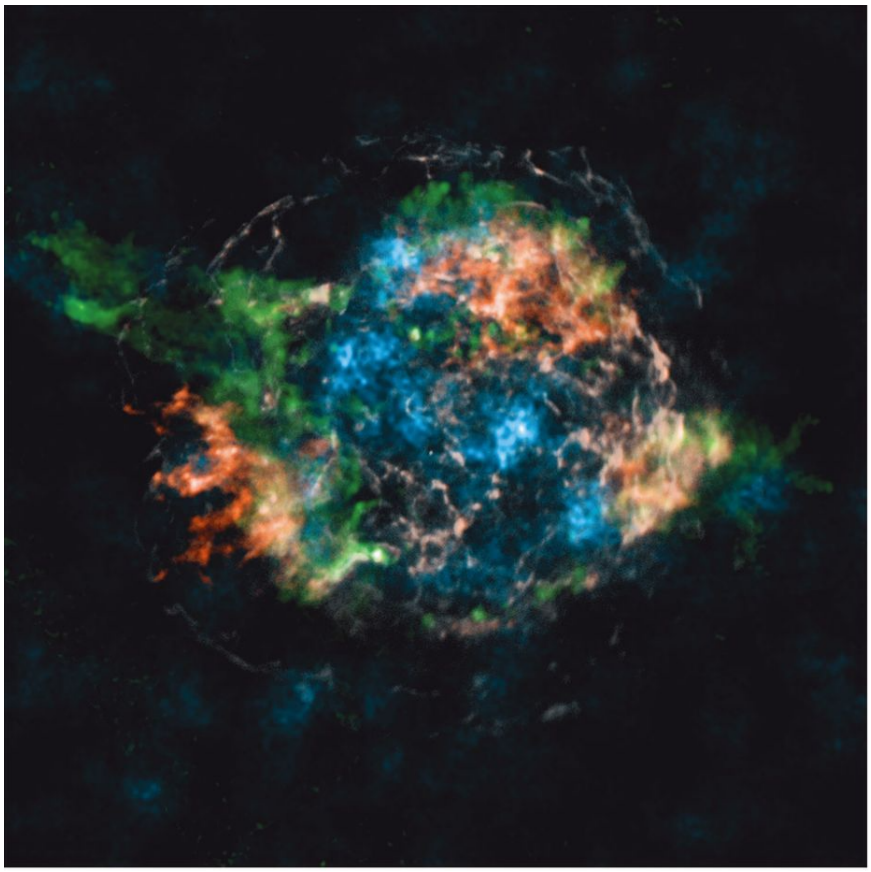

FIG. 30: Spatial distribution of X-ray lines from shock-heated Fe (red) and from radioactive decay of ^{44}Ti (blue) in the Cas A SNR as observed by Chandra and NuStar that indicate a strong anti-correlation between these two types of emission. Also shown are Si/Mg lines observed by Chandra (green) indicating the presence of a jet-counterjet structure that is also not correlated with the structure of the ^{44}Ti emission. The wide variations in the observed spatial distribution of these nucleosynthetic products suggests a high degree of asymmetry in the local conditions at the time of explosion [366]. Reproduced with permission from Grefenstette *et al.*, *Nature*, **506**, 339 (2014). Copyright 2014, SpringerNature

ginning of the explosion, but the final metal distribution is massively affected by the detailed progenitor structure [349]. Furthermore, Grefenstette *et al.* [366] observed an anti-correlation between the X-ray emission from both shock-heated Fe and the radioactive decay of ^{44}Ti (Figure 30). Such an anti-correlation may arise because the reverse shock simply hasn't penetrated far enough into the ejecta, in which case the majority of the Fe would remain unshocked hence unobserved. However, there are many regions where Fe is indeed observed but ^{44}Ti is not, which indicates an alternate production mechanism for the Fe in those regions as opposed to α-rich freeze-out, which ought to produce both together. Such a wide variation in nucleosynthetic production across the SNR suggests highly asymmetric local conditions during explosion and perhaps even in the progenitor itself.

More specifically, Couch *et al.* [367] stressed that real massive stars are not spherically symmetric, particularly near core collapse, and this can have dramatic implications for the CCSN mechanism. Wongwathanarat *et al.* [349] found that the most extended and fastest metal fingers and clumps are correlated with the biggest and fastest-rising plumes of neutrino-heated matter, which seed the growth of RTI at the C+O/He and He/H composition-shell interfaces effectively after the passage of the SN shock. Furthermore, the authors found that the extent of radial mixing, global asymmetry of the metal-rich ejecta, RT-induced fragmentation of initial plumes to smaller-scale fingers, and maximum Ni and minimum H velocities depend not only on the initial asphericity and explosion energy (which determine the shock and initial Ni velocities) but also on the density profiles and widths of C+O core and He shell and on the density gradient at the He/H transition. This can lead to the formation of reverse shocks as well as the unsteady shock propagation.

RTI also play an important role during the formation of massive star systems. Nuclear burning in stars more massive than ∼10 solar mass while they are still accreting. The radiation pressure exerted they exert on the gas and dust around them is stronger than their gravita-

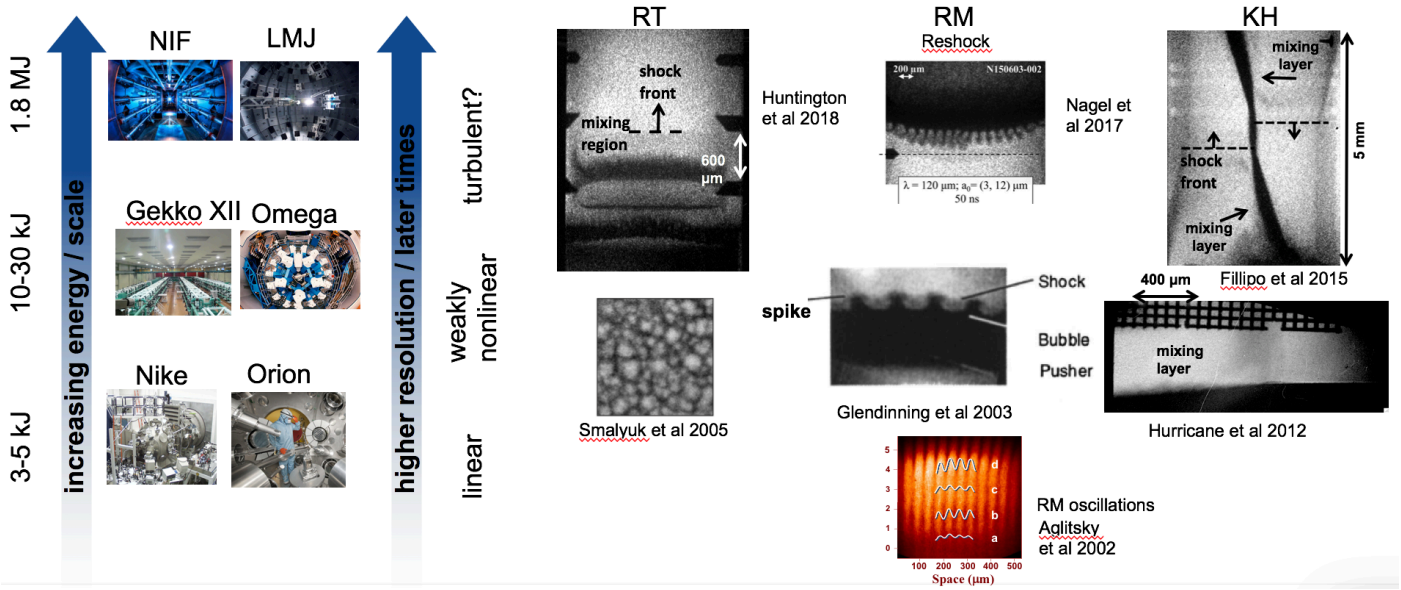

FIG. 31: HEDP facilities, showing higher energy, increased longer-time drive, and enhanced resolution.

tional attraction. This has historically been expected to inhibit growth by accretion and is inconsistent with observational evidence of stars in excess of 100 solar mass [368–370]. Two dimensional simulations that allow the formation of optically thick rotationally-supported disks to shield against radiation pressure indicate that radiation pressure halts stellar growth at 40 solar mass [371]. The RTI play a crucial role in overcoming the radiation barrier to stellar growth. Three-dimensional radiation-hydrodynamic simulations of the collapse of a massive prestellar core by Krumholz *et al.* [372] show that turbulence in the circumstellar material seeds RTI on the shell of radiation-pressure supported gas. These instabilities grow into dense, optically thick spikes that channel gas onto the growing massive star while allowing radiation to escape through optically thin bubbles. Using a new, highly accurate radiation algorithm that properly treats the absorption of the direct radiation field from stars and the re-emission and processing by interstellar dust, More recently, Rosen *et al.* confirmed that mass is channeled to the stellar system via gravitational and RTI using new tools to perform 3D radiation-hydrodynamic simulations and suggested that RT features should be present around accreting massive stars throughout their formation [373].

VI. TRANSITION CRITERIA

Intense lasers are now being used to recreate aspects of astrophysical phenomena in the laboratory. As we improve the capability of the HEDP facilities (see Figure 31), can we design the experiments on these platforms so transition to fully developed turbulence can occur? Smaller HED platforms (Nike [374] and Orion [375, 376]) only have very limited energy (3-5 kJ) available for studying the linear regime of the instabilities. An example of such study is about RMI oscillations by Aglitsky *et al.* [377]. With increased capacilty (10-30 kJ), Gekko XII [378, 379] and Omega [380] facilities offered an opportunity to study weakly nonlinear regime of the hydrodynamic instabilities, such as those for RTI [381], RMI [382], and KHI [383]. Now with significant laser energy at 1.8 MJ, the National Ignition Facility (NIF) [22, 384, 385] and the French megajoule laser project (LMJ) [386–388] provided much higher resolution and significantly later times. Researchers have been able to push into deeply nonlinear regimes of RTI [389–391], reshocked RMI [174], and KHI [392, 393]. Accurate and robust transition criteria will be critical for guiding the design activities for creating turbulent flows on HEDP platforms.

The need for such criteria is also clear for astrophysical flow studies. The following physics must be incorporated into the multi-physics codes. Specifically, the neutrino heating in the gain region drives convection and should be incorporated; the growth rate of convective instability must be large enough for sufficient growth before convective plumes are accreted; sufficient numerical resolution is required to reduce numerical dissipation (∼16× greater than current 3D simulations). Figure 32 shows the calculated evolution of the RTI induced flow at two different times using one of the modern multi-physics code [394]. Unfortunately, it is clear from Figure 33 that the inertial range that can be achieved from a modern multi-physics codes is rather limited [87, 395]. This situation shows that accurate and robust transition criteria will enable physicists to prepare and plan the major computational efforts that will achieve the relevant flow and mixing regimes.

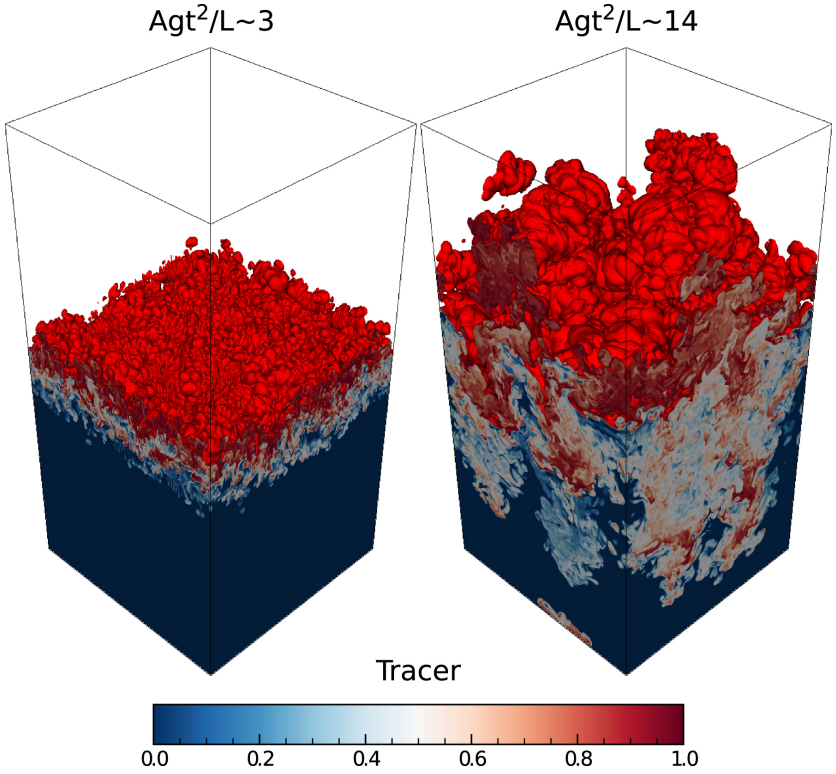

FIG. 32: Passive tracer concentration for the multi-mode 3D Rayleigh-Taylor test at two representative times [394]. Red values indicate higher concentration for the "heavy" fluid. The red surface is the 99% isocontour of the concentration. The resolution is $512^2 \times 1024$. Reproduced with permission from Skinner *et al.*, *Astrophysical J. Suppl.*, **241**, 7 (2019). Copyright 2019, Institute of Physics.

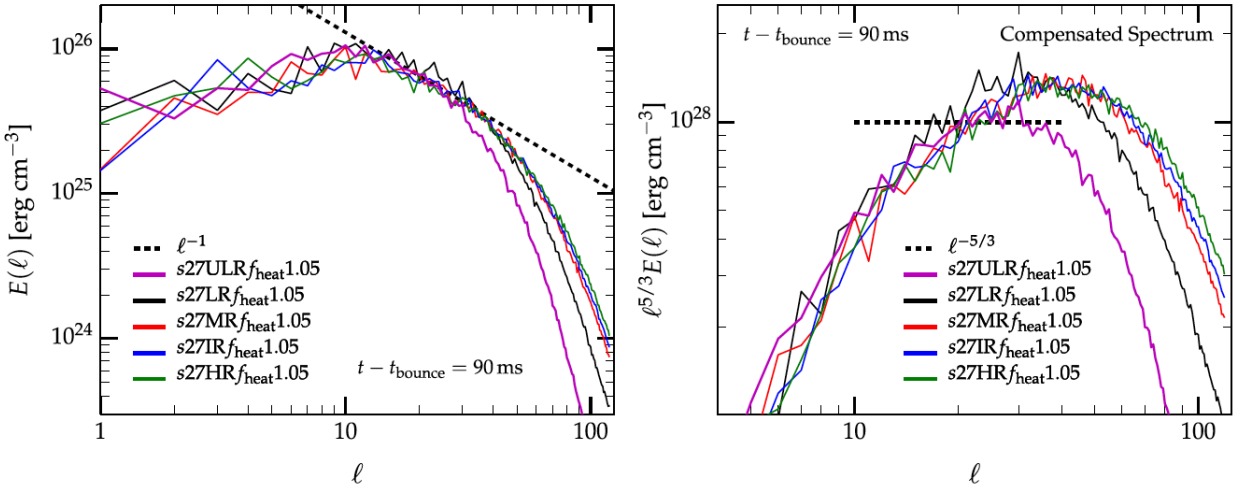

FIG. 33: Transverse energy spectra at different resolutions for one of the models [87]. Reproduced with permission from Abdikamalov *et al.*, *Astrophys.J.*, **808**, 70 (2015). Copyright 2015, Institute of Physics

A. Distinctive dynamics of RT and RM

The first step toward development of the transition criteria is to recall the time-dependent nature of the flows induced by hydrodynamic instabilities. There is a general consensus that at late times the RTI-induced mixing layer transitions to a turbulent state. The growth of the characteristic length scale of these flows (*e.g.* the mix layer width) increases, the Reynolds number of the flow also increases (though this may not be the case in some instances of RMI). Eventually, a critical Reynolds number is achieved where the flow becomes "unstable." At

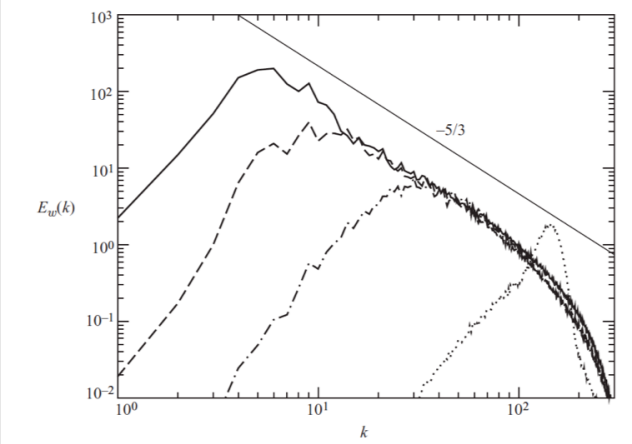

FIG. 34: Evolution of the vertical velocity spectrum computed in the $z = 0$ plane (nondimensional time: $\cdots$, 7; $\cdot - \cdot$, 11; - - -, 21; —, 33). A fiducial corresponding to $k^{-5/3}$ is drawn for reference. Reproduced with permission from Cook *et al.* [148], *J. Fluid Mech.*, **511**, 333 (2004). Copyright 2004, Cambridge Univ. Press.

this point, the emergence of ever more degrees of freedom (i.e., Fourier modes) that couple via the nonlinearities of the Navier-Stokes equations leads to a rapid proliferation of scales of motion. In spite of efforts to ensure that the initial conditions in an experiment are unimodal, these additional modes generally arise and may be due either to unresolved modes or motions in the initial conditions, or modes introduced via boundary conditions during the experiment.

Figure 34 illustrates the time-dependent evolution of the energy spectrum along the direction of gravity for a simulated RTI induced flow. At an early time, the energy spectrum, originated from initial perturbations at the interface, is located at high wavenumber. With the forcing provided by the gravity, the energy spectrum increases in magnitude, but the peak remains close to the the dominant initial wavelength. As time increases, the peak of the spectrum begins migrating toward lower wavenumbers, and at late-times, an inertial range forms [148].

It should be noted that the peak of the spectrum is inversely proportional to the mixing layer width. As a result, the decrease in the $k-$space location of the spectral peak is consistent with the mixing layer width increasing with the time. Also, Figure 35 shows that the total kinetic energy is also increasing with time. This is indicated in Figure 35 since the turbulent kinetic energy is simply equal to the integral of the energy spectrum [101].

The RMI in a planar geometry shows some similarities to the RTI, including the fact that it tends towards a statistically axisymmetric state. Many of the more sophisticated attempts to model the evolution of the RMI and RMML into the nonlinear regime have been proposed, many based on modifications of the methods proposed

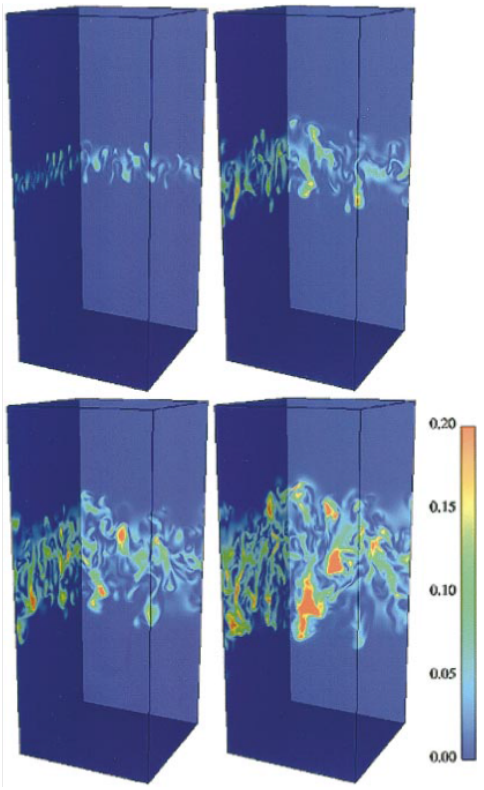

FIG. 35: Kinetic energy on side boundary planes of DNS domain [101]. Images were taken at nondimensional time 3, (upper left), 4 (upper right), 5 (lower left), and 6 (lower right). Reproduced with permission from Cook & Zhou, *Phys. Rev. E,* **66** 026312 (2002). Copyright 2002, American Phys. Soc.

for RTI, but using variations of the impulsive RTI analogy. The interested reader is referred to Refs. [7, 8, 159] for a more complete description.

The evolution of the energy spectrum of a simulated RMI induced flow is given in Figure 36 [396, 397]. However, unlike the RTI and the subsequent RTML, the RMML is not a driven turbulent field [398]. Once the shock has passed, there is no continued source of energy for the flow field and the initially deposited energy begins to decay similar with those of decaying turbulence [66, 399]. Therefore, the energy spectrum decreases in magnitude with the time.

Yet, as in the case of RTML, the peak of the spectrum also migrates to lower wavenumbers as the time evolves. Hence, the mixing layer width also increases with the time. For the given initial condition, the late-time energy scales as $k^{-3/2}$, a RM modified energy spectrum first suggested in Zhou [398].

It would be beneficial to recall the relationship between the mixing layer width and the dominating energy-containing range mode of the energy spectrum or correlation function. The Reynolds number, Equation 4, offers an important perspective. Although the Re can be defined in many fashion, the simplest one is based on the

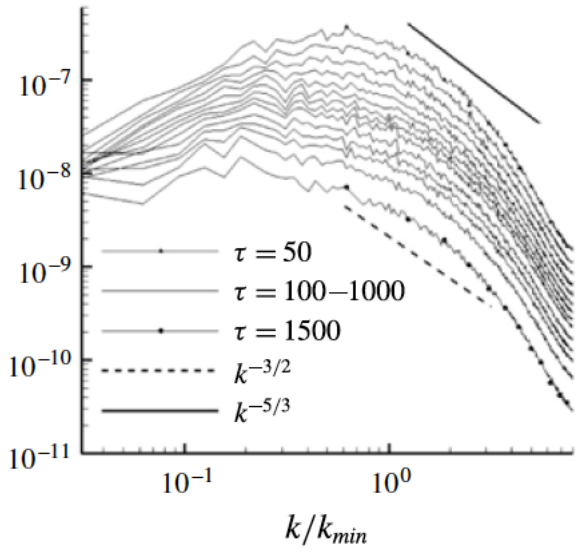

FIG. 36: The hybrid spectra of the radial turbulent kinetic energy averaged on the y and z planes in the bulk of the mixing layer for the 512 cross-section grid and the $k^{-3/2}$ guideline analytically predicted by Zhou [398]. Reproduced with permission from Oggian *et al. J. Fluid Mech.*, **779**, 411 (2015) [396]. Copyright 2015, Cambridge Univ. Press.

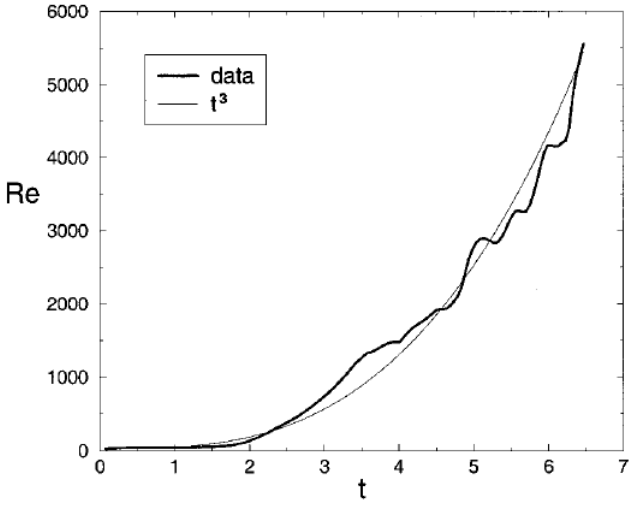

FIG. 37: Outer-scale Reynolds number, based on extent and rate of growth of RT mixing region [101]. Reproduced with permission from Cook & Zhou, *Phys. Rev. E,* **66** 026312 (2002). Copyright 2002, American Phys. Soc.

mixing layer width, $L = h$ and $u = \dot{h}$ as the typical velocity field. One further assumes $t_{s,0} = t_{b,0} = t_0$ for simplicity's sake

In the RT self-similar growth regime, it is trivial to show

$$Re = \frac{h\dot{h}}{\nu} = \frac{2(\alpha \mathcal{A} g)^2 (t+t_0)^3}{\nu}, \tag{59}$$

where $\alpha = \alpha_s + \alpha_b$. Thus, the Re growth asymptotically proportionally to t^3, a result that has been demonstrated in Figure 37.

Figure 38 [400] illustrates that the difference between the RTML and RMML. The usual analyses and experiments of the late stages of RMML, exemplified by Dimonte & Schneider [136], describe the "bubbles" and "spikes" using two different exponents. In this circumstance, the growth of the mixing layer is not self-similar. Other researchers, for example [181, 224, 225] have argued in favor of a single value of θ for the layer as a whole, implying $\theta_s = \theta_b$ (except for the singular case $\mathcal{A} = 1$ [401]). In this case, the Re of the RMML is given by

$$Re = \frac{\tilde{h}^2 \frac{\theta}{|t_0|} \left[\frac{t+t_0}{|t_0|}\right]^{2\theta-1}}{\nu}, \tag{60}$$

where $h = \tilde{h}\tau^\theta$ and $\tilde{h} = \tilde{h}_{s,0} + \tilde{h}_{b,0}$. Thus in this "self-similar" regime, the Reynolds number of the RM mixing layer grows as $t^{2\theta-1}$, and since $\theta < 1$, the growth in the Reynolds number is sublinear in time. Note also that Re decreases with time if $\theta < 0.5$.

For completeness, we noted that in the self-similar growth regime, the width of KH mixing layer at late-time grows as

$$h = \beta_u \Delta_u (t + t_0), \tag{61}$$

where Δ_u is the velocity difference across the layer. The Reynolds number of the KHI mixing layer can be represented as

$$Re = \frac{(\beta_u \Delta_u)^2 (t+t_0)}{\nu}. \tag{62}$$

Thus, the Re growth as a linear function of t,

Before closing this subsection, the fundamental dynamics behind RTML and RMML can be summarized as below

- For RTI, the flow starts with small scale turbulence at time = 0 (random noise for DNS for instance) and larger scales evolving with time;
- The RMML is initialized with the passage of the shock wave through the perturbed interface at time=0. The large-scales must emerge from the initial deposition of energy and inertia, before there can be a cascade and breaking down of the eddies to form smaller scales. This implies a very significant deposition of energy that is followed by sufficient time required to generate large scales while the energy is already "decaying".

Now we can delineate the distinctive potential for RTMI and RMMI regarding the onset of turbulence i.e., the time that a scale separation between the energy-containing and dissipation scales emerges. This onset of turbulence is hard to achieve for an RMI-induced flow because, after the initial energy deposition, the flow field is decaying. On the other hand, RT (and KH) are forced throughout their evolution, and it is relatively difficulty to conceive a mechanism wherein they do not become fully developed turbulence as long as the simulation size or the experimental apparatus is sufficiently large.

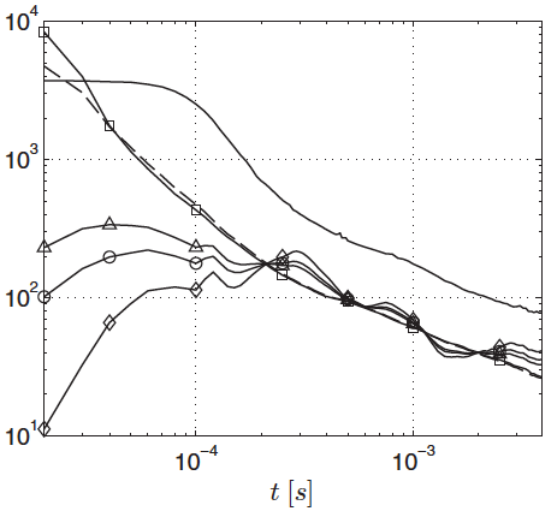

FIG. 38: Outer-scale Reynolds number, based on extent and rate of growth of RM mixing region (solid line) for a shock Mach number of $Ma = 1.5$ [400]. Temporal evolutions of different Reynolds number approximations, as defined in Ref. [48], are given by symbols. For details, see Table II of Tritschler *et al.* [400]. Reproduced with permission from *Phys. Rev. E*, **90**, 063001 (2014). Copyright 2014, American Phys. Soc.

B. Reynolds number criterion for transition

In order to define the transition criterion, it is necessary to invoke similarity analyses. Such analyses have been applied to many other branches of physics. For instance, in his fractal geometry studies, Mandelbrot remarks that the famous Hokusai's painting "The Great Wave off Kanagawa" (Figure 39a) is an example of self similarity [402]. It is interesting that a recent photograph (Figure 39b) appears to have almost precisely reproduced the artwork (Cartwright and Nakamura [403], see also, Dudley *et al.* [404]).

While not directly deduced from the governing Navier-Stokes equation, the Kolmogorov 1941 similarity analysis formed the cornerstone of turbulence theory. For our application of flows induced by hydrodynamic instabilities, it is appropriate to consider the energy transfer process (Figure 40) [406] [405, 406]. At an early time, the Re of the flow is low, the energy-containing and dissipation scales are not separated. However, an inertial range will be formed (for RT and KH, but perhaps not RM) at a late-time as Re increases, and the energy-containing and dissipation scales will be separated by an extended inertial range at a sufficiently late time.

1. *Mixing transition*

Dimotakis ([407]) suggested the notion of a mixing transition, which occurs when the Re is around 10^4. In this case, he observed that in many cases, a variety experiments showed a distinct transition from a low-mix state to a high mix-state. Yet, the Re associated by the mixing transition, $Re \sim 10^4$, corresponds to the starting point of the scale separation.

The mixing transition is evident in the evolution of the probability density function of the mole-fraction, which indicates an increase in mixed fluid. The increase in the mixing rate coincides with formation of an inertial range in the two-dimensional spectrum of vertical velocity [148].

At $Re = 10^3$ and $Sc \sim 1$, there is sufficient fine scale structure for the molecular mixing parameter to reach its plateau level. It could be argued that the flow is near to its self-similar state at $Re \sim 10^3, Sc \sim 1$ [78]. (The same paper suggests that $Re \sim 10^4$ is needed to get a high degree of molecular mixing at $Sc \sim 600$ consistent with Dimotakis' mixing transition).

Yet, at $Re \sim 10^4$ the separation between the energy-containing and dissipation scales is just beginning. In other words, the inertial range does not exist at this Re. However, a turbulent flow, according to any standard text book, mandates an established inertial range (see subsections II.B & II.C and Figure 6) and the Re should be much beyond that accorded by the mixing transition. Thus, the mixing transition is still far away from achieving a turbulent flow.

2. *Minimum state turbulence*

To ensure the integrity of the physics of the large-scale dynamics of the flows of interest, the corresponding large-scale modes computed or measured in a simulation or an experimental setting should not be contaminated because of their interaction with the dissipation range, which is not universal. This requirement can be satisfied by maintaining a sufficiently broad inertial range [408].

The only question is; what is the lowest Reynolds number that will provide a sufficiently long inertial range that separates the energy-containing and dissipation scale? Studying the energy transfer process and interacting scales, Zhou [409] determined that the lowest Re satisfies this condition is around 1.6×10^5. Figure 41 is a

sketch that summarizes the spatial transition criterion just described above. For the detailed definitions on several important length scales, see Zhou [409].

The *"minimum State"* is significant because it implies that one doesn't need to perform the numerical simulations or experimental measurements of extremely high *Re* flows. All that extra work would simply extend the length of the inertial range, which is well understood via self-similar analysis, and has little impact on the actual physical processes of interest. In other words, once the *"minimum State"* is achieved, the most important physics of the turbulence are already captured.

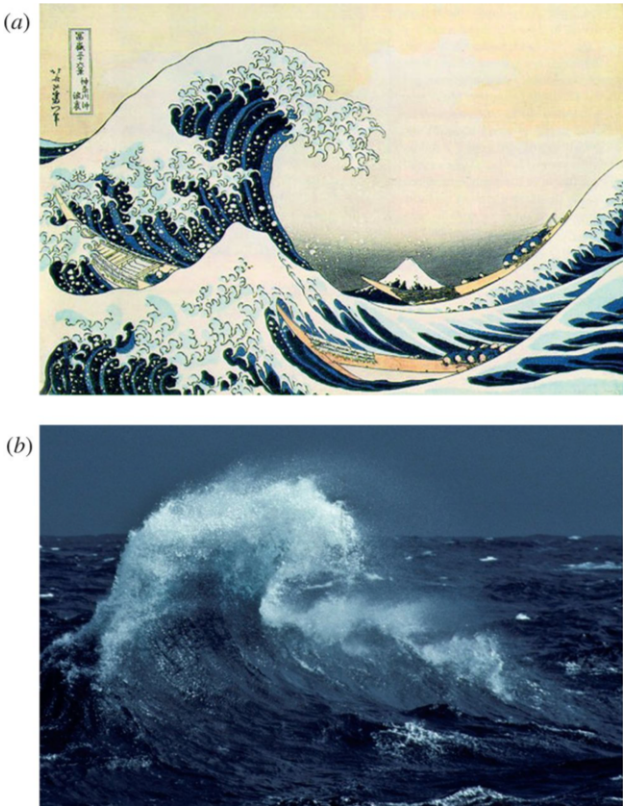

FIG. 39: Comparison of Hokusai's Great wave with an observation in sub-Antarctic water. (a) The great wave off Kanagawa (Kanagawa-oki nami-ura) woodcut by Katsushika Hokusai. (b) Photograph of a breaking wave in the sub-Antarctic waters of the Southern Ocean taken from the French research vessel Astrolabe during one of its regular voyages between Hobart and the Dumont d'Urville Station in Adélie Land. Note the transverse and longitudinal localization of the wave, which is remarkably similar to that depicted by Hokusai. (Photograph taken by V. Sarano in 1991.) Reproduced with permission from Dudley, Sarano, and Dias, *Notes Rec. R. Soc.*, **67**, 159 (2013).

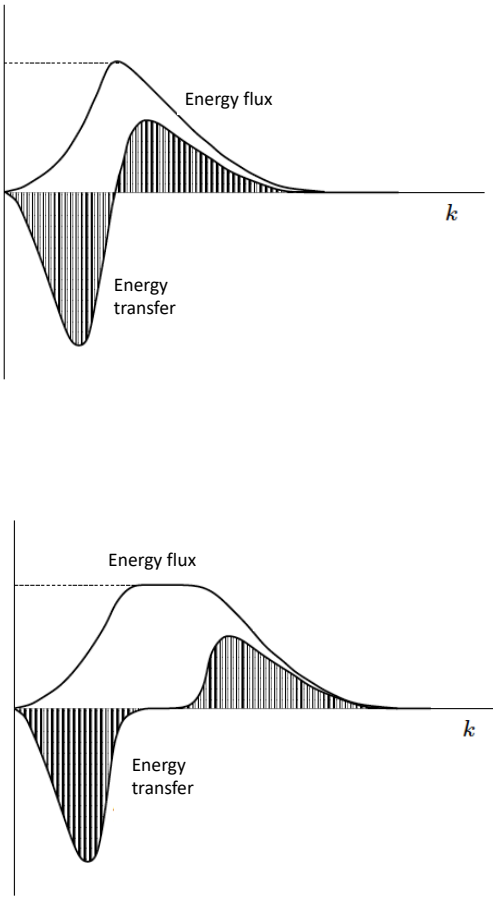

FIG. 40: The early and late time energy transfer processes. Schematic views, of the energy flux and energy transport spectrum as functions of wave number. Similar sketches can be found in McComb for making different points [406]. Reproduced with permission from Institute of Physics.

C. Temporal criterion of transition

While the spatial criterion of transition can be used to analyze results from a wide variety of spatially evolving turbulent experiments, the above discussion of the time-dependent nature of the flows induced by hydrodynamic instabilities suggests that certain conditions beyond a sufficiently high Reynolds number are required to achieve a state of strong mixing. In particular, a sufficient amount of time (or "distance" if the turbulence is spatially evolving) is required for the turbulence to establish a full cascade that enhances the mixing at fine scales.

Zhou *et al.* [410, 411], Robey *et al.* [412], and Zhou

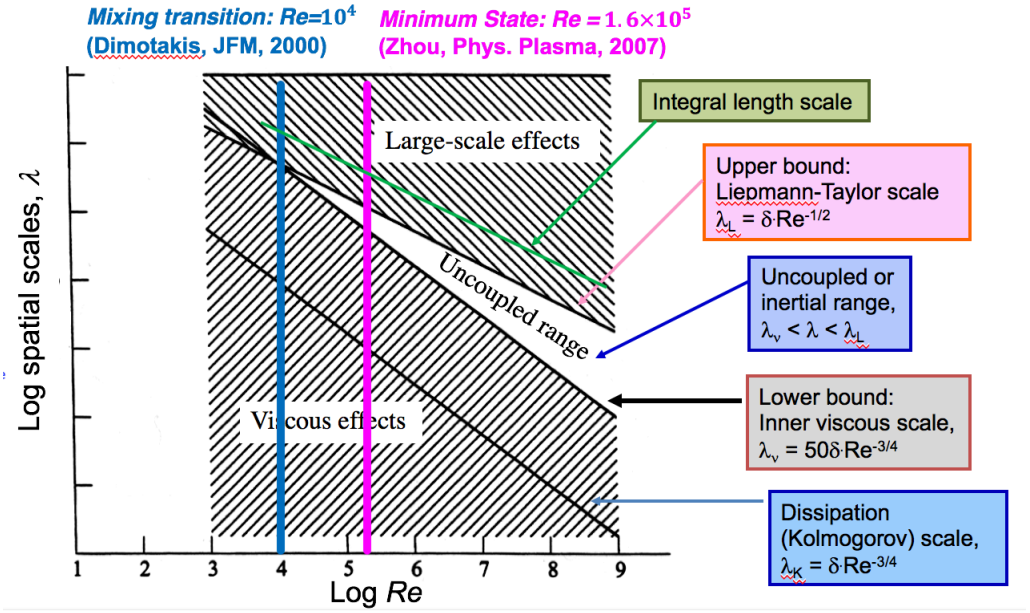

FIG. 41: *Spatial Transition.* The figure indicated the Reynolds numbers required for achieving the mixing transition of Dimotakis [407] and minimum state turbulence of Zhou [409]. Reproduced with permission from *J. Fluid Mech.*, **409**, 69 (2000). Copyright 2000, Cambridge Univ. Press. Reproduced from *Phys. Plasmas*, **14**, 082701 (2007), with the permission of AIP Publishing.

[409] extended the concepts to the cases of the temporal evolving RT and RM cases. These studies showed clearly that both high Reynolds number as well as sufficient time (or distance, in the spatial evolving cases) were required to achieve a transition to strongly molecularly mixing case. As noted in Drake *et al.*, [413], the Zhou–Robey hypothesis requires that the uncoupled fluctuations develop within laminar-flow regions established in the boundary layers created by viscous diffusion at locations of significant shear. A turbulent transition occurs when the widths of these boundary layers , λ_D=5 $(\nu t)^{1/2}$, have grown for a long enough time to become greater than the inner viscous scale.

Rose and Sulem [53] noted that the eddy-turn-over-time as the given size of an eddy divided by the typical velocity difference across the eddy. The eddy-turn-over-time is therefore proportional to the time required for the eddy to be distorted, and, in this distortion process, generate smaller eddies. Approximately one dominant, energy-containing eddy-turn over time corresponds to the mixing transition, as remarked by Drake *et al.*. Using the same language, it can be shown that about four eddy-turn over times will be needed for the flow to qualify for the fully-developed turbulent flows as defined by the minimum state.

An intuitive understanding can be gained by considering the evolution of the turbulent kinetic energy of simple isotropic turbulence as predicted by closure theory. The time required to establish a turbulence cascade from an initial non-cascading state was found by Lesieur & Schertzer [414] using the EDQNM closure. The EDQNM models is a "spectral model", i.e., it models the dynamic behavior of the turbulent energy spectrum for isotropic turbulence, and represents the non-local Fourier-space transfer terms with reasonable fidelity. Similar behavior was also observed by Clark & Zemach [415] who found the same phenomenon in EDQNM, but also in a much simpler spectral model due to Leith [416] that represents the cascade as a purely local transfer via a nonlinear diffusion. Both models exhibited the finite time onset of the cascade. The time of onset was referred to as the "catastrophe time" by Lesieur and Schertzer, and denoted it by t^*. Clark & Zemach observed that EDQNM established a cascade in approximately 4 initial eddy turnover times, whereas the Leith model established as cascade in approximately 2.3 eddy turnover times, where the eddy turnover time τ_e, was defined as

$$\tau_e = \left(K k_{0,max}^2\right)^{1/2}, \tag{63}$$

where K is the turbulent kinetic energy and $k_{0,max}$ is the wave number where the initial energy spectrum has its maximum value. Both models showed a weak dependence of the time required to achieve a full cascade on the viscosity, (or equivalently, the initial turbulent Reynolds number). Again, note that the wave number of the maximum of the spectrum is inversely proportional to the integral scales. Figure 42 shows the EDQNM-predicted evolution of the spectrum from a state exhibiting no inertial range to a state exhibiting a strong cascade.

Neither Lesieur & Schertzer [414] nor Clark & Zemach [415] commented on the significance of this finite time

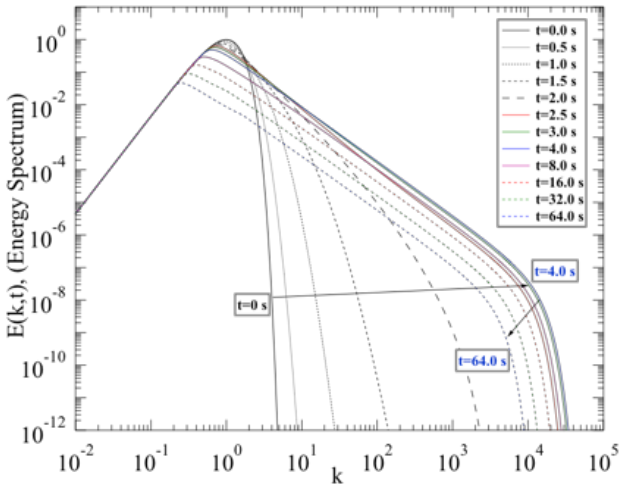

FIG. 42: Evolution of the energy spectrum for an isotropic decaying turbulence as predicted by the EDQNM model. Note that the spectrum establishes an inertial range in b $t = 4$. The initial turbulent kinetic energy was $K = 1$ and the peak of the initial spectrum was at $k = 1$, thus the initial eddy-turnover time is $\tau_e = 1$

onset of the cascade in relation to a transition process. However, Zhou & Robey [408–412], in their efforts to develop the temporal criterion of transition, connected this onset with the notion that the strong mixing occurs when the difference between the wave numbers characterizing the dissipative scales, $k_d \approx 1/\eta$ and those characterizing the integral scales, $k_L \approx 1/L$ is sufficiently larger than the nonlocality associated with the Fourier-space energy transfer in the cascade region.

The temporal transition criterion and its corresponding Reynolds number transition criterion discussed in last subsection (VI B) allow us to nicely correlate a number of important physics concepts. We will discuss these concepts in the remaining subsections of this section.

D. Transition criterion, Euler scaling, and laboratory astrophysics

The *"minimum state"* of the Reynolds number transition criteria is related to the Euler scaling of a given problem. Euler scaling is an important tool that allows us to represent astrophysical phenomena in the laboratory with intense lasers. As illustrated in Figure 43, the objective of laboratory astrophysics is to study the behavior of the long-time, large-spatial-scale astrophysics problems (e.g. [417]) on an HEDP platform with a short-time, small-spatial-scale target. A recent application of laboratory astrophysics studied how high energy fluxes may affect RTI growth in young supernova remnants (Figure 44). Kuranz *et al.* [418] developed a radiative shock stabilized planar RT platform in indirect drive with drive radiation temperatures T_R = 200-350 eV on NIF. These planar RT experiments used a strong shock launched into a doped plastic ablator which then enters a low-density SiO2 aerogel foam tamper region on the back side of the target. This creates a high temperature and a strong source of radiation and electron thermal diffusivity in the foam which can ablatively stabilize (reduce) the perturbation growth at the plastic-foam interface. For the low-drive case, the shocked foam is not hot enough to stabilize the RT growth and the predicted RT growth at the same interface distance traveled is 40% larger. Experiments on the NIF laser exhibit this effect. In comparing with supernova SN1993J, a Type II supernova, the authors found that the energy fluxes produced by heat conduction appear to be larger than the radiative energy fluxes, and large enough to have a significant effect on the RT growth, which could affect our understanding of young supernova remnants (Figure 45).

Euler scaling essentially relates the variables in the laboratory system to the astrophysics framework. Striking similarities exist between hydrodynamic instabilities in ICF capsule and core-collapse supernova explosion simulations as seen in Figure 46. Specifically, the transformation takes the following form

$$\mathbf{r} = a\mathbf{r}_1; \rho = b\rho_1; p = cp_1; t = a\sqrt{\frac{b}{c}}t_1; \mathbf{v} = \sqrt{\frac{c}{b}}.\mathbf{v}_1 (64)$$

A more complete discussion and applications of the Euler scaling can be found in Refs. [10, 89, 353, 421].

As noted already, many HEDP experiments have been carried out for KHI flows. An example of the evolution of traditional and counterflowing KHI induced flow obtained at the Omega laser facility can be seen in Figure 47 [24, 422] and Figure 48 [393], respectively. Euler scaling can be utilized to relate the facilities of increased energy. Figure 49 shows that the mixing layer width from the counterflowing shear experiments taken from both Omega and NIF can be nicely collapsed [423].

A key requirement for Euler scaling is that the Reynolds number must be high. However, the required spatial separation for the "minimum state" should be sufficient for this basic condition.

Another important issue is the potential impact of the transport coefficients [424–434] on the behavior of the flow. In ICF applications, the large increases in temperature will lead to significant increases in the molecular diffusivities and viscosities of the plasmas. It is suspected that such large increases will tend to damp out the turbulent fluctuations and reduce the turbulent mixing. An increase in the viscosities and diffusivities tends to preferentially damp the higher wavenumbers. Plasma viscosity may increase sufficiently with temperature as the flow evolves to prevent ICF implosions from becoming fully turbulent (Figure 50) [435].

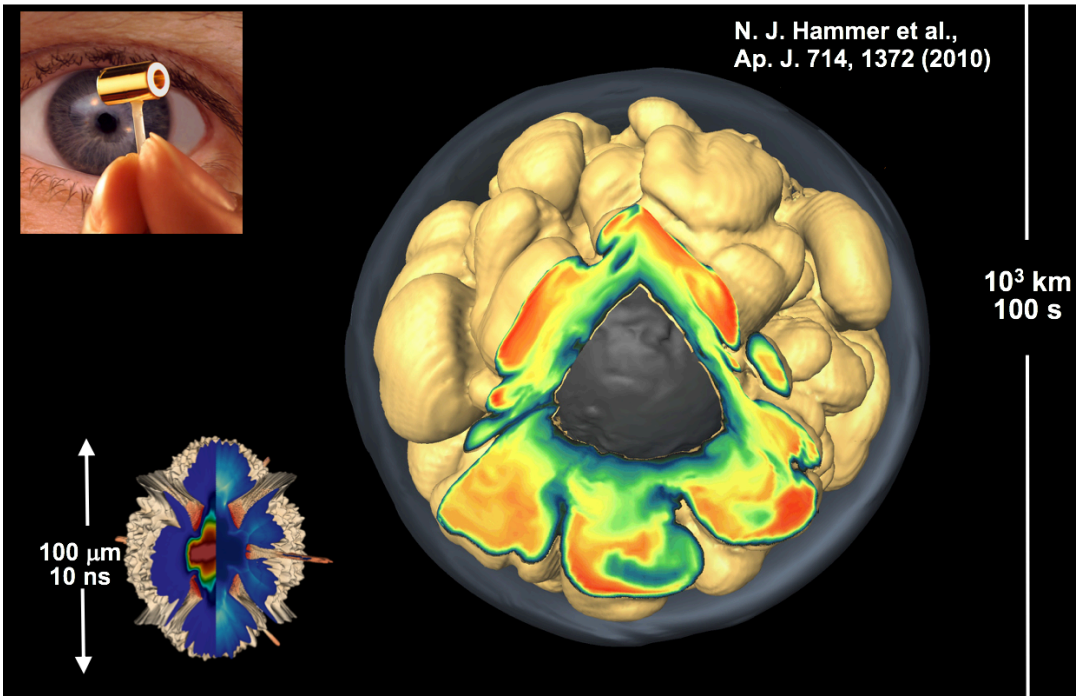

FIG. 43: The length- and time- scales of astrophysical flows and those generated in the HEDP platform. The SNe visualization is adopted from Hammer *et al.* [417]. Reproduced with permission from *Astrophys. J.*, **714**, 1371 (2010). Copyright 2010, Institute of Physics.

VII. BACK TO THE BEGINNING: THE IMPORTANCE OF ACCURATE INITIAL CONDITIONS

The initial conditions of a flow field, including the details of the initial perturbations, can have a significant impact on flows induced by instabilities (see for example, Figs. 51a and 51b [108] as well as Refs. [436–442]). Unfortunately, there are many different possibilities in nature and only limited cases have been investigated in sufficient detail regarding how the flows might develop differently with different initial conditions.

A. Interface perturbation

One striking aspect of RTML simulations is that the estimated growth rate coefficients, α_b and α_s in equation 55 derived from the simulations is typically significantly smaller than those determined experimentally–as discussed by [152], [223] and by [443]. The near constancy of α across a variety of Atwood numbers and initial conditions is the subject of some degree of scrutiny since its actual value may be a function of the initial condition(s) of the problem(s). This has been attributed to the existence of long wavelength modes, as Figure 52 suggests. Numerical simulations offer some advantages over actual experiments, in that a variety of geometries that can be numerically simulated with ease, whereas designing a comparable experiment may be quite difficult and costly. Likewise, the numerical simulations offer access to all variables associated with the evolution of the RTI, whereas some of these, e.g. pressure, are difficult to capture experimentally. The reader is also referred to Lim *et al.* [440] and Kaman *et al.*. [441] for an interesting perspective on the possible influence of unrecorded long wavelength contributions to the instability growth rate as well as a more broad discussion on the question of models for initial conditions.

To study the effect of initial amplitude and wavelength on RT-strength instability, Polavarapu *et al.* carried out a unique rotating wheel experiment [444]. Different sinusoidal perturbations were formed on an elastic-plastic material (mayonnaise) and accelerated in a test section, with air as the light fluid. It was found that the acceleration required for instability increased when initial amplitude and wavelength decreased.

For ARTI, Zhang *et al.* [445] argued that ablative stabilization of the nonlinear ARTI is not as effective as previously anticipated for large initial perturbations, a result of the dependence of α_b on initial perturbation and vorticity generation. Li and Ye suggested a successive picket drive for mitigating the ablative RMI [446].

Soulard *et al.* [447] focused on whether a loss of memory of initial conditions occurs at large scales for an idealized buoyancy-driven flow which is aimed at investigating RT turbulence. Recently, Soulard *et al.* [231] found that for an RMI flow large-scale initial conditions are preserved for the velocity spectrum but not for the

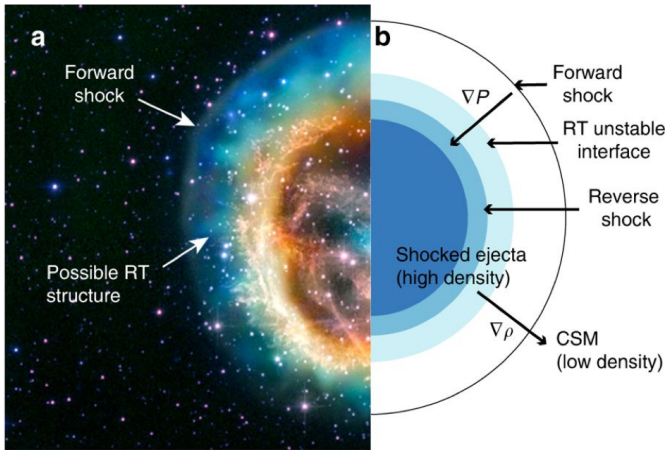

FIG. 44: Image of supernova remnant. (a) False-color image of SNR E0102.2-72. This object is believed to result from a core-collapse supernova about 1000 years ago. One can see the edge of the forward shock. The modulated boundary within it might be structuring of the ejecta-CSM interface produced by RT. The brighter, inner colors are attributed to emission from the higher-Z, interior portions of the ejecta. Image credit: X-ray (NASA/CXC/MIT/D. Dewey *et al.* and NASA/CXC/SAO/J. DePasquale); Optical (NASA/STScI). (b) Schematic (size and shape not to scale) of inner structures of the supernova that creates the opposing density and pressure gradients to create an RT unstable interface. Reproduced with permission from Kuranz *et al.* [418], *Nature Communications*, **9**, 1564 (2018); licensed under a Creative Commons Attribution (CC BY) license.

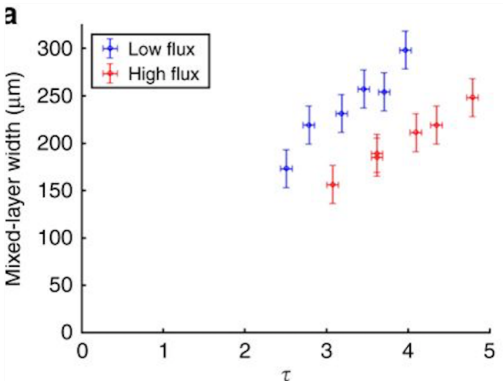

FIG. 45: Experimental mixed-layer width vs the RT growth factor, which is the number of instability e-foldings. The mixed-layer is smaller in the high-flux case, indicating a reduction in RT growth. The vertical error bars reflect the uncertainty of the location of the RT spike tip and bubble head, and the horizontal error reflects the uncertainty in the experimental time. Reproduced with permission from Kuranz *et al.* [418], *Nature Communications*, **9**, 1564 (2018); licensed under a Creative Commons Attribution (CC BY) license.

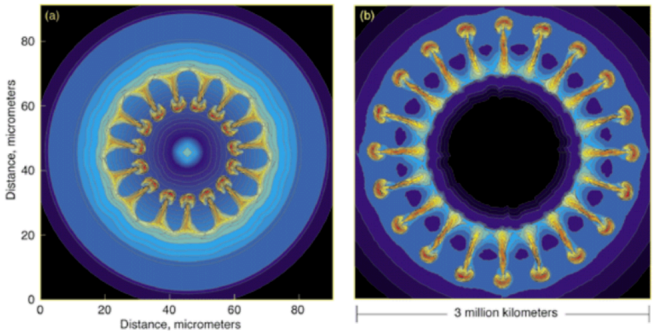

FIG. 46: Striking similarities exist between hydrodynamic instabilities in (left) inertial confinement fusion capsule implosions and (right) core-collapse supernova explosion. Image (left) is based on Sakagami and Nishihara [419]. Reproduced from *Phys. Fluids B*, **2**, 2715 (1990), with the permission of AIP Publishing; Image (right) is based on Hachisu *et al.,* [420]. Reproduced with permission from *Astrophs. J.*, **368**, L27 (1991). Copyright 1991, Institute of Physics.

concentration and concentration flux spectra. Moreover, the authors determined that large scales keep their initial anisotropy so that the turbulent mixing layer only partially return to isotropy.

Three methods can provide precise initial interface perturbations: paramagnetic fluids, dedicated HEDP with solid state target, and numerical simulations. The paramagnetic fluids allow one to craft the initial interface perturbation in a very precise manner (Figure 53) [448–451]. For dedicated HEDP, the initial conditions can be machined accurately on the solid state target. An example of this is the single-mode reshock RMI experiment shown in Figure 54, where the development of the instability from two distinctive initial amplitudes is illustrated in a planar geometry. As an another example, Merritt *et al.* [31] used counter-propagating shear experiments carried out at the OMEGA Laser Facility to evaluate the effect of target initial conditions, the characteristics of a tracer foil located at the shear boundary, on Kelvin-Helmholtz mixing layer evolution. A series of experiments illustrated that increasing the surface roughness (surface perturbation scale spectrum) can increase the relative mixing in the system - see Table I and Figure 55. Finally, desirable initial perturbations can be implemented in numerical simulations. Figure 52 shows the impact of "small random perturbations" and random long wavelength perturbations (k^{-3} spectrum) [442].

B. Density disparity

The effect of density disparity, represented by the Atwood number $\mathcal{A}$, is an especially interesting initial value problem [135, 136]. For RTI, one observes the sensitivity of the values of α_b and α_s as a function of $\mathcal{A}$. When

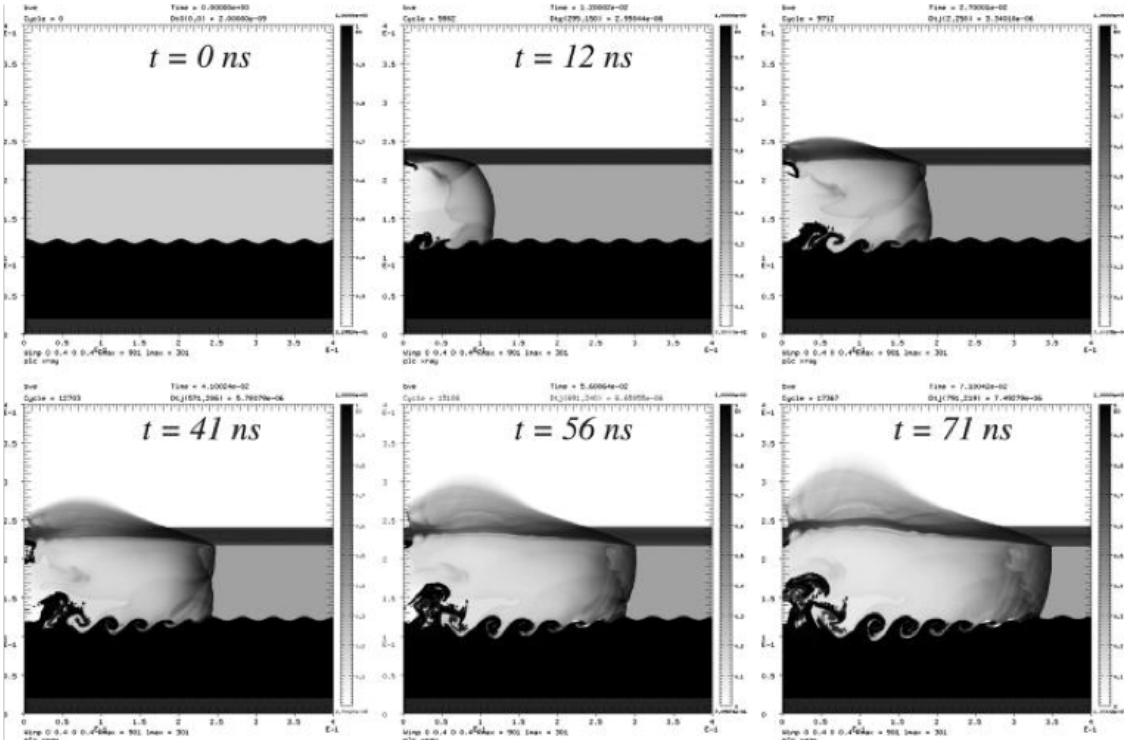

FIG. 47: Frames of 2D simulation results show the expected target behavior in a synthetic x-ray image as a function of time [24]. The simulation shows that the region of target to the left of x = 1 mm contains debris from the gold shield on the laser drive-end of the target, so the region of hydrodynamic interest is x ¿ 1 mm. As the primary shock moves from left to right in the low density foam, transmitted shocks move into the high density plastic part of the target (not visible), and reflected shocks are created in the post-shock flow region (visible in the upper half of the target). The small zero density voids visible above a few of the vortices in the late-time images are a numerical artifact of the synthetic x-ray software. While these 2D simulations did a good job of predicting the general experiment behavior, the best fidelity was obtained with 3D simulations performed many years later (see K. S. Raman, *et al.* [422]) [Reprinted with permission from Hurricane *et al.*, *Phys. Plasmas*, **16**, 056305, (2009), with the permission of AIP Publishing.].

Foil Type	**Surface finish (μm)** (Ra)	**Thickness (μm)**	**Interval (t) (ns)**	**Growth rate (μm/ns)**
Al smooth	0.45-0.50	20	10-14	15.3
Al roughened	2.21-2.88	20	10-14 (December)	20.0
			12-14 (May)	17.6

TABLE I: Mix half-width comparison for different aluminum tracer foil variations used in counter-propagating shear experiments conducted at the Omega laster facility. Data compiled from Tables I and III of Merritt *et al.* [31]. With permission from *Phys. Plasma*. The roughness metric is the average surface roughness (Ra), the arithmetic average of the absolute surface heights, taken separately for each side of each foil.

the density disparity is small, $\alpha_b \sim \alpha_s$. However, as the Atwood number of the flow approaches one, the value of α_s becomes much greater than α_b (see Figure 56, top panel). The similar situation is true for the RMI case, where one may also be concerned about whether there is a dependence of θ_b and θ_s on the Atwood number $\mathcal{A}$, as well as a difference between the pre-shock and post-shock Atwood number values themselves. The values of these scaling factors are fairly close when the density disparity is not large. Again, the value of θ_s becomes significantly higher than that of θ_b as $\mathcal{A} \to 1$ (see Figure 56, bottom panel).

Because of its importance, many efforts have been expended to study the dependence on the Atwood number using experimental measurements [141, 143], numerical simulations [102, 151, 235, 442, 452, 453], modeling [454, 455], and asymptotic study [456].

Naturally, the Atwood number effect should be re-

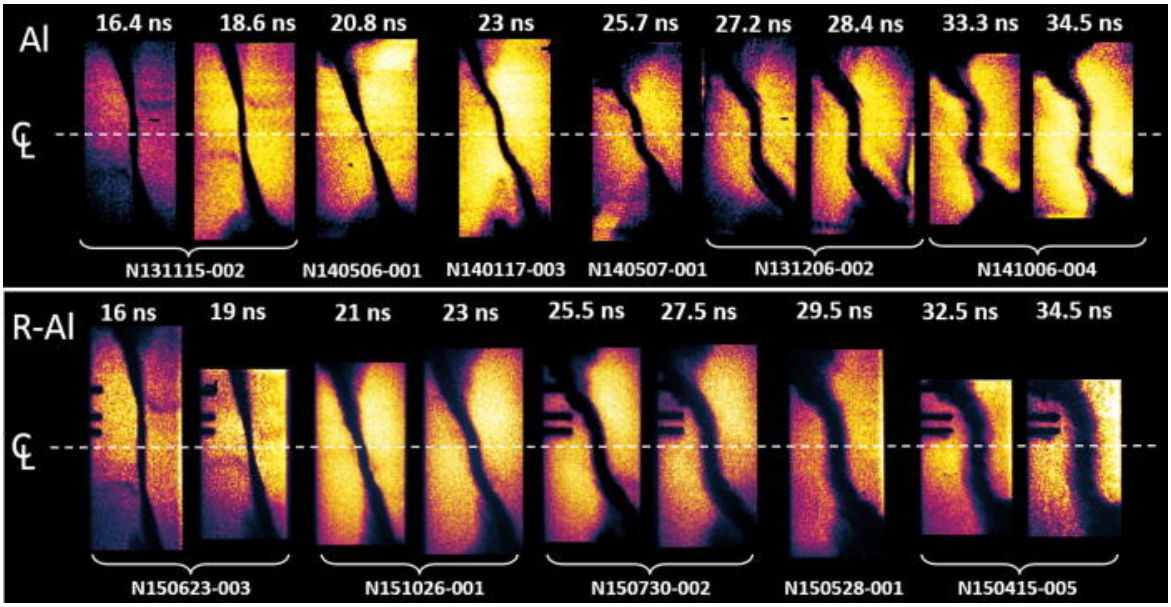

FIG. 48: The edge-view time history for smooth Al (top) and rough Al, R-Al, (bottom) from 16 ns to 34.5 ns with shot numbers indicated under the images [393]. Reproduced from Flippo *et al.*, *Phys. Plasmas*, **25**, 056315 (2018), with the permission of AIP Publishing.

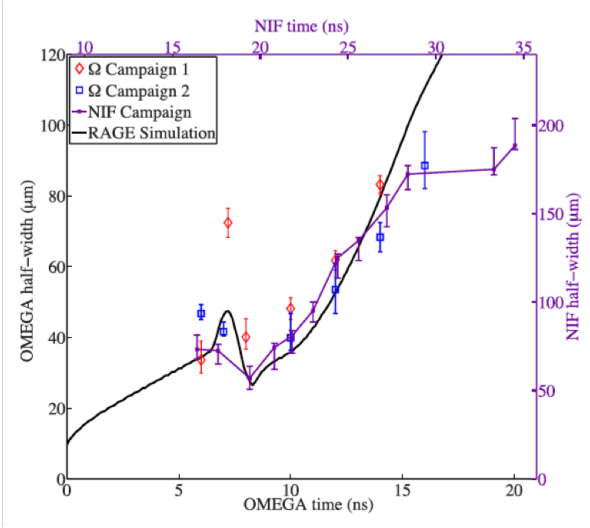

FIG. 49: Layer widths as a function of time at OMEGA and NIF. Left and bottom axes refer to widths and times of data from OMEGA, right and top axes show widths and times taken at NIF. The scaling between the two axes is such that the hydrodynamics are equivalent [423]. Reproduced from Doss *et al.*, *Phys. Plasmas*, **22**, 056303 (2015), with the permission of AIP Publishing.

flected in the difference values of virtual time origin for the spike and bubbles, when one takes the view point of $\theta_s = \theta_b$ as advocated in Refs. [181, 224, 225],. The stabilizing effect of a continuous density gradient was considered by Lord Rayleigh [1] and Lelevier *et al.* [315] in their pioneering works (see also Ref. [7]). To prepare a membrane-free interface in a vertical, square cross section, shock tube [166], the head-on flows mitigates diffusive effects, limiting the interface thickness [168].

C. Geometry

After their initial rocket-driven RTI experiments [134, 146], Smeeton and Youngs [457] and Youngs [458] carried out another series of rocket driven RTI experiments known as the "Tilted-Rig" experiments. The experiment consisted of a tank, with rockets attached at the top, filled with heavy fluid under light one, and then "tilted" on one side of the apparatus. The tilt produced an "angled interface" in relation to an acceleration history. A representative image is shown in Figure 57. The experiments of Holford *et al.* [459] showed that the high cumulative efficiency of mixing in RT instability at a horizontal interface is only slightly reduced by an interface tilt of up to 10°, despite the strong overturning that occurs. The "Tilted-Rig" experiments have been used to compare with numerical simulations [460] and RANS model development [461]. For such a tilted-rig RT experiment, Youngs [158] reported that the DNS and LES resulted in reasonable agreement.

Experimentally, Lawrie & Dalziel [462, 463] studied the RTI in tall tubes and found that the late-time scaling is been changed in the high-aspect-ratio domains. In the solution of the NS equations with negligible viscosity, the only relevant length scale is gt^2 [198]. Using molecular dynamics (MD) simulation, Kadau *et al.* [437] pointed out that the change in regime from t^2 behavior self-similarity can be broken only when the

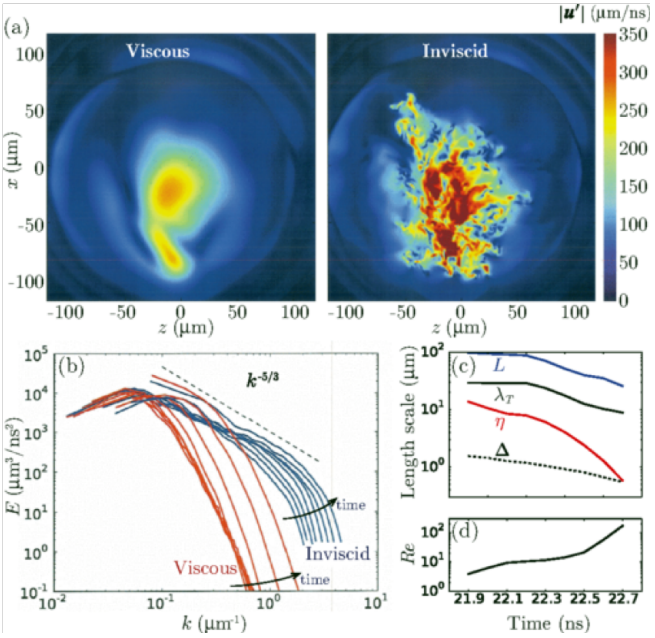

FIG. 50: Viscous effects on the fluctuating velocity. (a) Fluctuating velocity magnitude at 22.21 ns with (left) and without (right) viscosity. (b) Kinetic energy spectra in the hot spot from the viscous and inviscid simulations from 21.9 to 22.6 ns. (c) Turbulent length scales and (d) Reynolds number in the hot spot [435]. Reproduced with permission from Weber *et al.*, *Phys. Rev. E*, **89**, 053106 (2014). Copyright 2014, American Phys. Soc.

growth of structures horizontally is restricted by the system width, which then introduces an additional length scale into the problem. In confined RT turbulence, Boffetta *et al.* found the coexistence of Kolmogorov-Obukhov and Bolgiano-Obukhov scaling at small and large scales, respectively [464]. The wall effect is a concern for the reshock RMI experiments on the HEDP platform [465, 466].

Holder & Barton [467] reported an interesting RMI experiment with inverse chevron shock-tube laboratory experiments wherein low (air) and high (SF6) density gases are initially separated by wire mesh and membranes. This experiment has been repeated [468] using five inverse-chevron interfaces with different initial vertex angles. Therefore, the impact of initial amplitude-wavelength ratio on flow characteristics can be investigated. From a computational perspective, Grinstein *et al.* [469] used the inverse-chevron shock tube experiment to assess their xRAGE based ILES for shock-driven turbulent mixing. Zeng *et al.* studied interaction of a planar shock wave with a triangle-shaped sulfur hexafluoride (SF6) cylinder surrounded by air [470].

When the shock is oblique, the normal component of the shock generates the RMI, and the parallel component generates the KHI [202]. For shock tube experiments, the inclined interface has attracted considerable attention because it is a membraneless interface method

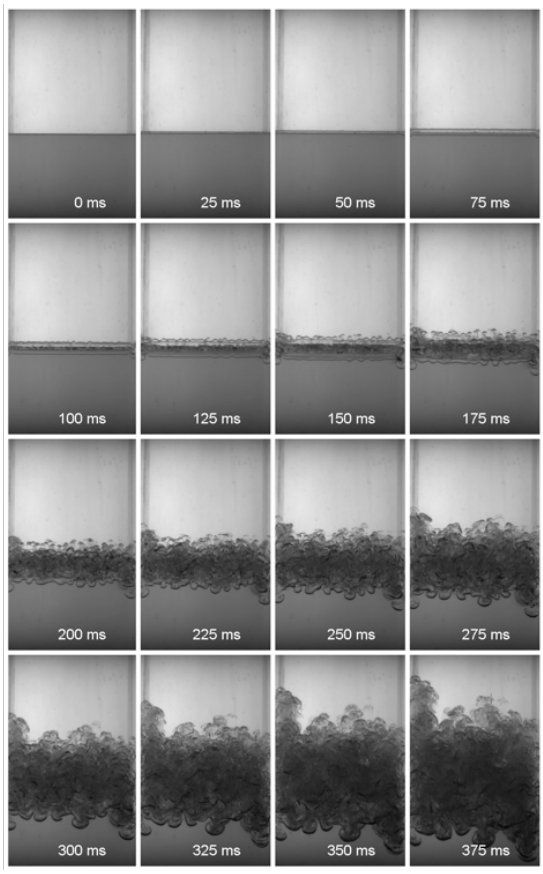

(a) RTI experiment performed at Univ Arizona. The initial perturbation was generated by vertically oscillating the liquid-filled tank.

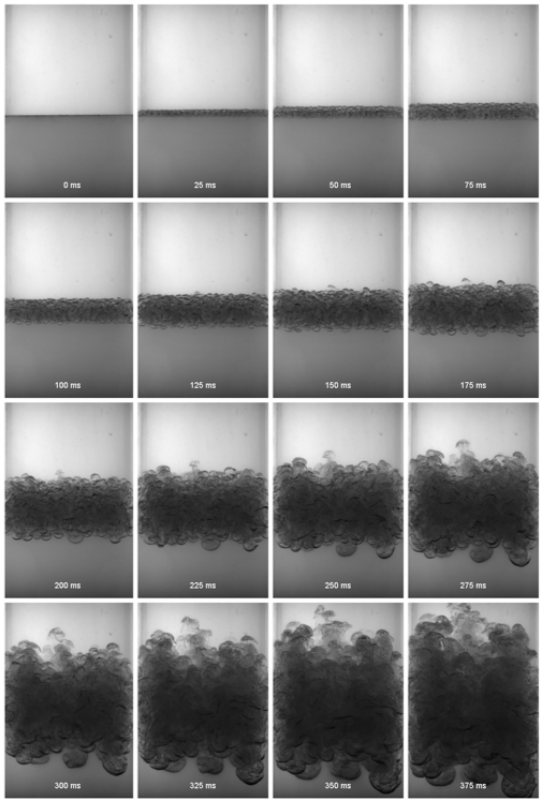

(b) RTI experiment performed at Univ Arizona. The initial perturbation was generated by random interfacial fluctuations from background noise. Figure 51. Reproduced with permission from Roberts and Jacobs [108], *J. Fluid Mech.*, **787**, 50 (2016). Copyright 2016, Cambridge Univ. Press

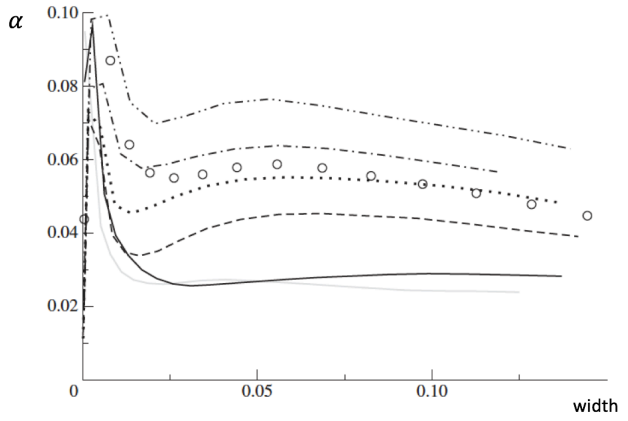

FIG. 52: Variation of α for RTI with integral mix width at $\rho_1/\rho_2 = 3$ and various values of the long wavelength parameter. Reproduced with permission from Youngs [442], *Phil. Trans. R. Soc. A*, **371**, 20120173 (2013). Reproduced with permission from the Royal Society.

where the interface is planar and rests at an angle to the incident shock front (Figs. 58-59). This offers a quantified interface where the initial vorticity deposition can be controlled precisely and easily predicted using the vorticity equation [471–475]. In particular, Mohaghar *et al.* [476] experimentally investigated a multi-mode inclined interface created via shear and buoyancy superposed on the dominant inclined perturbation. Analysis of mixing width, mixedness, mixed mass, and mixed-mass thickness is carried out to demonstrate the initial condition effect on the temporal development of this RMI flow at different scales (Fig. 60).

Lately, Rasmus *et al.* [477] studied the instability growth resulting from a shock interacting with a sinusoidally perturbed, oblique interface on the OMEGA EP laser. The authors further developed a model [36] that is consistent with the observation that the instability growth is dominated by RM at earlier time, but displays the late-time behavior and morphology of KH.

D. Initial flow fields

Bai *et al.* [478] and Liu *et al.* [479] performed a Mach 1.27 shock tube experiment with nonuniform SF_6 flows and found that the mixing layer grows faster in the low-density areas. Bai *et al.* [478, 480] and Xiao *et al.* [481] carried out numerical simulations of this experiments with a focus on the mixing width, vorticity, and circulation of the flow fields.

Biferale *et al.* [482] conducted direct numerical simulations of 3D RT flows with a nonuniform singular initial temperature background. As the turbulent Mach number has an upper bound [483, 484], the authors utilized the Navier-Stokes-Boussinesq equations, which justifies

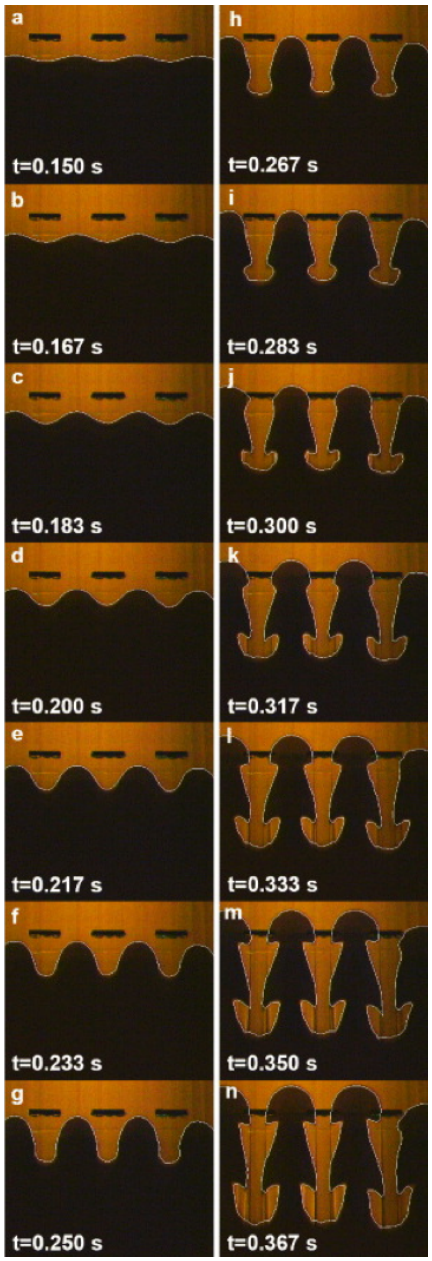

FIG. 53: Time evolution of RTI for an initial deformation of 12.5 mm wavelength. Fluid densities are 1398 and 773 kgm^3, respectively, and surface tension is 7.7 $\frac{mN}{m}$. The dark horizontal segments are magnetically permeable wires placed outside the cell, forcing the initial single-mode interface deformation. Renoult *et al.* [449] *Europhysics Letters*, **101**, 54001 (2013) with permission from European Physical Society.

the RTI-induced flow an effectively incompressible (or weakly compressible) one

$$\partial_t \mathbf{u} + \mathbf{u} \cdot \nabla \mathbf{u} = -\nabla p + \nu \nabla^2 \mathbf{u} - \tilde{\beta} \mathbf{g} T \tag{65}$$

$$\partial_t T + \mathbf{u} \cdot \nabla T = \kappa \nabla^2 T \tag{66}$$

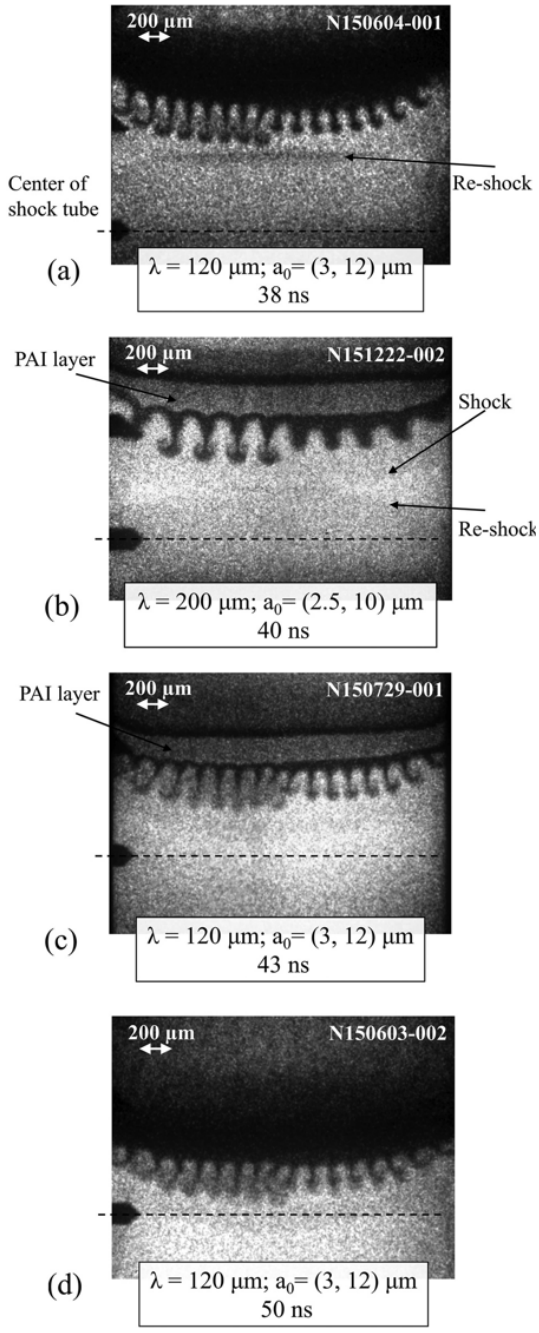

FIG. 54: Sequence of NIF images at 38, 40, 43, and 50 ns, obtained from different shots with identically-driven targets, with two different ripples side-by-side. Note: all 4 images are taken using the framing cameras. Reproduced from Nagel *et al.*, *Phys. Plasmas*, **24**, 072704 (2017), with the permission of AIP Publishing.

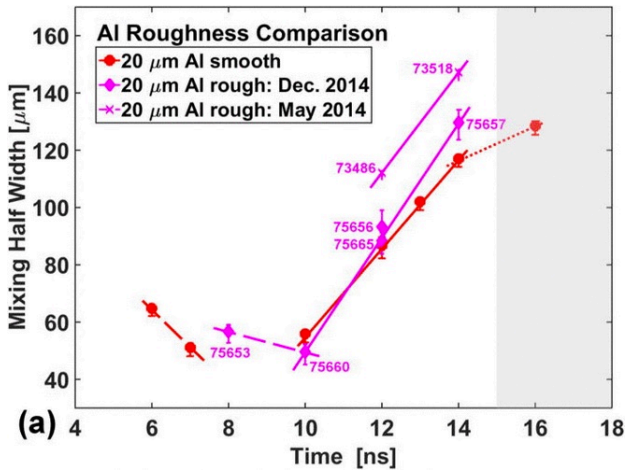

FIG. 55: Mix half-width comparison plots for different foil surface roughnesses for aluminum. The shot number for each data point is included in the plots. Reproduced from Merritt *et al.* [31], *Phys. Plasmas*, **22**, 062306 (2015), with the permission of AIP Publishing.

where T is the temperature, ν is the kinematic viscosity, κ is the the thermal diffusivity, and $\tilde{\beta}$ is the thermal expansion coefficient (assumed constant, independent of T). They reported that the long-time growth remains self-similar, but no longer proportional to t^2 and depends on the singularity exponent of the initial profile of the temperature.

E. Driving mechanisms

In addition to standard constant (RTI) or impulsive (RMI) acceleration, innovative experiments with variable accelerations have been carried out [485]. RTI with a complex acceleration history $g(t)$ consisting of consecutive periods of acceleration, deceleration, and acceleration is important in applications and difficult to model in engineering models [486–489].

The incident shock strength introduces another independent variable. For Mach numbers smaller than 3, the mix widths can be collapsed with downstream distance (or rescaled time), but the mixing rate versus downstream position showed steeper density gradients at early times for a higher Mach number case [490–492].

In several publications, Zou et al. [493] and Liao et al. [494] have studied non-standard RMI, where the instability is generated after a rippled shock (Ishizaki et al. [495]) passes a flat interface (see also, [496]). The non-standard RMI produces smaller instability growth than that of the standard RMI. Moreover, Zhang et al. [497] investigated the characteristics of the rippled shock and determined that the nonstandard instability is more sensitive to the initial shock strength than the traditional one.

As for reshocked RMI, Leinov *et al.* [190] and Jacobs *et al.* [191] have carefully studied various aspects of initial conditions. One of the unique aspects of reshock RMI is that the arrival timing of the reshock could be changed

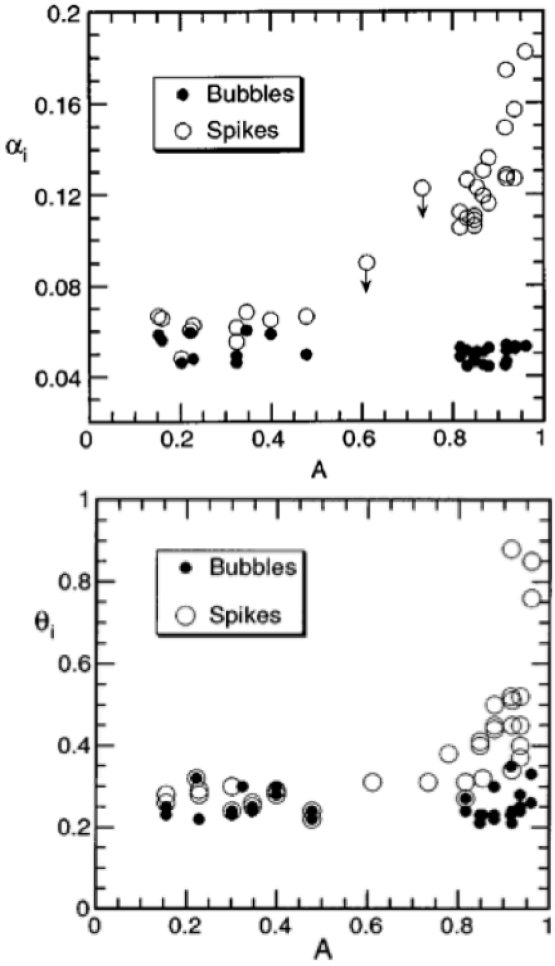

FIG. 56: The effects of the density disparity (Atwood number $\mathcal{A}$) on the α_b, α_s, θ_b, θ_s. Reproduced from Dimonte & Schneider [136], *Phys. Fluids*, **12**, 304 (2000), with the permission of AIP Publishing.

such that different flow morphologies are hit with the reflected shock that comes off a movable end wall (Figure 61). Power spectra at t=200-210 μs after reshock show that [498] some initial conditions cause the spectrum to become broader with fewer features (t=280 and 385 μs), while some still contain significant low-frequency peaks (t=90 and 170 μs). Increased mixing is indicated when the spectrum broadens and loses features [197, 492, 499, 500] - see Figure 62.

F. External factors and realistic initial conditions

Before moving on to the next section, we would like to remark on several issues. First, RTI, RMI, and KHI have found applications in the engineering processes [501–504] and combustion applications [93–95, 505, 506]. In fact, reactive RMI may play a fundamental role in turbulence-flame interactions. Chemical reactions and heat release fundamentally alter the behavior of turbulent mixing [507–510]. Recently, Vartdal & Osnes investigated the motion of interface perturbations in the presence of multiple interfaces. Depending on the configuration, each interface can be RT unstable or stable and damped [511]. Li *et al.* studied the role of rarefaction/compression waves in Richtmyer-Meshkov instability with reshock [512].

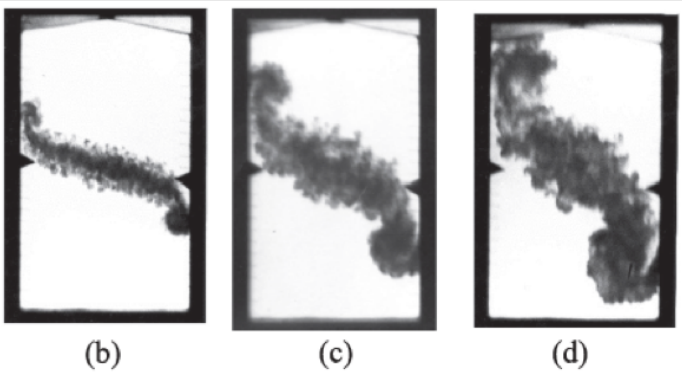

FIG. 57: NaI solution/hexane experiment. Rig tilted by 5° 46', Density ratio $\rho_1/\rho_2 = 2.9$. Acceleration $g = 35 \times g_0$. (a) 35.7 ms. (b) 54.9 ms. (c) 71.1 ms. Reproduced with permission from Youngs [458], *Physica D*, **3**, 270 (1989). Copyright 1989, Elsevier.

In many cases, multiple instabilities exist and must be treated at the same time [513–518], and the flows induced by hydrodynamic instabilities may be through a bed of solid particles [519] and subject to rotation [520–523], stratification [524–526] or magnetic field [527–530]. Indeed, the magnetic field must be accounted for in describing the evolution of RT unstable plumes within a solar prominence [531–533]. The Mie-Grüneisen equation of state [534–536] has been important for both the numerical [537] and analytical [538] studies of the RM instability.

The need to accurately characterize the initial conditions has been illustrated using estimated experimental initial conditions. A number of authors have reported that improved agreement with experiment can be achieved when compared with simulations using idealized initial conditions [76, 139, 142, 539–542].

Glimm and co-workers [440, 543–545] have obtained extremely impressive agreement of α coefficient between their simulations and a number of experimental measurements [134, 139, 457, 546]. More recently, they provided fresh perspectives regarding numerical simulations, including the roles of the initial conditions [547, 548].

VIII. CURRENT AND NEXT-GENERATION HYDRO DIAGNOSTICS

In laboratory experiments, Ramaprabhu and Andrews [549], Balakumar *et al.* [550], Tomkins *et al.* [197],

FIG. 58: A schematic diagram of the vertical shock tube and ancillary equipment [473]. Reproduced with permission from McFarland *et al.*, *Phys. Rev. E*, **92**, 013023 (2015). Copyright 2015, American Phys. Soc.

Gerashchenko and Prestridge [551], Mohaghar *et al.* [476, 552], Reese *et al.* [80], among others, have shown that simultaneous planar laser-induced fluorescence (PLIF) and particle image velocimetry (PIV) can be used to obtain the evolution of the density and velocity fields (Figure 63). While the PLIF images are processed to reveal the light-gas mole fraction, PIV particle image pairs yield corresponding two-component planar velocity results. With these diagnostic tools, Mohaghar *et al.* used both PIV and PLIF measurements to study the initial conditions in a variable density shock-drive flows. Charonko and Prestridge also performed simultaneous PIV and PLIF measurements for variable-density mixing in turbulent jets with coflow. It would be extremely desirable to be able to perform these measurements on HEDP platforms.

It is likely that many of the HED experiments designed to investigate other physics issues (not specifically to address turbulence or the transition to turbulence) do meet the *minimum state* criteria described in section VI. For example, in the work of Kuranz *et al.* [418], the Reynolds number was estimated to be 10^7, far exceeding the 1.6×10^5 [409] values that have been suggested as necessary to allow turbulent development. Moreover, despite single-mode initial conditions, such experiments will still contain non-uniformities at a range of sizes (down to very small scales) which promote the necessary separation of scales for turbulent development. In the single-mode HED experiments of Nagel et. al, the Liepmann-Taylor scale is calculate to be $\lambda_{LT} = 2.2\mu$m and the data is suggestive of the onset of turbulent mixing, but the diagnostics available precluded a more definitive assessment.

If current laser-driven HED experiments are reaching turbulent states, what diagnostics are needed to investigate these states? Measuring feature sizes below the LT scale–that is on the order of 1 μm and below–will be important. A static image with sufficient resolution to characterize the spectrum of scales, and in particular to observe the emergence and lengthening of the inertial subrange through the onset and development of turbulence, would be compelling. There are a number of promising diagnostics with the potential to make measurements with an order of magnitude improvement in resolution over the 10-20 μm resolution images that are now common. These include curved crystal imaging techniques [cite: CBI, LLE Cu imager], advanced x-ray optics [KB, KBfixed] and micro-machined diffraction gratings, or "zone plates." Computational methods also enable image reconstruction from "coded apertures," where spatial information is captured in edge-transfer projections, or penumbra. This technique has been employed for years by observational astronomers deciphering photon-starved high-energy images [553], but has only recently been applied to x-ray imaging of HED systems [554] (Figure 64).

These promising diagnostics and techniques will provide the first quantitative measurements of turbulent scales in HED systems. However, a more complete picture of turbulence from a static image will require additional factors of 10's or 100's to capture the smallest relevant scales. For example, the dissipative scale in the experiments of Nagel (where, recall, $\lambda_{LT} = 2.2\mu$m) was calculated to be 20 nm. Measurements at this scale will not only require current diagnostics techniques, but also completely novel experimental configurations. However, the capability to measure dynamic quantities, in addition to simply static measurements at increasing resolution, would provide important data for turbulence researchers.

Beyond static images, measurements that would provide insight in to HED turbulence include the concentration of the component fluids (mass or volume fraction in a given region), fluid density, and the three vectors

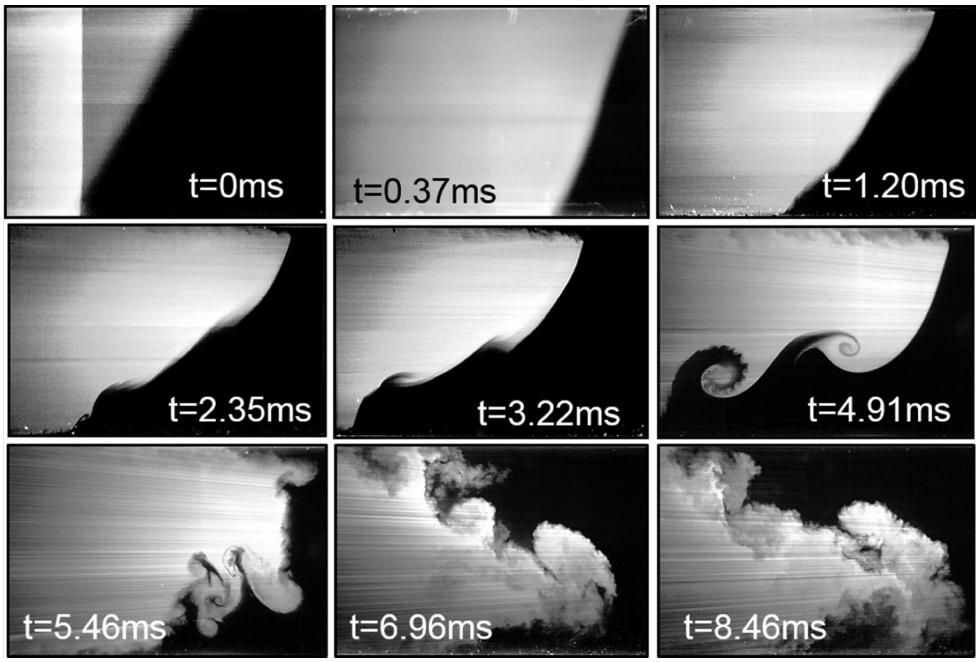

FIG. 59: Time series of experimental PLIF images showing the evolution of the 60° inclined interface through reshock. Reproduced with permission from McFarland *et al.*, *Phys. Rev. E*, **92**, 013023 (2015). Copyright 2015, American Phys. Soc.

of velocity. There are many other variables of interest (pressure, temperature, viscosity, etc), but this short list constitutes the essential parameters to assess turbulent flow. At present, the most pressing challenge in HED systems involves measurement of the fluid velocity fields.

For "classical fluids" experiments (systems a lower pressures and temperatures than the plasmas of interest here), the velocity vectors in the fluid flow are measured with techniques like particle imaging velocimetry (PIV)[555]. In principle the technique is a straightforward calculation of particle velocity, achieved by capturing pairs of images and measuring the distance a particle (or other identifiable voxel) has moved in a known time interval. Indeed, this method of calculating flow fields has even been applied to images that pre-date the algorithms needed for the calculation [556]. Figure 65 shows frames from films created by hydrodynamicist Ludwig Prandtl, as part of a series of films he created to illustrate unsteady flow around obstacles in the early 20^{th} century [557, 558]. The films recorded the motion of aluminum particles on the surface of water, and it was recently observed that the tracer density and image fidelity lended themselves to PIV analysis, also shown in Figure65. Despite its relatively simple requirements, PIV has only been used in a limited set of laser-driven experiments investigating low-density "dust clouds" [559], and broader use in HED conditions will require overcoming several challenges. Specifically, the resolution and signal-to-noise of x-ray imaging systems must be improved, the problem of developing appropriate tracer particles must be addressed, and single-line-of-sight (SLOS) image detectors must be developed to record pairs (or more) of co-registered images.

In a particle imaging velocimetry measurement, the image resolution ideally is small compared to the length scale of velocity gradients. That is, in a system with coherent flows (like laminar flow or the fluid motion in the linear or early-nonlinear phases of RT spike evolution), a system with few tracer particles or low resolution imaging still captures sufficiently dense velocity information to reconstruct the larger flow field. However, in non-linear or turbulent flows–the latter of which has a spatially isotropic distribution of velocity vectors–higher resolution images are necessary to capture the dynamics. As such the earlier discussion of image resolution applies here, with the added complication that the effective resolution is set by either the image system resolution, or the tracer particle size, whichever is *larger*. Given the limited resolving power (∼few microns) that is currently available or likely to be soon, the resolution of PIV adaptations to HED systems will likely be initially limited by the tracer particle size.

The contrast in an x-ray radiograph is determined by the degree of probe absorption through the target, and is related to the material density, material mass attenuation cross section, distance traversed by the probe x-ray, and

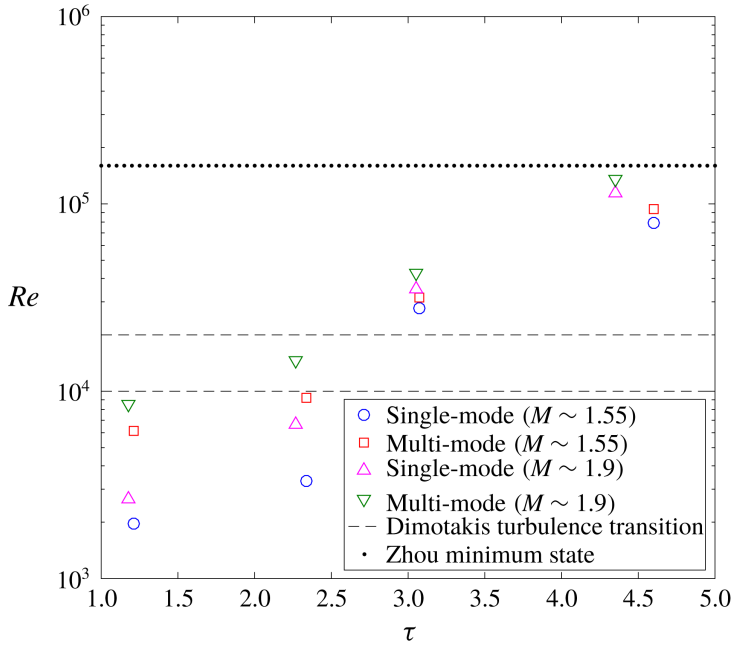

FIG. 60: Reynolds number estimation with non-dimensional time based on turbulent kinetic energy and mixed-mass thickness. Dashed lines indicate a threshold for turbulent mixing (Dimotakis [407]) and the dotted line indicates the minimum state criterion ($Re \approx 1.6 \times 10^5$, Zhou [409]). After reshock, there is a sharp increase in the Reynolds number, and mixing transition occurs in the flow. However, this flow is still not a fully developed turbulent flow, and does not meet the minimum state criterion to reproduce the spectral range corresponding to an astrophysical event [476]. Reproduced with permission from Mohaghar *et al.*, *J. Fluid Mech.*, **871**, 595 (2019). Copyright 2019, Cambridge University Press.

x-ray energy. To generate contrast, the technique may be enhanced by selectively "doping" regions with elements that strongly absorb the probe x-rays. An example of a selectively-doped x-ray radiography image is shown in Figure66. In this experiment, the "spikes" were composed of plastic, but the plastic on one half of the system contained trace iodine, which strongly absorbed at the x-ray probe energy of 9 keV. These spikes appear dark, while the x-ray contrast on the opposing side is lower and due only to density differences between the spikes and bubbles (for complete details on this experiment see Ref [174]). A similar technique could be used to generate the tracer particles that are necessary for PIV. For example, initially solid density plastic targets could be implanted with iodine-doped spheres. Initially, the resolution of the PIV measurement would be approximately the sphere size. After the deposition of vorticity generated by the passage of a strong shock, the tracer material would begin to mix with its surrounding, and the fidelity of the PIV images would begin to degrade. One may consider tracer particles that are less susceptible to mixing, but ideal tracer particles are also as non-perturbative as possible to the system under investigation. To first order this is a requirement on the density of the tracers, but for some systems may also require consideration of the thermal conductivity, compressibility, albedo, or other factors. These conditions limit the range of tracer materials that could be used in PIV measurements of HED systems.

In order to capture pairs (or more) of images that can be co-registered for particle tracking, a single camera must take several images in succession. This can be a challenge in HED systems because of the timescale on which the system evolves. Flows can move at hundreds of microns per nanosecond, so images must be taken quickly so that particles have not moved too far in the time interval between frames. In comparison to the continuous films of Prantdl that were possible in the 1920's, a full-frame imager (1024×1024 pixels) recording a continuous record with nanosecond resolution, as needed to "film" an hydrodynamic evolution in an HED system, would produce 1.3 Petabytes of data per second [560]. This exceeds current information IO bandwidths, and makes the clear the need for more modest "multi-frame" systems for HED imaging.

Traditionally, micro-channel plate (MCP) detectors have been used in HED settings to produce time-gated, 2D imaging, but these are limited to a single frame. Emerging technology like the hybrid-CMOS (h-CMOS) detectors from the Ultra-Fast X-ray Imaging (UXI) program at Sandia National Laboratories aim to address these shortcomings (Figure 67). In recently demonstrations, new h-CMOS detectors have captured pairs of 448 × 1024 pixel images with 2 nanosecond integration times

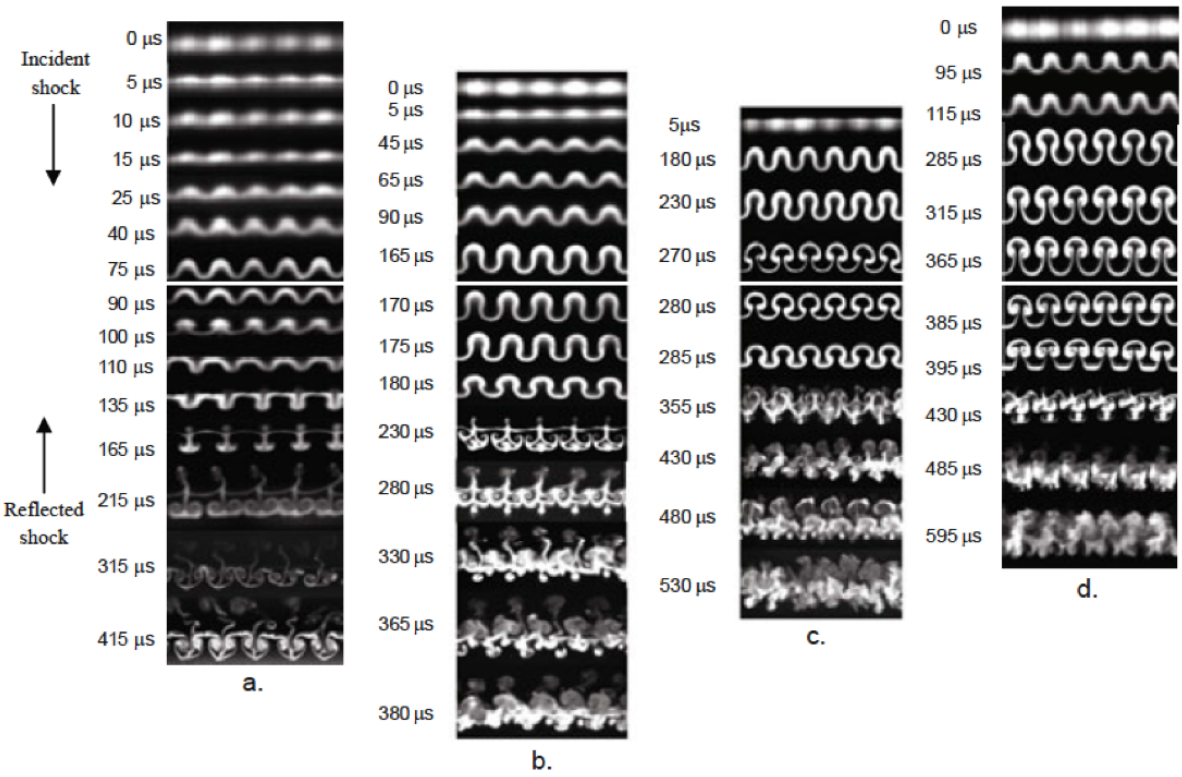

FIG. 61: Four different sets of experiments, each beginning with the varicose gas curtain (top), shocked with a Mach 1.2 shock that travels downward. Each experiment is then reshocked at a different time, as indicated below the white bar crossing the time series. Reshock occurs at time, t= a) 90 μs, b) 170 μs, c) 280 μs, and d) 385 μs. At late times, $t \approx 200$ μs after reshock, the large variation in mixing that occurs for each of the four cases is visible. Reproduced with permission from Prestridge *et al.* [498]. Copyright 2012, Springer.

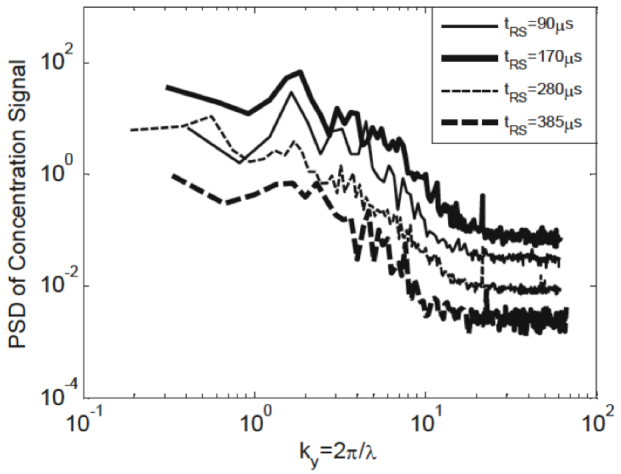

FIG. 62: Power spectra after reshock. Reproduced with permission from Prestridge *et al.* [498]. Copyright 2012, Springer.

[561]. The ability to record a pair of images along a single line of sight (that is, on the same detector) is a minimum requirement for the simplest form of 2-frame PIV. However, more detailed and accurate calculations can be performed with several images, each with co-registered particles. Such fast, multi-frame cameras cameras are in development by the UXI program and others, but not yet in widespread use [560, 562, 563].

Powerful diagnostics have been developed to characterizing flow fields relevant to turbulence in classical fluid experiments, including particle imaging velocimetry. However, adapting these techniques to HED hydrodynamics experiments will require new diagnostics and experimental methods. Robust techniques like x-ray radiography should be leveraged for this, but the spatial resolution and temporal control of the sources and detectors must be improved. Overcoming these challenges will permit novel and important measurements that elucidate the complicated physics of turbulence in high pressure systems.

IX. DOES 2D TURBULENCE RESEMBLE 3D TURBULENCE?

Due to the high computational cost and time-consuming nature of fully 3D simulations of hydrody-

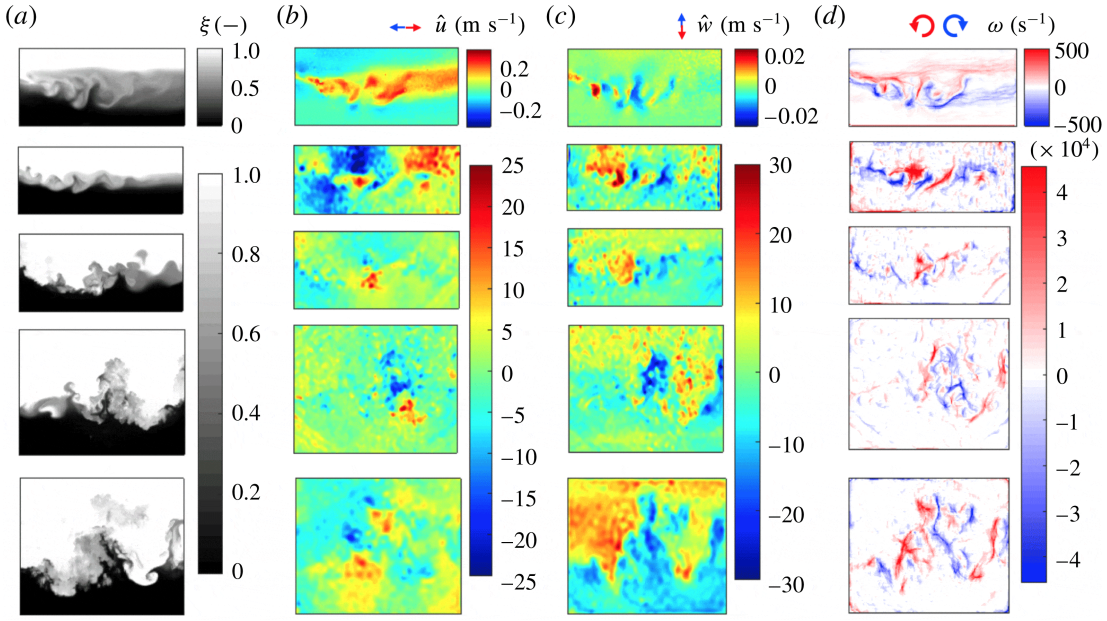

FIG. 63: Representative field evolution results for the Mach= 1.6 case. From left to right: concentration, global fluctuation transverse velocity, global-fluctuation streamwise velocity and vorticity. From top to bottom: IC, PS1, PS2, PS3, PS4. The authors refer to early time, such as PS1, and late time, such as PS4. PS1-4 are used even though these more correctly refer to spatial locations in the shock tube relative to the initial interface position. Reproduced with permission from Reese *et al.* [80], *J. Fluid Mech.*, **849**, 541 (2018). Copyright 2018, Cambridge University Press.

namic instabilities and turbulence, it is desirable to run computations in 2D where possible. But, does 2D turbulence resemble 3D turbulence? The relevance of idealized 2D turbulence to certain aspects of atmospheric motion has been emphasized in many works [564–567], and is due to the fact that large-scale motions (many hundreds of kilometers) in the atmosphere are approximately two dimensional. For instance, 2D turbulence has found success in understanding Hurricane Isidore from 20 to 26 September 2002 [568] and Jupiter's clouds [569]. Hence 2D simulations are useful in giving some indication of the amount of instability growth at an interface. The small-scale structures are, of course very different. Nevertheless, care should be taken as we illustrate below in two case studies in ICF and supernovae.

A. Vortex stretching and direct or inverse energy cascade

The Navier-Stokes equation can be recast into an equation for enstrophy [570–572] $\Omega = \omega^2$, where the vorticity is obtained by taking the curl of the velocity field, $\vec{\omega} = \nabla \times \mathbf{u}$:

$$\frac{\partial \Omega}{\partial t} = \rho^{-1}[\omega\omega \cdot \mathbf{S} + \omega \cdot \mathcal{B}\omega(\nabla \times \rho^{-1}\nabla \cdot \sigma)] \quad (67)$$

The first term on the right-hand side of the above equation is called the production from vortex stretching. The second term is the production from baroclinicity viscous dissipation and redistribution (Figure 68 [573]). Yet, the vortex-stretching term vanishes completely in a pure 2D flow. In 3D, vortex stretching triggers the transition to a fully turbulent flow field.

Furthermore, the energy transfer in a 2D flow is inverse-cascading [575–577], rather than forward cascading. Hence, it is not surprising that the 2D and 3D flows induced by RTI (Figure 69 [573]) and RMI (Figure 70 [574]) are clearly different. In fact, the statistics of the 2D case are probably more sensitive to outliers due to an exaggerated emphasis on bubble-merger and eddy-merger events. Recent simulations by Boffetta and Musacchio [578] at 32768^2 with forcing at moderate wavenumbers

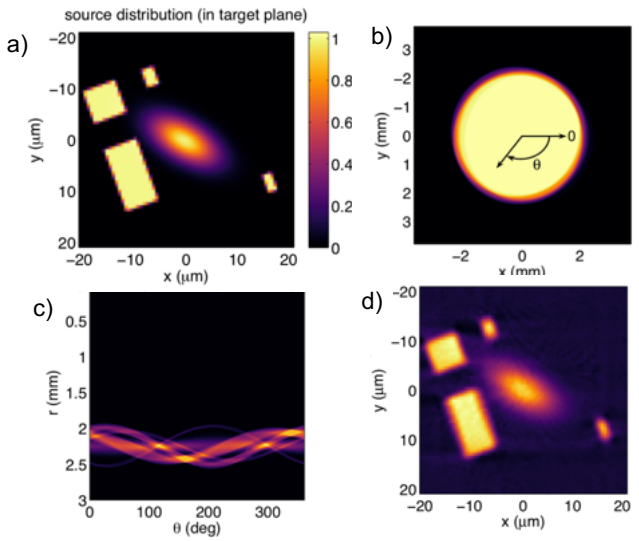

FIG. 64: Penumbral imaging is one of several techniques currently being developed to improve the spatial resolution in images of HED systems. In frame (a), a synthetic source distribution is assumed, including sharp and diffuse features of different sizes. The penumbral image cast by this source distribution is shown in frame (b), and computational techniques are used to derive the sinogram in frame (c). Finally, performing the inverse transform (frame d) nearly recovers the original image. Additional details and original images can be found in Ref. [554]. Reproduced from *Review of Scientific Instruments*, **87**, 11E201, (2016), with the permission of AIP Publishing.

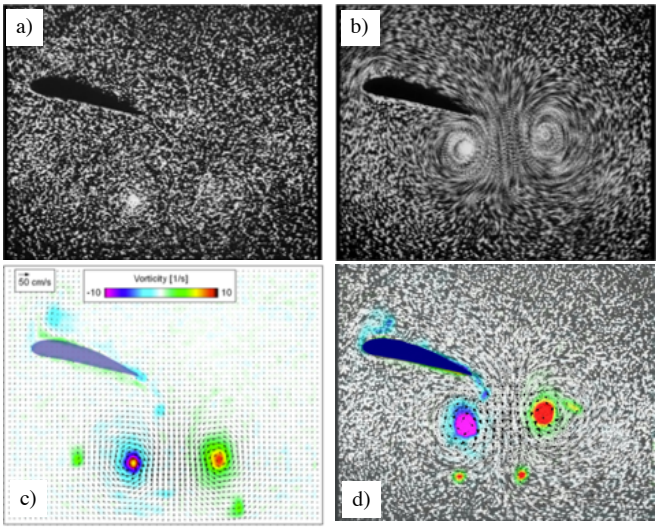

FIG. 65: Illustrating the robust nature of the PIV technique, researchers have post-processed frames of film from Prandtl *et. al* [557, 558] (a single frame from the original film is shown in (a), and a composite of several frames in (b)) with modern PIV algorithms to calculate vector fields from that original work (C. Willert and J. Kompenhans, *arXiv preprint*, https://arxiv.org/abs/1010.3149v1, October 2018 [556]). The results, shown in frames (c) and (d), can be compared to modern simulations in a more precise way that the film alone. Reproduced with permission.

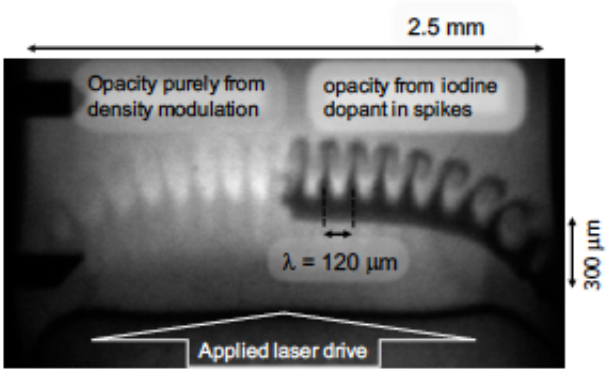

FIG. 66: Well-developed Rayleigh-Taylor spikes and bubbles are evident in this static image, and the technique of selectively doping portions of the target to improve image contrast is demonstrated. However, small-scale structure is well below the resolution limit and no information about velocities can be obtained.

clearly showed both a forward cascade and inverse cascade occurs simultaneously (Figure 71).

Due to the sensitivity to statistical outliers, 2D RTI and RMI simulations require a larger number of realizations to achieve statistical convergence. Since they tend to be characterized by inverse cascades so that the fine-scales are not characterized by a self-similar forward cascade, 2D RTI and RMI simulations tend to require higher grid resolutions than their 3D counterparts. Statistical convergence generally also requires an averaging over a suitable number of realizations of the flow field. A precise number is difficult to specify, but it does appear that more realizations may be required for 2D simulations than for 3D. It seems that any given class of initial conditions probably leads to an "envelope" of values for the RTI growth parameter, α and that the characteristics of this envelope are probably as relevant to "design problems" as is the simple average of the envelope. Indeed, Clark [579] indicated that as many as one hundred and four independent realizations at 1000^2 grid resolution where required achieve reasonable statistical convergence for 2D RTI simulations. Statistical convergence was achieved for 2D RMI simulations using 64 independent realizations and grid resolutions up to 4096^2 in the plane by Thornber and Zhou [580]. The fact that such a large resolution is required clearly demonstrates that 2D turbulence may not be as cost-effective as first envisioned. Pullin and Saffman [581] further claimed: "two-dimensional turbulence, ..is a consequence of the construction of large computers."

Finally, we note that molecular mixing occurs at the

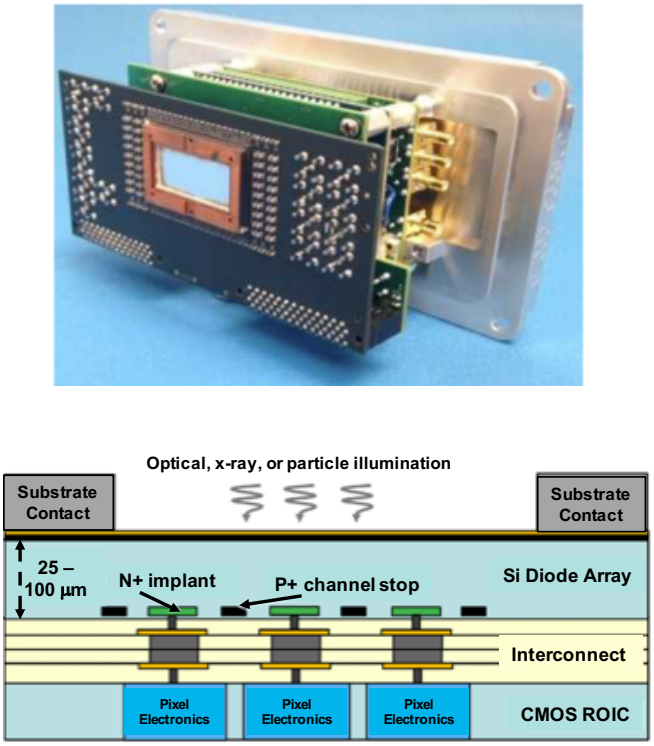

FIG. 67: Hybrid-CMOS detectors are capable of recording multiple images along the same line of sight, at the speeds necessary to permit PIV measurements in HED systems. Shown on the top is a photograph of a prototype camera, with a conceptual description of the electronics shown below, including the per-pixel readout electronics.

interfaces of the fluids, and the ratios of area-to-volume in three-dimensions are very different than the length-to-area ratios in two-dimensions. Therefore, care must be taken when discussing the mixing issues with 2D data.

B. 2D vs 3D in ICF

As noted already in subsection IV B, quantitative comparisons between simulation and experimental data from high-convergence NIF implosions have only proven feasible with these fully 3D, multi-effect simulations [290–293]. Examples of some of these 3D simulations of recent NIF implosion experiments are illustrated in Figure3. In each instance, the rendering shows a cutaway from the simulation at the time of peak neutron production (bang time) where the left cutaway shows ion temperature, the right cutaway mass density, and the outer bounding surface is the ablation front of the imploding shell. Progressing from left to right are simulations of a low foot implosion [303], a high foot implosion [308], and a recent implosion using high density carbon (HDC) in place of the previous plastic ablators [582, 583].

Evident in each of these simulations are deviations

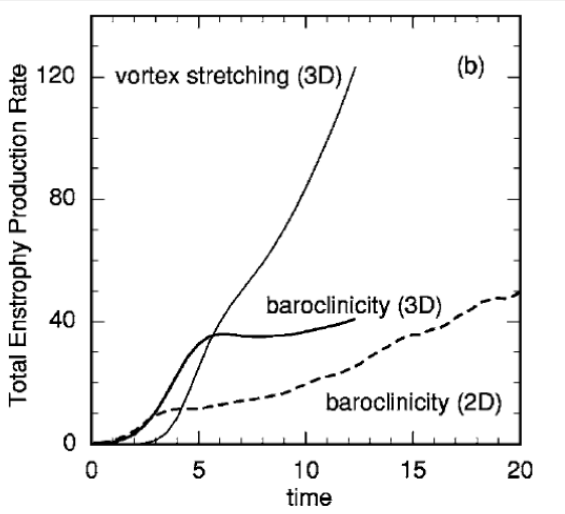

FIG. 68: Global enstrophy production rates from vortex stretching and baroclinicity from 3D DNS (solid lines) and 2D DNS (dashed lines), normalized per plane. Reproduced from Cabot, *Phys. Fluids*, **18**, 045101 (2006), with the permission of AIP Publishing.

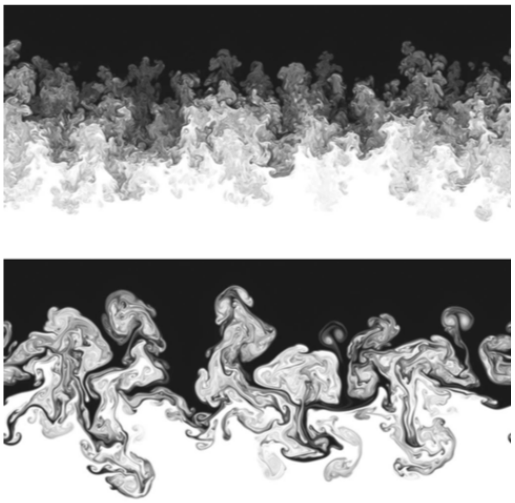

FIG. 69: Vertical slice of density from the 3D simulation (top) compared with the density field from a 2D simulation (bottom), both at t=25. Black is heavy fluid, and white is light fluid. Reproduced from Cabot, *Phys. Fluids*, **18**, 045101 (2006), with the permission of AIP Publishing.

from sphericity due to the growth of hydrodynamic instabilities and also due to long-wavelength asymmetries in the x-ray drive. The defects seeded by the capsule support tents, the ring-like distortions surrounding the north and south poles, are particularly evident in the low and high foot implosions, as are the broadband ablation front modulations in the low foot case. These are both a direct consequence of the coupled RM and

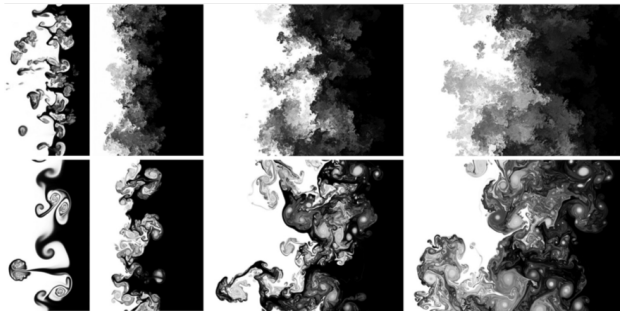

FIG. 70: Contours of the mass fraction of SF_6 from white (0.0) to black (0.8) in 3D (top) and 2D (bottom) showing the qualitative difference. Temporal evolution is from left to right for times $t = 2.0, 2.5, 4.0, 6.0$ ms. Reshock occurs at $t = 2.1$ ms and first shock at $t \approx 0.05$ ms. Reproduced from Olson & Greenough, *Phys. Fluids*, **26**, 101702 (2014), with the permission of AIP Publishing.

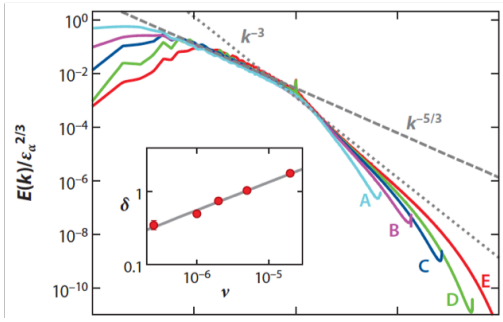

FIG. 71: Energy spectra for the simulation of Table I compensated with the inverse energy flux. Lines represent the two Kraichnan spectra $k^{-5/3}$ (dashed) and k^{-3} (dotted). The inset shows the correction to the Kraichnan exponent for the direct cascade 3 obtained from the minimum of the local slope of the spectra in the range $k_f < k < k_n u$ as a function of the viscosity. Here k_f and $k_n u$ correspond to the forcing and viscous wavenumber scales, respectively. Error bars are obtained from the fluctuations of the local slope. The line has a slope 0.38 and is a guide for the eyes. Reproduced with permission from Boffetta & Musacchio, *Phys. Rev. E*, **82**, 016307 (2010). Copyright 2010, American Phys. Soc.

RT instability growth in these implosions. Indeed, the under-performance of the low foot implosions compared to expectation is now principally understood to be due to strong ablation front instabilities, as illustrated by the figure, in some cases leading to the mixing of ablator material deep into the hot spot and poisoning the potential fusion burn [236, 237]. The substantial improvement in implosion symmetry going from left to right is obvious and corresponds to the nearly two order of magnitude improvement in neutron yield between these implosions. While the HDC implosion shows much less distortion of the hot spot, it remains far from perfect, however, and modulations of the ablation front as well as a local thinning of the confining shell from the tent defect are still visible. Reaching higher neutron yields on NIF will require continued mitigation efforts to reduce these instabilities.

Note that implosion experiments on NIF are inherently 3D in nature. This results not only from the fact that the initial target configuration at shot time is 3D but also due to the 3D x-ray drive conditions in NIF implosions. The consequences of this three-dimensionality are readily apparent in x-ray and neutron imaging data from NIF experiments which show modulated hot spots with obvious 3D structure. Three-dimensionality also has consequences for the simulated performance of NIF targets with 2D axisymmetric simulations typically predicting yields that are a factor of two or more higher than in analogous 3D simulations and in experiments. This difference can be ascribed to the fundamental difference in stagnation dynamics between 2D axisymmetric flows and realistic 3D flows. In 2D flows, material reaching the symmetry axis is by construction met by an exactly opposing flow. This perfect momentum balance maximizes the conversion of shell kinetic energy to hot spot internal energy, and hence maximizes the compression and heating of the hot spot material and thereby enhances the fusion reactivity. In realistic 3D flows, this perfect momentum balancing obviously does not occur. The conversion of kinetic to potential energy is then less efficient with more energy left in useless, residual hot spot flows. The well-known higher growth rate of nonlinear RT instabilities [584] in 3D versus 2D geometry also contributes to 2D vs. 3D differences. Specifically, the development of weak spots in the confining shell at ignition time that can rupture and cause a loss of confinement happens more rapidly in realistic 3D geometry leading to effectively shorter burn durations and lower hot spot pressures.

Figure 72 discussed many different sources of ICF instabilities [585, 586]. One of these is the jet of ablator material injected into the hot spot via the fill tube. Indeed, it was found that interaction with radiation drive seeds 3D flows and contaminants prevent efficient compression and heating of fuel. Again, fuel contamination in ICF involves complex 3D flows as the added degree of freedom in the 3D NIF simulation does reduce the simulated neutron yield- this is clearly an improvement with respect to the experimental data. 2D simulations under-predict the impact [587–589] (see Figure 73).

C. 2D vs 3D in supernovae

Janka *et al.* [590] stated that "supernova theory and 2D simulations are not in a marriage of love but rather a partnership of convenience that was enforced by the limitations of computing resources." Importantly, for numerical simulations to capture the effects of turbulence prop-

erly, 3D models are required. Historically, 1D models routinely either fail to explode without ad hoc prescriptions such as a mixing-length algorithm [e.g., 591] or else explode weakly as in the lower-mass O-Ne-Mg progenitor case [e.g., 592]. With 2D axisymmetry, turbulence exhibits a well-known inverse cascade from small scales to large [575], which may artificially aid the model to explode. Moreover, a popular simplification of neutrino transport using multiple 1D solutions via the so-called "ray-by-ray" approach (see, e.g., Marek & Janka [593]) tends in 2D to exaggerate the axial sloshing observed in those simulations, aiding explosion and possibly leading to the misattribution of the standing accretion shock instability (SASI) as the aiding factor [594].

Fully 3D numerical simulations of CCSNe are now in their adolescence. Simulations like those of [595] are able to capture the multidimensional effects of turbulence and various other important physics such as general-relativistic gravitational effects [596], inelastic neutrino scattering off electrons and nucleons [597], and the many-body correction to neutrino-nucleon scattering [598] that play a crucial role in the neutrino-heating mechanism of explosion. However, in simulations employing all the relevant physics as well as energy-dependent multi-species neutrino transport, the character of the turbulence is not yet fully realized, usually owing to the lack of sufficient resolution to capture the range of physical scales required for successful explosions in global CCSN models. One possible remedy to this problem is the inclusions of subgrid models of turbulence on the smallest scales in order to capture the full inertial range of the turbulent cascade and to assess its effects on the neutrino-heating mechanism [395].

X. OUTSTANDING ISSUES

There have been various computational approaches applied to predict and evaluate the ICF and astrophysical flows. The challenges are immense considering the variety of physical processes involved, the range of temporal and spatial scales that must be dealt with, and the underlying stochasticity of many of the processes, including the characterization of the initial perturbations that give rise to the instabilities we have discussed. For a direct numerical simulation (DNS), much longer times and higher resolutions than that of Cabot & Cook [149] and Cabot & Zhou [151] are needed in order for the horizontal velocity to develop a robust inertial range. The grid would need to be an order of magnitude larger in each dection [234]. Given that DNS is too costly of computer resources to be practical in the foreseeable future, physicists and analysts must rely on some form of modeling to assess the dynamic performance of engineering design. The two apparent leading candidates are the Reynolds-Averaged Navier-Stokes (RANS) models and the Large Eddy Simulation (LES) approach.

The LES approach is based on the assumption that, at sufficiently high Reynolds numbers, the turbulence dissipation rate is independent of the details of the viscous dissipation rate (e.g., [599–602]). This is consistent with Kolmogorov's theory so that, even as viscosity is varied, the spectral structure of the dominant eddy region and the cascade range scaling (and hence the dissipation rate) are independent of the viscosity. Implicit large eddy simulation (ILES) were specifically devised for the accurate simulation of flows with contact discontinuities and shocks –key aspects of the RM and compressible RT mixing processes [7]. Youngs [147] performed the first ILES of RTI induced flow and has recently compared the performance of ILES with that of DNS [158]. In an ILES algorithm, the viscosity does not influence the dissipation range scaling, but instead it is determined by the grid size. Thus if the grid resolution is sufficient to resolve at least part of the inertial range, the dissipative characteristics of the flow will be captured in a reasonable fashion [469, 603–605]. These dissipative and mixing processes are an important feature that current ILES models cannot reproduce in one and two dimensions. In applying the LES, or ILES approach, if the problem to be simulated does develop an inertial range, i.e., does cross into the fully-developed turbulence region, then the simulation must be done in three dimensions to capture the correct dissipative dynamics, unlike the RANS methodologies.

The RANS approach has been used since the mid-1960s for a variety of fluid dynamical problems with varying degrees of success. There are myriad of RANS-type models [8], but most of those applied to relevant problems have involved modeled transport equations for some subset of the second-order moments [606–617] a well as transport of either a turbulent length-scale (generally the turbulence length scale L [618–622] or the turbulent kinetic energy dissipation rate, $\mathcal{E}$ [623–625]).

A strength of the RANS models is that the three-dimensional cascade process is intrinsically integrated into the models via the derivations of their turbulent kinetic dissipation rate equations or, correspondingly, the derivation of the length-scale equations via equation 24. Thus they can be applied in calculations that are statistically one-dimensional or two-dimensional "on average" and still model the forward-cascade process of fully three-dimensional turbulence. If turbulence is a relevant process in a problem being simulated in just one or two dimensions, some tool such as a RANS turbulence model may be required to capture the dissipative mechanisms with any degree of physical fidelity. Thus, despite the approximate nature of the RANS closures, they are still useful and necessary for many practical applications. For a detailed review of these models, see Ref. [8].

The RANS models do have an embedded assumption regarding the relationship between the turbulent kinetic energy K, the integral length-scale, L and the turbulent kinetic energy dissipation rate $\mathcal{E}$ that assumes that the turbulence is fully developed at all times and that the turbulence spectra are self-similar. The LES approach

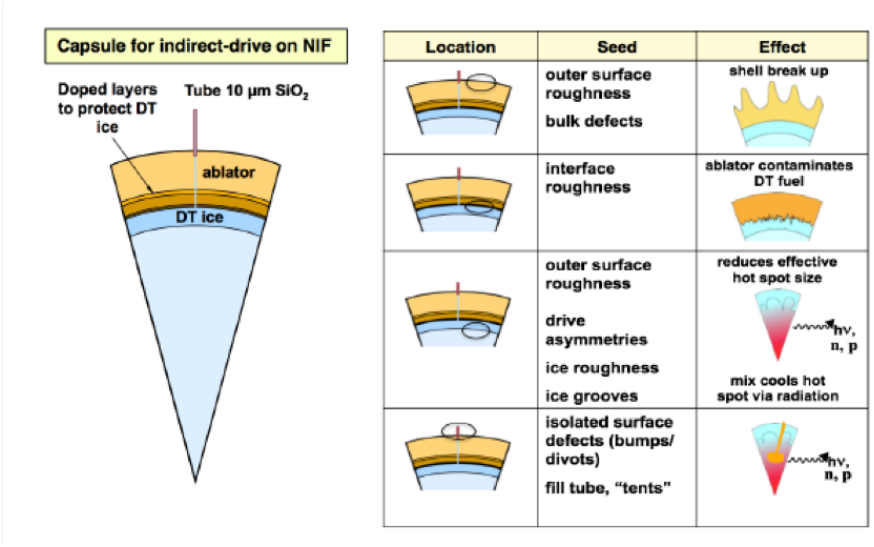

FIG. 72: Schematic of the capsule including DT ice layer showing the locations of unstable interfaces, seeds for the instability growth, and effects on implosion performance. Reproduced with permission from Smalyuk *et al.*, *J. of Instrumentation*, **12**, C06001 (2017). Copyright 2017, Institute of Physics.

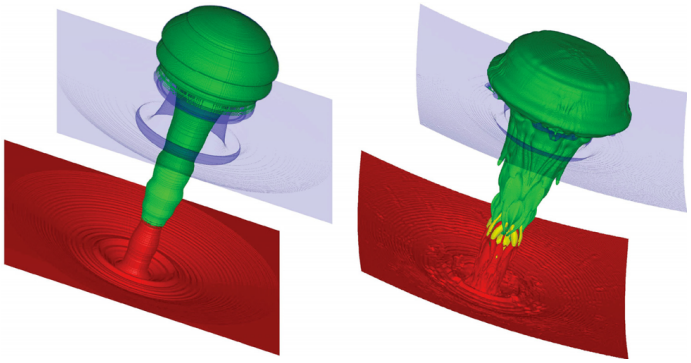

FIG. 73: Comparison of material distribution in the fill tube jet at t=4.8 ns for 2D (synthetically rotated) and 3D simulations of N161204. Red: ablator interfaces; blue: DT wetted foam/DT gas interface; green: fill tube glass; and yellow: glue. Reproduced from Haines *et al.*, *Phys. Plasmas*, **26**, 012707 (2019), with the permission of AIP Publishing.

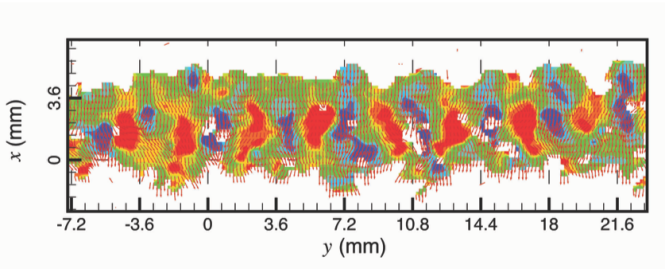

FIG. 74: Instantaneous streamwise velocity contours superimposed on the velocity vector field to show the presence of initial condition imprints after reshock at $t = 22.9$. Red and blue represent high and low streamwise velocity regions, respectively. Reproduced with permission from Balakumar *et al.*, *J. Fluid Mech.*, **696**, 67 (2012). Copyright 2012, Cambridge Univ. Press.

makes no such assumption. This tacit assumption implies that the current class of RANS models are incapable of simulating the transition to fully-developed turbulence since they assume that the inertial range is already established (cf. Refs. [626, 627]). This also makes initialization of such models, when the fluids may be quiescent, problematical when applied to HEDP and ICF-relevant problems. In addition, this assumption of self-similarity in the RANS models makes the incorporation of molecular viscous and diffusive effects problematical. Thus the RANS models generally do not represent the mixing transition with fidelity. Nor do they fully represent the effects of extreme temperature changes and the consequent changes in the molecular properties that occur in astrophysical flows and intense laser platforms.

It should be stressed that the quality of the data collected from laboratory experiments have advanced significantly. These direct laboratory measurements can be used to constrain and validate turbulence models. Ramaprabhu and Andrews [549], Balakumar *et al.* [500], Tomkins *et al.* [197], Mohaghar *et al.* [476, 552], Gerashchenko and Prestridge [551], Charonko [628] Lai *et al.* [629], Reese *et al.* [80] have demonstrated that the laboratory experiments can provide much-needed data for a detailed evaluation of the individual terms in RANS models. For instance, Reese *et al.* decomposed the Reynolds stresses into three terms and determined that the first term, the mean density-velocity correlation,

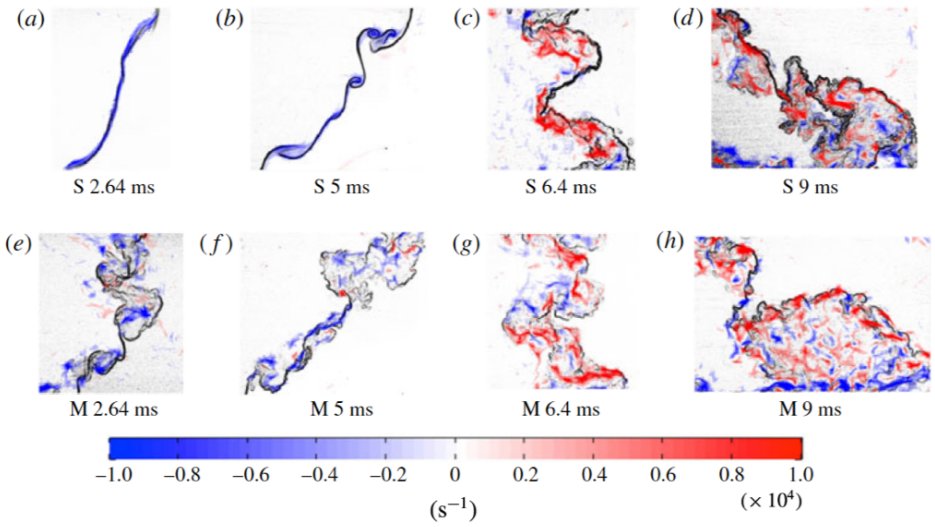

FIG. 75: Vorticity evolution overlaid on simulated Schlieren images for both cases. S refers to single-mode case and M refers to multi-mode case. Reproduced with permission from Mohaghar *et. al.*, *J. Fluid Mech.*, **831**, 779 (2017). Copyright 2017, Cambridge Univ. Press.

dominates. Reese *et al.* also investigated the turbulent mass-flux velocity, which is the primary turbulent source term for mixing and appears as a prefactor in the production term for the turbulent kinetic energy evolution equation. The experimental data indicated that larger values of turbulent mass-flux velocity in both directions are seen for higher Mach number case, indicating greater production of turbulent kinetic energy.

It is understandable that many experimental and simulation studies are carried out in planar geometry. This makes it significantly easier to isolate the physics. Yet, as the applications of our interest, the astrophysical flows and ICF, one must deal with the convergent geometry, The convergent geometry is a challenge as one must account for convergence of the flow, compressibility, and acceleration (the Bell-Plesset (BP) effects) [630–634]. Some recent work in this area can be found in Refs. [635–638].

A significant effort has devoted to the issue of the initial condition as it is a critical issue for understanding the physics and implementing the engineering models. Strong evidence has been presented that the imprint of initial conditions last to the end of their experiments (see Figures 74 and 75). The instantaneous streamwise velocity contours superimposed on the velocity vector field showed the presence of initial condition imprints after reshock at t= 22.9 [500]. The coherence of the large-wavelength spike and bubble features in the density field even after reshock leads to the conclusion that the memory of the largest scales is maintained (Mohaghar *et al.* [552]).

However, the Reynolds numbers in these experiments were not sufficiently high to transition to fully developed turbulence. It would be extremely useful to determine if the dependence of initial conditions could survive when the flows induced by hydrodynamic instabilities are allowed to transition to fully-developed turbulence. Consequently, much larger simulations and experiments are required so the process of transition to turbulence from the flows induced by instabilities can be observed in detail, and to determine if initial conditions are truly "forgotten."

XI. CONCLUSION

Significant efforts have been devoted to achieve greater understanding of how turbulence mixing induced by hydrodynamic instabilities evolves from the linear and weakly nonlinear regime to the fully turbulent regime. The goal of this review is to combine theory, simulation, experiment, and modeling to demonstrate how the same basic principles apply to hydrodynamic-instability induced turbulence mixing of all sizes, ranging from the microscopic scales of inertial confinement fusion capsule implosions to the mega-scales of supernova explosions. In particular, the spatial and temporal criteria required for hydrodynamic instability driven flows to transition to turbulence have been established through theoretical analysis. These findings have provided critical design guidance to high energy density physics (HEDP) and laboratory experiments investigating the minimum state Reynolds number and the amount of time necessary to transition to a turbulent flow. These criteria have become increasingly important because HEDP experiments are now poised to finally achieve a turbulent regime.

Impressive progress has been made, but major challenges are still confronting researchers. Of particular importance, we should finally be able to simulate the transition to turbulence from numerical simulations using exascale computers, and to demonstrate the transition ex-

perimentally on HEDP platforms and in laboratory experiments utilizing improved diagnostic tools.

Acknowledgments

The first author gratefully acknowledges helpful discussions with Drs. B.J. Alder, A. Banerjee, J.D. Bender, R. Bonazza, W.H. Cabot, A.W. Cook, A.J. Cunningham, T.R. Dittrich, F.F. Grinstein, M. Groom, B. Haines, J. W. Jacobs, R.I. Klein, S.A. MacLaren, K.O. Mikaelian, S.R. Nagel, P. Ramaprabhu, K. S. Raman, D. Ranjan, B. Thornber, R.J.R. Williams, and D.L. Youngs. This work was performed under the auspices of the U.S. Department of Energy by Lawrence Livermore National Laboratory under Contract DE-AC52-07NA27344. T.T.C. was supported by a Los Alamos National Laboratory subcontract to the University of New Mexico.

[1] Lord Rayleigh (John William Strutt), "Investigation of the character of the equilibrium of an incompressible heavy fluid of variable density," *Proceedings of the London Mathematical Society*, **14**, 170 (1883).

[2] G.I. Taylor, "The instability of liquid surfaces when accelerated in a direction perpendicular to their planes," *Proceedings of the Royal Society of London A,* **201**, 192 (1950).

[3] R.D. Richtmyer, "Taylor Instability in a Shock Acceleration of Compressible Fluids". *Communications on Pure and Applied Mathematics,* **13**, 297 (1960)

[4] E.E. Meshkov, "Instability of the Interface of Two Gases Accelerated by a Shock Wave," *Fluid Dynamics*, **4**, 101 (1969)

[5] Lord Kelvin (William Thomson), "Hydrokinetic solutions and observations," *Philosophical Magazine*, **42**, 362 (1871).

[6] H. von Helmholtz, "On the discontinuous movements of fluids," *Monatsberichte der Kniglichen Preussische Akademie der Wissenschaften zu Berlin*, **23**, 215 (1868).

[7] Y. Zhou, "Rayleigh-Taylor and Richtmyer-Meshkov instability induced flow, turbulence, and mixing. I," *Physics Reports*, **720-722**, 1 (2017).

[8] Y. Zhou, "Rayleigh-Taylor and Richtmyer-Meshkov instability induced flow, turbulence, and mixing. II," *Physics Reports*, **723-725**, 1 (2017).

[9] B. Müller, Fryxell, and D. Arnett, "Instability and clumping in SN1987A," *Astronomy and Astrophysics,* **251**, 505 (1991).

[10] B.A. Remington, R.P. Drake, D.D. Ryutov, "Experimental astrophysics with high power lasers and Z pinches," *Rev. Mod. Phys.*, **78**, 755 (2006).

[11] G. Rüdiger, Differential rotation and stellar convection: Sun and solar-type stars. Gordon and Breach, New York, 1989.

[12] R.F. González, J. Cantó, and A.C. Raga, "Analytical and numerical models of P Cygni's nebula," *Monthly Notices of the Royal Astronomical Society*, **480**, 5092 (2018).

[13] Y. Wang, B. Bao, C. Yang, L. Zhang, "The impact of different interstellar medium structures on the dynamical evolution of supernova remnants," *Monthly Notices of the Royal Astronomical Society*, **478**, 2948 (2018).

[14] S. V. Lebedev, A. Frank, and D. D. Ryutov, "Exploring astrophysics-relevant magnetohydrodynamics with pulsed-power laboratory facilities," *Rev. Mod. Phys.*, **91**, 025002 (2019).

[15] J.D. Lindl, "Development of the indirect-drive approach to inertial confinement fusion and the target physics basis for ignition and gain." *Phys. Plasmas*, **2**, 3933 (1995)

[16] J.D. Lindl, Inertial confinement fusion: the quest for ignition and energy gain using indirect drive. American Institute of Physics, 1998.

[17] S. Atzeni and J. Meyer-ter-Vehn. The physics of inertial fusion: beam plasma interaction, hydrodynamics, hot dense matter, Oxford University Press, Oxford UK, 2004.

[18] T. Ma, P. K. Patel, N. Izumi, P. T. Springer, M. H. Key, L. J. Atherton, M. A. Barrios, L. R. Benedetti, R. Bionta, E. Bond, D. K. Bradley, J. Caggiano, D. A. Callahan, D. T. Casey, P. M. Celliers, C. J. Cerjan, J. A. Church, D. S. Clark, E. L. Dewald, T. R. Dittrich, S. N. Dixit, T. Dppner, R. Dylla-Spears, D. H. Edgell, R. Epstein, J. Field, D. N. Fittinghoff, J. A. Frenje, M. Gatu Johnson, S. Glenn, S. H. Glenzer, G. Grim, N. Guler, S. W. Haan, B. A. Hammel, R. Hatarik, H. W. Herrmann, D. Hicks, D. E. Hinkel, L. F. Berzak Hopkins, W. W. Hsing, O. A. Hurricane, O. S. Jones, R. Kauffman, S. F. Khan, J. D. Kilkenny, J. L. Kline, B. Kozioziemski, A. Kritcher, G. A. Kyrala, O. L. Landen, J. D. Lindl, S. Le Pape, B. J. MacGowan, A. J. Mackinnon, A. G. MacPhee, N. B. Meezan, F. E. Merrill, J. D. Moody, E. I. Moses, S. R. Nagel, A. Nikroo, A. Pak, T. Parham, H. S. Park, J. E. Ralph, S. P. Regan, B. A. Remington, H. F. Robey, M. D. Rosen, J. R. Rygg, J. S. Ross, J. D. Salmonson, J. Sater, D. Sayre, M. B. Schneider, D. Shaughnessy, H. Sio, B. K. Spears, V. Smalyuk, L. J. Suter, R. Tommasini, R. P. J. Town, P. L. Volegov, A. Wan, S. V. Weber, K. Widmann, C. H. Wilde, C. Yeamans, and M. J. Edwards, "The role of hot spot mix in the low-foot and high-foot implosions on the NIF," *Phys. Plasmas*, **24**, 056311 (2017).

[19] E. C. Merritt, J. P. Sauppe, E. N. Loomis, T. Cardenas, D. S. Montgomery, W. S. Daughton, D. C. Wilson, J. L. Kline, S. F. Khan, M. Schoff, M. Hoppe, F. Fierro, R. B. Randolph, B. Patterson, L. Kuettner, R. F. Sacks, E. S. Dodd, W. C. Wan, S. Palaniyappan, S. H. Batha, P. A. Keiter, J. R. Rygg, V. Smalyuk, Y. Ping, and P. Amendt, "Experimental study of energy transfer in double shell implosions," *Phys. Plasmas*, **26**, 052702 (2019).

[20] B.A. Remington, H.-S. Park, D.T. Casey, R.M. Cavallo, D.S. Clark, C.M. Huntington, C.C. Kuranz, A.R. Miles, S.R. Nagel, K.S. Raman, and V.A. Smalyuk, "Rayleigh-Taylor instabilities in high-energy density settings on the National Ignition Facility," *Proc. of the National Acad. Sci.*, https://doi.org/10.1073/pnas.1717236115 (2018).

[21] H.-S. Park, R.E. Rudd, R.M. Cavallo, N.R. Barton, A. Arsenlis, J.L. Belof, K.J.M. Blobaum, B.S. El-dasher, J.N. Florando, C.M. Huntington, B.R. Maddox, M.J. May, C. Plechaty, S.T. Prisbrey, B.A. Remington, R.J. Wallace, C.E. Wehrenberg, M.J. Wilson, A.J. Comley, E. Giraldez, A. Nikroo, M. Farrell, G. Randall, and G.T.

Gray, III, "Grain-Size-Independent Plastic Flow at Ultrahigh Pressures and Strain Rates," *Phys. Rev. Lett.*, **114**, 065502.

[22] O. A. Hurricane and M.C. Herrmann, "High-energy-density physics at the National Ignition Facility," *Annu. Rev. of Nuclear and Particle Sci.*, **67**, 213 (2017).

[23] O.A. Hurricane, "Design for a high energy density Kelvin-Helmholtz experiment," *High Energy Density Physics*, **4**, 97 (2008).

[24] O.A. Hurricane, J.F. Hansen, H.F. Robey, B.A. Remington, M.J. Bono, E.C. Harding, R.P. Drake, C.C. Kuranz, "A high energy density shock driven Kelvin-Helmholtz shear layer experiment," *Phys. Plasmas*, **16**, 056305, (2009).

[25] E.C. Harding, J.F. Hansen, O.A. Hurricane, R.P. Drake, H.F. Robey, C.C. Kuranz, B.A. Remington, M.J. Bono, M.J. Grosskopf, R.S. Gillespie, "Observation of a Kelvin-Helmholtz Instability in a High-Energy-Density Plasma on the Omega Laser," *Phys. Rev. Lett*, **103**, 045005, 2009.

[26] L. Welser-Sherrill, J. Fincke, F. Doss, E. Loomis, K. Flippo, D. Offermann, P. Keiter, B. Haines, and F. Grinstein. "Two laser-driven mix experiments to study reshock and shear," *High Energy Density Physics*, **9**, 496 (2013).

[27] F.W. Doss, E.N. Loomis, L. Welser-Sherrill, J.R. Fincke, K.A. Flippo, and P.A. Keiter, "Instability, mixing, and transition to turbulence in a laser-driven counterflowing shear experiment," *Phys. Plasmas*, **20**, 012707 (2013).

[28] F.W. Doss, J.R. Fincke, E.N. Loomis, L. Welser-Sherrill, and K.A. Flippo, "The high-energy-density counterpropagating shear experiment and turbulent self-heating," *Phys. Plasmas*, **20**, 122704 (2013).

[29] G. Malamud, A. Shimony, W.C. Wan, C.A. Di Stefano, Y. Elbaz, C.C. Kuranz, P.A. Keiter, R.P. Drake, D. Shvarts, "A design of a two-dimensional, supersonic KH experiment on OMEGA-EP," *High Energy Density Phys.*, **9**, 672 (2013).

[30] C.A. Di Stefano, G. Malamud, M.T. Henry de Frahan, C.C. Kuranz, A. Shimony, S.R. Klein, R.P. Drake, E. Johnsen, D. Shvarts, V.A. Smalyuk, D. Martinez, "Observation and modeling of mixing-layer development in high-energy-density, blast-wave-driven shear flow," *Phys. Plasmas*, **21**, 056306 (2014).

[31] E.C. Merritt, F.W. Doss, E.N. Loomis, K.A. Flippo, J.L. Kline, "Modifying mixing and instability growth through the adjustment of initial conditions in a high-energy-density counter-propagating shear experiment on OMEGA," *Phys. Plasmas*, **22**, 062306 (2015).

[32] E.C. Merritt and F.W. Doss, "Wavelet analysis methods for radiography of multidimensional growth of planar mixing layers," *Review of Scientific Instruments*, **87**, 075103 (2016).

[33] E.C. Merritt, F.W. Doss, C.A. Di Stefano, K.A. Flippo, A.M. Rasmus, and D.W. Schmidt, "Demonstration of repeatability in a high-energy-density planar shear mixing layer experiment," *High Energy Density Physics*, **23**, 90 (2017).

[34] W.C. Wan, G. Malamud, A. Shimony, C.A. Di Stefano, M.R. Trantham, S.R. Klein, D. Shvarts, C.C. Kuranz, R.P. Drake, "Observation of single-mode, Kelvin-Helmholtz instability in a supersonic flow," *Phys. Rev. Lett.*, **115**, 145001 (2015).

[35] W.C. Wan, G. Malamud, A. Shimony, C.A. Di Stefano, M.R. Trantham, S.R. Klein, D. Shvarts, R.P. Drake, C.C. Kuranz, "Observation of dual-mode, Kelvin-Helmholtz instability vortex merger in a compressible flow," *Phys. Plasmas*, **24**, 055705 (2017).

[36] A.M. Rasmus, C. Di Stefano, K. Flippo, F.W. Doss, J. Kline, J. Hager, E. Merritt, T.R. Desjardins, W. Wan, T. Cardenas, D. Schmidt, P.M. Donovan, F. Fierro, J.I. Martinez, J. Zingale, C. Kuranz, "Shock-driven discrete vortex evolution on a high-Atwood number oblique interface," *Phys. Plasmas*, **25**, 032119 (2018).

[37] A.N. Kolmogorov, "The local structure of turbulence in incompressible viscous fluid for very large Reynolds numbers," *Dokl. Akad. Nauk SSSR*, **30**, 299 (1941).

[38] G.K. Batchelor, The theory of homogeneous turbulence. Cambridge university press, 1953.

[39] L.D. Landau, E.M. Lifshitz, Fluid mechanics. London: Pergamon 1987.

[40] U. Frisch, Turbulence: The legacy of A.N. Kolmogorov. Cambridge university press, Cambridge, UK 1995.

[41] J.C.R. Hunt, O.M. Phillips and D. Williams, (eds.). Turbulence and stochastic processes: Kolmogorov's ideas 50 years on. *Proc. R. Soc. A*, **434** (1991).

[42] C.L.M.H. Navier, "Memoire sur les lois du mouvement des fluides," *Mem. Acad. Sci. Inst. France,* **6**, 389 (1822)

[43] G.G. Stokes, "On the theories of the internal friction of fluids in motion," *Trans. Cambridge Philos. Soc.*, **8**, 287 (1845).

[44] A. S. Monin and A. M. Yaglom, Statistical Fluid Mechanics: Mechanics of turbulence, vol. 1, The MIT Press, Cambridge, MA, 1971.

[45] A. S. Monin and A. M. Yaglom, Statistical Fluid Mechanics: Mechanics of turbulence, vol. 2, The MIT Press, Cambridge, MA, 1975.

[46] R.B. Bird, W.E. Stewart, and E.N. Lightfoot. Transport phenomena. 2nd. John Wiley & Sons New York, 1960.

[47] J.O. Hinze, Turbulence, McGraw-Hill, 1975.

[48] S.B. Pope, Turbulent flows. Cambridge Univ. Press, 2001.

[49] Z. Warhaft, An introduction to thermal-fluid engineering: the engine and the atmosphere. Cambridge University Press, 1997.

[50] M. Van Dyke, An album of fluid motion, The Parabolic Press, Stanford, CA 1982.

[51] P. Dimotakis, R.C. Miake-Lye, and D.A. Papantoniou. "Structure and dynamics of round turbulent jets." *Phys. Fluids*, **26**, 3185 (1983).

[52] L.F. Richardson, Weather prediction by numerical process. Cambridge University Press (1922).

[53] H.A. Rose and P.L. Sulem, "Fully developed turbulence and statistical mechanics," *J. de Physique*, **39**, 441 (1978).

[54] U. Frisch, P.L. Sulem, and M. Nelkin, "A simple dynamical model of intermittent fully developed turbulence," *J. Fluid Mech.*, **87**, 719 (1978).

[55] T. Ishihara, Y. Kaneda, and J.C. Hunt, "Thin shear layers in high Reynolds number turbulence-DNS results," *Flow, Turbulence and Combustion*, **91**, 895 (2013).

[56] T. Ishihara, T. Gotoh, and Y. Kaneda, "Study of high-Reynolds number isotropic turbulence by direct numerical simulation," *Annual Review of Fluid Mechanics,* **41**,165 (2009).

[57] H. Tennekes and J.L. Lumley, A first course in turbulence. MIT press. 1972

[58] D. Jackson and B. Launder, "Osborne Reynolds and the

publication of his papers on turbulent flow," *Annu. Rev. Fluid Mech.* , **39**, 19 (2007).

[59] C. G. Speziale, "Analytical methods for the development of Reynolds-stress closures in turbulence." *Annual Review of Fluid Mechanics*, **23**, 107 (1991).

[60] K. Hanjalić, "Advanced turbulence closure models: a view of current status and future prospects." *International Journal of Heat and Fluid Flow*, **15**, 178 (1994).

[61] D.C. Wilcox, Turbulence modeling for CFD. DCW industries, La Canada, CA, 1998.

[62] F.H. Champagne, V.G. Harris, and S. Corrsin, "Experiments on nearly homogeneous turbulent shear flow," *J. Fluid Mech.*, **41**, 81 (1970).

[63] Y. Zhou and S. Oughton. "Nonlocality and the critical Reynolds numbers of the minimum state magnetohydrodynamic turbulence," *Phys. Plasmas,* **18**, 072304 (2011).

[64] Y. Zhou, "Interacting scales and energy transfer in isotropic turbulence." *Phys. Fluids A*, **5**, 2511 (1993).

[65] Y. Zhou, "Degrees of locality of energy transfer in the inertial range." *Phys. Fluids A*, **5**, 1092 (1993) .

[66] Y. Zhou and C. G. Speziale. "Advances in the fundamental aspects of turbulence: Energy transfer, interacting scales, and self-preservation in isotropic decay." *Applied Mechanics Reviews*, **51**, 267 (1998).

[67] K.R. Sreenivasan, "On the universality of the Kolmogorov constant," *Phys. Fluids,* **7**, 2778 (1995).

[68] P. K. Yeung and Y. Zhou, "Universality of the Kolmogorov constant in numerical simulations of turbulence," *Phys. Rev. E*, **56**, 1746 (1997).

[69] D. A. Donzis and K. R. Sreenivasan. "The bottleneck effect and the Kolmogorov constant in isotropic turbulence," *J. Fluid Mech.,* **657**, 171 (2010).

[70] T. Ishihara, K. Morishita, M. Yokokawa, A. Uno, and Y. Kaneda. "Energy spectrum in high-resolution direct numerical simulations of turbulence," *Phys. Rev. Fluids*, **1**, 082403 (2016).

[71] S.G Saddoughi and S.V. Veeravalli, "Local isotropy in turbulent boundary layers at high Reynolds number," *J. Fluid Mech.*, **268**, 333 (1994).

[72] H.L. Grant, R.W. Stewart, and A. Moilliet, "Turbulence spectra from a tidal channel," *J. Fluid Mech.*, **12**, 241 (1962).

[73] A.A. Praskovsky, E.B. Gledzer, M.Y. Karyakin, and Y. Zhou, "The sweeping decorrelation hypothesis and energy-inertial scale interaction in high Reynolds number flows," *J. Fluid Mech.*, **248**, 493 (1993).

[74] A. M. Obukhov, "Structure of the temperature field in a turbulent flow," *Izv. Akad. Nauk. SSSR, Geogr. i Geo z.,* **13**, 58 (1949).

[75] S. Corrsin, "On the Spectrum of Isotropic Temperature Fluctuations in an Isotropic Turbulence" *J. of Applied Physics,* **22**, 469 (1951).

[76] S.B. Dalziel, P. F. Linden, and D. L. Youngs, "Self-similarity and internal structure of turbulence induced by Rayleigh-Taylor instability," *J. Fluid Mech.*, **399** , 1 (1999).

[77] A. Banerjee and L.A.R. Mutnuri, "Passive and reactive scalar measurements in a transient high-Schmidt-number Rayleigh-Taylor mixing layer," *Experiments in Fluids,*, **53**, 717 (2012).

[78] N.J. Mueschke, O. Schilling, D.L. Youngs, and M.J. Andrews. "Measurements of molecular mixing in a high-Schmidt-number Rayleigh-Taylor mixing layer." *J. Fluid Mech.*, **632**, 17 (2009).

[79] P.L. OŃeill, D. Nicolaides, D. Honnery, and J. Soria, "Autocorrelation functions and the determination of integral length with reference to experimental and numerical data," in Proceedings of the 15th Australasian Fluid Mechanics Conference: Sydney, Australia, 13-17 December 2004, edited by M. Behnia, W. Lin, and G. D. McBain (The University of Sydney, 2004).

[80] D.T. Reese, A.M. Ames, C.D. Noble, J.G. Oakley, D.A. Rothamer, and R. Bonazza, "Simultaneous direct measurements of concentration and velocity in the Richtmyer-Meshkov instability," *J. Fluid Mech.*, **849**, 541 (2018).

[81] M. Bailey, Starry Night: Van Gogh at the Asylum, White Lion Publishing, London, UK (2018)

[82] J.L. Aragón, G.G. Naumis, M. Bai, M. Torres, and P.K. Maini, "Turbulent luminance in impassioned van Gogh paintings," J. of Mathematical Imaging and Vision," *J. of Mathematical Imaging and Vision*, **30**, 275 (2008).

[83] F. Anselmet, Y.l. Gagne, E. J. Hopfinger, and R. A. Antonia. "High-order velocity structure functions in turbulent shear flows." *J. Fluid Mech.,* **140**, 63 (1984).

[84] B. Castaing, Y. Gagne, and E.J. Hopfinger, "Velocity probability density functions of high Reynolds number turbulence," *Physica D* , **46** , 177 (1990).

[85] M. Kuhlen, S.E. Woosley, and G.A. Glatzmaier, "Carbon ignition in type Ia supernovae. II. A three-dimensional numerical model." *Astrophys.J.*, **640**, 407 (2006).

[86] S.E. Woosley, S. Wunsch, and M. Kuhlen, "Carbon ignition in type Ia supernovae: an analytic model," *Astrophys.J.*, **607**, 921 (2004).

[87] E. Abdikamalov, C.D. Ott, D. Radice, L.F. Roberts, R. Haas, C. Reisswig, P. Msta, H. Klion, and E. Schnetter, "Neutrino-driven turbulent convection and standing accretion shock instability in three-dimensional core-collapse supernovae," *Astrophys.J.*, **808**, 70 (2015).

[88] R.P. Drake, "Laboratory experiments to simulate the hydrodynamics of supernova remnants and supernovae," *J. of Geophysical Research: Space Physics*, **104**, 14505 (1999).

[89] D. Ryutov, R.P. Drake, J. Kane, E. Liang, B.A. Remington, and W.M. Wood-Vasey, "Similarity criteria for the laboratory simulation of supernova hydrodynamics," *Astrophys.J.*, **518**, 821 (1999).

[90] P.E. Dimotakis, "Turbulent mixing," *Annu. Rev. Fluid Mech.*, **37**, 329 (2005).

[91] V. Rudyak and A. Minakov, "Modeling and optimization of Y-type micromixers," *Micromachines*, **5**, 886 (2014).

[92] C. Segal, The scramjet engine: processes and characteristics, Cambridge University Press, Cambridge, UK 2011.

[93] M. Aslani & J. D. Regele, "Numerical simulation of finite disturbances interacting with laminar premixed flames," *Combustion Theory and Modelling*, **22**, 812 (2018).

[94] A.L. Kuhl, J.B. Bell, V.E. Beckner, K. Balakrishnan, and A.J. Aspden, "Spherical combustion clouds in explosions," *Shock Waves*, **23**, 233 (2013).

[95] A.L. Kuhl, K. Balakrishnan, J.B. Bell, and V.E. Beckner, "Turbulent combustion in aluminum-air clouds for different scale explosion fields," *AIP Conference Proceedings*, **1793**, 150001, (2017).

[96] M. Fernandez-Godino, F. Ouellet, R. Haftka, S.S. Balachandar, "Early time evolution of circumferential perturbation of initial particle volume fraction in explosive cylindrical multiphase dispersion," *ASME. J. Fluids Eng.*, **141**, 091302 (2019).

[97] A.W. Cook, "Enthalpy diffusion in multicomponent flows," *Phys. Fluids*, **21**, 055109 (2009).

[98] W.M. Kays and M.E. Crawford, Convective heat and mass transfer. 3rd Edition, McGraw Hill, New York, 1993.

[99] M. Lombardini, D.J. Hill, D. I. Pullin, and D. I. Meiron, "Atwood ratio dependence of Richtmyer-Meshkov flows under reshock conditions using large-eddy simulations." *J. Fluid Mech.*, **670**, 439 (2011).

[100] D. D. Joseph, "Fluid dynamics of two miscible liquids with diffusion and gradient stresses," *Eur. J. Mech. B/Fluids*, **9**, 565 (1990).

[101] A.W. Cook and Y. Zhou. "Energy transfer in Rayleigh-Taylor instability," *Phys. Rev. E,* **66** 026312 (2002).

[102] D. Livescu, "Numerical simulations of two-fluid turbulent mixing at large density ratios and applications to the Rayleigh-Taylor instability." *Phil. Trans. R. Soc. A,* **371**, 20120185 (2013).

[103] S. Chandrasekhar, Hydrodynamic and hydromagnetic Stability, Dover Books on Physics, 1961.

[104] D. H. Sharp, "Overview of Rayleigh-taylor instability," *Physica D,* **12**, 3 (1984).

[105] J. Prüss and G. Simonett. "On the Rayleigh-Taylor instability for the two-phase Navier-Stokes equations." *Indiana University Mathematics J.*, **59**, 1853 (2010).

[106] J. Prüess, G. Simonett, and M. Wilke. "The Rayleigh-Taylor instability for the Verigin problem with and without phase transition." *Nonlinear Differ. Equ. Appl.*, **26**. 18 (2019).

[107] F. Nguyen, J. -P. Laval, P. Kestener, A. Cheskidov, R. Shvydkoy, and B. Dubrulle, "Local estimates of Hölder exponents in turbulent vector fields," *Phys. Rev. E,* **99**, 053114 (2019)

[108] M. S. Roberts and J. W. Jacobs, "The effects of forced small-wavelength, finite-bandwidth initial perturbations and miscibility on the turbulent Rayleigh-Taylor instability," *J. Fluid Mech.,* **787**, 50 (2016).

[109] P. G. Drazin and W. H. Reid, Hydrodynamic stability, Cambridge University Press, 2004.

[110] S. W. Haan, "Onset of nonlinear saturation for Rayleigh-Taylor growth in the presence of a full spectrum of modes," *Phys. Rev. A,* **39**, 5812 (1989).

[111] S. W. Haan, "Weakly nonlinear hydrodynamic instabilities in inertial fusion." *Phys. Fluids B*, **3**, 2349 (1991)

[112] Y. Yang, Q. Zhang, and D. H. Sharp, "Small amplitude theory of Richtmyer-Meshkov instability," *Phys. Fluids*, **6**, 1856 (1994).

[113] J. Hecht, U. Alon, and D. Shvarts, "Potential flow models of Rayleigh-Taylor and Richtmyer-Meshkov bubble fronts," *Phys. Fluids*, **6**, 4019 (1994).

[114] D. Shvarts, U. Alon, D. Ofer, R. L. McCrory, and C. P. Verdon, "Nonlinear evolution of multimode Rayleigh-Taylor instability in two and three dimensions," *Phys. Plasmas*, **2**, 2465 (1995).

[115] D. Ofer, U. Alon, D. Shvarts, R. L. McCrory, and C. P. Verdon, "Modal model for the nonlinear multimode Rayleigh-Taylor instability," *Phys. Plasmas*, **3**, 3073 (1996).

[116] Q. Zhang and S.-I. Sohn, "An analytical nonlinear theory of Richtmyer-Meshkov instability," *Phys. Lett. A*, **212**, 149 (1996).

[117] Q. Zhang and S.-I. Sohn, "Nonlinear theory of unstable fluid mixing driven by shock wave," *Phys. Fluids*, **9**, 1106 (1997).

[118] V. N. Goncharov, "Analytical model of nonlinear, single-mode, classical Rayleigh-Taylor instability at arbitrary Atwood numbers," *Phys. Rev. Lett.*, **88**, 134502 (2002).

[119] K. O. Mikaelian, "Analytic approach to nonlinear Rayleigh-Taylor and Richtmyer-Meshkov instabilities," *Phys. Rev. Lett.*, **80**, 508 (1998).

[120] K. O. Mikaelian, "Explicit expressions for the evolution of single-mode Rayleigh-Taylor and Richtmyer-Meshkov instabilities at arbitrary Atwood numbers," *Phys. Rev. E*, **67**, 026319 (2003).

[121] K. O. Mikaelian, "Limitations and failures of the Layzer model for hydrodynamic instabilities," *Phys. Rev. E*, **78**, 015303 (2008).

[122] S.-I. Sohn, "Simple potential-flow model of Rayleigh-Taylor and Richtmyer-Meshkov instabilities for all density ratios," *Phys. Rev. E*, **67**, 026301 (2003).

[123] Q. Zhang and W. Guo. "Universality of finger growth in two-dimensional Rayleigh-Taylor and Richtmyer-Meshkov instabilities with all density ratios," *J. Fluid Mech.*, **786**, 47 (2016)

[124] Q. Zhang, S. Deng, and W. Guo. "Quantitative theory for the growth rate and amplitude of the compressible Richtmyer-Meshkov instability at all density ratios," *Phys. Rev. Lett.,* **121**, 174502 (2018).

[125] P. A. Lagerstrom, Matched asymptotic expansions, Springer, New York, 1988.

[126] C.M. Bender and S.A. Orszag. Advanced mathematical methods for scientists and engineers I: Asymptotic methods and perturbation theory. Springer, 2013.

[127] A. Pozzi, Applications of Padé Approximation theory in fluid dynamics, World Scientific, Singapore, 1994.

[128] P. Hunana, G. P. Zank, M. Laurenza, A. Tenerani, G. M. Webb, M. L. Goldstein, M. Velli, and L. Adhikari. "New closures for more precise modeling of Landau damping in the fluid framework," *Phys. Rev. Lett.*, **121**, 135101 (2018).

[129] S. Zetina, F.A. Godnez, and R. Zenit. "A hydrodynamic instability is used to create aesthetically appealing patterns in painting," *PloS One*, **10**, e0126135 (2015). https://doi.org/10.1371/journal.pone.0126135.

[130] E.M. de la Calleja, S. Zetina, and R. Zenit. "Rayleigh-Taylor instability creates provocative images in painting." *Phys. Fluids*, **26**, 091102 (2014).

[131] J. T. Waddell, C. E. Niederhaus, and J. W. Jacobs, "Experimental study of Rayleigh-Taylor instability: low Atwood number liquid systems with single-mode initial perturbations," *Phys. Fluids*, **13**, 1263 (2001).

[132] N. A. Inogamov, "The role of Rayleigh-Taylor and Richtmyer-Meshkiv instabilities in astrophysics: an introduction," *Astrophysics and Space Physics*, **10**, 1 (1999).

[133] D. J. Lewis, "The instability of liquid surfaces when accelerated in a direction perpendicular to their planes. II," *Proceedings of the Royal Society of London A,* **202**, 81 (1950),

[134] K. Read, "Experimental investigation of turbulent mixing by Rayleigh-Taylor instability," *Physica D,* **12**, 45 (1984).

[135] G. Dimonte and M. Schneider, "Turbulent Rayleigh-Taylor instability experiments with variable acceleration," *Phys. Rev. E,* **54**, 3740 (1996).

[136] G. Dimonte and M. Schneider, "Density ratio dependence of Rayleigh-Taylor mixing for sustained and impul-

sive acceleration histories," *Phys. Fluids*, **12**, 304 (2000).
[137] Y. A. Kucherenko, A. P. Pylaev, V. D. Murzakov, A. V. Belomestnih, V. N. Popov, and A. A. Tyaktev, "Experimental study into the Rayleigh-Taylor turbulent mixing zone heterogeneous structure," *Laser and Particle Beams*, **21**, 375 (2003).
[138] J. P. Wilkinson and J. W. Jacobs. "Experimental study of the single-mode three-dimensional Rayleigh-Taylor instability," *Phys. Fluids*, **19**, 124102 (2007).
[139] P. Ramaprabhu and M. J. Andrews, "Experimental investigation of Rayleigh-Taylor mixing at small Atwood numbers," *J. of Fluid Mechanics*, **502**, 233 (2004).
[140] A. Banerjee and M.J. Andrews, "Statistically steady measurements of Rayleigh-Taylor mixing in a gas channel," *Phys. Fluids,* **18**, 035107 (2006).
[141] A. Banerjee, W.N. Kraft, and M.J. Andrews, "Detailed measurements of a statistically steady Rayleigh-Taylor mixing layer from small to high Atwood numbers," *J. Fluid Mech.*, **659**, 127 (2010).
[142] M.J. Andrews and S.B. Dalziel. "Small Atwood number Rayleigh-Taylor experiments." *Philosophical Transactions of the Royal Society of London A*, **368**, 1663 (2010).
[143] B. Akula and D. Ranjan. "Dynamics of buoyancy-driven flows at moderately high Atwood numbers." *J. Fluid Mech.*, **795** 313 (2016).
[144] S. T. Weir, E. A. Chandler, and B. T. Goodwin, "Rayleigh-Taylor instability experiments examining feedthrough growth in an incompressible, convergent geometry," *Phys. Rev. Lett.*, **80**, 3763 (1998).
[145] E. E. Meshkov, N. V. Nevmerzhitsky, V. A. Pavlovskii, V. G. Rogatchev, and I. G. Zhidov, "Jelly technique applications in evolution study of hydrodynamic instabilities on unstable plane and cylindrical surfaces," in *Proceedings of the Fifth International Workshop on the Physics of Compressible Turbulent Mixing,* edited by R. Young, J. Glimm, and B. Boston (World Scienti
c, New Jersey, 1996) 167.
[146] D. L. Youngs, "Numerical simulation of turbulent mixing by Rayleigh-Taylor instability," *Physica D*, **12**, 32 (1984).
[147] D. L. Youngs, "Three-dimensional numerical simulation of turbulent mixing by Rayleigh-Taylor instability," *Phys. Fluids A*, **3**, 1312 (1991).
[148] A.W. Cook, W. Cabot, and P.L. Miller. "The mixing transition in Rayleigh-Taylor instability." *J. Fluid Mech.*, **511**, 333 (2004).
[149] W. Cabot and A. W. Cook, "Reynolds number effects on Rayleigh-Taylor instability with possible implications for type Ia supernovae," *Nature Physics,* **2**, 562 (2006).
[150] D. Livescu, J. R. Ristorcelli, M. R. . Petersen, and R. A. Gore, "New phenomena in variable-density Rayleigh-Taylor turbulence," *Physica Scripta*, T142, 014015 (2010).
[151] W. Cabot and Y. Zhou. "Statistical measurements of scaling and anisotropy of turbulent flows induced by Rayleigh-Taylor instability," *Phys. Fluids*, **25**, 015107 (2013).
[152] J. Glimm, J. W. Grove, X. L. Li, W. Oh, and D. H. Sharp, "A critical analysis of Rayleigh-Taylor growth rates," *J. Comput. Phys.* **169**, 652 (2001).
[153] G. Tryggvason and S. O. Unverdi, "Computations of three-dimensional Rayleigh-Taylor instability," *Phys. Fluids A*, **2**, 656 (1990),
[154] F.F. Grinstein, L.G. Margolin, and W.J. Rider, eds. Implicit large eddy simulation: computing turbulent fluid dynamics. Cambridge University Press, Cambridge, UK (2007).
[155] D Drikakis, "Advances in turbulent flow computations using high-resolution methods," *Progress in Aerospace Sciences*, **39** 405 (2003).
[156] D. Drikakis, F. Grinstein, and D. Youngs. "On the computation of instabilities and symmetry-breaking in fluid mechanics." *Progress in Aerospace Sciences*, **41**, 609 (2005).
[157] D. L. Youngs, "Application of monotone integrated large eddy simulation to Rayleigh-Taylor mixing," *Philosophical Transactions of the Royal Society of London A*, **367**, 2971 (2009).
[158] D.L. Youngs, "Rayleigh-Taylor mixing: direct numerical simulation and implicit large eddy simulation." *Physica Scripta*, **92**, 074006 (2017).
[159] M. Brouillette, "The Richtmyer-Meshkov instability," *Annual Review of Fluid Mechanics*, **34**, 445 (2002).
[160] G. Jourdan and L. Houas, "High-amplitude single-mode perturbation evolution at the Richtmyer-Meshkov instability," *Phys. Rev. Lett.*, **95**, 204502 (2005).
[161] K. O. Mikaelian, "Time evolution of density perturbations in accelerating stratified fluids," *Phys. Rev. A*, **28**, 1637 (1983).
[162] J. W. Jacobs and J. M. Sheeley, "Experimental study of incompressible Richtmyer-Meshkov instability," *Phys. Fluids*, **8**, 405 (1996).
[163] K. O. Mikaelian, "Exact, approximate, and hybrid treatments of viscous Rayleigh-Taylor and Richtmyer-Meshkov instabilities," *Phys. Rev. E*, **99**, 023112 (2019).
[164] J. K. Prasad, A. Rasheed, S. Kumar, and B. Sturtevant, "The late-time development of the Richtmyer-Meshkov instability," *Phys. Fluids*, **12**, 2108 (2000).
[165] L. Erez, O. Sadot, D. Oron, G. Erez, L.A. Levin, D. Shvarts, G. Ben-Dor, "Study of the membrane effect on turbulent mixing measurements in shock tubes, *Shock Waves*, **10**, 241 (2000)
[166] M. A. Jones and J. W. Jacobs, "A membraneless experiment for the study of Richtmyer-Meshkov instability of a shock-accelerated gas interface," *Phys. Fluids*, **9**, 3078 (1997).
[167] C.R. Weber, N.S. Haehn, J.G. Oakley, D.A. Rothamer, and R. Bonazza. "An experimental investigation of the turbulent mixing transition in the Richtmyer-Meshkov instability," *J. Fluid Mech.*, **748**, 457 (2014).
[168] R. Bonazza, A Review of the Richtmyer-Meshkov Instability from an Experimental Perspective. In: Ben-Dor G., Sadot O., Igra O. (eds) 30th International Symposium on Shock Waves 1. Springer, Cham (2017)
[169] M. Brouillette and B. Sturtevant, "Experiments on the Richtmyer-Meshkov instability: single-scale perturbations on a continuous interface," *J. Fluid Mech.*, **263**, 271 (1994).
[170] P. B. Puranik, J. G. Oakley, M. H. Anderson, and R. Bonazza, "Experimental study of the Richtmyer-Meshkov instability induced by a Mach 3 shock wave," *Shock Waves,* **13**, 413 (2004).
[171] W. T. Buttler, D. M. Oro, D. L. Preston, K. O. Mikaelian, F. J. Cherne, R. S. Hixson, F. G. Mariam, C. Morris, J. B. Stone, G. Terrones, and D. Tupa, "Unstable Richtmyer-Meshkov growth of solid and liquid metals in vacuum," *J. Fluid Mech.*, **703**, 60 (2012).

[172] M.B. Prime, W.T. Buttler, S.J. Fensin, D.R. Jones, R. Manzanares, D.T. Martinez, J.I. Martinez, D.W. Schmidt, and C.P. Trujillo, "Improved Richtmyer-Meshkov Instability Experiments for Very-High-Rate Strength and Application to Tantalum," In *Dynamic Behavior of Materials*, edited by J. Kimberley, L.E. Lamberson, and S. Mates (Springer, Cham, Switzerland 2019) Volume 1, p. 101.

[173] W.T. Buttler, R.J.R. Williams, F.M. Najjar, eds.. Ejecta physics, *Journal of Dynamic Behavior of Materials*, **3**, (2017). Available online at: https://link.springer.com/journal/40870/3/2/page/1.

[174] S.R. Nagel, K. S. Raman, C. M. Huntington, S. A. MacLaren, P. Wang, M. A. Barrios, T. Baumann, J. D. Bender, L. R. Benedetti, D. M. Doane, S. Felker, P. Fitzsimmons, K. A. Flippo, J. P. Holder, D. N. Kaczala, T. S. Perry, R. M. Seugling, L. Savage,1 and Y. Zhou, "A platform for studying the Rayleigh-Taylor and Richtmyer-Meshkov instabilities in a planar geometry at high energy density at the National Ignition Facility." *Phys. Plasmas,* **24**, 072704 (2017).

[175] K. Prestridge, "Experimental adventures in variable-density mixing," *Phys. Rev. Fluids*, **3**, 110501 (2018).

[176] ML Wong, D Livescu, SK Lele, High-resolution Navier-Stokes simulations of Richtmyer-Meshkov instability with re-shock arXiv preprint arXiv:1812.01785, 2018

[177] R.L. Holmes, G. Dimonte, B. Fryxell, M.L. Gittings, J.W. Grove, M. Schneider, D.H. Sharp, A.L. Velikovich, R.P. Weaver, and Q. Zhang. "Richtmyer-Meshkov instability growth: experiment, simulation and theory." *J. Fluid Mech.*, **389**, 55 (1999).

[178] D.J. Hill, C. Pantano, and D. I. Pullin. "Large-eddy simulation and multiscale modelling of a Richtmyer-Meshkov instability with reshock." *J. Fluid Mech.*, **557**, 29 (2006).

[179] T. Wang, J. S. Bai, P. Li, B. Wang, L. Du, and G. Tao. "Large-eddy simulations of the multi-mode Richtmyer-Meshkov instability and turbulent mixing under reshock." *High Energy Density Physics*, **19** 65 (2016).

[180] R.H. Cohen, W.P. Dannevik, A.M. Dimits, D.E. Eliason, A.A. Mirin, Y. Zhou, D.H. Porter, and P.R. Woodward. "Three-dimensional simulation of a Richtmyer-Meshkov instability with a two-scale initial perturbation," *Phys. Fluids*, **14**, 3692 (2002).

[181] B. Thornber, D. Drikakis, D. L. Youngs, and R. J. R. Williams. "The influence of initial conditions on turbulent mixing due to Richtmyer-Meshkov instability," *J. Fluid Mech.*, **654**, 99 (2010).

[182] F.F. Grinstein, A. A. Gowardhan, J. R. Ristorcelli, and A. J. Wachtor. "On coarse-grained simulations of turbulent material mixing." *Physica Scripta*, **86**, 058203 (2012).

[183] A.A. Gowardhan, J. R. Ristorcelli, and F.F. Grinstein. "The bipolar behavior of the Richtmyer-Meshkov instability," *Phys. Fluids*, **23**, 071701 (2011).

[184] M. Lombardini, D. I. Pullin, and D. I. Meiron. "Turbulent mixing driven by spherical implosions. Part 1. Flow description and mixing-layer growth," *J. Fluid Mech.*, **748**, 85 (2014).

[185] M. Lombardini, D. I. Pullin, and D. I. Meiron. "Turbulent mixing driven by spherical implosions. Part 2. Turbulence statistics." *J. Fluid Mech.,* **748** 113 (2014).

[186] C.C. Joggerst, A. Nelson, P. Woodward, C. Lovekin, T. Masser, C.L. Fryer, P. Ramaprabhu, M. Francois, and G. Rockefeller. "Cross-code comparisons of mixing during the implosion of dense cylindrical and spherical shells," *J. of Computational Physics*, **275**, 154 (2014).

[187] A. López Ortega, M. Lombardini, P. T. Barton, D. I. Pullin, and D. I. Meiron. "Richtmyer-Meshkov instability for elastic-plastic solids in converging geometries," *J. of the Mechanics and Physics of Solids*, **76** 291 (2015).

[188] Z. Wu, S. Huang, J. Ding, W. Wang and X. Luo, "Molecular dynamics simulation of cylindrical Richtmyer-Meshkov instability," *SCIENCE CHINA Physics, Mechanics & Astronomy*, 61, 114712 (2018).

[189] M. Vetter and B. Sturtevant. "Experiments on the Richtmyer-Meshkov instability of an air/SF 6 interface." *Shock Waves*, **4**, 247 (1995).

[190] E. Leinov, G. Malamud, Y. Elbaz, L.A., Levin, G. Ben-Dor, D. Shvarts, and O. Sadot, "Experimental and numerical investigation of the Richtmyer-Meshkov instability under re-shock conditions," *J. Fluid Mech.*, **626**, 449 (2009)

[191] J.W. Jacobs, V.V. Krivets, and V. Tsiklashvili, "Experiments on the Richtmyer-Meshkov instability with an imposed, random initial perturbation," *Shock Waves*, **23**, 407 (2013)

[192] K.O. Mikaelian, "Testing an analytic model for Richtmyer-Meshkov turbulent mixing widths," *Shock Waves*, **25**, 35 (2015).

[193] B. Thornber, D. Drikakis, D. L. Youngs, and R. J. R. Williams. "Growth of a Richtmyer-Meshkov turbulent layer after reshock," *Phys. Fluids*, **23**, 095107 (2011).

[194] V. K. Tritschler, B. J. Olson, S. K. Lele, S. Hickel, X. Y. Hu, and N.A. Adams. "On the Richtmyer-Meshkov instability evolving from a deterministic multimode planar interface," *J. Fluid Mech.*, **755**, 429 (2014)

[195] V. K. Tritschler, M. Zubel, S. Hickel, and N. A. Adams. "Evolution of length scales and statistics of Richtmyer-Meshkov instability from direct numerical simulations," *Phys. Rev. E*, **90**, 063001 (2014).

[196] O. Schilling and M. Latini. "High-order WENO simulations of three-dimensional reshocked Richtmyer-Meshkov instability to late times: dynamics, dependence on initial conditions, and comparisons to experimental data." *Acta Mathematica Scientia,* **30**, 595 (2010).

[197] C.D. Tomkins, B. J. Balakumar, G. Orlicz, K. P. Prestridge, and J. R. Ristorcelli. "Evolution of the density self-correlation in developing Richtmyer-Meshkov turbulence." *J. Fluid Mech.*, **735**, 288 (2013).

[198] T.T. Clark and Y. Zhou, "Self-similarity of two flows induced by instabilities," *Phys. Rev. E*, **68**, 066305 (2003).

[199] R.W. Metcalfe, S.A. Orszag, M.E. Brachet, S. Menon, and J.J. Riley. "Secondary instability of a temporally growing mixing layer," *J. Fluid Mech.*, **184**, 207 (1987).

[200] C.D. Winant and F.K. Browand. "Vortex pairing: the mechanism of turbulent mixing-layer growth at moderate Reynolds number." *J. Fluid Mech.*, **63**, 237 (1974).

[201] G.L. Brown and A. Roshko. "On density effects and large structure in turbulent mixing layers." *J. Fluid Mech.*, **64**, 775 (1974).

[202] K.O. Mikaelian, "Oblique shocks and the combined RayleighTaylor, KelvinHelmholtz, and RichtmyerMeshkov instabilities," *Phys. Fluids*, **6**, 1943 (1994).

[203] H. W. Liepmann and J. Laufer, Investigation of free turbulent mixing, Tech. Note 1257 (National Advisory Committee for Aeronautics, 1947).

[204] J. C. Lasheras, J. S. Cho, and T. Maxworthy. "On the

origin and evolution of streamwise vortical structures in a plane, free shear layer." *J. Fluid Mech.,* **172**, 231 (1986).

[205] L. P. Bernal and A. Roshko. "Streamwise vortex structure in plane mixing layers." *J. Fluid Mech.*, **170**, 499 (1986).

[206] J. H. Bell and R. D. Mehta, "Measurements of the streamwise vortical structures in a plane mixing layer," *J. Fluid Mech.*, **239**, 213 (1992).

[207] D. M. Snider and M. J. Andrews, "Rayleigh-Taylor and shear driven mixing with an unstable thermal stratification," *Phys. Fluids*, **6**, 3324 (1994).

[208] D.G. Schowalter, C.W. Van Van Atta, and J.C. Lasheras. "A study of streamwise vortex structure in a stratified shear layer." *J. Fluid Mech.*, **281**, 247 (1994).

[209] D. Papamoschou and A. Roshko, "The compressible turbulent shear layer: an experimental study," *J. Fluid Mech.*, **197**, 453 (1988).

[210] O. San and R. Maulik, "Stratified Kelvin-Helmholtz turbulence of compressible shear flows," *Nonlinear Processes in Geophysics*, **25**, 457 (2018).

[211] S. M. Rahman and O. San, "A localised dynamic closure model for Euler turbulence," *International J. of Computational Fluid Dynamics*, **32**, 326 (2019) DOI: 10.1080/10618562.2018.1533121

[212] Y.-B. Gan, A.-G. Xu, G.-C. Zhang, C.-D. Lin, H.-L. Lai, Z.-P. Liu, "Nonequilibrium and morphological characterizations of Kelvin-Helmholtz instability in compressible flows," *Front. Phys.*, **14**, 43602 (2019)

[213] C.D. Lin, K.H. Luo, Y.B. Gan, and Z.P. Liu, "Kinetic simulation of nonequilibrium Kelvin-Helmholtz instability," *Commun. Theor. Phys.*, **71**, 132 (2019).

[214] R.N. Silver, R. Gore, J. Greene, F. Harlow, and R. Whitman. "Radiographic Evidence for $k^{-5/3}$ Scaling of Density Power Spectra," *Phys. Rev. Letters*, **77**, 2471 (1996).

[215] G. Dimonte, "Dependence of turbulent Rayleigh-Taylor instability on initial perturbations." *Phys. Re. E*, **69**, 056305 (2004)

[216] K.O. Mikaelian, "Solution to Rayleigh-Taylor instabilities: Bubbles, spikes, and their scalings." *Phys. Rev. E*, **89**, 053009 (2014).

[217] N.K. Ibragimov, Elementary Lie group analysis and ordinary differential equations. New York: Wiley, 1999.

[218] P. J. Olver, Applications of Lie Groups to Differential Equations, Springer, Berlin, 1986.

[219] D. H. Sharp and J. A. Wheeler, Late Stage of Rayleigh-Taylor Instability, Tech. Rep. ADA009943 (Institute for Defense Analyses, Jason Division, Alexandria, Virginia, 1961).

[220] J. R. Ristorcelli and T. T. Clark. "Rayleigh-Taylor turbulence: self-similar analysis and direct numerical simulations." *J. Fluid Mech.*, **507** 213 (2004).

[221] J. W. Jacobs and S. B. Dalziel. "Rayleigh-Taylor instability in complex stratifications." *J. Fluid Mech.*, **542**, 251 (2005).

[222] D. H. Olson and J. W. Jacobs. "Experimental study of Rayleigh-Taylor instability with a complex initial perturbation." *Phys. Fluids*, **21**, 034103 (2009).

[223] G. Dimonte, D. L. Youngs, A. Dimits, S. Weber, M. Marinak, S. Wunsch, C. Garasi, A Robinson, MJ Andrews, P Ramaprabhu, AC Calder, B Fryxell, J Biello, L Dursi, P MacNeice, K Olson, P Ricker, R Rosner, F Timmes, H Tufo, Y-N Young, M Zingale, "A comparative study of the turbulent Rayleigh-Taylor instability using high-resolution three-dimensional numerical simulations: the Alpha-Group collaboration." *Phys. Fluids*, **16**, 1668 (2004).

[224] T.T. Clark and Y. Zhou. "Growth rate exponents of Richtmyer-Meshkov mixing layers." *ASME J. Appl. Mech.*, **73**, 461 (2006).

[225] B. Thornber, J. Griffond, O. Poujade, N. Attal, H. Varshochi, P. Bigdelou, P. Ramaprabhu, B. Olson, J. Greenough, Y. Zhou, O. Schilling, K. A. Garside, R. J. R. Williams, C. A. Batha, P. A. Kuchugov, M. E. Ladonkina, V. F. Tishkin, N. V. Zmitrenko, V. B. Rozanov, and D. L. Youngs, "Late-time growth rate, mixing, and anisotropy in the multimode narrowband Richtmyer-Meshkov instability: The θ-group collaboration." *Phys. Fluids*, **29**, 105107 (2017).

[226] Y. Elbaz and D. Shvarts. "Modal model mean field self-similar solutions to the asymptotic evolution of Rayleigh-Taylor and Richtmyer-Meshkov instabilities and its dependence on the initial conditions." *Phys. Plasmas*, **25**, 062126 (2018).

[227] S.A. Orszag, "Analytical theories of turbulence." *J. Fluid Mech.*, **41**, 363 (1970).

[228] M. Lesieur, Turbulence in fluids: stochastic and numerical modelling. Boston, MA: Nijhoff, 1987.

[229] P. Sagaut and C. Cambon. Homogeneous turbulence dynamics, Cambridge University Press, Cambridge, UK, 2008.

[230] Y. Zhou, "Renormalization group theory for fluid and plasma turbulence." *Phys. Rep.*, **488**, 1 (2010).

[231] O. Soulard, F. Guillois, J. Griffond, V. Sabelnikov, and S. Simoëns. "Permanence of large eddies in Richtmyer-Meshkov turbulence with a small Atwood number." *Phys. Rev. Fluids*, **3**, 104603 (2018).

[232] E. Villermaux, H. Rehab, and E. J. Hopfinger. "Shear instabilities in the near field of coaxial jets." *Phys. Fluids*, **10**, S2 (1998).

[233] B. Thornber, "Impact of domain size and statistical errors in simulations of homogeneous decaying turbulence and the Richtmyer-Meshkov instability." *Phys. Fluids*, **28**, 045106 (2016).

[234] Y. Zhou and W.H. Cabot, Time-dependent study of anisotropy in Rayleigh-Taylor instability induced turbulent fows with a variety of density ratios, The 16th International Workshop on the Physics of Compressible Turbulent Mixing (15-20 July 2018 at Marseille, France)

[235] Y. Zhou, W.H. Cabot, and B. Thornber, "Asymptotic behavior of the mixed mass in Rayleigh-Taylor and Richtmyer-Meshkov instability induced flows," *Phys. Plasmas*, **23**, 052712 (2016).

[236] T. Ma, P. K. Patel, N. Izumi, P. T. springer, M. H. Key, L. J. Atherton, L. R. Benedetti, D. K. Bradley, D. A. Callahan, P. M. Celliers, C. J. Cerjan, D. S. Clark, E. L. Dewald, S. N. Dixit, T. Dppner, D. H. Edgell, R. Epstein, s. Glenn, G. Grim, S. W. Haan, B. A. Hammel, D. Hicks, W. W. Hsing, O. S. Jones, S. F. Khan, J. D. Kilkenny, J. L. Kline, G. A. Kyrala, O. L. Landen, S. Le Pape, B. J. MacGowna, A. J. Mackinnon, A. G. MacPhee, N. B. Meezan, J. D. Moody, A. Pak, T. Parham, H.-S. Park, J. E. Ralph, s. P. Regan, B. A. Remington, H. F. Robey, J. S. Ross, B. K. Spears, V. Smalyuk, L. J. Suter, R. Tommasini, R. P. Town, S. V. Weber, J. D. Lindl, M. J. Edwards, S. H. Glenzer, and E. I. Moses, "Onset of hydrodynamic mix in high-velocity, highly compressed

inertial confinement fusion implosions," *Phys. Rev. Lett.*, **111**, 085004 (2013).

[237] S. P. Regan, R. Epstein, B. A. Hammel, L. J. Suter, H. A. Scott, M. A. Barrios, D. K. Bradley, D. A. Callahan, C. Cerjan, G. W. Collins, S. N. Dixit, T. Dppner, M. J. Edwards, D. R. Farely, K. B. Fournier, S. Glenn, S. H. Glenzer, I. E. Golovkin, S. W. Haan, A. Hamza, D. G. Hicks, N. Izumi, O. S. Jones, J. D. Kilkenny, J. L, Kline, G. A. Kyrala, O. L. Landen, T. Ma, J. J. MacFarlane, A. J. MacKinnon, R. C. Mancini, R. L. McCrory, N. B. Meezan, D. D. Meyerhofer, A. Nikroo, H.-S. Park, J. Ralph, B. A. Remington, T. C. Sangster, V. A. Smalyuk, R. T. Springer, and R. P. J. Town, "Hot-spot mix in ignition-scale inertial confinement fusion targets," *Phys. Rev. Lett.*, **111**, 045001 (2013).

[238] V. A. Smalyuk, R. E. Tipton, J. E. Pino, D. T. Casey, G. P. Grim, B. A. Remington, D. P. Rowley, S. V. Weber, M. Barrios, L. R. Benedetti, D. L. Bleuel, D. K. Bradley, J. A. Caggiano, D. A. Callahan, C. J. Cerjan, D. S. Clark, D. H. Edgell, M. J. Edwards, J. A. Frenje, M. Gatu-Johnson, V. Y. Glebov, S. Glenn, S.W. Haan, A. Hamza, R. Hatarik, W.W. Hsing, N. Izumi, S. Khan, J. D. Kilkenny, J. Kline, J. Knauer, O. L. Landen, T. Ma, J. M. McNaney, M. Mintz, A. Moore, A. Nikroo, A. Pak, T. Parham, R. Petrasso, D. B. Sayre, M. B. Schneider, R. Tommasini, R. P. Town, K. Widmann, D. C. Wilson, and C. B. Yeamans, "Measurements of an ablator-gas atomic mix in indirectly driven implosions at the National Ignition Facility." *Phys. Rev. Lett.*, **112**, 025002 (2014).

[239] J. S. Ross, H.-S. Park, R. Berger, L. Divol, N. L. Kugland, W. Rozmus, D. Ryutov, and S. H. Glenzer, "Collisionless Coupling of Ion and Electron Temperatures in Counterstreaming Plasma Flows," *Phys. Rev. Letters*, **110**, 145005 (2013)

[240] U. Kolberg and R. Schlickeiser, "Kinetic theory of small-amplitude fluctuations in astrophysical plasmas." *Physics Reports*, **783-785**, 1 (2018).

[241] C. M. Huntington, F. Fiuza, J. S. Ross, A. B. Zylstra, R. P. Drake, D. H. Froula, G. Gregori,?N. L. Kugland, C. C. Kuranz, M. C. Levy, C. K. Li, J. Meinecke, T. Morita, R. Petrasso, C. Plechaty, B. A. Remington, D. D. Ryutov, Y. Sakawa, A. Spitkovsky, H. Takabe and H.-S. Park, "Observation of magnetic field generation via the Weibel instability in interpenetrating plasma flows," *Nature Physics*, **11**, 173 (2015).

[242] W. L. Kruer, The Physics of Laser Plasma Interactions, Addison-Wesley, 1988.

[243] R. L. Berger, C. H. Still, E. A. Williams, and A. B. Langdon, "On the dominant and subdominant behavior of stimulated Raman and Brillouin scattering driven by nonuniform laser beams," *Phys. Plasmas*, **5**, 4337 (1998).

[244] R. M. G. M. Trines, F. Fiza, R. Bingham, R. A. Fonseca, O. Silva, R. A. Cairns and P. A. Norreys, "Simulations of efficient Raman amplification into the multipetawatt regime," *Nature Physics*, **7**, 87 (2011).

[245] G. Bateman, MHD instabilities. Cambridge, Mass., MIT Press, 1978.

[246] J.P. Freidberg, 1987. Ideal magnetohydrodynamics. Plenum Press; New York, NY

[247] J. Wesson and D.J. Campbell. Tokamaks, Oxford University Press, 2004.

[248] Y. Zhou, W. H. Matthaeus, and P. Dmitruk. "Colloquium: Magnetohydrodynamic turbulence and time scales in astrophysical and space plasmas," *Reviews of Modern Physics*, **76**, 1015 (2004).

[249] H. P. Furth, J. Killeen and M.N. Rosenbluth, "Finite-resistivity Instabilities of a Sheet Pinch," *The Phys. Fluids*, **6**, 459 (1963)

[250] W. Horton, D.-I. Choi, and W. M. Tang, "Toroidal drift modes driven by ion pressure gradients," *Phys. Fluids*, **24**, 1077 (1981)

[251] W. Horton and B. G. Hong, "Toroidal electron temperature gradient driven drift modes ," *Phys. Fluids*, **31**, 2971 (1988)

[252] L.I. Rudakov, R.Z. Sagdeev, "On the instability of a nonuniform rarefied plasma in a strong magnetic field," *Dokl. Akad. Nauk. SSSR*, **138**, 581 (1961) [Sov. Phys. Dokl. 6, 415 (1961)]

[253] A. M. Dimits J. F. Drake, A. B. Hassam, and B. Meerson, "Formation of streamers in plasma with an ion temperature gradient," *Phys. Fluids B,* **2**, 2591 (1990).

[254] B. B. Kadomtsev, Plasma turbulence, Academic Press, New York, 1965, p. 88.

[255] O. P. Pogutse, "Magnetic drift instability in a collisionless plasma," *Plasma Physics* **10**, 649 (1968).

[256] W.M. Tang, "Microinstability theory in tokamaks," *Nucl. Fusion*, **18**, 1089 (1978).

[257] L. E. Zakharov, "Helical equilibria and kink instabilities of a current-carrying plasma," *Sov. J. Plasma Phys.* **7**, 8 (1981).

[258] E. J. Strait, L. L. Lao, J. L. Luxon, and E. E. Reis, "Observation of poloidal current flow to the vacuum vessel wall during vertical instabilities in the DIII-D tokamak," *Nucl. Fusion*, **31**, 527 (1991).

[259] S. V. Mirnov and I. B. Semenov, "Investigation of the instabilities of the plasma string in the Tokamak-3 system by means of a correlation method," *Sov. Atom. Energy*, **30**, 22 (1971).

[260] S. von Goeler, W. Stodiek, and N. Sauthoff, "Studies of internal disruptions and m= 1 oscillations in tokamak discharges with soft-x-ray techniques," *Phys. Rev, Lett.*, **33**, 1201 (1974).

[261] K. McGuire, R. Goldston, M. Bell, M. Bitter, K. Bol, K. Brau, D. Buchenauer, T. Crowley, S. Davis, F. Dylla, H. Eubank, H. Fishman, R. Fonck, B. Grek, R. Grimm, R. Hawryluk, H. Hsuan, R. Hulse, R. Izzo, R. Kaita, S. Kaye, H. Kugel, D. Johnson, J. Manickam, D. Manos, D. Mansfield, E. Mazzucato, R. McCann, D. McCune, D. Monticello, R. Motley, D. Mueller, K. Oasa, "' M. Okabayashi, K. Owens, Park, M. Reusch, N. Sauthoff, G. Schmidt, S. Sesnic, J. Strachan, C. Surko, R. Slusher, H. Takahashi, F. Tenney, P. Thomas, H. Towner, J. Valley, and R. White, "Study of high-beta magnetohydrodynamic modes and fast-ion losses in PDX," *Phys. Rev. Lett.*, **50**, 891(1983).

[262] F. Wagner, G. Becker, K. Behringer, D. Campbell, A. Eberhagen, W. Engelhardt, G. Fussmaann, O. Gehre, J. Gernhardt, G. v. Gierke, G. Haas, M. Huang, F. Karger, M. Keilhacker, O. Klber, M. Kornherr, K. Lackner, G. Lisitano, G. G. Lister, H. M. Mayer, D. Meisel, E. R. Müller, H. Murmann, H. Niedermeyer, W. Poschenrieder, H. Rapp, H. Röhr, F. Schneider, G. Siller, E. Speth, A. Stäbler, K. H. Steuer, G. Venus, O. Vollmer, and Z. Yü, "Regime of improved confinement and high beta in neutral-beam-heated divertor discharges of the ASDEX tokamak," *Phys. Rev. Lett.* **49**, 1408 (1982)

[263] B. Lipschultz, B. LaBombard, E.S. Marmar, M.M. Pick-

rell, J.L. Terry, R. Watterson and S.M. Wolfe, "Marfe: an edge plasma phenomenon," *Nuclear Fusion*, **24**, 977 (1984).

[264] C. Holland, L. Schmitz, T. L. Rhodes, W. A. Peebles, J. C. Hillesheim, G. Wang, L. Zeng, E. J. Doyle, S. P. Smith, R. Prater, K. H. Burrell, J. Candy, R. E. Waltz, J. E. Kinsey, G. M. Staebler, J. C. DeBoo, C. C. Petty, G. R. McKee, Z. Yan, and A. E. White, "Advances in validating gyrokinetic turbulence models against L- and H-mode plasmas," *Phys. Plasmas*, **18**, 056113 (2011)

[265] B. N. Rogers, W. Dorland, and M. Kotschenreuther, "Generation and Stability of Zonal Flows in Ion-Temperature-Gradient Mode Turbulence," *Phys. Rev. Lett.*, **85**, 5336 (2000)

[266] A. M. Dimits, G. Bateman, M. A. Beer, B. I. Cohen, W. Dorland, G. W. Hammett, C. Kim, J. E. Kinsey, M. Kotschenreuther, A. H. Kritz, L. L. Lao, J. Mandrekas, W. M. Nevins, S. E. Parker, A. J. Redd, D. E. Shumaker, R. Sydora, and J. Weiland, "Comparisons and physics basis of tokamak transport models and turbulence simulations," *Phys. Plasmas*, **7**, 969 (2000)

[267] D. R. Ernst, J. Lang, W. M. Nevins, M. Hoffman, Y. Chen, W. Dorland, and S. Parker, "Role of zonal flows in trapped electron mode turbulence through nonlinear gyrokinetic particle and continuum simulation," *Phys. Plasmas*, **16**, 055906 (2009)

[268] D. R. Ernst, , K. H. Burrell, W. Guttenfelder, T. L. Rhodes, A. M. Dimits, R. Bravenec, B. A. Grierson, C. Holland, J. Lohr, A. Marinoni, G. R. McKee, C. C. Petty, J. C. Rost, L. Schmitz, G. Wang, S. Zemedkun, L. Zeng, and the DIII-D Team, "Role of density gradient driven trapped electron mode turbulence in the H-mode inner core with electron heating," *Phys. Plasmas*, **23**, 056112 (2016)

[269] D. R. Hatch, P. W. Terry, W. M. Nevins, and W. Dorland, "Role of stable eigenmodes in gyrokinetic models of ion temperature gradient turbulence," *Phys. Plasmas*, **16**, 022311 (2009)

[270] D. R. Hatch, M. J. Pueschel, F. Jenko, W. M. Nevins, P. W. Terry, and H. Doerk, "Magnetic stochasticity and transport due to nonlinearly excited subdominant microtearing modes," *Phys. Plasmas*, **20**, 012307 (2013)

[271] G. Seropian, A. C. Rust, and R. S. J. Sparks. "The gravitational stability of lenses in magma mushes: confined Rayleigh-Taylor instabilities." *J. of Geophysical Research: Solid Earth,* **123**, 3593 (2018).

[272] E. P. Velikhov, "Stability of an ideally conducting liquid flowing between cylinders rotating in a magnetic field", *J. Exptl. Theoret. Phys.*, **36**, 1398 (1959).

[273] S. Chandrasekhar, "The stability of non-dissipative Couette flow in hydromagnetics", *Proc. Natl. Acad. Sci.*, *46*, 253 (1960).

[274] G. Collinson, W.R. Paterson, C. Bard, J. Dorelli, A. Glocer, M. Sarantos, and R. Wilson, "New results from Galileo's first flyby of Ganymede: reconnection-driven flows at the low-latitude magnetopause boundary, crossing the cusp, and icy ionospheric escape," *Geophysical Research Letters*, **45**, 3382 (2018)

[275] H. Karimabadi, V. Roytershteyn, H. X. Vu, Y. A. Omelchenko, J. Scudder, W. Daughton, A. Dimmock, K. Nykyri, M. Wan, D. Sibeck, M. Tatineni, A. Majumdar, B. Loring, and B. Geveci, "The link between shocks, turbulence, and magnetic reconnection in collisionless plasmas," Phys. Plasmas, **21**, 062308 (2014)

[276] D.H. Mackay, J.T. Karpen, J.L. Ballester, B. Schmieder, G. Aulanier, "Physics of solar prominences: II-magnetic structure and dynamics," *Space Sci. Rev.*, **151**, 333 (2010).

[277] J. Nuckolls, L. Wood, A. Thiessen, G. Zimmerman, "Laser compression of matter to super-high densities: Thermonuclear (CTR) applications," *Nature*, **239**, 139 (1972).

[278] E. I. Moses, R. N. Boyd, B. A. Remington, C. J. Keane, and R. Al-Ayat, "The National Ignition Facility: Ushering in a new age for high energy density science," *Phys. Plasmas*, **16**, 041006 (2009).

[279] R. S. Craxton, K. S. Anderson, T. R. Boehly, V. N. Goncharov, D. R. Harding, J. P. Knauer, R. L. McCrory, P. W. McKenty, D. D. Meyerhofer, J. F. Myatt, A. J. Schmitt, J. D. Sethian, R. W. Short, S. Skupsky, W. Theobald, W. L. Kruer, K. Tanaka, R. Betti, T. J. B. Collins, J. A. Delettrez, S. X. Hu, J. A. Marozas, A. V. Maximov, D. T. Michel, P. B. Radha, S. P. Regan, T. C. Sangster, W. Seka, A. A. Solodov, J. M. Soures, C. Stoeckl, and J. D. Zuegel, "Direct-drive inertial confinement fusion: A review." *Phys. Plasmas*, **22**, 110501 (2015).

[280] M. D. Rosen, "The physics issues that determine inertial confinement fusion target gain and driver requirements: A tutorial," *Phys. Plasmas*, **6**, 1690 (1999).

[281] O. L. Landen, K. L. Baker, D. S. Clark, V. N. Goncharov, B. A. Hammel, D. D. Ho, O. A. Hurricane, J. D. Lindl, E. N. Loomis, L. Masse, C. Mauche, J. L. Milovich, J. L. Peterson, V. A. Smalyuk, S. A. Yi, A. L. Velikovich, and C. Weber, "Indirect-drive ablative Richtmyer Meshkov node scaling," *J. Phys. Conf.*, **717**, 012034 (2016).

[282] S. E. Bodner, "Rayleigh-Taylor instability and laser-pellet fusion." *Phys. Rev. Lett.*, **33**, 761 (1974).

[283] H. Takabe, K. Mima, L. Montierth, and R. L. Morse,"Self-consistent growth rate of the Rayleigh-Taylor instability in an ablatively accelerating plasma," *Phys. Fluids*, **28**, 3676 (1985).

[284] J. D. Kilkenny, S. G. Glendinning, S. W. Haan, B. A. Hammel, J. D. Lindl, D. Munro, B. A. Remington, S. V. Weber, J. P. Knauer, and C. P. Verdon. "A review of the ablative stabilization of the Rayleigh-Taylor instability in regimes relevant to inertial confinement fusion." *Phys. Plasmas*, **1**, 1379 (1994).

[285] B. A. Hammel, S. W. Haan, D. S. Clark, M. J. Edwards, S. H. Langer, M. M. Marinak, M. V. Patel, J. D. Salmonson, and H. A. Scott, "High-mode Rayleigh-Taylor growth in NIF ignition capsules," *High Energy Density Phys.*, **6**, 171 (2010).

[286] D. S. Clark, S. W. Haan, A. W. Cook, M. J. Edwards, B. A. Hammel, J. M. Koning, and M. Marinak, "Short-wavelength and three-dimensional instability evolution in National Ignition Facility ignition capsule designs," *Phys. Plasmas*, **18**, 082701 (2011).

[287] M.M. Marinak, G. D. Kerbel, N. A. Gentile, O. Jones, D. Munro, S. Pollaine, T. R. Dittrich, and S. W. Haan. "Three-dimensional HYDRA simulations of National Ignition Facility targets." *Phys. Plasmas*, **8**, 2275 (2001).

[288] M. Gittings, R. Weaver, M. Clover, T. Betlach, N. Byrne, R. Coker, E. Dendy, R. Hueckstaedt, K. New, W. R. Oaks, D. Ranta, and R. Stefan, "The RAGE radiation-hydrodynamic code." *Computational Science & Discovery*, **1**, 015005 (2008).

[289] I.V. Igumenshchev, V. N. Goncharov, F. J. Marshall, J. P. Knauer, E. M. Campbell, C. J. Forrest, D. H. Froula, V. Yu. Glebov, R. L. McCrory, S. P. Regan, T. C. Sangster, S. Skupsky, and C. Stoeckl, "Three-dimensional modeling of direct-drive cryogenic implosions on OMEGA." *Phys. Plasmas*, **23**, 052702 (2016).

[290] D. S. Clark, D. E. Hinkel, D. C. Eder, O. S. Jones, S. W. Haan, B. A. Hammel, M. M. Marinak, J. L. Milovich, H. F. Robey, L. J. Suter, and R. P. J. Town, "Detailed implosion modeling of deuterium-tritium layered experiments on the National Ignition Facility," *Phys. Plasmas*, **20**, 056318 (2013).

[291] D. S. Clark, M. M. Marinak, C. R. Weber, D. C. Eder, S. W. Haan, B. A. Hammel, D. E. Hinkel, O. S. Jones, J. L. Milovich, P. K. Patel, H. F. Robey, J. D. Salmonson, S. M. Sepke, and C. A. Thomas, "Radiation hydrodynamics modeling of the highest compression inertial confinement fusion ignition experiment from the National Ignition Campaign," *Phys. Plasmas*, **22**, 022703 (2015).

[292] D. S. Clark, C. R. Weber, J. L. Milovich, J. D. Salmonson, A. L. Kritcher, S. W. Haan, B. A. Hammel, D. E. Hinkel, O. A. Hurricane, O. S. Jones, M. M. Marinak, P. K. Patel, H. F. Robey, S. M. Sepke, and M. J. Edwards, "Three-dimensional simulations of low foot and high foot implosion experiments on the National Ignition Facility," *Phys. Plasmas*, **23**, 056302 (2016).

[293] D. S. Clark, A. L. Kritcher, J. L. Milovich, J. D. Salmonson, C. R. Weber, S. W. Haan, B. A. Hammel, D. E. Hinkel, M. M. Marinak, M. V. Patel, and S. M. Sepke, "Capsule modeling of high foot implosion experiments on the National Ignition Facility," *Plasma Phys. And Control. Fusion*, **59**, 055006 (2017).

[294] H. J. Kull and S. I. Anisimov, "Ablative stabilization in the incompressible Rayleigh-Taylor instability," *Phys. Fluids*, **29**, 2067 (1986).

[295] J. Sanz, "Self-consistent analytical model of the Rayleigh-Taylor instability in inertial confinement fusion." *Phys. Rev. Lett.*, **73**, 2700 (1994).

[296] R. Betti, V. N. Goncharov, R. L. McCrory, and C. P. Verdon, "Self-consistent cutoff wave number of the ablative Rayleigh-Taylor instability," *Phys. Plasmas*, **2**, 3844 (1995).

[297] V. N. Goncharov, R. Betti, R. L. McCrory, P. Sorotokin, and C. P. Verdon, "Self-consistent stability analysis of ablation fronts with large Froude numbers," *Phys. Plasmas*, **3**, 1402 (1996).

[298] V. N. Goncharov, R. Betti, R. L. McCrory, and C. P. Verdon, "Self-consistent stability analysis of ablation fronts with small Froude numbers," *Phys. Plasmas*, **3**, 4665 (1996).

[299] K. S. Budil, B. A. Remington, T. A. Peyser, K. O. Mikaelian, P. L. Miller, N. C. Woolsey, W. M. Wood-Vasey, and A. M. Rubenchik. "Experimental comparison of classical versus ablative Rayleigh-Taylor instability." *Phys. Rev. Lett.*, **76**, 4536 (1996).

[300] S. G. Glendinning, S. N. Dixit, B. A. Hammel, D. H. Kalantar, M. H. Key, J. D. Kilkenny, J. P. Knauer, D. M. Pennington, B. A. Remington, R. J. Wallace, and S. V. Weber, "Measurement of a dispersion curve for linear-regime Rayleigh-Taylor growth rates in laser-driven planar targets," *Phys. Rev. Lett.,* **78**, 3318 (1997).

[301] S. G. Glendinning, S. G., J. Colvin, S. Haan, D. H. Kalantar, O. L. Landen, M. M. Marinak, B. A. Remington, R. Wallace, C. Cherfils, N. Dague, L. Divol, D. Galmiche, and A. L. Richard, "Ablation front Rayleigh-Taylor growth experiments in spherically convergent geometry." *Phys. Plasmas,* **7**, 2033 (2000).

[302] K. S. Budil, B. Lasinski, M. J. Edwards, A. S. Wan, B. A. Remington, S. V. Weber, S. G. Glendinning, L. Suter, and P. E. Stry. "The ablation-front Rayleigh-Taylor dispersion curve in indirect drive." *Phys. Plasmas*, **8**, 2344 (2001).

[303] M. J. Edwards, P. K. Patel, J. D. Lindl, L. J. Atherton, S. H. Glenzer, S. W. Haan, J. D. Kilkenny, O. L. Landen, E. I. Moses, A. Nikroo, R. Petrasso, T. C. Sangster, P. T. Springer, S. Batha, R. Benedetti, L. Bernstein, R. Betti, D. L. Bleuel, T. R. Boehly, D. K. Bradley, J. A. Caggiano, D. A. Callahan, P. M. Celliers, C. J. Cerjan, K. C. Chen, D. S. Clark, G. W. Collins, E. L. dewald, L. Divol, S. Dixit, T. Deoppner, D. H. Edgell, J. E. Rai, M. Farrell, R. J. Fortner, J. Frenje, M. B. Gatu Johnson, E. Giraldez, V. Yu. Glebov, G. Grim, B. A. Hammel, A. V. Hamza, D. R. Harding, S. P. Hatchett, N. Hein, H. W. Herrmann, D. Hicks, D. E. Hinkel, M. Hoppe, W. W. Hsing, N. Izumi, B. Jacoby, O. S. Jones, D. Kalantar, R. Kauffman, J. L. Kline, J. P. Knauer, J. A. Koch, B. J. Kozioziemski, G. Kyrala, K. N. LaFortune, S. Le Pape, R. J. Leeper, R. Lerche, T. Ma, B. J. MacGaowan, A. J. MacKinnon, A. Macphee, E. R. Mapoles, M. M. Marinak, M. Mauldin, P. W. McKenty, M. Meezan, P. A. Michel, J. Milovich, J. D. Moody, M. Moran, D. H. Munro, C. L. Olson, K. Opachich, A. E. Pak, T. Parham, H.-S. Park, J. E. Ralph, S. P. Regan, B. Remington, H. Rinderknecht, H. F. Robey, M. Rosen, S. Ross, J. D. Salmonson, J. Sater, D. H. Schneider, F. H. Sguin, S. M. Sepke, D. A. Shaughnessy, V. A. Smalyuk, B. K. Spears, C. Stoeckl, W. Stoeffl, L. Suter, C. A. Thomas, R. Tommasini, R. P. Town, S. V. Weber, P. J. Webner, K. Widman, M. Wilke, D. C. Wilson, C. B. Yeamans, and A. Zylstra, "Progress towards ignition on the National Ignition Facility," *Phys. Plasmas*, **20**, 070501 (2013).

[304] S.H. Glenzer, D.A. Callahan, A.J. Mackinnon, J.L. Kline, G. Grim, E.T. Alger, R.L. Berger, L.A. Bernstein, R. Betti, D.L. Bleuel, T.R. Boehly, D.K. Bradley, S.C. Burkhart, R. Burr, J.A. Caggiano, C. Castro, D.T. Casey, C. Choate, D.S. Clark, P.M. Celliers, C.J. Cerjan, G.W. Collings, E.L. Dewald, P. DiNiicola, J.M. DiNicola, L. Divol, S. Dixit, T. Doeppner, R. Dylla-Spears, E. Dzenitis, M. Eckart, G. Erbert, D. Farley, J.E. Fair, D. Fittinghoff, M. Frank, L.J.A. Frenje, S. Friedrich, M.G. Gatu Johnson, C. Gibson, E. Giraldez, V. Yu. Glebov, S. Glenn, N. Guler, S.W. Haan, B.J. Haid, B.A. Hammel, A.V. Hamza, C.A. Haynam, G.M. Heestand, M. Hermann, H.W. Herrmann, D.G. Hicks, D.E. Hinkel, J.P. Holder, D.M. Holunda, J.B. Horner, W.W. Hsing, H. Huang, N. Izumi, M. Jackson, O.S. Jones, D. H. Kalantar, R. Kauffman, J.D. Kilkenny, R. Kirkwood, J. Klingmann, T. Kohut, J.P. Knauer, J.A. Koch, B. Kozioziemski, G.A. Kyrala, A.L. Kritcher, J. Kroll, K. La Fortune, R. Lowe-Webb, T.Ma, J. McNaney, A.G. Macphee, T.N. Malsbury, E. Mapoles, C.D. Marshall, N. B. Meezan, F. Merrill, P. Michel, J.D. Moody, A.S. Moore, M. Moran, K.A. Moreno, D.H. Munro, B.R. Nathan, A. Nikroo, R.E. Olsen, C.D. Orth, A.E. Pak, P.K. Patel, T. Parham, R. Petrasso, J.E. Ralph, S.P. Regan, H. Rinderknecht, H.F. Robey, J.S. Ross, M.D. Rosen, R. Sacks, J.D. Salmonson, R. Saunders, J. Sater, C. Sangster, M.B. Schneider, F.H. Séguin, S.M. Sepke, M.J.

Shaw, B.K. Spears, P.T. Springer, W. Stoeffl, L.J. Suter, C.A. Thomas, R. Tommasini, R.P.J. Town, C. Walters, S. Weaver, S.V. Weber, P.J. Wegner, P.K. Whitman, K. Widmann, C.C. Widmayer, C.H. Wilde, D.C. Wilson, B. Van Wonterghem, B.J. MacGowan, L.J. Atherton, M.J. Edwards, and E.I. Moses, "Cryogenic thermonuclear fuel implosions on the National Ignition Facility," *Phys. Plasmas*, **19**, 056318 (2012).

[305] V.A. Smalyuk, M. Barrios, J.A. Caggiano, D.T. Casey, C.J. Cerjan, D.S. Clark, M.J. Edwards, J.A. Frenje, M. Gatu-Johnson, V.Y. Glebov, G. Grim, S.W. Haan, B.A. Hammel, A. Hamza, W.W. Hsing, O. Hurricane, J.D. Kilkenny, J.L. Kline, J.P. Knauer, O.L. Landen, J.D. Lindl, T. Ma, J.M. McNaney, M. Mintz, A. Moore, A. Nikroo, T. Parham, J.L. Peterson, R. Petrasso, L. Pickworth, J.E. Pino, K. Raman, S.P. Regan, B.A. Remington, H.F. Robey, D.P. Rowley, D.B. Sayre, R.E. Tipton, S.V. Weber, K. Widmann, D.C. Wilson, C.B. Yeamans, "Hydrodynamic instability growth and mix experiments at the National Ignition Facility," *Phys. Plasmas*, **21**, 056301, (2014).

[306] V.A. Smalyuk, D.T. Casey, D.S. Clark, M.J. Edwards, S.W. Haan, A. Hamza, D.E. Hoover, W.W. Hsing, O. Hurricane, J.D. Kilkenny, J. Kroll, O.L. Landen, A. Moore, A. Nikroo, J.L. Peterson, K. Raman, B.A. Remington, H.F. Robey, S.V. Weber, K. Widmann, "First measurements of hydrodynamic instability growth in indirectly driven implosions at the National Ignition Facility," *Phys. Rev. Lett.*, **112**, 185003, (2014).

[307] H.-S. Park, O.A. Hurricane, D.A. Callahan, D.T. Casey, E.L. Dewald, T.R. Dittrich, T. Döppner, D.E. Hinkel, L.F. Berzak Hopkins, S. Le Pape, T. Ma, P.K. Patel, B.A. Remington, H.F. Robey, J. Salmonson, J.L. Kline, "High-Adiabat, high-foot inertial confinement fusion implosion experiments on the National Ignition Facility," *Phys. Rev. Lett.*, **112**, 055001, (2014).

[308] T.R. Dittrich, O.A. Hurricane, D.A. Callahan, E.L. Dewald, T. Döppner, D.E. Hinkel, L.F. Berzak Hopkins, S. Le Pape, T. Ma, J.L. Milovich, J.C. Moreno, P.K. Patel, H.-S. Park, B.A. Remington, J. Salmonson, "Physics Design Basis for a High-foot/High-Adiabat Inertial Confinement Fusion Capsule for the NIF," *Phys. Rev. Lett.*, **112**, 055002, 2014.

[309] O.A. Hurricane, D.A. Callahan, D.T. Casey, E.L. Dewald, T.R. Dittrich, T. Döppner, M.A. Barrios Garcia, D.E. Hinkel, L.F. Berzak Hopkins, P. Kervin, J.L. Kline, S. Le Pape, T. Ma, A.G. MacPhee, J.L. Milovich, J. Moody, A.E. Pak, P.K. Patel, H.-S. Park, B.A. Remington, H.F. Robey, J.D. Salmonson, P.T. Springer, R. Tommasini, L.R. Benedetti, J.A. Caggiano, P. Celliers, C. Cerjan, R. Dylla-Spears, D. Edgell, M.J. Edwards, D. Fittinghoff, G.P. Grim, N. Guler, N. Izumi, J.A. Frenje, M. Gatu Johnson, S. Haan, R. Hatarik, H. Herrmann, S. Khan, J. Knauer, B.J. Kozioziemski, A.L. Kritcher, G. Kyrala, S.A. Maclaren, F.E. Merrill, P. Michel, J. Ralph, J.S. Ross, J.R. Rygg, M.B. Schneider, B.K. Spears, K. Widmann, C.B. Yeamans, "The High-Foot Campaign on the National Ignition Facility," *Phys. Plasmas*, **21**, 056314, (2014).

[310] K. S. Raman, V. A. Smalyuk, D. T. Casey, S. W. Haan, D. E. Hoover, O. A. Hurricane, J.J. Kroll, A. Nikroo, J. L. Peterson, B. A. Remington, H. F. Robey, D. S. Clark, B.A. Hammel, O. L. Landen, M. Marinak, D. H. Munro, K. J. Peterson, J. Salmonson, "An in-flight radiography platform to measure hydrodynamic instability growth in inertial confinement fusion capsules at the National Ignition Facility," *Phys. Plasmas*, **21**, 072710, (2014).

[311] O.A. Hurricane, D.A. Callahan, D.T. Casey, P.M. Celliers, C. Cerjan, E.L. Dewald, T.R. Dittrich, T. Döppner, D.E. Hinkel, L.F. Berzak Hopkins, J.L. Kline, S. Le Pape, T. Ma, A.G. MacPhee, J.L. Milovich, A. Pak, H.-S. Park, P.K. Patel, B.A. Remington, J.D. Salmonson, P.T. Springer, R. Tommasini, "The achievement of fuel gain exceeding unity in an inertially confined fusion implosion," *Nature*, **506**, 343, (2014).

[312] D.T. Casey, V.A. Smalyuk, K.S. Raman, J.L. Peterson, L. Berzak-Hopkins, D.A. Callahan, D.S. Clark, E.L. Dewald, T.R. Dittrich, M.J. Edwards, S.W. Haan, B.A. Hammel, A. Hamza, D.E. Hinkel, D. Hoover, W.W. Hsing, O.A. Hurricane, J.D. Kilkenny, J.J. Kroll, O.L. Landen, A.S. Moore, A. Nikroo, H.-S. Park, B.A. Remington, H.F. Robey, J.R. Rygg, J.D. Salmonson, K. Widmann, "Reduced instability growth with high adiabat ('high-foot') implosions at the National Ignition Facility, *Phys. Rev. E*, **90**, 011102(R), (2014).

[313] J.L. Peterson, D.T. Casey, O.A. Hurricane, K.S. Raman, H.F. Robey, and V.A. Smalyuk, "Validating hydrodynamic growth in National Ignition Facility implosions," *Phys. Plasmas*, **22**, 056309, 2015.

[314] R. Betti, V.N. Goncharov, R.L. McCrory, and C.P. Verdon, "Growth rates of the ablative Rayleigh-Taylor instability in inertial confinement fusion," *Phys. Plasmas*, **5** 1446-54 (1998).

[315] R. LeLevier, G.J. Lasher, and F. Bjorklund, Effect of a density gradient on Taylor instability (No. UCRL-4459). Radiation Lab., Univ. of Calif., Livermore, 1955.

[316] A. Casner, V. A. Smalyuk, L. Masse, I. Igumenshchev, S. Liberatore, L. Jacquet, C. Chicanne, P. Loiseau, O. Poujade, D. K. Bradley, H. S. Park, and B. A. Remington, "Designs for highly nonlinear ablative Rayleigh-Taylor experiments on the NIF," *Phys. Plasmas*, **19**, 082708 (2012)

[317] A. Casner, L. Masse, S. Liberatore, P. Loiseau, P. E. Masson-Laborde, L. Jacquet, D. Martinez, A. S. Moore, R. Seugling, S. Felker, S. W. Haan, B. A. Remington, V. A. Smalyuk, M. Farrell, E. Giraldez, and A. Nikroo, "Probing the deep nonlinear stage of the ablative Rayleigh-Taylor instability in indirect drive experiments on the National Ignition Facility," *Phys. Plasmas*, **22**, 056302 (2015)

[318] A. Casner, C Mailliet, S F Khan, D Martinez, N Izumi, D Kalantar, P Di Nicola, J M Di Nicola, E Le Bel, I Igumenshchev, V T Tikhonchuk, B A Remington, L Masse, and V A Smalyuk, "Long-duration planar direct-drive hydrodynamics experiments on the NIF," *Plasma Phys. and Cont. Fusion*, **60**, 014012 (2018)

[319] D. Batani, S. Baton, A. Casner, S. Depierreux, M. Hohenberger, O. Klimo, M. Koenig, C. Labaune, X. Ribeyre, C. Rousseaux, G. Schurtz, W. Theobald, and V.T. Tikhonchuk, "Physics issues for shock ignition," *Nucl. Fusion*, **54**, 054009 (2014)

[320] R. Betti and O.A. Hurricane, "Inertial-confinement fusion with lasers," *Nature Phys.*, **12**, 435 (2016).

[321] L. Berzak Hopkins, S. Le Pape, L. Divol, A. Pak, E.L. Dewald, D.D. Ho, N.B Meezan, S. Bhandarkar, L.R. Benedetti, T. Bunn, J. Biener, J. Crippen, D. Casey, D.S. Clark, D.H. Edgell, N. Fittinghoff, M. Gatu Johnson, C. Goyon, S.W. Haan, R. Hatarik, M. Havre, D.

Hinkel, H. Huang, N. Izumi, J. Jaquez, O. Jones, S. Khan, A.L. Kritcher, C. Kong, G. Kyrala, O.L. Landen, T. Ma, A.G. MacPhee, B. MacGowan, A.J. MacKinnon, M. Marinak, J.L. Milovich, M. Millot, P. Michel, A. Moore, S.R. Nagel, A. Nikroo, P.K. Patel, J.E. Ralph, H.F. Robey, S. Ross, N. Rice, S. Sepke, V.A. Smalyuk, P.A. Sterne, D. Strozzi, M.Stadermann, P.L. Volegov, C.R. Weber, C. Yeamans, D.A. Callahan, O.A. Hurricane, R.P.J. Town, M. J. Edwards, "Toward a burning plasma state using diamond ablator inertially confined fusion (ICF) implosions on the National Ignition Facility (NIF)," *Plasma Phys. and Cont. Fusion*, **61**, 014023 (2019)

[322] O.A. Hurricane, D.A. Callahan, P.T. Springer, M.J. Edwards, P. Patel, K. Baker, D.T. Casey, L. Divol, T. Döppner, D.E. Hinkel, L. F. Berzak Hopkins, A. Kritcher, S. Le Pape, S. Maclaren, L. Masse, A. Pak, L. Pickworth, J. Ralph, C. Thomas, A. Yi, A. Zylstra, "Beyond alpha-heating: driving inertially confined fusion implosions toward a burning-plasma state on the National Ignition Facility," *Plasma Phys. and Cont. Fusion*, **61**, 014033 (2019)

[323] O. A. Hurricane, P. T. Springer, P. K. Patel, D. A. Callahan, K. Baker, D. T. Casey, L. Divol, T. Dppner, D. E. Hinkel, M. Hohenberger, L. F. Berzak Hopkins, C. Jarrott, A. Kritcher, S. Le Pape, S. Maclaren, L. Masse, A. Pak, J. Ralph, C. Thomas, P. Volegov, and A. Zylstra, "Approaching a burning plasma on the NIF," *Phys. Plasmas*, **26**, 052704 (2019)

[324] C.R. Weber, T. Döppner, D.T. Casey, T.L. Bunn, L.C. Carlson, R.J. Dylla-Spears, B.J. Kozioziemski, A.G. MacPhee, A. Nikroo, H.F. Robey, J.D. Sater, V.A. Smalyuk, "First measurements of fuel-ablator interface instability growth in inertial confinement fusion implosions on the National Ignition Facility," *Phys. Rev. Lett.*, **117**, 075002 (2016).

[325] K. Kifonidis, T. Plewa, H-Th Janka, and E. Müller. "Non-spherical core collapse supernovae-I. Neutrino-driven convection, Rayleigh-Taylor instabilities, and the formation and propagation of metal clumps." *Astronomy and Astrophysics*, **408**, 621 (2003).

[326] U. Hwang, J. M. Laming, C. Badenes, F. Berendse, J. Blondin, D. Cioffi, T. DeLaney et al. "A million second Chandra view of Cassiopeia A." *Astrophys. J.*, **615**, L117 (2004).

[327] J.J. Hester, "WFPC2 studies of the Crab Nebula. III. Magnetic Rayleigh-Taylor instabilities and the origin of the filaments," *Astrophys.J.*, **456**, 225 (1996)

[328] Gaia Collaboration et al., "Gaia data release 2 - observational Hertzsprung-Russell diagrams," *Astronomy & Astrophysics*, **616**, A10 (2018).

[329] The method of energy transfer becomes very important here. For conduction or diffusive transport, the structure is well described by simple ODEs, but for convective transport, one can use mixing-length theory to approximate the convective turbulence in a statistical way or else resort to more expensive numerical calculations.

[330] For low-mass stars ($\lesssim$0.8 $M_\odot$), the subsequent evolution is theoretical, since they can remain on the main sequence for up to $\sim$1000 times the age of the universe, hence their post-main-sequence phases have not yet been observed.

[331] The Pauli exclusion principle of quantum mechanics prevents two electrons in a plasma from occupying the same quantum state. Thus, as matter is forced into a smaller and smaller volume, electrons must occupy states with increasingly higher energies. This provides an effective pressure that is able to resist the inward self-gravitational force on the core even when thermal pressure alone cannot.

[332] To early observers, these nebulae appeared round and planet-like, and although they have nothing to do with planets, this term has persisted.

[333] This was named after Indian astrophysicist Subrahmanyan Chandrasekhar, who was the first to calculate the value for a relativistic, degenerate gas of particles.

[334] M. M. Phillips, "The absolute magnitudes of Type IA supernovae," *Astrophys. J. Lett.*, **413**, L105 (1993).

[335] M. Gilfanov and A. Bogdán. "An upper limit on the contribution of accreting white dwarfs to the type Ia supernova rate." *Nature*, **463**, 924 (2010).

[336] M. Smith, R.C. Nichol, B. Dilday, J. Marriner, R. Kessler, B. Bassett, D. Cinabro, J. Frieman, P. Garnavich, S.W. Jha, H. Lampeitl, M. Sako, D.P. Schneider, and J. Sollerman, "The SDSS-II Supernova Survey: parameterizing the type Ia supernova rate as a function of host galaxy properties," *Astrophys. J.*, **755**, 61 (2012).

[337] M.D. Stritzinger, B.J. Shappee, A.L. Piro, C. Ashall, E. Baron, P. Hoeflich, S. Holmbo, T.W.-S. Holoien, M. M. Phillips, C. R. Burns, C. Contreras, N. Morrell, and M.A. Tucker, "Red versus blue: early observations of thermonuclear supernovae reveal two distinct populations?" *Astrophys. J. Lett.*, **864**, L35 (2018).

[338] D. Kushnir, B. Katz, S. Dong, E. Livne, and R. Fernndez. "Head-on collisions of white dwarfs in triple systems could explain type Ia supernovae." *Astrophys. J. Lett.*, **778**, L37 (2013).

[339] In a typical carbon-oxygen white dwarf, the onset of carbon burning raises the temperature to $\sim 10^8$ K with a central density of $\sim 10^9$ g cm^{-3} giving a kinematic viscosity of $\sim$1 cm^2 s^{-1}. The characteristic length scale is $\sim$100 km and the characteristic velocity is $\sim$100 km s^{-1}, hence the physical Reynolds number can be estimated to be $\mathcal{R}e \approx 10^{14}$.

[340] This unit of was named after Hans Bethe, a German-American nuclear physicist who led the Theoretical Division at Los Alamos National Laboratory in the development of the first atomic weapons during World War II and who was later awarded the Nobel Prize for his contributions to the theory of stellar nucleosynthesis.

[341] K. Nomoto & M. Hashimoto, "Presupernova evolution of massive stars," *Phys. Rep.*, **163**, 13 (1988).

[342] A. Burrows, "Convection and the mechanism of type II supernovae," *Astrophys.J. Letters*, 318, L57 (1987).

[343] D. Radice, A. Burrows, D. Vartanyan, M.A. Skinner, & J.C. Dolence, "Electron-capture and low-mass iron-core-collapse supernovae: new neutrino-radiation-hydrodynamics simulations," *Astrophys.J.*, **850**, 43 (2017).

[344] H.T. Janka, K. Langanke, A. Marek, G. Martnez-Pinedo, and B. Müller, "Theory of core-collapse supernovae," *Physics Reports*, **442**, 38 (2007).

[345] A. Burrows, "Colloquium: Perspectives on core-collapse supernova theory," *Reviews of Modern Physics*,**85**, 245 (2013).

[346] M. Taylor, D. Cinabro, B. Dilday, L. Galbany, R.R. Gupta, R. Kessler, J. Marriner, R.C. Nichol, M. Richmond, D. P. Schneider, and J. Sollerman, "The core col-

lapse supernova rate from the SDSS-II supernova survey," *Astrophys.J.*, **792**, 135 (2014).

[347] S. M. Couch & C. D. Ott, "The role of turbulence in neutrino-driven core-collapse supernova explosions," *Astrophys.J.*, **799**, 5 (2015).

[348] Q. A. Mabanta & J. W. Murphy, "How turbulence enables core-collapse supernova explosions," *Astrophys.J.*, **856**, 22 (2018).

[349] A. Wongwathanarat, E. Mller, and H-Th. Janka. "Three-dimensional simulations of core-collapse supernovae: from shock revival to shock breakout." *Astronomy & Astrophysics*, **577**, A48 (2015).

[350] D. Branch and J. C. Wheeler. Supernova explosions. Berlin: Springer, 2017.

[351] W.D. Arnett, J.N. Bahcall, R.P. Kirshner, and S. E. Woosley. "Supernova 1987A." *Annual Review of Astronomy and Astrophysics*, **27**, 629 (1989).

[352] W. Hillebrandt and P. Höflich, "The supernova 1987a in the large magellanic cloud," *Rep. Prog. Phys.* **52**, 1421 (1989).

[353] B.A. Remington, R. P. Drake, H. Takabe, and D. Arnett. "A review of astrophysics experiments on intense lasers." *Phys. Plasmas*, **7**, 1641 (2000).

[354] B. Müller, S. Wanajo, H-Th Janka, A. Heger, D. Gay, and S. A. Sim. "Simulations of electron capture and low-mass iron core supernovae." *Memorie della Societa Astronomica Italiana,"* **88**, 288 (2017).

[355] B. Müller, D.W. Gay, A. Heger, T.M. Tauris, and S.A. Sim. "Multidimensional simulations of ultrastripped supernovae to shock breakout." *Monthly Notices of the Royal Astronomical Society*, **479**, 3675 (2018).

[356] P.C. Duffell and D. Kasen. "Rayleigh-Taylor instability in interacting supernovae: implications for synchrotron magnetic fields." *Astrophys.J.,* **842**, 18 (2017).

[357] Y. Zhou and W. H. Matthaeus. "Phenomenology treatment of magnetohydrodynamic turbulence with nonequipartition and anisotropy." *Phys. Plasmas*, **12**, 056503 (2005).

[358] T. Inoue, J. Shimoda, Y. Ohira, and R. Yamazaki. "The origin of radially aligned magnetic fields in young supernova remnants." *Astrophys.J. Lett.,* **772**, L20 (2013).

[359] J. Shimoda, T. Akahori, A. Lazarian, T. Inoue, and Y. Fujita. "Discovery of Kolmogorov-like magnetic energy spectrum in Tycho's supernova remnant by two-point correlations of synchrotron intensity." *Monthly Notices of the Royal Astronomical Society,* **480**, 2200 (2018).

[360] M. C. Anderson and L. Rudnick, "The deceleration powering of synchrotron emission from the ejecta contents in supernova remnant Cassiopeia A," *Astrophys. J.*, **441**, 307 (1995).

[361] J.I. Reed, J. J. Hester, A. C. Fabian, and P. F. Winkler, "The three dimensional structure of the Cassiopeia A supernova remnant. I. The spherical shell," *Astrophys. J.*, **440**, 706 (1995).

[362] J. W. Keohane, L. Rudnick, and M. C. Anderson, "A comparison of the x-ray and radio emission from the supernova remnant Cassiopeia A," *Astrophys. J.*, **466**, 309 (1996).

[363] J. P. Hughes, C. E. Rakowski, D. N. Burrows, and P. O. Slane, "Nucleosynthesis and mixing in Cassiopeia A," *Astrophys. J. Lett.*, **528**, L109 (2000).

[364] V. Trimble, "Motions and structure of the filamentary envelope of the Crab Nebula," *Astronomical J.,* **73**, 535 (1968)

[365] J.M. Blondin and R.A. Chevalier. "Pulsar wind bubble blowout from a supernova." *Astrophys. J.*, **845**, 139 (2017).

[366] B. W. Grefenstette, F. A. Harrison, S. E. Boggs, S. P. Reynolds, C. L. Fryer, K. K. Madsen, D.R. Wik, A. Zoglauer, C. I. Ellinger, D. M. Alexander, H. An, D. Barret, F. E. Christensen, W. W. Craig, K. Forster, P. Giommi, C. J. Hailey, A. Hornstrup, V. M. Kaspi, T. Kitaguchi, J. E. Koglin, P. H. Mao, H. Miyasaka, K. Mori, M. Perri, M. J. Pivovaroff, S. Puccetti, V. Rana, D. Stern, N. J. Westergaard & W. W. Zhang, "Asymmetries in core-collapse supernovae from maps of radioactive 44 Ti in Cassiopeia A." *Nature*, **506**, 339 (2014).

[367] S.M. Couch, E. Chatzopoulos, W. D. Arnett, and F. X. Timmes. "The three-dimensional evolution to core collapse of a massive star." *Astrophys. J. Lett.*, **808**, L21 (2015).

[368] C. Weidner and P. Kroupa. "Evidence for a fundamental stellar upper mass limit from clustered star formation." *Monthly Notices of the Royal Astronomical Society,* **348**, 187 (2004).

[369] D.F. Figer, "An upper limit to the masses of stars." *Nature*, **434**, 192 (2005).

[370] P.A. Crowther, O. Schnurr, R. Hirschi, N. Yusof, R.J. Parker, S.P. Goodwin, and H. A. Kassim. "The R136 star cluster hosts several stars whose individual masses greatly exceed the accepted 150 $M_\odot$ stellar mass limit." *Monthly Notices of the Royal Astronomical Society*, **408**, 731 (2010).

[371] H.W. Yorke and C. Sonnhalter. "On the formation of massive stars." *Astrophys.J.*, **569**, 846 (2002).

[372] M.R. Krumholz, R.I. Klein, C.F. McKee, S.S.R. Offner, and A.J. Cunningham. "The formation of massive star systems by accretion." *Science*, **323**, 754 (2009).

[373] A.L. Rosen, M.R. Krumholz, C.F. McKee, and R.I. Klein. "An unstable truth: how massive stars get their mass." *Monthly Notices of the Royal Astronomical Society*, **463**, 2553 (2016).

[374] S. P. Obenschain, S. E. Bodner, D. Colombant, K. Gerber, R. H. Lehmberg, E. A. McLean, A. N. Mostovych, M. S. Pronko, C. J. Pawley, A. J. Schmitt, J. D. Sethian, V. Serlin, J. A. Stamper, C. A. Sullivan, J. P. Dahlburg, J. Gardner, Y. Chan, A. V. Deniz, J. Hardgrove, T. Lehecka, and M. Klapish, "The Nike KrF laser facility: performance and initial target experiments." *Phys. Plasmas*, **3**, 2098 (1996).

[375] N. Hopps, C. Danson, S. Duffield, D. Egan, S. Elsmere, M. Girling, E. Harvey et al. "Overview of laser systems for the Orion facility at the AWE." *Applied Optics,* **52**, 3597 (2013).

[376] N. Hopps, K. Oades, J. Andrew, C. Brown, G. Cooper, C. Danson, S. Daykin et al. "Comprehensive description of the Orion laser facility." *Plasma Physics and Controlled Fusion*, **57**, 064002 (2015).

[377] Y. Aglitskiy, A. L. Velikovich, M. Karasik, V. Serlin, C. J. Pawley, A. J. Schmitt, S. P. Obenschain, A. N. Mostovych, J. H. Gardner, and N. Metzler, "Direct observation of mass oscillations due to ablative Richtmyer-Meshkov instability and feedout in planar plastic targets." *Phys. Plasmas*, **9**, 2264 (2002).

[378] C. Yamanaka, Y. Kato, Y. Izawa, K. Yoshida, T. Yamanaka, T. Sasaki, M. Nakatsuka, T. Mochizuki, J. Kuroda, and S. Nakai, "Nd-doped phosphate glass laser systems for laser-fusion research," *IEEE J. Quantum*

Electron. QE-17, 1639 (1981)

[379] K. Mima, Y. Kato, H. Azechi, K. Shigemori, H. Takabe, N. Miyanaga, T. Kanabe, T. Norimatsu, H. Nishimura, H. Shiraga, M. Nakai, R. Kodama, K. A. Tanaka, M. Takagi, M. Natatsuka, K. Nishihara, T. Yamanaka, and S. Nakai, "Recent progress of implosion experiments with uniformity-improved GEKKO XII laser facility at the Institute of Laser Engineering, Osaka University," *Phys. Plasmas*, **3**, 2077 (1996)

[380] T.R. Boehly, D.L. Brown, R.S. Craxton, R.L. Keck, J.P. Knauer, J.H. Kelly, T.J. Kessler, S.A. Kumpan, S.J. Loucks, S.A. Letzring, F.J. Marshall, R.L. McCrory, S.F.B Morse, W. Seka, J.M. Soures, C.P. Verdon, "Initial performance results of the OMEGA laser system." *Optics communications*, **133**, 495 (1997).

[381] V. A. Smalyuk, O. Sadot, J. A. Delettrez, D. D. Meyerhofer, S. P. Regan, and T. C. Sangster. "Fourier-space nonlinear Rayleigh-Taylor growth measurements of 3D laser-imprinted modulations in planar targets." *Phys. Rev. Lett.*, **95**, 215001 (2005).

[382] S.G. Glendinning, J. Bolstad, D. G. Braun, M. J. Edwards, W. W. Hsing, B. F. Lasinski, H. Louis, A. Miles, J. Moreno, T. A. Peyser, B. A. Remington, H. F. Robey, E. J. Turano, C. P. Verdon, and Y. Zhou, "Effect of shock proximity on Richtmyer-Meshkov growth." *Phys. Plasmas*, **10**, 1931 (2003).

[383] O. A. Hurricane, V. A. Smalyuk, K. Raman, O. Schilling, J. F. Hansen, G. Langstaff, D. Martinez et al. "Validation of a turbulent kelvin-helmholtz shear layer model using a high-energy-density omega laser experiment." *Phys. Rev. Lett.*, **109**, 155004 (2012).

[384] G.H. Miller, E.I. Moses, and C.R. Wuest. "The National Ignition Facility." *Optical Engineering*, **43**, 2841 (2004).

[385] E.I. Moses and C.R. Wuest. "The National Ignition Facility: status and plans for laser fusion and high-energy-density experimental studies." *Fusion Science and Technology*, **43**, 420 (2003).

[386] M.L. Andé, "The French megajoule laser project (LMJ)." *Fusion Engineering and Design*, **44**, 43 (1999).

[387] C. Cavailler, "Inertial fusion with the LMJ." *Plasma Physics and Controlled Fusion*, **47**, B389 (2005).

[388] A. Casner, G. Rigon, B. Albertazzi, Th Michel, T. Pikuz, A. Faenov, P. Mabey, N. Ozaki, Y. Sakawa, T. Sano, J. Ballet, P. Tzeferacos, D. Lamb, E. Falize, G. Gregori, and M. Koenig, "Turbulent hydrodynamics experiments in high energy density plasmas: scientific case and preliminary results of the TurboHEDP project." *High Power Laser Science and Engineering*, **6**, e44 (2018).

[389] C. M. Huntington, A. Shimony, M. Trantham, C. C. Kuranz, D. Shvarts, C. A. Di Stefano, F. W. Doss, R. P. Drake, K. A. Flippo, D. H. Kalantar, S. R. Klein, J. L. Kline, S. A. MacLaren, G. Malamud, A. R. Miles, S. T. Prisbrey, K. S. Raman, B. A. Remington, H. F. Robey, W. C. Wan, and H.-S. Park, "Ablative stabilization of Rayleigh-Taylor instabilities resulting from a laser-driven radiative shock," *Phys. Plasmas*, **25**, 052118 (2018)

[390] A. Casner, C. Mailliet, G. Rigon, S. F. Khan, D. Martinez, B. Albertazzi, T. Michel, T. Sano, Y. Sakawa, P. Tzeferacos, D. Lamb, S. Liberatore, N. Izumi, D. Kalantar, P. Di Nicola, J.M. Di Nicola, E. Le Bel, I. Igumenshchev, V. Tikhonchuk, B.A. Remington, J. Ballet, E. Falize, L. Masse, V.A. Smalyuk, and M. Koenig, "From ICF to laboratory astrophysics: ablative and classical Rayleigh-Taylor instability experiments in turbulent-like regimes." *Nuclear Fusion*, **59**, 032002 (2019).

[391] D. A. Martinez, V. A. Smalyuk, J. O. Kane, A. Casner, S. Liberatore, and L. P. Masse. "Evidence for a bubble-competition regime in indirectly driven ablative Rayleigh-Taylor instability experiments on the NIF." *Phys. Rev. Lett.*, **114**, 215004 (2015).

[392] K.A. Flippo, F.W. Doss, J.L. Kline, E.C. Merritt, D. Capelli, T. Cardenas, B. DeVolder, F. Fierro, C.M. Huntington, L. Kot, E.N. Loomis, S.A. MacLaren, T.J. Murphy, S.R. Nagel, T.S. Perry, R.B. Randolph, G. Rivera, and D.W. Schmidt, "Late-time mixing sensitivity to initial broadband surface roughness in high-energy-density shear layers," *Phys. Rev. Letters*, **117**, 225001 (2016).

[393] K. A. Flippo, F. W. Doss, E. C. Merritt, B. G. DeVolder, C. A. Di Stefano, P. A. Bradley, D. Capelli, T. Cardenas, T. R. Desjardins, F. Fierro, C. M. Huntington, J. L. Kline, L. Kot, S. Kurien, E. N. Loomis, S. A. MacLaren, T. J. Murphy, S. R. Nagel, T. S. Perry, R. B. Randolph, A. Rasmus, and D. W. Schmidt, "Late-time mixing and turbulent behavior in high-energy-density shear experiments at high Atwood numbers," *Phys. Plasmas*, **25**, 056315 (2018).

[394] M.A. Skinner, J.C. Dolence, A. Burrows, D. Radice, and D. Vartanyan. "Fornax: a flexible code for multiphysics astrophysical simulations," *Astrophysical J. Suppl.*, **241**, 7 (2019).

[395] D. Radice, E. Abdikamalov, C.D. Ott, P. Mösta, S.M. Couch, and L.F. Roberts. "Turbulence in core-collapse supernovae." *J. Phys. G*, **45**, 053003 (2018).

[396] T. Oggian, D. Drikakis, D. L. Youngs, and R. J. R. Williams. "Computing multi-mode shock-induced compressible turbulent mixing at late times," *J. Fluid Mech.*, **779**, 411 (2015).

[397] T. Oggian, D. Drikakis, D.L. Youngs, and R.J.R. Williams. "A Hybrid compressible-incompressible computational fluid dynamics method for Richtmyer-Meshkov Mixing," *ASME J. of Fluids Engineering*, **136**, 091210 (2014).

[398] Y. Zhou, "A scaling analysis of turbulent flows driven by Rayleigh-Taylor and Richtmyer-Meshkov instabilities." *Phys. Fluids*, **13**, 538 (2001).

[399] S.R. Yoffe and W.D. McComb, "Onset criteria for freely decaying isotropic turbulence," *Phys. Rev. Fluids*, **3**, 104605 (2018).

[400] V. K. Tritschler, M. Zubel, S. Hickel, and N. A. Adams. "Evolution of length scales and statistics of Richtmyer-Meshkov instability from direct numerical simulations." *Phys. Rev. E*, **90**, 063001 (2014).

[401] R.J.R. Williams, "The late time structure of high density contrast, single mode Richtmyer-Meshkov flow," *Phys. Fluids*, **28**, 074108 (2016).

[402] B.B. Mandelbrot, The fractal geometry of nature. Vol. 1. New York: WH freeman, 1982.

[403] Cartwright, Julyan HE, and Hisami Nakamura. "What kind of a wave is Hokusai's Great wave off Kanagawa?" *Notes and Records of the Royal Society*, **63**, 119 (2009).

[404] J.M. Dudley, V. Sarano, and F. Dias. "On Hokusai's Great wave off Kanagawa: localization, linearity and a rogue wave in sub-Antarctic waters." *Notes Rec. R. Soc.*, **67**, 159 (2013).

[405] P.A. Davidson, Turbulence: an introduction for scientists and engineers. Oxford University Press, Oxford, UK, 2015.

[406] D. McComb, "Scale-invariance in three-dimensional isotropic turbulence: a paradox and its resolution." *J. Phys. A*, **41**, 075501 (2008).

[407] P.E. Dimotakis, "The mixing transition in turbulent flows," *J. Fluid Mech.*, **409**, 69 (2000).

[408] Y. Zhou, A. C. Buckingham, F. Bataille, and L. Mathelin. "Minimum state for high Reynolds and Péclet number turbulent flows." *Physics Letters A*, **373**, 2746 (2009).

[409] Y. Zhou, "Unification and extension of the similarity scaling criteria and mixing transition for studying astrophysics using high energy density laboratory experiments or numerical simulations." *Phys. Plasmas*, **14**, 082701 (2007).

[410] Y. Zhou, H.F. Robey, and A.C. Buckingham. "Onset of turbulence in accelerated high-Reynolds-number flow." *Phys. Rev. E*, **67**, 056305 (2003).

[411] Y. Zhou, B. A. Remington, H. F. Robey, A. W. Cook, S. G. Glendinning, A. Dimits, A. C. Buckingham, G. B. Zimmerman, E. W. Burke, T. A. Peyser, W. Cabot, and D. Eliason, "Progress in understanding turbulent mixing induced by Rayleigh-Taylor and Richtmyer-Meshkov instabilities." *Phys. Plasmas*, **10**, 1883 (2003).

[412] H.F. Robey, Y. Zhou, A. C. Buckingham, P. Keiter, B. A. Remington, and R. P. Drake. "The time scale for the transition to turbulence in a high Reynolds number, accelerated flow." *Phys. Plasmas*, **10**, 614 (2003).

[413] R.P. Drake, E.C. Harding, and C.C. Kuranz. "Approaches to turbulence in high-energy-density experiments." *Physica Scripta*, **T132**, 014022 (2008).

[414] M. Lesieur and D. Schertzer, "Dynamique des gros tourbillons et dcroissance de lénergie cintique en turbulence tridimensionelle isotrope á grand nombre de Reynolds." *J. Méch.* **17**, 607 (1978).

[415] T.T. Clark and C. Zemach. "Symmetries and the approach to statistical equilibrium in isotropic turbulence." *Phys. Fluids*, **10**, 2846 (1998).

[416] C.E. Leith, "Diffusion approximation to inertial energy transfer in isotropic turbulence." *Phys. Fluids,* **10**, 1409 (1967).

[417] N.J. Hammer, H.T. Janka, and E. Müller, "Three-dimensional simulations of mixing instabilities in supernova explosions," *Astrophys. J.*, **714**, 1371 (2010).

[418] C.C. Kuranz, H-S. Park, Channing M. Huntington, Aaron R. Miles, Bruce A. Remington, T. Plewa, M. R. Trantham, H. F. Robey, D. Shvarts, A. Shimony, K. Raman, S. MacLaren, W. C. Wan, F. W. Doss, J. Kline, K. A. Flippo, G. Malamud, T. A. Handy, S. Prisbrey, C. M. Krauland, S. R. Klein, E. C. Harding, R. Wallace, M. J. Grosskopf, D. C. Marion, D. Kalantar, E. Giraldez & R. P. Drake, "How high energy fluxes may affect Rayleigh-Taylor instability growth in young supernova remnants." *Nature Communications*, **9**, 1564 (2018).

[419] H. Sakagami, and K. Nishihara, "Rayleigh-Taylor instability on the pusher-fuel contact surface of stagnating targets," *Phys. Fluids B*, **2**, 2715 (1990).

[420] I. Hachisu, T. Matsuda, K. Nomoto, and T. Shigeyama, "Rayleigh-Taylor instabilities and mixing in the helium star models for Type Ib/Ic supernovae," *Astrophs. J.*, **368**, L27 (1991).

[421] D.D. Ryutov, "Scaling laws for dynamical plasma phenomena." *Phys. Plasmas*, **25**, 100501 (2018).

[422] K.S. Raman, O. A. Hurricane, H-S. Park, B. A. Remington, H. Robey, V. A. Smalyuk, R. P. Drake, C. M. Krauland, C. C. Kuranz, J. F. Hansen, and E. C. Harding, "Three-dimensional modeling and analysis of a high energy density Kelvin-Helmholtz experiment." *Phys. Plasmas*, **19**, 092112 (2012).

[423] F.W. Doss FW, J.L. Kline, K.A. Flippo, T.S. Perry, B.G. DeVolder, I. Tregillis, E.N. Loomis, E.C. Merritt, T.J. Murphy, L. Welser-Sherrill, J.R. Fincke, "The Shock/Shear platform for planar radiation-hydrodynamics experiments on the National Ignition Facility," *Phys. Plasmas*, **22**, 056303 (2015).

[424] J.G. Clérouin, M.H. Cherfi, and G. Zérah, "The viscosity of dense plasmas mixtures," *Europhysics Letters*, **42**, 37 (1998).

[425] M.S. Murillo, "Viscosity estimates of liquid metals and warm dense matter using the Yukawa reference system." *High Energy Density Physics*, **4**, 49 (2008).

[426] T. Haxhimali, R.E. Rudd, W.H. Cabot, F.R. Graziani, "Shear viscosity for dense plasmas by equilibrium molecular dynamics in asymmetric Yukawa ionic mixtures," *Phys. Rev. E*, **92**, 053110 (2015).

[427] A.N. Simakov and K. Molvig, "Electron transport in a collisional plasma with multiple ion species," *Phys. Plasmas*, **21**, 024503 (2014).

[428] A.N. Simakov and K. Molvig, "Hydrodynamic description of an unmagnetized plasma with multiple ion species. I. General formulation, *Phys. Plasmas*, **23**, 032115 (2016).

[429] A.N. Simakov and K. Molvig, "Hydrodynamic description of an unmagnetized plasma with multiple ion species. II. Two and three ion species plasmas." *Phys. Plasmas,* **23**, 032116 (2016).

[430] B.M. Haines, E.L. Vold, K. Molvig, C. Aldrich, R. Rauenzahn, "The effects of plasma diffusion and viscosity on turbulent instability growth," *Phys. Plasmas*, **21**, 092306 (2014).

[431] L.G. Stanton and M.S. Murillo. "Ionic transport in high-energy-density matter." *Phys. Rev. E*, **93**, 043203 (2016).

[432] C. Ticknor, J. D. Kress, L. A. Collins, J. Clérouin, P. Arnault, and A. Decoster. "Transport properties of an asymmetric mixture in the dense plasma regime." *Phys. Rev. E*, **93**, 063208 (2016)

[433] E.L. Vold, A.S. Joglekar, M.I. Ortega, R. Moll, D. Fenn, K. Molvig, "Plasma viscosity with mass transport in spherical inertial confinement fusion implosion simulations," *Phys. Plasmas*, **22**, 112708 (2015).

[434] E.L. Vold, R.M. Rauenzahn, C.H. Aldrich, K. Molvig, A.N. Simakov, B.M. Haines, "Plasma transport in an Eulerian AMR code," *Phys. Plasmas*, **24**, 042702 (2017).

[435] C. R. Weber, D. S. Clark, A. W. Cook, L. E. Busby, and H. F. Robey. "Inhibition of turbulence in inertial-confinement-fusion hot spots by viscous dissipation." *Phys. Rev. E*, **89**, 053106 (2014).

[436] K. Kadau, T.C. Germann, N.G. Hadjiconstantinou, P.S. Lomdahl, G. Dimonte, B.L. Holian, and B.J. Alder. "Nanohydrodynamics simulations: An atomistic view of the Rayleigh-Taylor instability." *Proceedings of the National Academy of Sciences*, **101**, 5851 (2004).

[437] K. Kadau, C. Rosenblatt, J.L. Barber, T.C. Germann, Z. Huang, P. Carlés, and B.J. Alder. "The importance of fluctuations in fluid mixing." *Proceedings of the National Academy of Sciences,* **104**, 7741 (2007).

[438] P. Ramaprabhu, G. Dimonte, and M. J. Andrews. "A numerical study of the influence of initial perturbations on the turbulent Rayleigh-Taylor instability." *J. Fluid*

Mech., **536**, 285 (2005).

[439] A. Banerjee and M.J. Andrews. "3D simulations to investigate initial condition effects on the growth of Rayleigh-Taylor mixing." *International J. of Heat and Mass Transfer*, **52**, 3906 (2009).

[440] H. Lim, J. Iwerks, J. Glimm, and D.H. Sharp. "Nonideal Rayleigh-Taylor mixing." *Proceedings of the National Academy of Sciences,* **107**, 12786 (2010).

[441] T. Kaman, J. Melvin, P. Rao, R. Kaufman, H. Lim, Y. Yu, J. Glimm, and D. H. Sharp. "Recent progress in turbulent mixing." *Physica Scripta*, **T155**, 014051 (2013).

[442] D.L. Youngs, "The density ratio dependence of self-similar Rayleigh-Taylor mixing." *Phil. Trans. R. Soc. A*, **371**, 20120173 (2013).

[443] G. Dimonte, P. Ramaprabhu, D. L. Youngs, M. J. Andrews, and R. Rosner. "Recent advances in the turbulent Rayleigh-Taylor instability." *Phys. Plasmas*, **12**, 056301 (2005).

[444] R. Polavarapu, P. Roach, and A. Banerjee, "Rayleigh-Taylor-instability experiments with elastic-plastic materials," *Phys. Rev. E*, **99**, 053104 (2019)

[445] H. Zhang, R. Betti, R. Yan, D. Zhao, D. Shvarts, and H. Aluie. "Self-Similar Multimode Bubble-Front Evolution of the Ablative Rayleigh-Taylor Instability in Two and Three Dimensions." *Phys. Rev. Letters*, **121**, 185002 (2018).

[446] M. Li and W.-H. Ye, "Successive Picket Drive for Mitigating the Ablative Richtmyer-Meshkov Instability," *Chin. Phys. Lett.*, **36**, 25201 (2019).

[447] O. Soulard, J. Griffond, and B.-J. Gréa, "Large- analysis of self-similar unstably stratified homogeneous turbulence," *Phys. Fluids*, **26**, 015110 (2014).

[448] R. Adkins, E.M. Shelton, M.-C. Renoult, P. Carles, and C. Rosenblatt. "Interface coupling and growth rate measurements in multilayer Rayleigh-Taylor instabilities." *Phys. Rev. Fluids*, **2**, 062001 (2017).

[449] M.-C. Renoult, P. Carles, S. Ferjani, and C. Rosenblatt. "2D Rayleigh-Taylor instability: Interfacial arc-length vs. deformation amplitude." *Europhysics Letters*, **101**, 54001 (2013).

[450] J. White, J. Oakley, M. Anderson, and R. Bonazza. "Experimental measurements of the nonlinear Rayleigh-Taylor instability using a magnetorheological fluid." *Phys. Rev. E*, **81**, 026303 (2010).

[451] V. Tsiklashvili, P.E. Romero Colio, O.A. Likhachev, and J.W. Jacobs. "An experimental study of small Atwood number Rayleigh-Taylor instability using the magnetic levitation of paramagnetic fluids." *Phys. Fluids*, **24**, 052106 (2012).

[452] G.C. Burton, "Study of ultrahigh Atwood-number Rayleigh-Taylor mixing dynamics using the nonlinear large-eddy simulation method." *Phys. Fluids*, **23**, 045106 (2011).

[453] Q. Chen, L. Li, Y.H. Zhang, and B.L. Tian, "Effects of the Atwood number on the Richtmyer-Meshkov instability in elastic-plastic media," *Phys. Rev. E*, **99**, 053102 (2019)

[454] A. Shimony, G. Malamud, and D. Shvarts, "Density Ratio and Entrainment Effects on Asymptotic Rayleigh-Taylor Instability", *ASME J. of Fluids Engineering*, **140**, 050906 (2018).

[455] W.H. Liu, C.P. Yu, P. Wang, Z. Fu, L.L. Wang, and Y.L. Chen, "Finite-thickness effect of the fluids on bubbles and spikes in RichtmyerMeshkov instability for arbitrary Atwood numbers," *Plasma Sci. Technol.,* **21**, 025001 (2019).

[456] M. Dong, Z.F. Fan, and C.X. Yu, "Multiple eigenmodes of the Rayleigh-Taylor instability observed for a fluid interface with smoothly varying density. II. Asymptotic solution and its interpretation," *Phys. Rev. E*, **99**, 013109 (2019).

[457] V. S. Smeeton and D.L. Youngs, "Experimental Investigation of Turbulent Mixing by Rayleigh-Taylor Instability III," AWE Report No. O 35/87. (1987).

[458] D.L. Youngs, "Modeling Turbulent Mixing by Rayleigh-Taylor Instability," *Physica D*, **3**, 270 (1989).

[459] J. M. Holford, S. B. Dalziel, and D.L. Youngs. "Rayleigh-Taylor instability at a tilted interface in laboratory experiments and numerical simulations." *Laser and Particle Beams*, **21**, 419 (2003).

[460] M.J. Andrews, D.L. Youngs, D. Livescu, and T. Wei. "Computational studies of two-dimensional Rayleigh-Taylor driven mixing for a tilted-rig." *ASME J. of Fluids Engineering*, **136**, 091212 (2014).

[461] N.A. Denissen, B. Rollin, J.M. Reisner, and M.J. Andrews. "The tilted rocket rig: a Rayleigh-Taylor test case for RANS models." *ASME J. of Fluids Engineering*, **136**, 091301 (2014).

[462] A.G.W. Lawrie and S.B. Dalziel. "Turbulent diffusion in tall tubes. I. Models for Rayleigh-Taylor instability." *Phys. Fluids*, **23**, 085109 (2011).

[463] A.G.W. Lawrie and S.B. Dalziel. "Turbulent diffusion in tall tubes. II. Confinement by stratification." *Phys. Fluids*, **23**, 085110 (2011).

[464] G. Boffetta, F. De Lillo, A. Mazzino, and S. Musacchio. "Bolgiano scale in confined Rayleigh-Taylor turbulence." *J. Fluid Mech.* **690** 426 (2012).

[465] P. Wang, Y. Zhou, S.A. MacLaren, C.M. Huntington, K.S. Raman, F.W. Doss, and K.A. Flippo, "Three- and two-dimensional simulations of counter-propagating shear experiments at high energy densities at the National Ignition Facility," *Phys. Plasmas*, **22**, 112701 (2015).

[466] P. Wang, K.S. Raman, S.A. MacLaren, C.M. Huntington, S.R. Nagel, K.A. Flippo, and S.T. Prisbrey. "Three-dimensional design simulations of a high-energy density reshock experiment at the National Ignition Facility." *ASME J. of Fluids Engineering,* **140**, 041207 (2018).

[467] D.A. Holder, C.J. Barton, Shock-tube richtmyer-meshkov experiments: inverse chevron and half height, in *Proceedings of the Ninth International Workshop on the Physics of Compressible Turbulent Mixing*, University of Cambridge, UK, 2004.

[468] X. Guo, J. Ding, X. Luo, and Z. Zhai, "Evolution of a shocked multimode interface with sharp corners," *Phys. Rev. Fluids*, **3**, 114004 (2018)

[469] F.F. Grinstein, J. A. Saenz, J. C. Dolence, T. O. Masser, R. M. Rauenzahn, and M. M. Francois. "Effects of operator splitting and low Mach-number correction in turbulent mixing transition simulations." *Comput. Math. Appl.*, **78** 437 (2019).

[470] W.G. Zeng, J.H. Pan, Y.X. Ren and Y.T. Sun, "Numerical study on the turbulent mixing of planar shock-accelerated triangular heavy gases interface," *Acta Mechanica Sinica*, **34**, 855 (2018).

[471] J.A. McFarland, J.A. Greenough, and D. Ranjan. "Computational parametric study of a Richtmyer-Meshkov instability for an inclined interface." *Phys. Rev.*

E, **84**, 026303 (2011).

[472] J.A. McFarland, D. Reilly, S. Creel, C. McDonald, T. Finn, and D. Ranjan. "Experimental investigation of the inclined interface Richtmyer-Meshkov instability before and after reshock." *Experiments in Fluids*, **55**, 1640 (2014).

[473] J.A. McFarland, D. Reilly, W. Black, J. A. Greenough, and D. Ranjan. "Modal interactions between a large-wavelength inclined interface and small-wavelength multimode perturbations in a Richtmyer-Meshkov instability." *Phys. Rev. E*, **92**, 013023 (2015).

[474] D. Reilly, J. McFarland, M. Mohaghar, and D. Ranjan. "The effects of initial conditions and circulation deposition on the inclined-interface reshocked Richtmyer-Meshkov instability." *Experiments in Fluids*, **56**, 168 (2015).

[475] M. Hahn, D. Drikakis, D.L. Youngs, R.J.R. Williams, "Richtmyer-Meshkov turbulent mixing arising from an inclined material interface with realistic surface perturbations and reshocked flow," *Phys. Fluids*, **23**, 046101 (2011).

[476] M. Mohaghar, J. Carter, G. Pathikonda, and D. Ranjan, "The transition to turbulence in shock-driven mixing: effects of Mach number and initial conditions, *J. Fluid Mech.*, **871**, 595 (2019).

[477] A. M. Rasmus, C. A. Di Stefano, K. A. Flippo, F. W. Doss, C. F. Kawaguchi, J. L. Kline, E. C. Merritt, T. R. Desjardins, T. Cardenas, D. W. Schmidt, P. M. Donovan, F. Fierro, L. A. Goodwin, J. I. Martinez, T. E. Quintana, J. S. Zingale, and C. C. Kuranz, "Shock-driven hydrodynamic instability of a sinusoidally perturbed, high-Atwood number, oblique interface," *Phys. Plasmas*, **26**, 062103 (2019)

[478] J.-S. Bai, J.-H. Liu, T. Wang, L.Y. Zou, P. Li, and D.-W. Tan. "Investigation of the Richtmyer-Meshkov instability with double perturbation interface in nonuniform flows." *Phys. Rev. E*, **81**, 056302 (2010).

[479] J.H. Liu, D.W. Tan, J.S. Bai, W.B. Wang, L.Y. Zou, X. Zhang, "Experimental study of Richtmyer-Meshkov instability in nonuniform flow by shock tube," *J. Exp. Mech.*, **27**, 160 (2012).

[480] J.-S. Bai, B. Wang, T. Wang, and K. Liu. "Numerical simulation of the Richtmyer-Meshkov instability in initially nonuniform flows and mixing with reshock." *Phys. Rev. E*, **86**, 066319 (2012).

[481] J.-X. Xiao, J.-S. Bai, and T. Wang. "Numerical study of initial perturbation effects on Richtmyer-Meshkov instability in nonuniform flows." *Phys. Rev. E*, **94**, 013112 (2016).

[482] L. Biferale, G. Boffetta, A.A. Mailybaev, and A.A. Scagliarini, "Rayleigh-Taylor turbulence with singular non-uniform initial conditions," *Phys. Rev. Fluids*, **3**, 092601(R) (2018)

[483] J. P. Mellado, S. Sarkar, and Y. Zhou, "Large-eddy simulation of Rayleigh-Taylor turbulence with compressible miscible fluids," *Phys. Fluids*, **17**, 076101 (2005).

[484] A. Scagliarini, L. Biferale, M. Sbragaglia, K. Sugiyama, and F. Toschi, "Lattice Boltzmann methods for thermal flows: Continuum limit and applications to compressible Rayleigh-Taylor systems," *Phys. Fluids*, **22**, 055101 (2010).

[485] G. Dimonte, P. Ramaprabhu, and M. Andrews. "Rayleigh-Taylor instability with complex acceleration history." *Phys. Rev. E*, **76**, 046313 (2007).

[486] D. Livescu, T. Wei, and M. R. Petersen. "Direct numerical simulations of Rayleigh-Taylor instability." *J. of Physics: Conference*, **318**, 082007 (2011).

[487] P. Ramaprabhu, V. Karkhanis, and A. G. W. Lawrie. "The Rayleigh-Taylor Instability driven by an accel-decel-accel profile." *Phys. Fluids*, **25**, 115104 (2013).

[488] D. Aslangil, A. Banerjee, and A.G.W. Lawrie. "Numerical investigation of initial condition effects on Rayleigh-Taylor instability with acceleration reversals." *Phys. Rev. E*, **94**, 053114 (2016).

[489] G. Boffetta, M. Magnani, S. Musacchio, "Suppression of Rayleigh-Taylor turbulence by time-periodic acceleration," *Phys. Rev. E*, **99**, 033110 (2019)

[490] B. Motl, J. Oakley, D. Ranjan, C. Weber, M. Anderson, and R. Bonazza. "Experimental validation of a Richtmyer-Meshkov scaling law over large density ratio and shock strength ranges." *Phys. Fluids*, **21**, 126102 (2009).

[491] G. C. Orlicz, B. J. Balakumar, C. D. Tomkins, and K. P. Prestridge. "A Mach number study of the Richtmyer-Meshkov instability in a varicose, heavy-gas curtain." *Phys. Fluids*, **21**, 064102 (2009).

[492] K.P. Prestridge, G. Orlicz, S. Balasubramanian, and B. J. Balakumar. "Experiments of the Richtmyer-Meshkov instability." *Phil. Trans. R. Soc. A*, **371**, 20120165 (2013).

[493] L.Y. Zou, J. Liu, S. Liao, X. Zheng, Z. Zhai, and X. Luo. "Richtmyer-Meshkov instability of a flat interface subjected to a rippled shock wave." *Phys. Rev. E*, **95**, 013107 (2017).

[494] S. Liao, W. Zhang, H. Chen, L.Y. Zou, J. Liu, and X. Zheng, "Atwood number effects on Richtmyer-Meshkov instabiliy induced by a nonuniform shock wave," *Phys. Rev. E*, **99**, 013103 (2019)

[495] R. Ishizaki, K. Nishihara, H. Sakagami, and Y. Ueshima. "Instability of a contact surface driven by a nonuniform shock wave." *Phys. Rev. E*, **53**, R5592 (1996).

[496] J. G. Wouchuk and F. Cobos-Campos. "Kinetic energy of the rotational flow behind an isolated rippled shock wave." *Physica Scripta*, **93**, 094003 (2018).

[497] W. Zhang, Q. Wu, L.Y. Zou, X. Zheng, X. Li, X. Luo, and J. Ding. "Mach number effect on the instability of a planar interface subjected to a rippled shock." *Phys. Rev. E*, **98**, 043105 (2018).

[498] K.P. Prestridge, S. Balasubramanian, G.C. Orlicz, Effects of initial conditions on mixing in Richtmyer-Meshkov turbulence experiments. In: K. Kontis (eds) 28th International Symposium on Shock Waves. Springer, Berlin, Heidelberg (2012)

[499] S. Balasubramanian, G. C. Orlicz, K. P. Prestridge, and B. J. Balakumar. "Experimental study of initial condition dependence on Richtmyer-Meshkov instability in the presence of reshock." *Phys. Fluids,* **24**, 034103 (2012).

[500] B. J. Balakumar, G. C. Orlicz, J. R. Ristorcelli, S. Balasubramanian, K. P. Prestridge, and C. D. Tomkins, "Turbulent mixing in a Richtmyer-Meshkov fluid layer after reshock: velocity and density statistics," *J. Fluid Mech.,* **696**, 67 (2012).

[501] S. Khoddam, L. Tian, T. Sapanathan, P.D. Hodgson, and A. Zarei-Hanzaki. "Latest developments in modeling and characterization of joining metal based hybrid materials." *Advanced Engineering Materials,* **20**, 1800048 (2018).

[502] M. Matys, K. Nishihara, M. Danielova, J. Psikal, G. Korn, S. V. Bulanov, "Generation of collimated quasi-mono-energetic ion beams using a double layer target with interface modulations," Proc. SPIE 11037, Laser Acceleration of Electrons, Protons, and Ions V, 110370Z (24 April 2019)

[503] S. M. J. Raad, H. Hassanzadeh, J. Ennis-King, "On the dynamics of twocomponent convective dissolution in porous media," *Water Resources Research*, (2019) doi: 10.1029/2018WR024572

[504] J.X.F. Ribeiro, R. Liao, A.M. Aliyu, W. Luo, Z. Liu, "Experimental study of horizontal two- and three-phase flow characteristics at low to medium liquid loading conditions," *Heat Mass Transfer*, (2019). https://doi.org/10.1007/s00231-019-02616-y

[505] O. A. Azarova and L. G. Gvozdeva. "Control of triple-shock configurations in high-speed flows over a cylindrically blunted plate in gases for different Mach numbers." *Proceedings of the Institution of Mechanical Engineers, Part G: J. of Aerospace Engineering*, (2018) DOI: 10.1177/0954410018795942

[506] T.A.Lapushkina, A.V. Erofeeva, O.A.Azarova, O.V. Kravchenko, "Interaction of a plane shock wave with an area of ionization instability of discharge plasma in air," *Aerospace Science and Technology*, **85**, 347 (2019). https://doi.org/10.1016/j.ast.2018.12.020

[507] N. Attal and P. Ramaprabhu. "Numerical investigation of a single-mode chemically reacting Richtmyer-Meshkov instability." *Shock Waves*, **25**, 307 (2015).

[508] N. Attal, P. Ramaprabhu, J. Hossain, V. Karkhanis, M. Uddin, J. R. Gord, and S. Roy. "Development and validation of a chemical reaction solver coupled to the FLASH code for combustion applications." *Computers & Fluids*, **107**, 59 (2015).

[509] N. Attal, Interfacial instabilities in reacting flows, PhD dissertation, The University of North Carolina at Charlotte, 2016

[510] H. Varshochi, The turbulent reacting Richtmyer-Meshkov Instability: A new canonical problem in non-premixed combustion, PhD dissertation, The University of North Carolina at Charlotte, 2016

[511] M. Vartdal and A. N. Osnes, "Linear motion of multiple superposed viscous fluids," *Phys. Rev E*, **99**, 043104 (2019).

[512] H.F. Li, Z.W. He, Y.S. Zhang, and B.L. Tian, "On the role of rarefaction/compression waves in Richtmyer-Meshkov instability with reshock," *Phys. Fluids*, **31**, 054102 (2019).

[513] E.E. Meshkov, "Some peculiar features of hydrodynamic instability development," *Phil. Trans. R. Soc. A*, **371**, 20120288 (2013).

[514] B. Akula, P. Suchandra, M. Mikhaeil, and D. Ranjan. "Dynamics of unstably stratified free shear flows: an experimental investigation of coupled Kelvin-Helmholtz and Rayleigh-Taylor instability." *J. Fluid Mech.*, **816**, 619 (2017).

[515] B. J. Olson, J. Larsson, S. K. Lele, and A. W. Cook. "Nonlinear effects in the combined Rayleigh-Taylor/Kelvin-Helmholtz instability." *Phys. Fluids*, **23**, 114107 (2011).

[516] S. Lugomer, "Laser-generated Richtmyer-Meshkov and Rayleigh-Taylor instabilities. III. Near-peripheral region of Gaussian spot." *Laser and Particle Beams*, **35**, 597 (2017).

[517] S. Lugomer, "Laser-generated Richtmyer-Meshkov and Rayleigh-Taylor instabilities in a semiconfined configuration: bubble dynamics in the central region of the Gaussian spot," *Phys. Scr.*, **94**, 015001 (2019).

[518] F. Chen, A. Xu, and G. Zhang. "Collaboration and competition between Richtmyer-Meshkov instability and Rayleigh-Taylor instability." *Phys. Fluids*, **30**, 102105 (2018).

[519] G. Sardina, L. Brandt, G. Boffetta, and A. Mazzino. "Buoyancy-driven flow through a bed of solid particles produces a new form of Rayleigh-Taylor turbulence." *Phys. Rev. Lett.*, **121**, 224501 (2018).

[520] G. F. Carnevale, P. Orlandi, Y. Zhou, and R. C. Kloosterziel. "Rotational suppression of Rayleigh-Taylor instability." *J. Fluid Mech.*, **457**, 181 (2002).

[521] K.A. Baldwin, M.M. Scase, and R.J.A. Hill. "The inhibition of the Rayleigh-Taylor instability by rotation." *Scientific Reports*, **5**, 11706 (2015).

[522] G. Boffetta, A. Mazzino, and S. Musacchio. "Rotating Rayleigh-Taylor turbulence." *Phys. Rev. Fluids*, **1**, 054405 (2016).

[523] M.M. Scase and R.J.A. Hill. "Centrifugally forced Rayleigh-Taylor instability." *J. Fluid Mech.*, **852**, 543 (2018).

[524] M.S. Davies Wykes, & S.B. Dalziel, "Efficient mixing in stratified flows: experimental study of a Rayleigh-Taylor unstable interface with an otherwise stable stratification," *J. Fluid Mech.*, **756**, 1027 (2014).

[525] M.S. Davies Wykes, G.O. Hughes, & S.B. Dalziel, "On the meaning of mixing efficiency for buoyancy driven mixing in stratified turbulent flows,' *J. Fluid Mech.*, **781**, 261 (2015).

[526] R.J.R. Williams, "Rayleigh-Taylor mixing between density stratified layers." *J. Fluid Mech.*, **810**, 584 (2017).

[527] R. Samtaney, "Suppression of the RichtmyerMeshkov instability in the presence of a magnetic field," *Phys. Fluids*, **15**, L53 (2003).

[528] W. Mostert, V. Wheatley, R. Samtaney, and D.I. Pullin, "Effects of magnetic fields on magnetohydrodynamic cylindrical and spherical Richtmyer-Meshkov instability," *Phys. Fluids*, **27**, 104102 (2015).

[529] R. Banerjee, "Nonlinear RayleighTaylor instability with horizontal magnetic field," *Indian J. Phys.*, (2019). https://doi.org/10.1007/s12648-019-01521-8

[530] Y. Liu, Z.-H. Chen, C. Zheng, "Kelvin-Helmholtz instability in anisotropic viscous magnetized fluid," *Acta Physica Sinica*, **68**, 035201 (2019)

[531] A. Hillier, "The magnetic Rayleigh-Taylor instability in solar prominences," *Reviews of Modern Plasma Physics*, **2**, 1 (2018).

[532] S.K. Mishra, T. Singh, P. Kayshap, and A. K. Srivastava, "Evolution of magnetic Rayleigh-Taylor instability into the outer solar corona and low interplanetary space," *Astrophys. J.*, **856**, 86. (2018).

[533] S.K. Mishra and A. K. Srivastava, "The evolution of magnetic Rayleigh-Taylor unstable plumes and hybrid KH-RT instability into a loop-like eruptive prominence," *Astrophys. J.*, **874**, 57. (2019).

[534] S. von Hoerner, "Lösungen der hydrodynamischen Gleichungen mit linearem Verlauf der Geschwindigkeit," *Z. Naturforsch. A*, **10**, 687 (1955)

[535] W. Häfele, "Zur analytishen Behandlung ebener, starker, instationärer Stowellen," *Z. Naturforsch. A*, **10**, 1006 (1955)

[536] V. B. Adamskii, "Integration of a system of autosimulating equations for the problem of a short duration shock in a cold gas." *Soviet Phys. Acoust.* (English Transl.) **2**, 1 (1956).

[537] G. M. Ward and D. I. Pullin, "A study of planar Richtmyer- Meshkov instability in fluids with Mie-Grüneisen equations of state," *Phys. Fluids*, **23**, 076101 (2011).

[538] A. L. Velikovich and J. L. Giuliani. "Solution of the Noh problem with an arbitrary equation of state." *Phys. Rev. E*, **98**, 013105 (2018).

[539] P. Ramaprabhu and M.J. Andrews, "On the initialization of RayleighTaylor simulations," *Phys. Fluids*, **16**, L59 (2004).

[540] N.J. Mueschke, M.J. Andrews, and O. Schilling. "Experimental characterization of initial conditions and spatio-temporal evolution of a small-Atwood-number Rayleigh-Taylor mixing layer." *J. Fluid Mech.,* **567**, 27 (2006).

[541] N.J. Mueschke and O. Schilling. "Investigation of Rayleigh-Taylor turbulence and mixing using direct numerical simulation with experimentally measured initial conditions. I. Comparison to experimental data." *Phys. Fluids*, **21**, 014106 (2009).

[542] O. Schilling and N.J. Mueschke. "Analysis of turbulent transport and mixing in transitional Rayleigh-Taylorunstable flow using direct numerical simulation data." *Phys. Fluids*, **22**, 105102 (2010).

[543] X. Liu, E. George, W. Bo, and J. Glimm. "Turbulent mixing with physical mass diffusion." *Phys. Rev. E*, **73**, 056301 (2006).

[544] J. Glimm, D.H. Sharp, T. Kaman, and H. Lim. "New directions for Rayleigh-Taylor mixing." *Philosophical Transactions of the Royal Society A*, **371**, 20120183 (2013).

[545] E. George, J. Glimm, X.-L. Li, Y.-H. Li, and X.-F. Liu,"Inuence of scale-breaking phenomena on turbulent mixing rates," *Phys. Rev. E*, **73**, 016304 (2006).

[546] N.J. Mueschke, Experimental and numerical study of molecular mixing dynamics in Rayleigh-Taylor unstable flows, PhD dissertation, Texas A & M University, 2008.

[547] H. Zhang, T. Kaman, D. She, B. Cheng, J. Glimm and D. H. Sharp. "V&V for Turbulent Mixing in the Intermediate Asymptotic Regime," *Pure and Applied Mathematics Quarterly*, **14**, 193 (2018)

[548] J. Glimm, B. Cheng, D. H. Sharp and T. Kaman. "A crisis for the V&V of turbulence simulations," arXiv:1901.07380, Los Alamos National Laboratory preprint LA-UR-19-20285, 2019.

[549] P. Ramaprabhu and M.J. Andrews, "Simultaneous measurements of velocity and density in buoyancy-driven mixing," *Experiments in fluids*, **34**, 98 (2003).

[550] B. J. Balakumar, G. C. Orlicz, C. D. Tomkins, & K. P. Prestridge, "Simultaneous particle-image velocimetry-planar laser-induced fluorescence measurements of Richtmyer-Meshkov instability growth in a gas curtain with and without reshock," *Phys. Fluids*, **20**, 124103 (2008).

[551] S. Gerashchenko and K. Prestridge. "Density and velocity statistics in variable density turbulent mixing." *J. of Turbulence*, **16**, 1011 (2015).

[552] M. Mohaghar, J. Carter, B. Musci, D. Reilly, J. McFarland, and D. Ranjan, "Evaluation of turbulent mixing transition in a shock-driven variable-density flow," *J. Fluid Mech.*, **831**, 779 (2017).

[553] E. Caroli, J. B. Stephen, G. Di Cocco, L. Natalucci, and A. Spizzichino. "Coded aperture imaging in x- and gamma-ray astronomy," *Space Science Reviews*, **45** 349 (1987).

[554] B. Bachmann, T. Hilsabeck, J. Field, N. Masters, C. Reed, T. Pardini, J. R. Rygg, N. Alexander, L. R. Benedetti, T. Döppner, A. Forsman, N. Izumi, S. LePape, T. Ma, A. G. MacPhee, S. Nagel, P. Patel, B. Spears, and O. L. Landen. "Resolving hot spot microstructure using x-ray penumbral imaging," *Review of Scientific Instruments*, **87**, 11E201, (2016).

[555] M. Raffel, C. E. Willert, and J. Kompenhans. Particle Image Velocimetry, Springer-Verlag, Berlin Heidelberg, 1998.

[556] C. Willert and J. Kompenhans. "PIV analysis of ludwig prandtl's historic flow visualization films," https://arxiv.org/abs/1010.3149v1, (2018).

[557] L. Prandtl. "Die entstehung von wirbeln in einer flüssigkeit kleinster reibung," *Zeitschrift für Flugtechnik und Motorluftschiffahrt*, **18**, 489 (1927).

[558] L. Prandtl. "Entstehung von wirbeln bei wasserströmungen - 1. entstehung von wirbeln und künstliche beeinflussung der wirbelbildung," *Institut für Wis- senschaftlichen Film (IWF)*, 1936.

[559] J. F. Hansen, W. van Breugel, E. M. Bringa, B. Eberly, G. A. Graham, B. A. Remington, E. A. Taylor, and A.G.G.M. Tielens. "A new method to generate dust with astrophysical properties," *J. of Instrumentation*, **6**, P05010, (2011).

[560] L. Claus, T. England, L. Fang, G. Robertson, M. Sanchez, D. Trotter, A. Carpenter, M. Dayton, P. Patel, and J. L. Porter. "Design and characterization of an improved, 2 ns, multi-frame imager for the ultra-fast x-ray imager (uxi) program at sandia national laboratories," Proc. SPIE 10390, Target Diagnostics Physics and Engineering for Inertial Confinement Fusion VI, 103900A (24 August 2017).

[561] L. Claus, G. Robertson, L. Fang, R. Kay, M. W. Kimmel, M. Sanchez, J. W. Stahoviak, D. Trotter, and J. L. Porter. "Initial characterization results of a 1024x448, 25-um multi-frame camera with 2ns integration time for the Ultrafast X-ray Imager (UXI) program at Sandia National Laboratories," Proc. SPIE 9966, Target Diagnostics Physics and Engineering for Inertial Confinement Fusion V, 99660F (19 September 2016).

[562] S. R. Nagel, A. C. Carpenter, J. Park, M. S. Dayton, P. M. Bell, D. K. Bradley, B. T. Funsten, B. W. Hatch, S. Heerey, J. M. Hill, J. P. Holder, E. R. Hurd, C. C. Macaraeg, P. B. Patel, R. B. Petre, K. Piston, C. A. Trosseille, K. Engelhorn, T. J. Hilsabeck, T. M. Chung, A. K. L. Dymoke-Bradshaw, J. D. Hares, L. D. Claus, T. D. England, B. B. Mitchell, J. L. Porter, G. Robertson, and M. O. Sanchez. "The dilation aided single–line–of–sight x–ray camera for the national ignition facility: Characterization and fielding," *Review of Scientific Instruments*, **89**, 10G125, (2018).

[563] K. Engelhorn, T. J. Hilsabeck, J. Kilkenny, D. Morris, T. M. Chung, A. Dymoke-Bradshaw, J. D. Hares, P. Bell, D. Bradley, A. C. Carpenter, M. Dayton, S. R. Nagel, L. Claus, J. Porter, G. Rochau, M. Sanchez, S. Ivancic, C. Sorce, and W. Theobald. "Sub-nanosecond single line-of-sight (slos) x-ray imagers,". *Review of Scientific Instruments*, **89**, 10G123, (2018).

[564] J.G. Charney, "Geostrophic turbulence," *J. Atmos.*

Sci., **28**, 1087 (1971).

[565] K.S. Gage, "Evidence for a $k^{-5/3}$ law inertial range in mesoscale two-dimensional turbulence," *J. Atmos. Sci.*, **36**, 1950 (1979)

[566] J.R. Herring, "Statistical theory of quasi-geostrophic turbulence." *J. Atmos. Sci.*, **37**, 969 (1980).

[567] D.K. Lilly, "Stratified turbulence and the mesoscale variability of the atmosphere," *J. Atmos. Sci.*, **40**, 749 (1983)

[568] J.A. Zhang, K.B. Katsaros, P.G. Black, S. Lehner, J.R. French, and W.M. Drennan, "Effects of roll vortices on turbulent fluxes in the hurricane boundary layer," *Boundary-layer Meteorology*, **128**, 173 (2008).

[569] R.M.B. Young and P.L. Read. "Forward and inverse kinetic energy cascades in Jupiter's turbulent weather layer." *Nature Physics*, **13**, 1135 (2017).

[570] R.H. Kraichnan and D. Montgomery. "Two-dimensional turbulence." *Reports on Progress in Physics*, **43**, 547 (1980).

[571] P. Tabeling, "Two-dimensional turbulence: a physicist approach," *Phys. Rep.*, **362**, 1 (2002).

[572] G. Boffetta and R.E. Ecke, "Two-dimensional turbulence," *Annual Review of Fluid Mechanics,* **44**, 427 (2012).

[573] W. Cabot, "Comparison of two- and three- dimensional simulations of miscible Rayleigh-Taylor instability." *Phys. Fluids*, **18**, 045101 (2006).

[574] B.J. Olson and J.A. Greenough, "Comparison of two-and three- dimensional simulations of miscible Richtmyer-Meshkov instability with multimode initial conditions." *Phys. Fluids*, **26**, 101702 (2014).

[575] R.H. Kraichnan, "Inertial ranges in two-dimensional turbulence." *Phys. Fluids*, **10**, 1417 (1967).

[576] C.E. Leith, "Diffusion approximation for two-dimensional turbulence." *Phys. Fluids*, **11**, 671 (1968).

[577] G.K. Batchelor, "Computation of the energy spectrum in homogeneous two-dimensional turbulence." *Phys. Fluids*, **12**, II-233 (1969).

[578] G. Boffetta and S. Musacchio. "Evidence for the double cascade scenario in two-dimensional turbulence." *Phys. Rev. E*, **82**, 016307 (2010).

[579] T.T. Clark, "A numerical study of the statistics of a two-dimensional Rayleigh-Taylor mixing layer." *Phys. Fluids*, **15**, 2413 (2003).

[580] B. Thornber and Y. Zhou. "Numerical simulations of the two-dimensional multimode Richtmyer-Meshkov instability." *Phys. Plasmas*, **22**, 032309 (2015).

[581] D. I. Pullin and P. G. Saffman. "Vortex dynamics in turbulence." *Annual review of fluid mechanics*, **30**, 31 (1998).

[582] S. Le Pape, L.F. Berzak Hopkins, L. Divol, A. Pak, E. Dewald, N. B. Meezan, D. D-M. Ho, S. F. Khan, A. J. Mackinnon, C. Weber, C. Goyon, J. S. Ross, J. Ralph, J. Milovich, M. Millot, L. R. Bennedetti, N. Izumi, G. A. Kyrala, T. Ma, S. R. Nagel, D. Edgell, A. G. MacPhee, B. J. MacGowan, P. Michel, D. Strozzi, D. N. Fittinghoff, D. Casey, R. Hatarik, P. Volegov, C. Yeamans, M. Gatu-Johnson, J. Biener, N. G. Rice, M. Stadermann, S. Bhandarkar, S. Haan, P. Patel, D. Callahan, and O. A. Hurricane, "Fusion energy output greater than the kinetic energy of an imploding shell at the National Ignition Facility," *Phys. Rev. Lett.* **120**, 245003 (2018).

[583] K. L. Baker, C. A. Thomas, D. T. Casey, S. Khan, B. K. Spears, R. Nora, T. Woods, J. L. Milovich, R. L. Berger, D. Strozzi, D. Clark, M. Hohenberger, O. A. Hurricane, D. A. Callahan, O. L. Landen, B. Bachmann, R. Benedetti, R. Bionta, P.M. Celliers, D. Fittinghoff, C. Goyon, G. Grim, R. Hatarik, N. Izumi, M. Gatu Johnson, G. Kyrala, T. Ma, M. Millot, S. R. Nagel, A. Pak, P. K. Patel, D. Turnbull, P. L. Volegov, and C. Yeamans, "High-performance indirect-drive cryogenic implosions at high adiabat on the National Ignition Facility," *Phys. Rev. Lett.*, **121**, 135001 (2018).

[584] D. Layzer, "On the instability of superposed fluids in a gravitational field," *Astrophys. J.* **122**, 1 (1955).

[585] V. A. Smalyuk, H. F. Robey, D. T. Casey, D. S. Clark, T. Dóppner, S. W. Haan, B. A. Hammel et al. "Mix and hydrodynamic instabilities on NIF." *J. of Instrumentation*, **12**, C06001 (2017).

[586] V. A. Smalyuk, H. F. Robey, C. L. Alday, P. Amendt, C. Aracne-Ruddle, J. R. Bigelow, T. Bunn et al. "Review of hydro-instability experiments with alternate capsule supports in indirect-drive implosions on the National Ignition Facility." *Phys. Plasmas,* **25**, 072705 (2018).

[587] B.M. Haines, F.F. Grinstein, and J.R. Fincke. "Three-dimensional simulation strategy to determine the effects of turbulent mixing on inertial-confinement-fusion capsule performance." *Phys. Rev. E*, **89**, 053302 (2014).

[588] B.M. Haines, C. H. Aldrich, J. M. Campbell, R. M. Rauenzahn, and C. A. Wingate. "High-resolution modeling of indirectly driven high-convergence layered inertial confinement fusion capsule implosions." *Phys. Plasmas*, **24**, 052701 (2017).

[589] B.M. Haines, R.E. Olson, W. Sweet, S.A. Yi, A.B. Zylstra, P.A. Bradley, F. Elsner, H. Huang, R. Jimenez, J.L. Kline, and C. Kong, "Robustness to hydrodynamic instabilities in indirectly driven layered capsule implosions," *Phys. Plasmas*, **26**, 012707 (2019).

[590] H.-Th Janka, T. Melson, and A. Summa. "Physics of core-collapse supernovae in three dimensions: a sneak preview." *Annual Review of Nuclear and Particle Science*, **66** 341 (2016).

[591] J. R. Wilson, "Supernovae and post-collapse behavior," in *Numerical Astrophysics*, ed. J. Centrella, JM LeBlanc, RL Bowers. Jones and Bartlett, Boston (1985) 422.

[592] F.S. Kitaura, H.-Th Janka, and W. Hillebrandt. "Explosions of O-Ne-Mg cores, the Crab supernova, and subluminous type II-P supernovae." *Astronomy & Astrophysics*, **450**, 345 (2006).

[593] A. Marek and H.-Th Janka. "Delayed neutrino-driven supernova explosions aided by the standing accretion-shock instability." *Astrophys. J.*, **694**, 664 (2009).

[594] M.A. Skinner, A. Burrows, and J.C. Dolence. "Should one use the ray-by-ray approximation in core-collapse supernova simulations?" *Astrophys. J.*, **831**, 81 (2016).

[595] D. Vartanyan, A. Burrows, D. Radice, M. A. Skinner, and J. Dolence. "A successful 3D core-collapse supernova explosion model." *Monthly Notices of the Royal Astronomical Society*, **482**, 351 (2018).

[596] M. Rampp and H.-T. Janka. "Radiation hydrodynamics with neutrinos-Variable Eddington factor method for core-collapse supernova simulations." *Astronomy & Astrophysics,* **396**, 361 (2002).

[597] T.A. Thompson, A. Burrows, and P.A. Pinto. "Shock breakout in core-collapse supernovae and its neutrino signature." *Astrophys. J.*, **592**, 434 (2003).

[598] C. J. Horowitz, O. L. Caballero, Z. Lin, E. O'Connor,

& A. Schwenk, "Neutrino-nucleon scattering in supernova matter from the virial expansion," *Phys. Rev. C*, **95**, 025801 (2017).

[599] P. Sagaut, Large eddy simulation for incompressible flows: an introduction. 3rd edition, Springer, Berlin, 2006.

[600] C. Meneveau and J. Katz, "Scale-invariance and turbulence models for large-eddy simulation." *Annual Review of Fluid Mechanics*, **32**, 1 (2000).

[601] J. A. Domaradzki and N. A. Adams, "Direct modelling of subgrid scales of turbulence in large eddy simulations," *J. Turbul.*, **3**, 024 (2002).

[602] D. Dupuy, A. Toutant, and F. Bataille, "A posteriori tests of subgrid-scale models in an isothermal turbulent channel flow." *Phys. Fluids*, **31**, 045105 (2019).

[603] Y. Zhou, F.F. Grinstein, A.J. Wachtor, and B.M. Haines. "Estimating the effective Reynolds number in implicit large-eddy simulation." *Phys. Rev. E*, **89**, 013303 (2014).

[604] Y. Zhou and B. Thornber. "A comparison of three approaches to compute the effective Reynolds number of the implicit Large-Eddy simulations." *ASME J. of Fluids Engineering*, **138**, 070905 (2016).

[605] S. Rahman and O. San, "A relaxation filtering approach for two-dimensional RayleighTaylor instability-induced flows," *Fluids*, **4**, 78 (2019).

[606] O. Sadot, L. Erez, U. Alon, D. Oron, L. A. Levin, G. Erez, G. Ben-Dor, and D. Shvarts. "Study of nonlinear evolution of single-mode and two-bubble interaction under Richtmyer-Meshkov instability." *Phys. Rev. Lett.*, **80**, 1654 (1998).

[607] B. Cheng, J. Glimm, and D. H. Sharp. "Density dependence of Rayleigh-Taylor and Richtmyer-Meshkov mixing fronts." *Physics Letters A*, **268**, 366 (2000).

[608] B. Cheng, J. Glimm, and D. H. Sharp. "A three-dimensional renormalization group bubble merger model for Rayleigh-Taylor mixing." *Chaos: An Interdisciplinary J. of Nonlinear Science*, **12**, 267 (2002).

[609] D. Oron, L. Arazi, D. Kartoon, A. Rikanati, U. Alon, and D. Shvarts. "Dimensionality dependence of the Rayleigh-Taylor and Richtmyer-Meshkov instability late-time scaling laws." *Phys. Plasmas*, **8**, 2883 (2001).

[610] D.L. Youngs, "Numerical simulation of mixing by Rayleigh-Taylor and Richtmyer-Meshkov instabilities," *Laser and Particle Beams*, **12**, 725 (1994).

[611] Y. Zhou, G.B. Zimmerman, and E.W. Burke. "Formulation of a two-scale transport scheme for the turbulent mix induced by Rayleigh-Taylor and Richtmyer-Meshkov instabilities." *Phys. Rev. E*, **65**, 056303 (2002).

[612] B. Thornber, M. Groom and D. Youngs, "A five-equation model for the simulation of miscible and viscous compressible fluids," *J. of Computational Physics*, **372**, 256 (2018)

[613] D. Besnard, F. Harlow, R. Rauenzahn, and C. Zemach, Turbulence transport equations for variable-density turbulence and their relationship to two-field models, Los Alamos National Laboratory LA-12303-MS, 1992.

[614] A. Banerjee, R.A. Gore, and M.J. Andrews. "Development and validation of a turbulent-mix model for variable-density and compressible flows." *Phys. Rev. E*, **82**, 046309 (2010).

[615] J.D. Schwarzkopf, D. Livescu, R.A. Gore, R.M. Rauenzahn, and J. R. Ristorcelli. "Application of a second-moment closure model to mixing processes involving multicomponent miscible fluids." *J. Turbul.,* **12** N49 (2011).

[616] O. Grégoire, D. Souffland, and S. Gauthier. "A second-order turbulence model for gaseous mixtures induced by Richtmyer-Meshkov instability." *J. Turbul.*, **6**, N29 (2005).

[617] J.D. Schwarzkopf, D. Livescu, J.R. Baltzer, R. A. Gore, and J. R. Ristorcelli. "A two-length scale turbulence model for single-phase multi-fluid mixing." *Flow, Turbulence and Combustion*, **96**, 1 (2016).

[618] G. Dimonte and R. Tipton. "K-L turbulence model for the self-similar growth of the Rayleigh-Taylor and Richtmyer-Meshkov instabilities." *Phys. Fluids*, **18**, 085101 (2006).

[619] I. W. Kokkinakis, D. Drikakis, D. L. Youngs, and R. J. R. Williams. "Two-equation and multi-fluid turbulence models for Rayleigh-Taylor mixing." *International J. of Heat and Fluid Flow,* **56**, 233 (2015).

[620] BE Morgan & ME Wickett, "Three-equation model for the self-similar growth of Rayleigh-Taylor and Richtmyer-Meskov instabilities," *Phys. Rev. E*, **91**, 043002 (2015).

[621] BE Morgan, O Schilling, TA Hartland, "Two-length-scale turbulence model for self−similar buoyancy−, shock−, and shear−driven mixing," *Phys. Rev. E*, **97**, 013104 (2018).

[622] I. W. Kokkinakis, D. Drikakis, and D. L. Youngs, "Modeling of Rayleigh-Taylor mixing using single-fluid models." *Phys. Rev. E*, **99**, 013104 (2018).

[623] C. Mügler and S. Gauthier, "Two-dimensional Navier-Stokes simulations of gaseous mixtures induced by Richtmyer-Meshkov instability," *Phys. Fluids*, **12**, 1783 (2000).

[624] J.T. Morn-Lpez and O. Schilling. "Multicomponent Reynolds-averaged Navier-Stokes simulations of reshocked Richtmyer-Meshkov instability-induced mixing." *High Energy Density Physics*, **9**, 112 (2013).

[625] O Schilling and N.J. Mueschke, "Turbulent transport and mixing in transitional Rayleigh-Taylor unstable flow: A priori assessment of gradient-diffusion and similarity modeling," *Phys. Rev. E*, **96**, 063111 (2017).

[626] B. Rollin, M.J. Andrews, "On generating initial conditions for turbulence models: the case of Rayleigh-Taylor instability turbulent mixing," *J. Turbul.*, **14**, 77 (2013).

[627] M.A. Brown, C.A. Batha, R.J.R. Williams, "Statistics for assessing mixing in a finite element hydrocode," *ASME J. Fluids Eng.*, **136**, 091103 (2014).

[628] J.J. Charonko and K.P. Prestridge. "Variable-density mixing in turbulent jets with coflow." *J. Fluid Mech.*, **825**, 887 (2017).

[629] C.C. Lai, J.J. Charonko, and K. Prestridge, "A Kármán-Howarth-Monin equation for variable-density turbulence," *J. Fluid Mech.,* **843**, 382 (2018).

[630] G. I. Bell, Taylor instability on cylinders and spheres in the small amplitude approximation, Los Alamos Scientific Laboratory Report No. LA-1321, 1951.

[631] M. S. Plesset, "On the stability of fluid flows with spherical symmetry," *J. Appl. Phys.*, **25**, 96 (1954).

[632] K.O. Mikaelian, "Stability and mix in spherical geometry." *Phys. Rev. Lett.*, **65**, 992 (1990).

[633] K.O. Mikaelian, "Rayleigh-Taylor and Richtmyer-Meshkov instabilities and mixing in stratified spherical shells." *Phys. Rev. A*, **42**, 3400 (1990).

[634] K.O. Mikaelian, "Rayleigh-Taylor and Richtmyer-Meshkov instabilities and mixing in stratified cylindrical

shells." *Phys. Fluids*, **17**, 094105 (2005).
[635] M. Vandenboomgaerde, P. Rouzier, D. Souffland, L. Biamino, G. Jourdan, L. Houas, and C. Mariani. "Nonlinear growth of the converging Richtmyer-Meshkov instability in a conventional shock tube." *Phys. Rev. Fluids*, **3**, 014001 (2018).
[636] I. Boureima, P. Ramaprabhu, and N. Attal. "Properties of the turbulent mixing layer in a spherical implosion." *ASME J. of Fluids Engineering*, **140**, 050905 (2018).
[637] X. Luo, F. Zhang, J. Ding, T. Si, J. Yang, Z. Zhai, and C.-Y. Wen. "Long-term effect of Rayleigh-Taylor stabilization on converging Richtmyer-Meshkov instability." *J. Fluid Mech.*, **849**, 231 (2018).
[638] Z. Wu, S. Huang, J. Ding, W. Wang, and X. Luo. "Molecular dynamics simulation of cylindrical Richtmyer-Meshkov instability." *Sci. China-Phys. Mech. Astron.*, **61**, 114712 (2018).